KU LEUVEN

FACULTY OF SCIENCE

The influence of an interior magnetic field on gravity-mode oscillations of intermediate-mass stars

Jordan Van Beeck

Supervisor: Prof. Dr. C. Aerts
Instituut voor Sterrenkunde,
Department of Physics & Astronomy,
KU Leuven

Co-supervisors:
Dr. T. Van Reeth, Dr. D. M. Bowman
Instituut voor Sterrenkunde,
Department of Physics & Astronomy,
KU Leuven

Thesis presented in
fulfillment of the requirements
for the degree of Master of Science
in Astronomy & Astrophysics

Academic year 2018-2019

Preface

In the opening paragraph of his book, *The Internal Constitution of the Stars* (Eddington, 1926), Sir Arthur Stanley Eddington asked himself the question:

> Our telescopes may probe farther and farther into the depths of space; but how can we ever obtain certain knowledge of that which is hidden behind substantial barriers? What appliance can pierce throught the outer layers of a star and test the conditions within?

The appliance that can be used to probe the deep stellar interior is asteroseismology, the Music of the Stars (Aerts et al., 2010). Indeed, as discussed in great detail in Aerts et al. (2010), sound waves (otherwise known as "pressure" or p modes) propagate inside stars, generating temperature variations at the stellar surface that are detected through variable light output in time.

However, as was mentioned in Aerts et al. (2010): "It is not as simple as that!" Other waves propagate inside stars that are not acoustic. Equally important are e.g. the "gravity" or g modes that propagate inside these stars, where the restoring force of the pulsation is not the pressure gradient, but buoyancy. These modes are the ones that let us explore the deep interior of stars, however, most of these modes only properly revealed themselves when time series from the National Aeronautics and Space Administration (NASA) *Kepler* satellite became available. Typically, several assumptions and simplifications are made to study wave propagation inside stars. Pulsation models are typically obtained from introducing small perturbations to the equations that govern the structure of an equilibrium model of a star. In the earliest models, stars were approximated as being homogeneous spheres that do not rotate and are not magnetic. The quote "It is not as simple as that!" has to be repeated when one considers how rotation and magnetism affect the equilibrium models and the pulsation models. Earlier work has shown the (major) importance of rotation on both equilibrium and pulsation models. As will be shown in this work, the pulsation models are sometimes strongly affected by the presence of a weak internal magnetic field, whose effects on the equilibrium model are thought to be negligible. It remains to be elucidated however, how strong internal magnetic fields interact with both models.

The inspiration for this work originated from the findings of Fuller et al. (2015), who investigated how a potential internal magnetic field interacts with the pulsation modes inside evolved red giant stars. Observations of these stars indicated that some of these stars display variability that cannot be explained with conventional models: they exhibit some 'missing' modes. As Fuller et al. (2015) explained in great detail, and as is summarized in the introduction, the stellar internal magnetic fields can greatly affect pulsation modes, causing some to become trapped in the deep interior. This might be an explanation for the origin of the 'missing' modes, although other authors depict other mechanisms to be the cause (e.g. Mosser et al., 2017). This standing problem might be resolved by detecting such internal magnetic fields in their progenitors, the less evolved stars considered in this work. Therefore, it provided the direct incentive to start our work.

If it had not been for the presentation given by Prof. Dr. Jim Fuller when visiting Leuven, I would not have known about this issue, and would not have proposed this topic to my supervisor Prof. Dr. Conny Aerts. Therefore, I would like to thank Jim for providing the incentive that sparked this interesting work!

I would like to thank Conny for guiding me through the whole process of writing this thesis, allowing me to pursue this interesting topic, providing me with mental support when needed, introducing me to the contacts that have proven to be invaluable to this work, and for the pleasant atmosphere throughout all of our discussions. The quote from her book (Aerts et al., 2010) mentioned earlier in this preface was surely invoked in some of these discussions! Moreover, she also gave me the opportunity to present a small part of this work on the *Nederlandse Astronomenconferentie* (NAC), for which I am grateful.

I would like to thank my two co-supervisors Dr. Dominic Bowman and Dr. Timothy Van Reeth for also guiding me through the whole process of writing this thesis. They have always been ready to respond to my (many) questions in an appropriate way, stimulating me to further develop parts of the concepts in this work. They provided me with the essential viewing point of the observational asteroseismologist/astronomer, allowing me to express potential observational diagnostics in a way that can easily be verified through observations in the near future. They provided me with mental support when I discovered yet another flaw in my computational setup. (Although the final setup worked out quite well, as discussed in our conclusions.) Dominic first introduced me to the GYRE pulsation code, the pulsation code that has proven of great value to this work, and Timothy further expanded my knowledge. Finally, Timothy showed me how to deal with some of my pythonic struggles. For all that, I am indefinitely grateful!

I would like to thank Prof. Dr. Stéphane Mathis and Dr. Vincent Prat, the co-developers of the formalism used in this work and co-authors of the publication that explains the basics of this formalism, developed during the first semester of academic year 2018-2019. They provided me numerous times with theoretically oriented advice during the biannual MAMSIE/CEA/Newcastle meetings, and were always available through e-mail. Especially Vincent has been greatly accessible and has lightened the mood numerous times during our meetings, for which I am very grateful. Certainly, they proved to be invaluable in the development of our formalism, which is explored in greater detail in this work than was done in the publication. I hope we can convert our mutually beneficial professional relation into more publications on this endearing topic in the near future!

I would like to thank my office roommates Dr. Dylan Kee, Ana Escorza Santos, Shreeya Shetye and Karan Dsilva for taking me up as one of their own, showing me what it means to take part in academic matters as well as less academic matters. They provided me on several occasions with the necessary feedback, helped me with my pythonic and less pythonic struggles, made the office look like a Christmas tree at appropriate times, and in general ensured that I had a great time whilst writing this thesis and finishing up my coursework. Numerous interesting discussions were sparked throughout the year, many of which were not necessarily related to the topic of this work. However, these comments surely enriched my knowledge and changed my view on the academic world. For that, I can only be grateful!

I would like to thank Mathias Michielsen, a PhD student that helped with the onset of the development of my computational setup, providing me with useful comments related to how to optimally generate a grid of stellar evolution and pulsation models. For that, I am very grateful!

I would like to thank my friends/fellow students for providing me with the necessary support throughout the past two academic years. Indeed, my fellow students, such as Joris Hermans and Sven Nys, provided me with a further critical outlook on the results of this work. They further made life enjoyable throughout the sometimes stressful years, joining me on several endeavours in which we explored numerous astrophysical problems, providing witty comments when suited. They (Joris Hermans and Sven Nys) even joined me at the NAC, presenting their more observationally oriented, interesting work on pulsations in specific types of stars. I would thus like to thank them for these enjoyable years!

Lastly, I would like to thank my family (especially my parents) for their support whilst piecing together this thesis throughout the year. I have not always been the most enjoyable person near the deadlines, for which I can only apologize. Nevertheless, they always helped me get on track with the numerous projects in which I was involved. They showed me that life should not always revolve around the stars, even though our planet revolves around one. I cannot list the numerous moments for which I am grateful. In short, they made me the person I am today!

Summary

Stars make up most of the visible baryonic matter in the universe. They significantly influence their immediate surroundings by means of their activity and couple back (chemically) on galactic scales through their winds and explosions. The physics of these important objects is well-described globally. However, some key aspects remain to be elucidated, among which their interior magnetic properties.

We will treat magnetic fields inside OBA spectral type main-sequence stars, which burn hydrogen in their core, providing a framework to derive observational constraints. In order to characterize these internal fields, we cannot rely on conventional methods, as we need to probe the near-core regions. This can be done with gravity-mode (g mode) asteroseismology, the study of stellar g mode oscillations. These are detected in long time series obtained with the NASA *Kepler* satellite and probe the region of interest. Our method provides a unique way to infer interior magnetism in stars, not yet available in the scarce literature available on this topic. We consider a poloidal-toroidal axisymmetric field and derive a general formalism, within the Traditional Approximation of Rotation (TAR), that allows one to describe rapidly rotating magnetic stars. Moreover, we explicitly calculate the Hough functions, allowing us to describe subinertial modes.

We investigated how the stellar fundamental parameters and some numerical parameters connected with code implementation affect the main diagnostic in g mode asteroseismology: period spacing patterns. The effect of the numerical parameters is found to be negligible, providing us with a robust computational setup. The rotation rate affects the magnetic influence significantly, reducing it with increasing rotation rate. Magnetic influence scales with field strength, and only the strongest field exerts significant influence on the mode frequencies. The field structure and corresponding effect is widely differing throughout the star's evolution on the main sequence. Stars at the end of their main sequence burning phase are found to be excellent probes of internal magnetic fields. The three considered parameters that describe internal chemical mixing each exert a slightly different influence. No clear changes in the mode frequencies were found when changing metallicity.

Finally, we also investigated the phenomenon of mode bumping, where different g modes propagating inside the star interact. This typically did not receive much attention for the stars considered in the literature so far. However, we show that both rotation and magnetism can lead to such interaction, potentially confusing the mode identification.

The considered set of stars are the potential progenitors of a specific type of red giant stars that do not display expected dipole mode variability. One of the possible explanations of the origin of this missing variability is the presence of a strong internal magnetic field, that is inherited from their progenitors (the main sequence stars considered here).

We conclude that moderately strong internal magnetic fields inside OBA spectral type main-sequence stars are detectable with the derived formalism. In the near future, this formalism will be expanded to include more realistic magnetic field configurations, looking at ways of generalizing the conclusions drawn here, and will apply our theoretical predictions in the seismic modelling of stars observed with the NASA *Kepler* satellite.

Vulgarizing Summary

Stars make up most of the visible matter in the universe. Effectively, stars are the efficient nuclear reactors of our universe, processing the elements/nuclides and shaping their immediate surroundings, e.g. making life possible on earth. They spend most of their lives fusing hydrogen in their core, the so-called main sequence life phase. In this work we only consider such (easily observable) stars, and assume them to be slightly more massive than our Sun.

Their evolution is dictated by the equations of stellar structure and evolution theory, as clarified in the first chapter. These can describe global aspects quite well. However, some key aspects remain to be elucidated, among which their interior magnetic properties. One of the key questions theorists ask themselves is how strong magnetic fields inside these stars affect stellar structure and evolution. For simplicity, we investigate weak internal magnetic fields of main sequence stars, so that the overall effect on the internal structure is negligible.

In order to characterize such internal fields, we cannot rely on conventional methods which do not probe the deep interior. Instead, we rely on gravity-mode (g mode) asteroseismology, the study of stellar oscillations or pulsation modes that are restored by the Archimedes force/buoyancy. These are detected in long time series observed with the NASA *Kepler* satellite and indirectly provide information on the deep stellar interior.

In this work we derived a new formalism that provides a unique way to infer magnetism inside stars, not yet available in current literature, providing a more sophisticated magnetic field model and corresponding model of the magnetic influence on the pulsation mode frequencies. We strongly increased the sample of stars that could be studied, as the formalism allows one to include the effect of rapid rotation, a common feature for the considered type of star, allowing us to derive observational constraints on internal magnetic fields. In addition, we explored how different stellar and pulsation models are affected by the internal magnetic field. We found that numerical parameters have negligible influence on mode frequencies, which provides us with a robust computational setup. In addition, field structure and magnetic influence on mode frequencies are found to vary with evolutionary state. Stars at the end of the main sequence are found to be excellent targets for characterizing internal magnetic fields. Increasing rotation generally decreases the magnetic influence, whereas other parameters produce secondary, slightly differing effects.

The characterized magnetic fields inside these stars can be linked to a phenomenon observed in stars that are more evolved (stars that have stopped core hydrogen fusion). Several of these stars have been observed to display peculiar variability, the origin of which has been investigated in the literature. One of the possible origins are strong magnetic fields in the deep interior that have been inherited from an earlier evolutionary phase (i.e. the main sequence).

We conclude that moderately strong internal magnetic fields inside main sequence stars slightly heavier than our Sun are detectable with the derived formalism. In the near future, we will apply our formalism in the modelling of stars observed with the NASA *Kepler* satellite, and will develop more sophisticated field models, in order to generalize the conclusions drawn here.

Contents

1 — Introduction

The theory of stellar structure and evolution (SSE) is very important for modern astronomy and astrophysics research. It explains how stars, which encompass most of the visible matter in the universe, evolve. Stars significantly influence their surroundings, on largely varying spatial and time scales. For example, stellar gravity and luminosity dominate planetary motions and act as the primary source of energy for most planets and are therefore also decisive for habitability, respectively (see e.g. de Pater and Lissauer, 2015; Gallet et al., 2016). In addition, planetary systems are formed from the dusty discs created due to angular momentum conservation of collapsing molecular clouds around young stellar objects (YSOs) (see e.g. Ward-Thompson and Whitworth, 2015; Armitage, 2010). Smaller (spatial) scale phenomena, such as stellar mass loss and the composition of stellar outflows, affect both star and galaxy formation, e.g. by changing the composition on timescales shorter than galactic timescales of stars being born (see e.g. Kippenhahn et al., 2012; Hopkins et al., 2014, and references therein). The ejecta from evolved stars also chemically enrich the interstellar medium. They contain the products of the nuclear burning processes inside the star and form (icy) dust grains on which organic compounds might form (see e.g. Kwok, 2004, 2008).

Global aspects of stellar structure and evolution are currently well-understood. However, other key aspects of stellar structure remain unclear, such as internal stellar rotation, deep internal mixing and both external and internal magnetism (see e.g. Zahn, 1992; Maeder, 2009; Aerts et al., 2014, 2019). In this thesis, we take a closer look at stellar magnetism, using asteroseismology, the study of stellar structure by analysis of stellar pulsations (Aerts et al., 2010).

Stellar pulsations cause fluctuations in stellar luminosity, which can be observed. Thanks to the high-precision long-timebase photometry, obtained with recent space missions such as the NASA *Kepler* space telescope (Koch et al., 2010) and the *Transiting Exoplanet Survey Satellite* (TESS; Ricker et al., 2015), stellar variability that is undetectable from the ground, has been observed (Aerts et al., 2010). To analyse the interior structure of a variable star, the observed pulsations are identified and used as input for asteroseismic modelling, which consists of comparing the observed pulsation frequencies with the theoretical frequencies for a grid of stellar models (for recent examples see e.g. Aerts et al., 2018; Buysschaert et al., 2018; Hendriks and Aerts, 2018; Mombarg et al., 2019).

Due to a lack of (observational) constraints, the effects of magnetic fields in SSE are often neglected. We will determine the effect of magnetic fields on stellar pulsation frequencies, including rotational influence due to the Coriolis force, providing a new perspective on the origin of the phenomenon of missing dipole modes in about one quarter of red giant stars observed by *Kepler* (see Section (1.2)).

In first instance, we constrain ourselves to intermediate-mass main-sequence (MS) stars. Recent studies indicate that these stars are typically (quasi-)uniformly rotating, irrespective of their rotation rate, which covers $[0 - 80\%]$ of the Roche critical rotation rate (Van Reeth et al., 2018).

1.1 Structure and evolution of intermediate-mass main-sequence stars

The equations of stellar structure

For a spherically symmetric star in hydrostatic equilibrium, the following set of differential equations describe its structure and evolution (Kippenhahn et al., 2012):

$$\frac{\partial r}{\partial m} = \frac{1}{4\pi r^2 \rho} \ , \tag{1.1}$$

$$\frac{\partial P}{\partial m} = -\frac{Gm}{4\pi r^4} \ , \tag{1.2}$$

$$\frac{\partial l}{\partial m} = \varepsilon_n - \varepsilon_\nu - C_P \frac{\partial T}{\partial t} + \frac{\delta}{\rho}\frac{\partial P}{\partial t} \ , \tag{1.3}$$

$$\frac{\partial T}{\partial m} = -\frac{GmT}{4\pi r^4 P}\nabla = -\frac{GmT}{4\pi r^4 P}\left(\frac{\mathrm{d}\ln T}{\mathrm{d}\ln P}\right) \ , \tag{1.4}$$

$$\frac{\partial X_i}{\partial t} = \frac{m_i}{\rho}\left(\sum_j r_{ji} - \sum_k r_{ik}\right) \ , \ i = 1, \ldots, I \ . \tag{1.5}$$

Equation (1.1) is the Lagrangian (i.e. in terms of mass coordinates) formulation of the continuity equation (where r is the radial coordinate, m is the mass coordinate ($r, m = 0$ in the stellar centre) and ρ is the density), expressing the conservation of mass in the different mass shells of the spherically symmetric star. Equation (1.2) is the equation of hydrostatic equilibrium with G being the gravitational constant, and P being the gas pressure, where the forces due to the (outward) pressure gradient and gravity cancel each other. In fact, it is a specific expression that is derived from the more general conservation of momentum equation $-\frac{\partial P}{\partial m} - \frac{Gm}{4\pi r^4} = \frac{1}{4\pi r^2}\frac{\partial^2 r}{\partial t^2}$, in which the 'extra' term signifies the inertia of mass elements undergoing accelerated radial motions (Kippenhahn et al., 2012). Equation (1.3) describes the conservation of energy, where l is the local luminosity of the mass element considered. It can be derived by looking at the heat per unit mass added to the shell dq in a time interval dt, which is defined as $dq = \left(\varepsilon - \frac{\partial l}{\partial m}\right) dt$, where ε contains two contributions: ε_n and ε_ν. Nuclear burning acts as a source, characterized by ε_n, which is the nuclear energy released per unit mass per second. In addition, neutrinos, formed by nuclear fusion processes taking place in the stellar core, present a significant energy loss, characterized by ε_ν. An expression for dq in the absence of nuclear burning is given by the first law of thermodynamics: $dq = du + Pdv$ (with u the internal energy and $v = 1/\rho$ the specific volume), which can be transformed into $dq = C_P dT - \frac{\delta}{\rho} dP$ by making use of several thermodynamic relations (see e.g. Kippenhahn et al., 2012), where $C_P = \left(\frac{\mathrm{d}q}{\mathrm{d}T}\right)_P$, dT is the change in temperature of the mass element, $\delta = -\left(\frac{\partial \ln \rho}{\partial \ln T}\right)_P$ and where dP is the change in pressure of the

mass element. Combining this with the previously obtained equation for $\frac{\partial l}{\partial m}$ yields the energy equation defined above (Equation (1.3)).

Equation (1.4) is the energy transport equation, where T is the temperature of the mass element and where hydrostatic equilibrium is assumed. It will be discussed in more detail in the next subsection. Finally, Equation (1.5) describes the isotope abundance changes inside the star (i.e. the nuclear reaction networks), where X_i is the fraction of a unit mass consisting of nuclei of type i, m_i the mass of these nuclei, and where r_{ij} are the reaction rates of nuclear processes that create nuclei of type i, whereas r_{ji} are the reaction rates of nuclear processes that destroy them, for any of the nuclei $i = 1 \dots I$ which are involved in such reactions. Equation (1.5) does not account for mixing processes in the interior, although they do induce transport of nuclei between neighbouring mass shells over time.

During the main sequence, which is the stage of core hydrogen burning, local adjustments to mechanical equilibrium and energy transport occur on typical timescales shorter than the time scale of changes in chemical composition, so that the first four equations can effectively be decoupled from Equation (1.5), by itself a set of equations. The given set of four equations can be solved for the relevant quantities if they are coupled with an equation of state (EOS) that describes the variation of density ρ as a function of P, T and chemical composition X_j (Kippenhahn et al., 2012).

Stellar convection

If radiation is the sole transporter of energy (i.e. $\nabla = \nabla_{\rm rad}$), Equation (1.4) can be simplified as (Kippenhahn et al., 2012):

$$\frac{\partial T}{\partial m} = -\frac{GmT}{4\pi r^4 P}\nabla_{rad} = -\frac{3\kappa(m)l(m)}{64\pi^2 ac(r(m))^4(T(m))^3} \ , \tag{1.6}$$

where $\kappa(m)$ is the Rosseland mean opacity, a is the radiation density constant, and c is the speed of light. However, if $\nabla_{\rm rad}$ becomes very high, transport by means of radiation becomes ineffective, so that energy transport will mainly be done by means of convection, where (macroscopic) mass elements with a temperature higher than their environment will rise, and subsequently dissipate. In addition to transport of energy, this will also cause these convective regions to be well-mixed chemically. In order to determine the regions of convective energy transport, the Ledoux criterion can be used (see e.g. Aerts et al., 2010):

$$\nabla_{\rm ad} + \frac{\varphi}{\delta}\nabla_\mu < \nabla_{\rm rad} \ , \tag{1.7}$$

where

$$\nabla_{\rm ad} = \left(\frac{{\rm d}\ln T}{{\rm d}\ln P}\right)_S \ , \ \varphi = \left(\frac{\partial \ln \rho}{\partial \ln \mu}\right)_{P,T} \ , \ \delta = -\left(\frac{\partial \ln \rho}{\partial \ln T}\right)_{P,\mu} \ , \ \nabla_\mu = \left(\frac{\partial \ln \mu}{\partial \ln P}\right) \ , \tag{1.8}$$

with S the entropy and μ the local mean molecular weight. Here, $\nabla_{\rm ad}$ is the adiabatic temperature variation of the mass elements. The chemical gradient ∇_μ has a stabilising effect on convection.

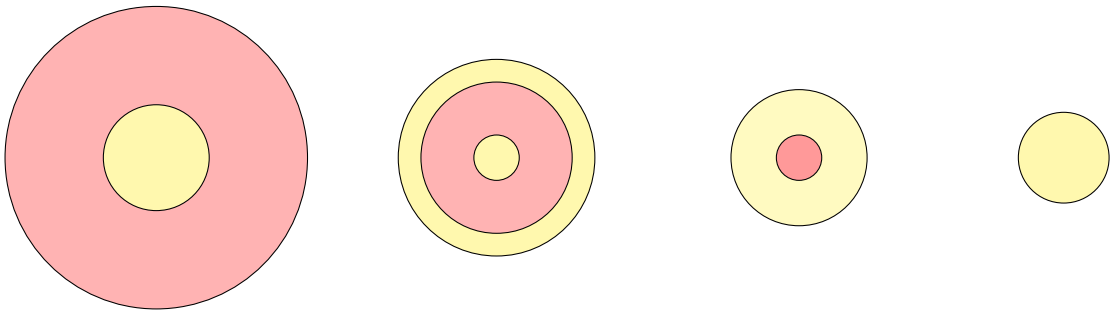

$M \gtrsim 2.0\ M_\odot$ **OBA stars** | $1.2\ M_\odot \lesssim M \lesssim 2.0\ M_\odot$ **≈ F stars** | $0.5\ M_\odot \lesssim M \lesssim 1.2\ M_\odot$ | $M \lesssim 0.5\ M_\odot$

Figure 1.1: Representation of the regions of differing energy transport inside stars of differing masses throughout the main sequence, assuming solar metallicity. Radiative regions are indicated in red, whereas convective regions are indicated in yellow. The approximate mass and spectral type is given underneath.

Convective energy transport is often described using the mixing length theory (MLT). The energy transport is then computed as a function of a typical mean free path l_m of the convective elements:

$$l_m = \alpha_{\mathrm{MLT}} H_p \ , \tag{1.9}$$

where α_{MLT} is the mixing length parameter expressing the efficiency of convection and H_p is the local pressure scale height, defined as $H_p = -dr/d\ln P$. This leads to difficulties in describing the boundaries between convective and radiative zones. Within the mixing length theory such a boundary is sharp and discontinuous, whereas physically, one would expect a more gradual transition, where convective elements can penetrate the radiative regions. This is then typically taken into account by defining so-called overshooting regions, where another parameter (which also depends on the local pressure scale height), the overshooting parameter f_{ov}, expresses the extent of the overshooting region. The (model-dependent) version of our overshooting criterion will be covered in Section (3.1).

Stellar evolution of intermediate-mass stars (until the red giant phase)

All stars are born in regions of high-density interstellar dust and gas. They are dense enough to shield molecular species from the interstellar radiation field, and hence are referred to as molecular clouds. These regions become unstable to gravitational contraction if the mass contained in the (molecular) clouds is high enough. A common criterion to determine the required critical mass is the so-called Jeans criterion (e.g. Ward-Thompson and Whitworth, 2015). The contraction will lead to the fragmentation of the original cloud, where each fragment will be subject to the formation of a disk with a massive core. These so-called protostars will heat up due to mass accretion from their disks. Eventually, most of the mass in the disk will be accreted onto the protostar. If enough mass was present in the disk, the central object will become hot enough to start fusing hydrogen and becomes a zero-age main sequence (ZAMS) star (e.g. Ward-Thompson and Whitworth, 2015).

The class of intermediate-mass main-sequence stars consists of stars with masses ranging from 1.2 to 8.0 solar masses ($M_\odot$), if they have solar metallicity (Aerts et al.,

2019). The typical internal structure of these (main-sequence) stars is indicated in Figure (1.1), showing that for most intermediate-mass stars a convective core persists throughout the main sequence. The stellar structure throughout the main sequence evolution is mainly determined by the stellar mass, although metallicity (i.e. how many elements are present that are heavier than hydrogen and helium) plays a secondary role (see e.g. Hirschi et al., 2008). After nearly all hydrogen inside the core has been exhausted, the terminal age main sequence (TAMS) star loses most of its outward radiative pressure, previously provided by the photons produced by the core nuclear hydrogen-burning processes. The core will become isothermal in the absence of energy sources (see e.g. Kippenhahn et al., 2012). Following the TAMS phase, hydrogen fusion will take place in the near-core regions (so-called shell burning), adding more helium to the core. The maximum extent to which the He-filled core can grow in mass (without shrinkage) is given by the Schönberg-Chandrasekhar (SC) limit $q_{\rm SC}$ (Schönberg and Chandrasekhar, 1942):

$$q_0 \equiv \frac{M_c}{M} \leq q_{\rm SC} = 0.37 \left(\frac{\mu_{\rm env}}{\mu_{\rm core}} \right)^2 \approx 0.09 \ , \tag{1.10}$$

where M_c is the core mass, M is the stellar mass, μ_{env} is the molecular weight of the (H-rich) envelope and where μ_{core} is the molecular weight of the helium core ($\mu_{core} \simeq 4/3$). As long as the core mass is lower than the SC limit, the core is in thermal equilibrium, and the star is called a subgiant.

After reaching the SC limit, the core starts to contract, the characteristic timescale given by the Kelvin-Helmholtz contraction timescale, which is much shorter than the nuclear timescale of hydrogen burning ($\tau_{KH} \ll \tau_{nuc}$). In that stage, the outer regions expand rapidly, greatly increasing the stellar radius. This phase is called the red giant phase, where next to a non-burning He core growing in mass, yet contracting in radius, a burning hydrogen shell is present. In stars more massive than $\approx 2.3 M_\odot$ hydrogen shell burning will continue until the core temperature is high enough to start core helium burning in non-degenerate conditions. In stars less massive than $\approx 2.3 M_\odot$ however, the electrons in the helium core become degenerate before the temperature for onset of helium burning can be reached. In that case, the electron degeneracy contributes to the pressure gradient that supports the weight of the envelope. As a result, the onset of the core helium burning phase is unstable, the so-called helium flash, a thermal runaway reaction (see e.g. Kippenhahn et al., 2012, for a detailed description). We will not consider any stars/stellar models beyond this life phase, instead referring readers to an excellent reference on stellar evolution theory (Kippenhahn et al., 2012).

1.2 'Missing' dipole mixed modes inside red giant stars

Red giants are characterized by their expanding convective envelope and contracting radiative core. p modes, standing acoustic waves where the pressure gradient acts as the dominant restoring force (see Chapter (2) for a rigorous mathematical definition), are excited in the envelope due to stochastic energy input from turbulent near-surface convection. They subsequently propagate inwards as long as their angular frequency ω is smaller than a critical acoustic frequency S_l. Where $\omega = S_l$ a boundary forms,

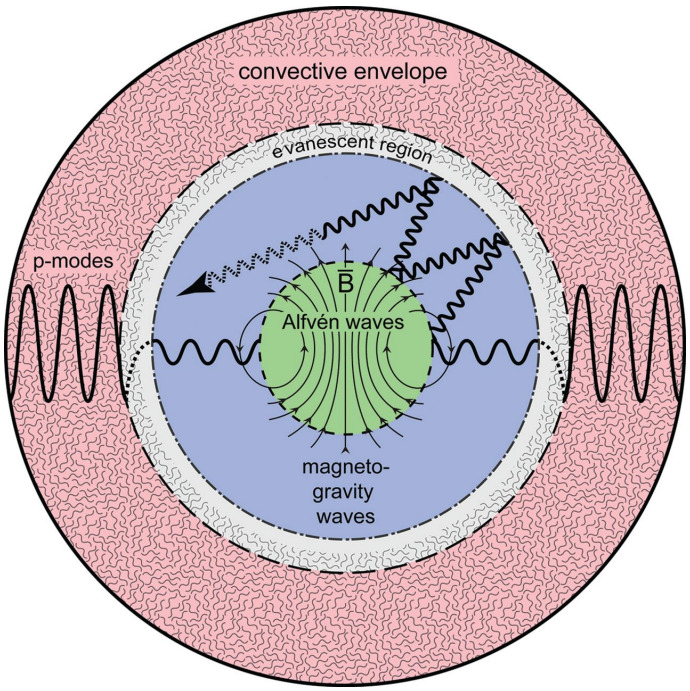

Figure 1.2: Illustration of the dipole ($l = 1$) pulsation mode propagation inside red giants, as envisaged by Fuller et al. (2015). In the presence of a strong (near-)core magnetic field, gravity waves are scattered to high angular degree l (see Section (2.1) for a rigorous definition), become trapped in the core, and eventually dissipate. Figure taken from Fuller et al. (2015).

at which part of the mode flux is reflected, whereas the rest continues its journey towards the core, as illustrated in Figure (1.2). In the (deep) stellar interior these modes change behaviour and can couple to so-called gravity modes or g modes, which are standing waves for which buoyancy acts as the dominant restoring force. They propagate in the radiative core as long as their frequency is smaller than the local buoyancy frequency or Brunt-Väisälä frequency N, defined as:

$$N^2 = g\left[\frac{1}{\Gamma_1 P}\frac{\mathrm{d}P}{\mathrm{d}r} - \frac{1}{\rho}\frac{\mathrm{d}\rho}{\mathrm{d}r}\right] \ , \tag{1.11}$$

where $\Gamma_1 = (\partial \ln P/\partial \ln \rho)_{\mathrm{ad}}$ and where $g = GM/R^2$ is the surface gravity.
For a fully ionized gas, a more conceptual description of N is given by:

$$N^2 \approx \left(\frac{g^2\rho}{P}\right)(\nabla_{\mathrm{ad}} - \nabla + \nabla_\mu) \ , \tag{1.12}$$

so that in the region of nuclear burning (where μ increases with depth), ∇_μ makes a positive contribution to N^2. In between the convective envelope and radiative core, a small evanescent region exists (as indicated in grey in Figure (1.2)), in which the mode amplitude decays exponentially. Hence, p modes that want to couple with g modes (and vice versa) have to 'tunnel' through this region. If they have sufficient amplitude, they can couple and become so-called mixed modes, which display both g and p mode character.

In 'normal' red giant stars, the wave energy that tunnels into the core also tunnels back out (eventually) to produce the observed mixed oscillation modes at the surface, where the coefficient for wave transmission for tunneling through the evanescent zone is given by $T = \exp\left[-\int_{r_1}^{r_2} dr \sqrt{-(S_l^2 - \omega^2)(N^2 - \omega^2)/(c_s^2\omega^2)}\right]$, with

r_1 and r_2 the lower and upper bounds of the evanescent zone, and c_s the local sound speed (Cantiello et al., 2016). The fraction of wave energy transmitted through that zone is then equal to T^2.

However, 20% of red giants (in the *Kepler* field) exhibit 'missing' mixed modes, or rather, modes whose amplitudes are significantly suppressed (Mosser et al., 2012a). Most of the modes observed are near the $\nu_{\max}$ frequency determined by the evolutionary state of the star (generally: the larger $\nu_{\max}$, the younger the star). The visibility of stellar oscillations critically depends on how they are driven and damped. Two possible origins for the 'missing' mixed modes are discussed in literature: either strong internal magnetic fields suppress/scatter these modes (Fuller et al., 2015), or a strong yet unknown coupling formalism (where T is modified) needs to be used (Mosser et al., 2017).

The strong near-core magnetic field mechanism of Fuller et al. (2015) essentially alters the mixed mode geometry, which leads to the 'trapping' of modes in the near-core region, as these modes can no longer 'tunnel' through the evanescent region. Earlier work showed, when considering the interaction of gravity modes with a horizontal magnetic field, that sufficiently strong magnetic fields will reflect these waves, whereas weaker fields partially reflect or refract such waves (Rogers and MacGregor, 2010; MacGregor and Rogers, 2011). In effect, since the horizontal motion of the waves distort magnetic field lines, the magnetic tension force, which is the restoring force for the (magnetic) Alfvén waves, becomes strong enough to act as a restoring force, in addition to buoyancy. Fuller et al. (2015) were therefore able to derive a critical magnetic field strength $B_c = \sqrt{\pi\rho/2}\,(\omega^2 r/N)$: the strength above which 'normal' g modes are converted into Alfvén waves and modified g modes (differing in mode geometry, described by e.g. the angular degree l, which is more rigorously defined in Section (2.1)). This was explored in detail with the 2D simulations performed by Lecoanet et al. (2017), finding results that agree with the conclusions of Fuller et al. (2015). Hence, if the magnitude of the radial component of the magnetic field exceeds B_c, mixed mode propagation will stop. Moreover, since this critical field strength increases with the pulsation frequency, the field strengths necessary for this mechanism to work vary throughout red giant evolution: more evolved stars require a lower field strength than less evolved red giants to become critical. Typical field strengths needed for suppression are $B_c \geq 10^4 - 10^6$G (Fuller et al., 2015). In addition, this means that for a given field strength an angular transition frequency ω_c should exist, where modes with angular frequencies below ω_c propagate and modes with angular frequencies greater than ω_c do not.

The Mosser et al. (2017) formalism, on the other hand, relies on the results of Takata (2016a,b), which provide an improved description of the p and g mode coupling in non-magnetic red giants. A thorough observational study of red giants that exhibit these 'missing' mixed modes then led Mosser et al. (2017) to conclude that these stars are similar to 'normal' red giants, if the modified expression for T is used. In addition, their damping mechanism does not significantly impact stellar structure, nor does it change properties of the mode propagation regions. Therefore, the 'missing' mixed modes are not missing but instead are strongly coupled, implying that these oscillations cannot be fully suppressed in the radiative core, in contrast with the necessary assumption of the Fuller et al. (2015) formalism. Hence, they conclude that another damping mechanism must be found, which only partially damps the dipole ($l = 1$) mixed modes.

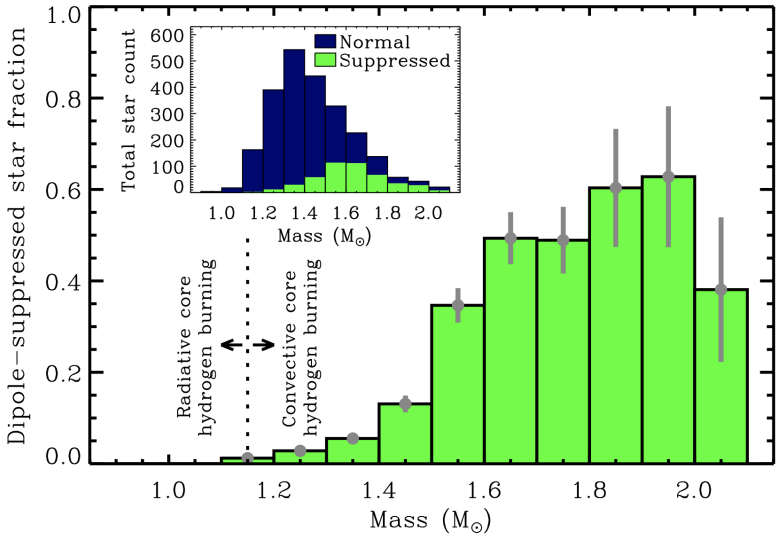

Figure 1.3: Fraction of red giants showing suppressed dipole mixed modes, in function of stellar mass. Figure taken from Stello et al. (2016).

The strong internal magnetic fields proposed by Fuller et al. (2015) can only be present if they are a remnant of earlier phases of stellar formation and evolution (such as the main sequence stars considered in this work), assuming that the magnetic field flux is conserved. This assumption can be justified by considering that the ohmic timescale $t_{Ohm} = H_P^2/\eta$, i.e. the time a stable magnetic field needs to diffuse across a pressure scale height H_P in a radiative region, is quite large in stellar plasma's, where the magnetic diffusivity η is low. Cantiello et al. (2016) therefore assume that fields present at the end of the main sequence are frozen in their Lagrangian mass coordinate. If this is the case, the magnetic flux is conserved, so that the TAMS magnetic field strength can provide an estimate for the red giant field strength: $B_{\rm RG} = B_{\rm MS}\,(r_{\rm MS}/r_{\rm RG})^2$, where $B_{\rm MS}$ is the field strength at the moment when the convective core has its largest extent, $r_{\rm MS}$ is the radius of the mass shell at TAMS, and $r_{\rm RG}$ is the radius of the mass shell in which hydrogen shell burning takes place (Fuller et al., 2015; Cantiello et al., 2016).

A study of 3600 red giant stars by Stello et al. (2016), characterized the mass range of red giants for which mode suppression with the Fuller et al. (2015) mechanism most likely occurs, shown in Figure (1.3). Moreover, they provided an updated critical magnetic field strength range required to suppress the mixed modes, ranging from 10^4 G for evolved red giants (of widely differing masses) to $3{*}10^6$ G for younger red giants (see figure 4 of Stello et al., 2016). Cantiello et al. (2016) state that these magnetic fields are likely remnants from main sequence dynamo action, where a fraction of kinetic energy due to convective motions in the convective core is converted into magnetic energy (see e.g. Brandenburg and Subramanian, 2005). Their scale and magnitude critically depend on the importance of rotation, as derived in Cantiello et al. (2016). They find typical field strengths of $B_{MS} \sim 10^4 - 10^5$ G, but note that smaller-scale and amplitude magnetic fields can still be generated in the absence of rapid rotation. Moreover, Augustson et al. (2016) generated megagauss strength fields in their magneto-hydrodynamics (MHD) simulations of core convection in massive B-type stars.

None of these studies, however, looked at how to provide observational constraints to characterize the internal magnetic fields present during the precursor main-sequence phase of these red giants. This is the aim of this work. The main sequence internal stellar magnetic field model that will be used in this work was derived by Duez and Mathis (2010). It represents a dipolar, axisymmetric field, resembling the typical field geometries observed at stellar surfaces (see Section (3.2.3)). This field was specifically designed to resemble a so-called fossil field, which is thought to be a remnant of the pre-main-sequence phase evolution of a main sequence star. It is suitable to obtain a first glimpse of internal near-core stellar magnetic fields of (pulsating) intermediate-mass main-sequence stars, by looking at how these fields affect the pulsation frequencies.

In the near future, more complex field geometries will be considered, opening up possibilities to further test the Fuller et al. (2015) hypothesis by means of asteroseismology of intermediate-mass g-mode pulsators, numerous of which have been observed by the NASA *Kepler* satellite.

1.3 Main goals of this thesis

The best way to probe these near-core magnetic fields is by considering their effect on gravity mode pulsations which probe this very region (see e.g. Aerts et al., 2010). The main goals of this work therefore consist of:

1. Identifying how internal magnetic fields affect frequencies of stellar gravity mode pulsations. This will be translated in a criterion for detectability.

2. Identifying how different stellar fundamental parameters affect the Duez and Mathis (2010) magnetic field structure and determining the corresponding effect on stellar gravity mode pulsation frequencies.

As will become clear further on, part of this master thesis research was published as:

Period spacings of gravity modes in rapidly rotating magnetic stars I. Axisymmetric fossil field with poloidal and toroidal components

V. Prat, S. Mathis, B. Buysschaert, **J. Van Beeck**, D. M. Bowman, C. Aerts, and C. Neiner

Accepted (in press) for publication in Astronomy & Astrophysics on 14th May 2019 and pre-print available at: https://arxiv.org/abs/1903.05620.

2 — Theory of gravity-mode oscillations

2.1 Non-rotating, non-magnetic stars

Equations (1.1) - (1.5) describe a stellar model in (hydrostatic) equilibrium. Throughout the evolution of the star, there will often be processes that cause it to oscillate around its equilibrium state. The impact of these pulsations is typically small, so that the equilibrium stellar model is only slightly perturbed.

The pulsations are described by the 'pulsation equations', which can be obtained by applying linear perturbations to Equations (1.1) - (1.5). In a non-rotating, non-magnetic, spherically symmetric star, these pulsations can be described using spherical harmonic functions, so that the components of the Lagrangian displacement $\boldsymbol{\xi}$ (i.e. displacement of local mass elements) caused by a pulsation with angular frequency ω_n and quantum numbers n, l and m, expressed in spherical coordinates (r, θ, φ), where θ denotes the colatitude and φ is the longitude, are equal to (e.g. Smeyers and Van Hoolst, 2010; Aerts et al., 2010):

$$\begin{aligned}
\xi_{n,r}(r,\theta,\varphi,t) &= A_n(r) Y_l^m(\theta,\varphi) e^{-i\omega_n t} \ , \\
\xi_{n,\theta}(r,\theta,\varphi,t) &= \frac{B_n(r)}{r} \frac{\partial Y_l^m(\theta,\varphi)}{\partial \theta} e^{-i\omega_n t} \ , \\
\xi_{n,\varphi}(r,\theta,\varphi,t) &= \frac{B_n(r)}{r\sin\theta} \frac{\partial Y_l^m(\theta,\varphi)}{\partial \varphi} e^{-i\omega_n t} \ .
\end{aligned} \tag{2.1}$$

$A_n(r)$ and $B_n(r)$ are the amplitudes of radial and horizontal displacement, respectively. $Y_l^m(\theta,\varphi)$ is a spherical harmonic function given by:

$$Y_l^m(\theta,\varphi) = (-1)^m \sqrt{\frac{2l+1}{4\pi}\frac{(l-m)!}{(l-m)!}} P_l^m(\cos\theta)\, e^{im\varphi} \tag{2.2}$$

where P_l^m is an associated Legendre function (Abramowitz and Stegun, 1972).

The quantum numbers n, l and m express the pulsation geometry: the radial order n is related to the number of radial nodes, the spherical degree l expresses the number of surface nodal lines and the azimuthal order m is equal to the number of surface nodal lines that pass through the symmetry axis of the star, hence $l \geq |m|$. Traditionally, pulsation modes where $l = |m|$ are referred to as sectoral modes, pulsations with $0 < |m| < l$ are referred to as tesseral modes, and pulsations with $m = 0$ are labelled zonal modes. In a similar way, pulsations with $l = 0$ are referred to as radial modes, whereas nonradial modes have $l \neq 0$. If $l = 1$, the pulsation mode is called a dipole mode, whose radial components are displayed in Figure (2.1). If $l =$

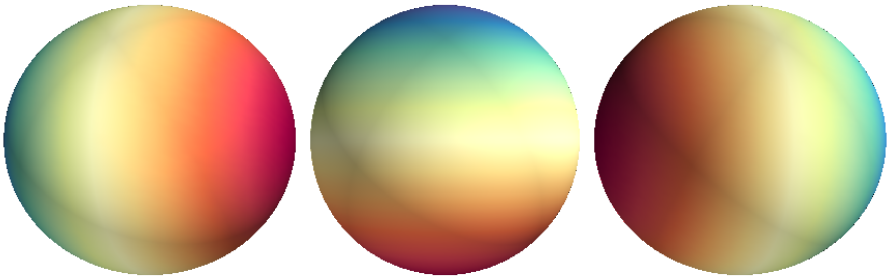

Figure 2.1: Representation of the radial component of the $l = 1$ dipole modes in a non-rotating, non-magnetic star. From left to right: retrograde ($m = -1$) sectoral mode, zonal mode ($m = 0$), and prograde ($m = 1$) sectoral mode. White bands represent positions of the surface nodes, whereas the red and blue regions represent sections of the star that are moving in (out) and/or heating (cooling) at any given time, the behaviour oscillating in time.

2, it is labelled as a quadrupole mode, and so forth. As noted by Van Reeth (2017), the quantum numbers n, l and m have a strong impact on pulsation characteristics, so that a correct geometric mode identification in observational studies is essential.

In this work we will only consider linear, adiabatic oscillations, for which the Lagrangian perturbation of the entropy is equal to zero, so that the following pulsation equations hold for a non-rotating, non-magnetic star (Aerts et al., 2010):

$$\rho' = \frac{\rho}{\Gamma_1 P} P' + \rho\, \xi_r \left(\frac{1}{\Gamma_1 P} \frac{\mathrm{d}P}{\mathrm{d}r} - \frac{1}{\rho} \frac{\mathrm{d}\rho}{\mathrm{d}r} \right) , \tag{2.3}$$

$$\frac{\mathrm{d}\xi_r}{\mathrm{d}r} = -\left(\frac{2}{r} + \frac{1}{\Gamma_1 P} \frac{\mathrm{d}P}{\mathrm{d}r} \right) \xi_r + \frac{1}{\rho c_s^2} \left(\frac{S_l^2}{\omega^2} - 1 \right) P' + \frac{l(l+1)}{\omega^2 r^2} \Phi' , \tag{2.4}$$

$$\frac{\mathrm{d}P'}{\mathrm{d}r} = \rho \left(\omega^2 - N^2 \right) \xi_r + \frac{1}{\Gamma_1 P} \frac{\mathrm{d}P}{\mathrm{d}r} P' - \rho \frac{\mathrm{d}\Phi'}{\mathrm{d}r} , \tag{2.5}$$

$$\frac{1}{r^2} \frac{\mathrm{d}}{\mathrm{d}r} \left(r^2 \frac{\mathrm{d}\Phi'}{\mathrm{d}r} \right) = 4\pi G \left(\frac{P'}{c_s^2} + \frac{\rho \xi_r}{g} N^2 \right) + \frac{l(l+1)}{r^2} \Phi' , \tag{2.6}$$

where $c_s^2 = \Gamma_1 P / \rho$ is the local sound speed, $S_l^2 = l(l+1) c_s^2 / r^2 = k_h^2 c_s^2$ is the Lamb frequency (with k_h the horizontal wavenumber), N is the Brunt-Väisälä or buoyancy frequency, Φ is the gravitational potential (defined by Poisson's equation), and where x' denotes an Eulerian perturbation of the quantity x (i.e. the perturbation of that quantity at a given point). In order to close this (complete) system of pulsation equations, boundary conditions need to be fulfilled (Smeyers and Van Hoolst, 2010). At the stellar centre, the radial component of the Lagrangian displacement must be finite. At the stellar surface the Lagrangian perturbation of pressure must be zero: $\left(P' + (\boldsymbol{\xi} \cdot \nabla) P \right)_R = 0$. However, since P_R is considered to be negligible compared to the central pressure (i.e. $P_R = 0$), the condition imposes that the divergence of the Lagrangian displacement must be finite at the surface (see e.g. Smeyers and Van Hoolst, 2010). Finally, the continuity of the gravitational potential and its gradient at the surface require that $\left(\frac{\mathrm{d}\Phi'}{\mathrm{d}r} \right)_R + \Phi'_R (l+1)/R = -\left(4\pi G \rho A_n(r) \right)_R$.

When l or $|n|$ are large, the Eulerian perturbation of the gravitational potential Φ' is small (compared to ρ'), allowing one to neglect it, the so-called Cowling approximation (Cowling, 1941). Even though this changes the properties of some modes (which we do not consider here), it has computationally been proven to be

valid for high-order, high-degree modes (Robe, 1968; Christensen-Dalsgaard, 1991). In this approximation, the pulsation equations reduce to (Aerts et al., 2010):

$$\frac{\mathrm{d}\xi_r}{\mathrm{d}r} = -\left(\frac{2}{r} - \frac{1}{\Gamma_1}H_p^{-1}\right)\xi_r + \frac{1}{\rho c_s^2}\left(\frac{S_l^2}{\omega^2} - 1\right)P' \ , \tag{2.7}$$

$$\frac{\mathrm{d}P'}{\mathrm{d}r} = \rho\left(\omega^2 - N^2\right)\xi_r - \frac{1}{\Gamma_1}H_p^{-1}P' \ , \tag{2.8}$$

where H_p is the local pressure scale height defined earlier. For high radial order modes, this system of equations can be approximated by (Aerts et al., 2010):

$$\frac{\mathrm{d}^2\xi_r}{\mathrm{d}r^2} = \frac{\omega^2}{c_s^2}\left(1 - \frac{N^2}{\omega^2}\right)\left(\frac{S_l^2}{\omega^2} - 1\right)\xi_r = -K_s(r)\xi_r \ . \tag{2.9}$$

Hence, given the pulsations equations in their crudest form, the pulsation behaviour is determined by the characteristic frequencies S_l and N. The local behaviour of ξ_r depends on the sign of $K_s(r)$: if $K_s(r) > 1$, ξ_r is a local oscillating function of r, whereas if $K_s(r) < 0$, the function is either exponentially increasing or decreasing locally. The oscillatory solutions are obtained for the following conditions (Aerts et al., 2010):

$$|\omega| > |N| \ \text{ and } \ |\omega| > S_l \ , \tag{2.10}$$

$$|\omega| < |N| \ \text{ and } \ |\omega| < S_l \ . \tag{2.11}$$

whereas the evanescent solutions inside the star are defined by:

$$|N| < |\omega| < S_l \ , \tag{2.12}$$

$$S_l < |\omega| < |N| \ . \tag{2.13}$$

In general, one of the oscillating regions is dominant for a given pulsation mode, with the solution decaying exponentially away from it (Aerts et al., 2010). Nonradial stellar pulsations can then be categorized according to their dominant restoring force. For non-rotating, non-magnetic stars, two main pulsation types can be distinguished: pressure/acoustic modes (fulfilling condition (2.10)) and gravity modes (fulfilling condition (2.11)). Hence, the oscillatory solutions thus define the so-called pulsation cavities (for a non-rotating, non-magnetic star), which are the regions inside the star in which the modes are trapped. The boundaries of this trapping region can then be found at points where $K_s(r) = 0$, known as the turning points.

Gravity Modes

Gravity modes or g modes are pulsations with buoyancy as the dominant restoring force. Therefore, these modes can only propagate in radiative regions inside a star, since buoyancy is precisely the force driving convection. G modes are most sensitive to the properties of the deep stellar interior, where $\omega \ll N$ and $\omega \ll S_l$ hold, and cannot be purely radial. The wave vector $\boldsymbol{k}$ and Lagrangian displacement vector $\boldsymbol{\xi}$ (assuming $\xi \propto \exp\{i(\boldsymbol{k}\cdot\boldsymbol{r} - \omega t)\}$) in spherical coordinates (r, θ, φ) can be written as (e.g. Aerts et al., 2010):

$$\boldsymbol{k} = k_r\boldsymbol{e}_r + k_\theta\boldsymbol{e}_\theta + k_\varphi\boldsymbol{e}_\varphi = k_r\boldsymbol{e}_r + \boldsymbol{k}_H \ , \tag{2.14}$$

$$\boldsymbol{\xi} = \xi_r\boldsymbol{e}_r + \xi_\theta\boldsymbol{e}_\theta + \xi_\varphi\boldsymbol{e}_\varphi = \xi_r\boldsymbol{e}_r + \boldsymbol{\xi}_H \ , \tag{2.15}$$

so that for these low-frequency waves in stably stratified regions, one obtains: $\boldsymbol{k}\cdot\boldsymbol{\xi} = k_r\xi_r + \boldsymbol{k}_H \cdot \boldsymbol{\xi}_H \approx 0$ if the anelastic approximation $\nabla \cdot (\rho\boldsymbol{\xi}) \approx 0$, which filters out high-frequency acoustic waves, is used. Hence, the following holds: $\xi_r/\xi_h \approx -k_H/k_r$. The dispersion relation for internal gravity waves is the following (e.g. Aerts et al., 2010):

$$\omega^2 = \frac{N^2}{1 + k_r^2/k_H^2} \ . \tag{2.16}$$

Since $\omega^2 \ll N^2$, $k_H^2 \ll k_r^2$ must hold: the displacement of these modes is predominantly horizontal: $||\boldsymbol{\xi}_h|| \gg \xi_r$ (i.e. these modes are transversal). Moreover, if oscillations are locally regarded as plane waves, $k_H^2 = l\,(l+1)\,/r^2$, so that the radial component of the wave vector is given by (Aerts et al., 2010):

$$k_r^2 = \frac{l(l+1)}{r^2}\left(\frac{N^2}{\omega^2} - 1\right) \approx \frac{l(l+1)}{r^2}\left(\frac{N^2}{\omega^2}\right) \ , \tag{2.17}$$

where a region of $k_r^2 > 0$ is propagative and a region of $k_r^2 < 0$ is evanescent. Shibahashi (1979) and Tassoul (1980) independently showed that for a non-rotating, chemically homogeneous star, pulsation periods P_{nl} in the asymptotic regime (where $n \gg l$) are given by:

$$P_{nl} = \frac{\Pi_0}{\sqrt{l(l+1)}}\,(n + \alpha_{l,g}) \ , \tag{2.18}$$

where

$$\Pi_0 = 2\pi^2 \left(\int_{r_1}^{r_2} N\frac{dr}{r}\right)^{-1} \ , \tag{2.19}$$

with $\alpha_{l,g}$ a constant depending on the boundaries r_1 and r_2 of the mode trapping region, and Π_0 the buoyancy radius. This leads to regular spacings in period between modes with the same degree l and consecutive radial orders n:

$$\Delta\Pi_l = \frac{\Pi_0}{\sqrt{l(l+1)}} \ . \tag{2.20}$$

However, stars are not chemically homogeneous. As mentioned in Section (1.1), a convective core exists in intermediate-mass stars throughout the MS, which can either grow or shrink. A growing convective core leads to discontinuity in chemical composition at the boundary, whereas a receding core leaves behind a μ-gradient zone near the core.
Miglio et al. (2008) showed that varying the local average molecular weight (e.g. due to a shrinking convective core on the MS) modifies the g mode resonant cavity and causes mode trapping. This leads to dips in the period spacing patterns, as can be seen in Figure (2.2) for a typical 3 $M_\odot$ stellar model. A steeper chemical gradient results in stronger dips, whereas the periodicity of the dips (in the period spacing pattern) indicates the location of the mode trapping region. If more mixing is considered, the average period spacing value decreases and the chemical gradient is washed out, reducing the presence of dips.

Mode excitation

Stars that are observed to be pulsating, do so in their natural modes of oscillation. As some stars have been observed to be pulsating for many decades, it seems that stellar pulsation is a relatively stable phenomenon. However, some of the mode energy will inevitably be lost as the pulsations propagate throughout the stellar interior, damping the pulsations. Hence, pulsations can only occur if they are driven by some mechanism. Two main types of mechanisms that can drive stellar pulsations can be discerned.

The first, stochastic excitation, is commonly present in stars with a sufficiently large convective envelope, such as our Sun. In this case, stars resonate stochastically at their characteristic pulsation frequencies, due to turbulent convective motions in these envelopes.

The second main pulsation driving mechanism, the κ or heat engine mechanism, is present in the intermediate-mass stars that will be studied in this work. As (radiative) energy transfer within the star is not efficient enough within a specific mass shell, periodic heating and cooling of this mass shell ensues, driving the pulsations. Usually, the κ mechanism is present in a partial ionization layer in the envelope of the star. In such a layer, the temperature dependence of the ion opacity modifies the efficiency of energy transfer, providing a driving mechanism for the pulsation.

We will not go further into detail on this subject and instead refer the reader to e.g. Chapter 3.7 of Aerts et al. (2010) for an in-depth discussion of current mode excitation theory. The reason we neglect this is that in order to characterize the internal magnetic field of a target, we will make use of observed oscillation modes, which are in any case excited, irrespective of whether excitation theory predicts their excitation or not.

Pulsations in A-F-type stars: γ Doradus stars

γ Doradus (γ Dor) stars are late A- to early F-type main-sequence stars with masses ranging from 1.3 to 1.9 $M_{\odot}$ (Mombarg et al., 2019). They present multiperiodic photometric and spectroscopic variation with periods typically ranging from 0.3 to 5.0 days and amplitudes typically less than 50 mmag (e.g. Aerts et al., 2010). Their pulsations are multiperiodic high-order nonradial g modes. This makes them a prime target for our study, as these pulsations probe the near-core region, in which the magnetic field in the Fuller et al. (2015) model is strongest (see Sections (2.3) and (3.2.3)). Since they typically exhibit frequencies that are close to their rotation frequency (e.g. Bouabid et al., 2013), the effects of rotation on the stellar pulsations are large and have to be considered in detail. The excitation mechanism for these stars is the convective flux blocking by the HeII partial ionization zone at the bottom of their convective envelope (see e.g. Grigahcène et al., 2005; Dupret et al., 2005b,a). They are representative for the lower mass range of the stellar model grid considered in this work.

Pulsations in B-type stars: Slowly Pulsating B stars

Slowly pulsating B-type stars (SPB stars) (first termed as such by Waelkens (1991)) are mid-B spectral type main-sequence stars that exhibit multiperiodic photometric and spectroscopic variability, with periods typically ranging from 0.5 to 5.0 days and

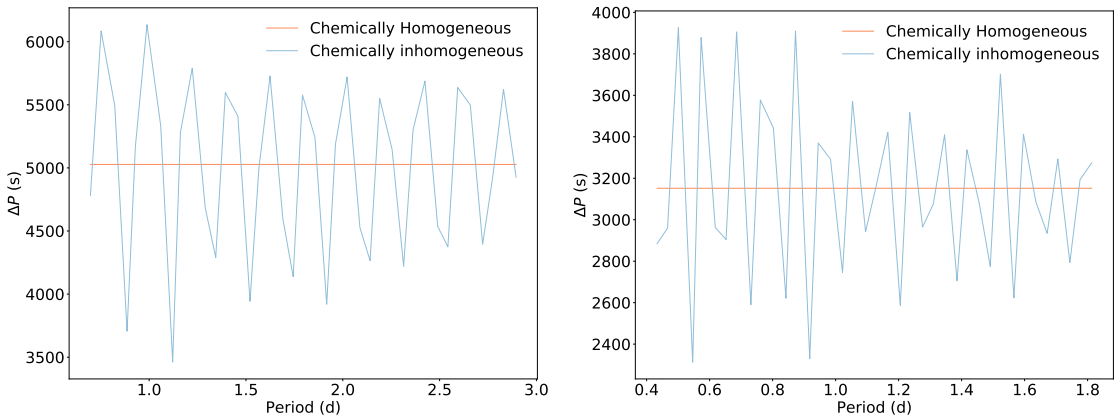

Figure 2.2: Typical period spacing patterns for zonal dipole modes ($l = 1, m = 0$) in a non-rotating non-magnetic, chemically inhomogeneous 3 $M_\odot$ main-sequence star (i.e. a low mass SPB-like star), at different evolutionary stages (left: mid-MS, right: TAMS). The effect of the shrinking convective core is clearly visible. The asymptotic constant period spacing $\Delta\Pi_l$ (defined in Equation (2.20)) is overplotted, representing the period spacing between g modes in a chemically homogeneous star.

amplitudes typically less than 50 mmag (e.g. Aerts et al., 2010). Their pulsations are also (low-degree) high-order nonradial g modes, like those of γ Dor stars (e.g. Moravveji et al., 2016). SPB stars range in mass from $3M_\odot$ to $7M_\odot$, hence the lower mass SPB stars are also a prime target for our study (Aerts et al., 2010). Since they are larger, their buoyancy radius Π_0 is different from γ Dor stars. The g modes of SPB stars are excited by the heat engine mechanism, driven by an opacity enhancement due to iron-group elements, also called the *Z Bump*, at a temperature of approximately 200 000 K (see e.g. Gautschy and Saio, 1993; Dziembowski et al., 1993; Pamyatnykh, 1999). Moderate to fairly rapid rotation is a well-established property of SPB stars (Huang et al., 2010). Low-mass SPB stars are representative for the upper mass range of our stellar model grid.

2.2 Influence of rotation

2.2.1 Influence on stellar evolution models

Generally, the mechanics of rotating stars are studied in the Roche approximation (Kippenhahn et al., 2012). One then assumes that the gravitational potential Φ is the same as if the total mass of the star were concentrated at the centre of the star, so that $\Phi = -GM/R$ is spherically symmetric. Assuming solid-body rotation, one can then derive an expression for the deformation of the star due to centrifugal force. In fact, an expression can be derived for the so-called critical volume or Roche lobe, which is the volume at which the centrifugal potential equals the gravitational potential. The rotation rate at which the star fills its critical volume or Roche lobe (Ω_c) is estimated as (see e.g. Kippenhahn et al., 2012):

$$\Omega_c \approx \sqrt{\frac{8GM}{27R_{\rm P}^3}}\ , \tag{2.21}$$

where $R_{\rm P}$ is the polar radius, which is not larger than the equatorial radius $R_{\rm eq}$ if the star is rotating. This corresponds approximately to a surface whose equatorial radius

is 50% larger than its polar radius. Indeed, this can easily be derived by equating the gravitational acceleration with the centrifugal acceleration at the equator. Taking $\Phi = -GM/R_{\rm eq}$ as the gravitational potential and $V = -R_{\rm eq}^2\Omega_{\rm rot}^2/2$ as the centrifugal potential (i.e. assuming solid body rotation), one needs to ensure that $\nabla\Phi + \nabla V = 0$ holds. Therefore $\Omega_c = \sqrt{GM/R_{\rm eq}^3}$, which corresponds to Equation (2.21) if $R_{\rm eq} \approx 1.5R_{\rm P}$. The effect of the centrifugal force on the polar radius $R_{\rm P}$ is small, so that $R_{\rm P}$ in Equation (2.21) is sometimes replaced by the radius of the non-rotating stellar model.

We assume that in our stellar models the deformation due to centrifugal acceleration is small enough to neglect it. The deformation of the star affects the low-density outer envelope more significantly than the high-density core, so that g-modes are less influenced, justifying our approximation (Dintrans and Rieutord, 2000; Reese et al., 2006; Ballot et al., 2010). Nevertheless, rotation has a significant influence on the assumptions made for stellar modelling. It induces latitudinal dependence of the radiative energy transport, temperature, etc. (von Zeipel, 1924; Maeder et al., 2008; Maeder, 2009). This leads to a myriad of hydrodynamic flows and instabilities that cause mixing and angular momentum transport inside these stars (e.g. Maeder, 2009; Aerts et al., 2019). An overview of such hydrodynamic instabilities is presented in Aerts et al. (2019). Moreover, as the core contracts whilst the envelope expands during evolution, the rotation profile changes. Even though extensive theory has been developed to describe these rotationally-induced instabilities (e.g. Pinsonneault, 1997), implementing these processes in evolution codes involves free parameters. Therefore, such transport processes are subject to considerable uncertainties, as they cannot be properly calibrated/constrained with classical observations and few have been tested against simulations (Aerts et al., 2019).

2.2.2 Influence on pulsation models

It is well-known that rotation can significantly affect properties of stellar oscillations, if their frequencies are comparable to or smaller than the rotation frequency (e.g. Lee and Saio, 1997). The Coriolis force and distortion of the equilibrium star due to the centrifugal force are complicating factors, making it hard to study the oscillations of rotating stars. In this work we restrict ourselves to including the rotational effects for the description of the oscillations, treating the equilibrium models as spherical. This is appropriate as long as the star rotates slower than about 80% of its critical rotation rate (Ouazzani et al., 2017).

The latitudinal dependence of a normal mode in a rotating star can e.g. not be expressed by a single spherical harmonic function, but instead requires a linear combination of an infinite number of terms proportional to spherical harmonics with different l and m (Zahn, 1966; Berthomieu et al., 1978). The coupling amongst the terms with different l becomes significant when the (angular) normal mode frequencies are comparable to or smaller than the (angular) frequency of rotation. In most parts of stellar radiation zones $2||\mathbf{\Omega}|| \ll N$, where $\mathbf{\Omega} = \Omega\,(r,\theta)\,\boldsymbol{e}_z = \Omega_V \boldsymbol{e}_r + \Omega_H \boldsymbol{e}_\theta = \Omega\cos\theta \boldsymbol{e}_r - \Omega\sin\theta \boldsymbol{e}_\theta$ is the rotation vector (Mathis, 2009). In the general case the magnitude of the rotation vector depends on both the radius and the latitude (differential rotation). In this work, we restrict ourselves to a uniformly rotating star, with Ω constant, as observations by e.g. Van Reeth et al. (2018) indicated that

quasi-uniform rotation is a good approximation for describing pulsations in γ Dor stars. This allows us to adopt the so-called Traditional Approximation of Rotation (TAR) for low-frequency waves, when $\omega \ll N$, where ω signifies the angular pulsation frequency in the co-rotating frame. The TAR assumes that $2\ \Omega < \omega$, so that the latitudinal component of the rotation vector, $-\Omega \sin\theta \boldsymbol{e}_\theta$, can be neglected in the equations. This implies that the radial component of the Coriolis force is assumed to be negligible with respect to buoyancy and that radial displacements are limited by buoyancy and small compared to horizontal components (like in the non-rotating g mode case). The star should be a slow to moderately fast rotator, when compared to its critical angular rotation frequency, reaching up to 80% of Ω_c (Ouazzani et al., 2017), defined within the Roche model (see section 2.2.1), and the Cowling approximation (Cowling, 1941) should be justified. Moreover, the TAR inherently assumes that the star is spherically symmetric, i.e. centrifugal deformation is neglected, allowing for variable separation in radial and horizontal eigenfunctions (as in the non-rotating case), so that the eigenmodes can be computed efficiently (Eckart and Gillis, 1961; Longuet-Higgins, 1968; Lee and Saio, 1997; Townsend, 2003; Mathis, 2009; Ouazzani et al., 2017).

We have shown (in the appendix) that, for a uniformly rotating star, and assuming a Lagrangian displacement $\boldsymbol{\xi} \propto e^{-i\omega t}$ with ω the angular pulsation frequency in the corotating frame (and t the time), the linearized momentum equation can be written as (Prat et al., 2019):

$$\omega^2 \boldsymbol{\xi} + i\omega \boldsymbol{\mathcal{B}}(\boldsymbol{\xi}) + \boldsymbol{\mathcal{C}}(\boldsymbol{\xi}) = 0\ , \tag{2.22}$$

where $\boldsymbol{\mathcal{B}}(\boldsymbol{\xi}) = 2\ \boldsymbol{\Omega} \times \boldsymbol{\xi}$ is the Coriolis operator, $\boldsymbol{\Omega} = \Omega \boldsymbol{e}_z$ is the rotation vector, and $\boldsymbol{\mathcal{C}}(\boldsymbol{\xi})$ is an operator describing forces that do not depend on the pulsation frequency. In the non-magnetic case, the latter describes the effect of pressure and buoyancy forces: $\boldsymbol{\mathcal{C}}(\boldsymbol{\xi}_0) = -\nabla P'/\rho\ +\ \rho' \nabla P/\rho^2$, where P' and ρ' are the pressure and density Eulerian perturbations of the equilibrium values P and ρ, respectively. Adopting the TAR, the Coriolis operator reduces to: $\boldsymbol{\mathcal{B}}(\boldsymbol{\xi}) = 2\ \Omega\ \cos\theta\ \boldsymbol{e}_r \times \boldsymbol{\xi}$, where θ is defined as the colatitude and $\boldsymbol{e}_r$ is the radial unit vector.

The equation of motion perturbed by an additional force that does not depend on ω is then obtained by applying the following first-order perturbations:

$$\omega = \omega_0 + \varepsilon\ \omega_1\ , \tag{2.23}$$

$$\boldsymbol{\xi} = \boldsymbol{\xi}_0 + \varepsilon\ \boldsymbol{\xi}_1\ , \tag{2.24}$$

$$\boldsymbol{\mathcal{C}} = \boldsymbol{\mathcal{C}}_0 + \varepsilon\ \boldsymbol{\mathcal{C}}_1\ , \tag{2.25}$$

so that one obtains the following (first-order) perturbed and unperturbed equations of motion:

$$\omega_0^2 \boldsymbol{\xi}_0 + i\omega_0 \boldsymbol{\mathcal{B}}(\boldsymbol{\xi}_0) + \boldsymbol{\mathcal{C}}_0(\boldsymbol{\xi}_0) = 0\ , \tag{2.26}$$

$$-\omega_1 \left[2\omega_0 \boldsymbol{\xi}_0 + i\boldsymbol{\mathcal{B}}(\boldsymbol{\xi}_0)\right] = \boldsymbol{\mathcal{C}}_1(\boldsymbol{\xi}_0) + \omega_0^2 \boldsymbol{\xi}_1 + i\omega_0 \boldsymbol{\mathcal{B}}(\boldsymbol{\xi}_1) + \boldsymbol{\mathcal{C}}_0(\boldsymbol{\xi}_1)\ . \tag{2.27}$$

If one then uses the fact that the operators $i\boldsymbol{\mathcal{B}}$ and $\boldsymbol{\mathcal{C}}$ are Hermitian, the scalar product of the first-order perturbed equation with $\boldsymbol{\xi}_0$, leads to the following (general) expression for the (angular) frequency perturbation of the gravito-inertial modes:

$$\omega_1 = -\frac{\langle \boldsymbol{\xi}_0, \boldsymbol{\mathcal{C}}_1(\boldsymbol{\xi}_0) \rangle}{2\omega_0 \langle \boldsymbol{\xi}_0, \boldsymbol{\xi}_0 \rangle + \langle \boldsymbol{\xi}_0, i\boldsymbol{\mathcal{B}}(\boldsymbol{\xi}_0) \rangle}\ , \tag{2.28}$$

where the scalar product is defined as $\langle \boldsymbol{\xi}, \boldsymbol{\zeta} \rangle = \int_V \rho\ \boldsymbol{\xi}^* \cdot \boldsymbol{\zeta} dV$, with * denoting the complex conjugate.

Proof. Perturbing Equation (2.22) yields:

$$\begin{aligned}(\omega_0 + \varepsilon\ \omega_1)^2\ (\boldsymbol{\xi}_0 + \varepsilon\ \boldsymbol{\xi}_1) + i\,(\omega_0 + \varepsilon\ \omega_1)\,\boldsymbol{\mathcal{B}}\,(\boldsymbol{\xi}_0 + \varepsilon\ \boldsymbol{\xi}_1)\\ + (\boldsymbol{C}_0 + \varepsilon\ \boldsymbol{C}_1)\,(\boldsymbol{\xi}_0 + \varepsilon\ \boldsymbol{\xi}_1) = 0\ .\end{aligned}$$

The zeroth order contribution is equal to:

$$\omega_0^2\boldsymbol{\xi}_0 + i\omega\boldsymbol{\mathcal{B}}(\boldsymbol{\xi}_0) + \boldsymbol{C}_0(\boldsymbol{\xi}_0) = 0\ ,$$

the first order (in ε) contribution is:

$$\left(2\omega_0\ \omega_1\ \boldsymbol{\xi}_0 + \omega_0^2\boldsymbol{\xi}_1\right) + i\,(\omega_0\boldsymbol{\mathcal{B}}(\boldsymbol{\xi}_1) + \omega_1\boldsymbol{\mathcal{B}}(\boldsymbol{\xi}_0)) + (\boldsymbol{C}_0(\boldsymbol{\xi}_1) + \boldsymbol{C}_1(\boldsymbol{\xi}_0)) = 0\ ,$$

the second order contribution is:

$$\left(\omega_1^2\boldsymbol{\xi}_0 + 2\omega_0\omega_1\boldsymbol{\xi}_1\right) + i\,(\omega_1\boldsymbol{\mathcal{B}}(\boldsymbol{\xi}_1)) + (\boldsymbol{C}_1(\boldsymbol{\xi}_1)) = 0\ ,$$

and the third order 'contribution' is $\omega_1^2\boldsymbol{\xi}_1 = 0$.
We only consider terms up to first order. Taking into account the fact that $i\boldsymbol{\mathcal{B}}$ and $\boldsymbol{\mathcal{C}}$ are Hermitian:

$$\begin{aligned}\langle\boldsymbol{\xi}, i\boldsymbol{\mathcal{B}}(\boldsymbol{\xi}')\rangle &= \langle i\boldsymbol{\mathcal{B}}(\boldsymbol{\xi}), \boldsymbol{\xi}'\rangle\ ,\\ \langle\boldsymbol{\xi}, \boldsymbol{C}(\boldsymbol{\xi}')\rangle &= \langle\boldsymbol{C}(\boldsymbol{\xi}), \boldsymbol{\xi}'\rangle\ ,\end{aligned}$$

one can derive Equation (2.28) by taking the scalar product of the first order equation with $\boldsymbol{\xi}_0$:

$$\begin{aligned}&\left\langle\boldsymbol{\xi}_0, \left(2\omega_0\omega_1\boldsymbol{\xi}_0 + \omega_0^2\boldsymbol{\xi}_1\right) + i\,(\omega_0\boldsymbol{\mathcal{B}}(\boldsymbol{\xi}_1) + \omega_1\boldsymbol{\mathcal{B}}(\boldsymbol{\xi}_0)) + (\boldsymbol{C}_0(\boldsymbol{\xi}_1) + \boldsymbol{C}_1(\boldsymbol{\xi}_0))\right\rangle = 0\\ \Leftrightarrow\ &\omega_1\left\{2\omega_0\,\langle\boldsymbol{\xi}_0, \boldsymbol{\xi}_0\rangle + \langle\boldsymbol{\xi}_0, i\boldsymbol{\mathcal{B}}(\boldsymbol{\xi}_0)\rangle\right\} + \langle\boldsymbol{\xi}_0, \boldsymbol{C}_1(\boldsymbol{\xi}_0)\rangle\\ &+ \left\{\omega_0^2\,\langle\boldsymbol{\xi}_0, \boldsymbol{\xi}_1\rangle + i\omega_0\,\langle\boldsymbol{\xi}_0, \boldsymbol{\mathcal{B}}(\boldsymbol{\xi}_1)\rangle + \langle\boldsymbol{\xi}_0, \boldsymbol{C}_0(\boldsymbol{\xi}_1)\rangle\right\} = 0\\ \Leftrightarrow\ &\omega_1\left\{2\omega_0\,\langle\boldsymbol{\xi}_0, \boldsymbol{\xi}_0\rangle + \langle\boldsymbol{\xi}_0, i\boldsymbol{\mathcal{B}}(\boldsymbol{\xi}_0)\rangle\right\} + \langle\boldsymbol{\xi}_0, \boldsymbol{C}_1(\boldsymbol{\xi}_0)\rangle\\ &+ \left\{\omega_0^2\,\langle\boldsymbol{\xi}_0, \boldsymbol{\xi}_1\rangle + i\omega_0\,\langle\boldsymbol{\mathcal{B}}(\boldsymbol{\xi}_0), \boldsymbol{\xi}_1\rangle + \langle\boldsymbol{C}_0(\boldsymbol{\xi}_0), \boldsymbol{\xi}_1\rangle\right\} = 0\\ \Leftrightarrow\ &\omega_1 = -\frac{\langle\boldsymbol{\xi}_0, \boldsymbol{C}_1(\boldsymbol{\xi}_0)\rangle}{2\omega_0\,\langle\boldsymbol{\xi}_0, \boldsymbol{\xi}_0\rangle + \langle\boldsymbol{\xi}_0, i\boldsymbol{\mathcal{B}}(\boldsymbol{\xi}_0)\rangle}\end{aligned}$$

□

Furthermore, the unperturbed Lagrangian displacements/eigenfunctions for gravito-inertial waves in spherical coordinates (r,θ,φ) are given by:

$$\boldsymbol{\xi}_0 = [\xi_r(r)H_r(\theta), \xi_h(r)H_\theta(\theta), i\xi_h(r)H_\varphi(\theta)]\, e^{i(m\varphi - \omega_0 t)}\ , \tag{2.29}$$

where m is the azimuthal order, and H_r, H_θ, and H_φ are the radial, latitudinal, and azimuthal Hough function, respectively, which describe the latitudinal behaviour of the Lagrangian displacements due to oscillation (as mentioned before). The radial Hough function H_r is obtained by solving the Laplace tidal equation eigenvalue

problem (Hough, 1898; Longuet-Higgins, 1968; Lee and Saio, 1997; Townsend, 2003; Aerts et al., 2010):

$$\mathcal{L}_\nu H_r = -\lambda H_r \ , \tag{2.30}$$

where λ is the eigenvalue (which reduces to $l(l+1)$ in the non-rotating case, for modes with degree l), $\nu = 2\Omega/\omega$ is the spin parameter: the inverse of the local Rossby number, signifying the ratio of the local inertial frequency to the wave's local frequency (e.g. Mathis, 2009), and $\mathcal{L}_s$ is the (classical) Laplace tidal operator:

$$\mathcal{L}_\nu \equiv \frac{\mathrm{d}}{\mathrm{d}\mu}\left(\frac{1-\mu^2}{1-\nu^2\mu^2}\frac{\mathrm{d}}{\mathrm{d}\mu}\right) + \frac{1}{1-\nu^2\mu^2}\left[\frac{m\nu\,(1+\nu^2\mu^2)}{1-\nu^2\mu^2} - \frac{m^2}{1-\mu^2}\right] \tag{2.31}$$

where $\mu = \cos\theta$ is a modified latitudinal variable. The radial Hough function will reduce to the classical associated Legendre polynomial P_l^m in the non-rotating case. A representation of the latitudinal and longitudinal variation of the radial component of Equation (2.29) is given in Figure (2.3) for typical pulsation parameters and rotation frequencies of γ Dor pulsators (see e.g. Van Reeth, 2017; Ouazzani et al., 2018). The latitudinal and azimuthal Hough functions are respectively given by (Prat et al., 2019):

$$H_\theta \sin\theta = \frac{\frac{\mathrm{d}H_r}{\mathrm{d}\theta}\sin\theta - m\nu H_r\cos\theta}{1-\nu^2\cos^2\theta} \ , \tag{2.32}$$

$$H_\varphi \sin\theta = \frac{mH_r - \nu\frac{\mathrm{d}H_r}{\mathrm{d}\theta}\sin\theta\cos\theta}{1-\nu^2\cos^2\theta} \ , \tag{2.33}$$

where $\frac{\mathrm{d}H_r}{\mathrm{d}\theta}$ denotes the total latitudinal derivative of H_r. H_φ has the same parity as H_r with respect to $\theta = \frac{\pi}{2}$, whereas H_θ has the opposite parity. We provide a full derivation of the Laplace tidal operator and the lattitudinal and azimuthal Hough function in the appendix. Even though the validity of the solutions obtained within the TAR is not guaranteed in the sub-inertial regime, as the spatial structure of the obtained waves does not include the development of shear layers (see e.g. Dintrans and Rieutord, 2000; Mathis, 2009), one can, to a fair approximation use it to study sub-inertial waves ($\omega < 2\Omega$), which are often excited in rapidly rotating stars (e.g. Neiner et al., 2012; Moravveji et al., 2016; Saio et al., 2018). In this case, as noted by Prat et al. (2019), the full Hough functions need to be used instead of spherical harmonics (see Section (2.1)), as these waves are trapped in an equatorial belt[1].

In fact, Townsend (2003) states that the key to deriving asymptotic solutions to Laplace's tidal equations lies in noting that the spin parameter ν appears in product with the modified latitudinal coordinate μ, so that, in order for the Hough functions to remain finite for large $|\nu|$, the Hough functions can only be appreciably different from zero in a narrow equatorial region of small $|\mu|$ (the equatorial belt/waveguide). This essentially prevents low-frequency waves from propagating towards high latitudes. Townsend (2003) demonstrated that, when the eigenvalue of Laplace's tidal equations is not equal to m^2, one can write the Hough functions in terms of Hermite polynomials of integer 'meridional order' $s \geq 0$. A rederivation of the governing

[1]Nevertheless it seems that Hough functions were not calculated explicitly in (most) literature concerning gravity modes predating Prat et al. (2019), instead resorting to approximate forms.

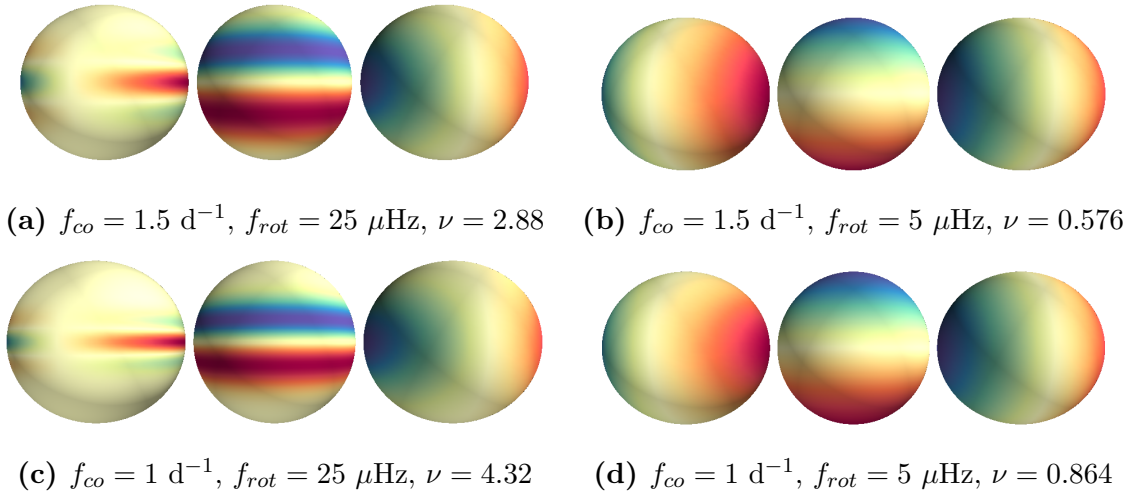

(a) $f_{co} = 1.5$ d^{-1}, $f_{rot} = 25$ μHz, $\nu = 2.88$ **(b)** $f_{co} = 1.5$ d^{-1}, $f_{rot} = 5$ μHz, $\nu = 0.576$

(c) $f_{co} = 1$ d^{-1}, $f_{rot} = 25$ μHz, $\nu = 4.32$ **(d)** $f_{co} = 1$ d^{-1}, $f_{rot} = 5$ μHz, $\nu = 0.864$

Figure 2.3: Representation of the radial component of $l = 1$ dipole modes in rotating stars ($H_r(\theta)e^{im\varphi}$, where H_r is calculated with the method described in Section (3.2.2)). From left to right in each subfigure: $(l, m) = (1, -1)$; $(l, m) = (1, 0)$; $(l, m) = (1, 1)$. Near-core rotation frequency bounds (f_{rot}) are obtained from figure 5 in Ouazzani et al. (2018), near the start of the MS. Pulsation frequency bounds in the co-rotating frame (f_{co}) are selected from the ensemble study by Van Reeth et al. (2016) of 40 γ Dor stars, where we list the approximate lower and mid values. Observed zonal modes ($m = 0$) have a frequency of ≈ 1 d^{-1} (Van Reeth et al., 2016). Spin parameters ν are listed. The color scheme is the same as in Figure (2.1). For ease of comparison we list the pulsation frequencies in μHz: 1 d^{-1} $\simeq 11.57$ μHz, 1.5 d^{-1} $\simeq 17.36$ μHz; and the rotation frequencies in d^{-1}: 5 μHz $\simeq 0.432$ d^{-1} and 25 μHz $\simeq 2.16$ d^{-1}.

equations, in which a small error is noted, is shown in the appendix. Utilizing Taylor's series expansions, he then found an expression for the eigenvalue of Laplace's tidal equations for gravito-inertial modes equal to:

$$\lambda \approx \nu^2(2s+1)^2 + \mathcal{O}(\nu) \ . \tag{2.34}$$

Moreover, he derived an expression for the loci $\mu = \pm \mu_{1/2}$ at which the latitudinal Hough function transitions from the oscillatory to the exponential regime (i.e. where the second derivative with respect to μ vanishes), by taking into account that Laplace's tidal equations are satified only if:

$$2s + 1 = (\sqrt{\lambda})\nu\mu_{1/2}^2 \Leftrightarrow \mu_{1/2} = \sqrt{\frac{2s+1}{\nu\sqrt{\lambda}}} \ . \tag{2.35}$$

Filling in the approximate eigenvalue solution for gravito-inertial modes then yields the following waveguide boundary (at which the radial Hough function is maximal):

$$\mu_{1/2} \approx \frac{1}{|\nu|} \ . \tag{2.36}$$

Hence, for rapidly rotating stars (large ν), the modes will be trapped equatorially in a region defined by $|\mu| \leq |\nu^{-1}|$, as supported by numerical solutions of e.g. Bildsten et al. (1996). This equatorial mode trapping can readily be observed in Figure (2.3), where the equatorial belts become narrower for increasing spin parameter ν.

Taking the assumptions of the TAR into account, Mathis (2009) derived the dispersion relation for gravito-inertial waves (transversal waves restored by both

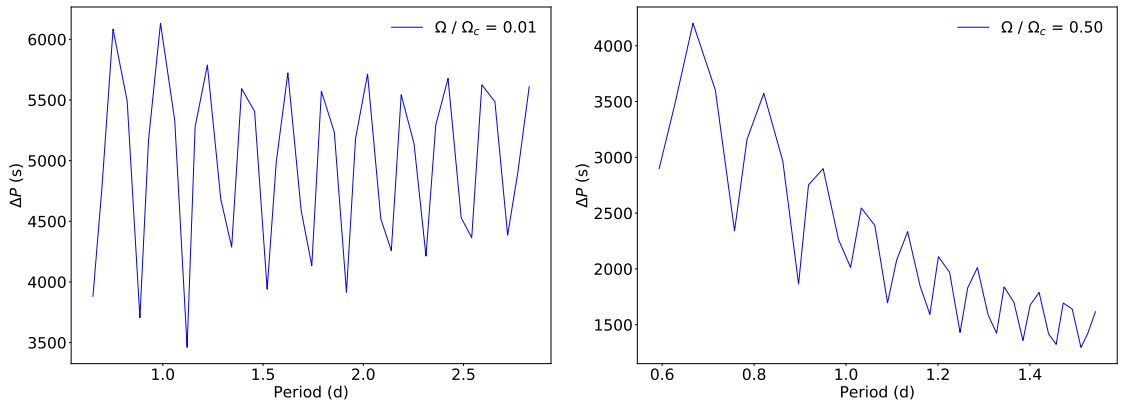

Figure 2.4: Typical period spacing patterns for zonal dipole modes ($l = 1, m = 0$) in rotating 3 $M_\odot$ mid-MS main-sequence stars, with different rotation rates (left: 1% Ω_c, right: 50% Ω_c, where Ω_c is given by Equation (2.21).), calculated in the TAR. The inherent tilt due to rotation is clearly visible, increasing with increasing angular rotation frequency. Patterns for other considered masses in my model grid are similar.

buoyancy and the Coriolis force):

$$k_r^2(r) = \frac{N^2}{\omega^2}\frac{\lambda_{l,m}(\nu)}{r^2} \ . \tag{2.37}$$

For a non-rotating star, $\nu = 0$ and $\lambda_{l,m}(0) = l(l+1)$, reducing Equation (2.37) to its non-rotating equivalent (Equation (2.17)), taking into account the assumption $\omega \ll N$.

In fact, the more general dispersion relation derived by Unno et al. (1989) leads one to derive the same conclusion as the one obtained for g modes in section 2.1: gravito-inertial waves, like g modes, are primarily transversal, with the radial component of their wave vector and the horizontal component of their displacement dominating (i.e. $k_V = k_r \gg k_H$ and $||\boldsymbol{\xi}_H|| \gg \xi_V = \xi_r$).

From Equation (2.37) one can then deduce the following asymptotic expression for the (high radial order) g mode pulsation periods of rotating stars within the TAR (e.g. Bouabid et al., 2013; Van Reeth et al., 2016; Ouazzani et al., 2017; Christophe et al., 2018):

$$P_{co} \approx \frac{\Pi_0}{\sqrt{\lambda_{l,m}(\nu)}}\left(n_g + \alpha_g\right) \ , \tag{2.38}$$

where α_g is a phase term depending on the stellar structure (cfr. $\alpha_{l,g}$), Π_0 is the buoyancy radius (see Section (2.1)), and $\lambda_{l,m}(\nu)$ is the eigenvalue of Laplace's tidal equations. Hence, for a chemically homogeneous, non-magnetic (rotating) star, the asymptotic period spacing of g modes in the co-rotating frame with the same degree l is:

$$\Delta P_{co} \approx \frac{\Pi_0}{\sqrt{\lambda_{l,m}(\nu)}} \ . \tag{2.39}$$

In principle, the degree l should be replaced with $k = l - |m|$, in order to avoid confusion about mode identification in (rapidly) rotating stars (e.g. Lee and Saio, 1997).

Rotation tilts asymptotic period spacing patterns, the degree of tilt depending on the mode geometry and angular rotation frequency, the latter dependence shown in Figure (2.4). Inherently this can easily be conceptualized by considering that inertial frequencies are observed. Indeed, $f_{inertial} = f_{co} + m f_{rot}$, so that the obtained modes should contain a general tilt, that changes with the rotation frequency $f_{rot} = \Omega_{rot}/2\pi$. By increasing the rotation rate, toroidal modes (and toroidal contributions to previously spheroidal-only modes) also become important, which can potentially couple with different spheroidal contributions (due to e.g. the Coriolis force) causing the period spacing pattern to be modified (see e.g. Saio et al., 2018). Considering the same modes in the TAR will thus yield some deviations from this tilt estimate. In the inertial reference frame zonal modes are less affected, prograde modes ($m > 0$), which propagate in the direction of rotation, will receive a (strong) downward tilt, because $P_{inertial} = P_{co}/(1 - mP_{co}/P_{rot})$. Retrograde modes ($m < 0$), propagating against the rotation, will receive an 'overall' upward tilt.

Hence, a detailed analysis of period spacing patterns is an efficient way of constraining the interior stellar structure (Van Reeth, 2017). Multiple such studies have been performed in the past (e.g. Van Reeth et al., 2016; Moravveji et al., 2016; Ouazzani et al., 2017; Van Reeth, 2017; Van Reeth et al., 2018; Ouazzani et al., 2018; Li et al., 2019b,a; Mombarg et al., 2019). A general methodological framework to study the gravity mode frequencies in stars with a convective core has been constructed (Aerts et al., 2018).

2.3 Influence of magnetic field

2.3.1 Influence on stellar evolution models

If the stellar magnetic field $\boldsymbol{B}$ is strong enough, it will significantly alter particle motion in the stellar plasma. Particularly, so-called magnetized plasmas are anisotropic: they respond differently to forces which are parallel and perpendicular to the direction of $\boldsymbol{B}$. Hence, the Lorentz force is expected to (greatly) contribute to small-scale mixing processes and affect stellar evolution.

The so-called plasma β parameter, which is defined as the ratio of the thermal energy density (nkT, with n the number density of all plasma species and T their temperature, where k is Boltzmann's constant) to the magnetic energy density ($B^2/2\mu_0$, where μ_0 is the vacuum permeability), can be used to probe the degree of magnetization of the plasma. The plasma energy density is conventionally identified with the pressure p, so that the plasma β for species 'x' is defined as (Goedbloed and Poedts, 2004; Fitzpatrick, 2015):

$$\beta_x = \frac{2\mu_0 n_x k T_x}{B^2} = \frac{2\mu_0 p_x}{B^2} \tag{2.40}$$

yielding a total β:

$$\beta = \sum_x \beta_x \tag{2.41}$$

In the deep stellar interior, we expect β to be large, given the large central density and temperature. Hence, we don't expect the near-core plasma to be magnetized.

Several magnetohydrodynamic instabilities can occur in (differentially) rotating stars, which contribute to mixing and angular momentum transport. An overview of these instabilities is given in Aerts et al. (2019). Angular momentum transport inside stars throughout their evolution is in dire need of improvement (Aerts et al., 2019), starting to diverge from theoretical predictions already during main-sequence evolution (see e.g. Eggenberger et al., 2017; Townsend et al., 2018; Tayar and Pinsonneault, 2018). The origin of missing angular momentum transport in stellar models is a current (hot) topic of research, with magnetism and (non-standing) internal gravity waves (IGWs) being two important considered mechanisms (Aerts et al., 2019). For the first, magnetic stresses need to be taken into account in the stellar interior, whereas for the latter direct excitation by convective plumes entering the radiative zone (i.e. the convective overshoot) is important. Two recent examples of studies considering these angular momentum transport mechanisms are Fuller et al. (2019) and Edelmann et al. (2019), for magnetic transport and IGW transport, respectively. Moreover, rotational, magnetic and chemical mixing effects and angular momentum transport are intrinsically linked. For example, the differential rotation profile inside radiative zones of rotating magnetic stars is thought to be smoothed in the presence of magnetic fields (see e.g. Ferraro, 1937; Moss, 1992; Spruit, 1999; Mathis and Zahn, 2005; Zahn, 2011). This validates our assumption of uniform rotation in Section (2.2.2). This led Press (1981); Browning et al. (2004) to conclude that, in the presence of a magnetic field, matter should lose its inertia quicker when overshooting the convective core boundary, resulting in smaller convective core overshooting regions (Buysschaert et al., 2018). In addition, the shear layers that come to exist in the stellar interior due to the breakup of IGWs contribute to local chemical mixing, further affecting the stellar structure (Aerts et al., 2019). Finally, magnetic fields also affect the dissipation and propagation of IGWs in stellar interiors at the convective core boundary: they can be completely blocked (toroidal field), or trapped along the poloidal field lines (poloidal field), as was discussed in Aerts et al. (2019).

Hence, these mechanisms affect the mixing in the overshoot region, and thus change the amount of hydrogen available for the core through convective overshoot, affecting main-sequence lifetime. Mixing inside rotating magnetic stars is thus expected to be different from mixing inside rotating and non-rotating (non-magnetic) stars.

2.3.2 Influence on pulsation models

Previous work

It is a well-known fact that the presence of a magnetic field induces splitting of stellar oscillation frequencies, as first determined by Ledoux and Simon (1957). Throughout the years, this effect was modelled using a perturbative approach (see e.g. Shibahashi and Takata, 1993). However, near the surface the magnetic pressure dominates over the plasma pressure (i.e. surface plasma is characterized by low plasma β). Hence, near the surface, the acoustic modes therefore couple with the Alfvén modes and non-perturbative treatments (see e.g. Bigot et al., 2000) should be used. Hasan and Christensen-Dalsgaard (1992) analytically determined the frequency shift of p and g modes in an isothermal plasma due to a homogenous vertical magnetic field (using the full magneto-hydrodynamics (MHD) equations), and found that even a weak

field (i.e. $\beta \gg 1$) can produce significant g mode frequency shifts, whereas the effect on the p-mode spectrum is relatively weak. Therefore, g mode frequency shifts are thought to be a good diagnostic to probe the internal magnetic field of stars.

A more realistic magnetic field configuration (than the vertical field considered by Hasan and Christensen-Dalsgaard (1992)) was considered by Hasan et al. (2005), who investigated how a purely poloidal, axisymmetric field affects the frequencies of high radial order g modes in a (very) slowly rotating star, resulting in a frequency perturbation (in the co-rotating frame) determined by:

$$\frac{\delta\omega}{\omega} = S_c B_0^2 = \frac{1}{8\pi\omega^2}\left[\frac{B_0^2}{\rho_c R^2}\right]\mathfrak{C}_{l,m}\mathfrak{I}\ , \tag{2.42}$$

where ρ_c is the central mass density, S_c is the 'magnetic splitting coefficient', which increases rapidly with period because it is proportional to ω^{-2} and $\mathfrak{I}$ increases with period, B_0 is the magnetic field amplitude scaling factor,

$$\mathfrak{I} = \frac{\int \left|\frac{2}{x^2}\frac{\mathrm{d}}{\mathrm{d}x}\left(xb(x)\xi_h\right)\right|^2 x^2 dx}{\int |\xi_h|^2 \left(\frac{\rho}{\rho_c}\right) x^2 dx}\ , \tag{2.43}$$

and

$$\mathfrak{C}_{l,m} = \frac{\int \left[\left|\cos\theta \frac{\partial Y_l^m}{\partial\theta}\right|^2 + m^2\left|\frac{\cos\theta}{\sin\theta}Y_l^m\right|^2\right]\sin\theta d\theta}{l(l+1)\int |Y|^2 \sin\theta d\theta}\ , \tag{2.44}$$

where $x = r/R$ is a normalized radial coordinate, $b(x)$ is the radial component of $\boldsymbol{B}$, and Y_l^m are spherical harmonic functions. As already pointed out by Ledoux and Simon (1957), the fact that this equation does not depend on the sign of m indicates that the magnetic field reduces the $2l+1$ degeneracy of the eigenmodes to $l+1$ (Hasan et al., 2005). Hence, instead of talking about frequency splitting, one should rather call this phenomenon a magnetic frequency shift.

Although the Hasan et al. (2005) formalism presented a step forwards in the modelling of internal magnetic fields, the authors only considered non-rotating and (very) slowly rotating stars. Moreover, theoretical and numerical studies show that the stability of fossil magnetic fields requires a mixed configuration with both poloidal and toroidal components, extending deep within the radiative stellar envelope (e.g. Tayler, 1973; Markey and Tayler, 1973; Braithwaite and Spruit, 2004; Braithwaite and Nordlund, 2006; Braithwaite, 2007, 2008; Featherstone et al., 2009; Braithwaite, 2009; Duez and Mathis, 2010).

Our work

We (Prat et al., 2019) therefore developed a new formalism. My role in this work has been to derive the governing relations originally developed by Dr. Vincent Prat independently, as well as validate the implementation for the numerical computations. For simplicity, the poloidal-toroidal field configuration is assumed to be axisymmetric and dipolar, yielding the following analytical magnetic field prescription (in spherical coordinates (r,θ,φ)):

$$\boldsymbol{B} = B_0\left[b_r(r)\cos\theta, b_\theta(r)\sin\theta, b_\varphi(r)\sin\theta\right]\ , \tag{2.45}$$

where B_0 is an amplitude scaling factor, and θ is the colatitude. The magnetic field is assumed to be weak, such that the effect of the unperturbed Lorentz force on the equilibrium state (of the stellar model) is negligible (as indicated in e.g. Duez and Mathis, 2010). In order to derive the mode frequency perturbations due to the magnetic field, the ideal MHD assumptions are made (see e.g. Goedbloed and Poedts, 2004):

1. *Collisionality*: the timescale between collisions should be much smaller than other characteristic timescales, so that Maxwellian velocity distributions (for the individual plasma species) can be used. This implies that plasma densities should be high, as expected in a stellar (near-core) plasma, so that only long-timescale phenomena (i.e. collective plasma behaviour) are relevant.

2. *Macroscopic scales*: The plasma dynamics described by the non-dissipative MHD equations still includes phenomena on small length (λ) and time (τ) scales. Hence, in the ideal MHD assumption only large length and time scales are considered:

$$\lambda_{\rm MHD} \sim a \gg r_{c,i} \ , \qquad \tau_{\rm MHD} \sim \frac{a}{v_A} \gg \omega_{c,i}^{-1} \ ,$$

   where a is the typical length scale of the considered plasma system, $\boldsymbol{v}_A = \frac{\boldsymbol{B}}{\sqrt{\mu_0 \rho}}$ is the Alfvén velocity, which characterises the propagation of magnetic waves (μ_0 is the vacuum permeability), $r_{c,i}$ are ion cyclotron radii defined as $r_c \approx v_{th,i}/\omega_{c,i}$, the radius of the circular motion of a charged particle in the presence of a uniform magnetic field with $v_{th,i} = \sqrt{kT_i/m_i}$ the thermal velocity of ionic species 'i' (T_i and m_i are the species temperature and mass, respectively). $\omega_{c,i}$ are the (angular) ion cyclotron frequencies, defined by $\omega_{c,i} = |q_i|B/m_i$ with q_i the ionic species charge. This allows us to consider the plasma as a *single* conducting fluid, without distinguishing the individual species. Therefore, we describe the bulk plasma behaviour.

3. *Ideal fluids*: Plasma dynamics are only considered on short timescales for which macroscopic plasma variables can be considered constant:

$$\tau_{\rm MHD} \ll \tau_{\rm R} \sim \frac{a^2}{\eta} \ ,$$

   where $\tau_{\rm R}$ is the timescale of resistive decay of the magnetic field, and where η is the magnetic resistivity of the fluid. This assumption can be justified by a dimensional analysis of the different terms in the resistive MHD induction equation (Goedbloed and Poedts, 2004; Maeder, 2009):

$$\frac{\partial \boldsymbol{B}}{\partial t} = \nabla \times (\boldsymbol{v} \times \boldsymbol{B}) - \mu_0^{-1} \nabla \times (\eta \nabla \times \boldsymbol{B}) \ . \tag{2.46}$$

   Taking V, B and L to be characteristic values of velocity, magnetic field and length scale, the dimensions of the two terms on the right hand side are:

$$\nabla \times (\boldsymbol{v} \times \boldsymbol{B}) \propto \frac{V\ B}{L} \ , \qquad \mu_0^{-1} \nabla \times (\eta \nabla \times \boldsymbol{B}) \propto \frac{\eta\ B}{\mu_0\ L^2} \ . \tag{2.47}$$

The ratio of the dimensions of both terms is a dimensionless number known as the magnetic Reynolds number (R_m):

$$R_m = \frac{\frac{V\ B}{L}}{\frac{\eta B}{\mu_0 L^2}} = \frac{V\ L\ \mu_0}{\eta}\ . \tag{2.48}$$

In astrophysical situations, L is expected to be very large, so that the second term is negligible (R_m is large), hence justifying our approach. Moreover, Ohmic dissipation is negligible compared to thermal diffusion (Mathis and de Brye, 2011). In addition, this means that we ought to verify that the electrons (and ions) in the near-core regions are not (partially) degenerate, as degenerate matter clearly does not behave as a typical plasma. However, for the considered mass range and evolutionary stage in our stellar model grid (see Section (3.1)), electron/ion degeneracy is not important (see e.g. Kippenhahn et al., 2012).

With the ideal MHD assumptions, the Eulerian perturbation to the magnetic field ($\boldsymbol{B}'$) due to the oscillation displacement reads:

$$\boldsymbol{B}' = \nabla \times (\boldsymbol{\xi}_0 \times \boldsymbol{B})\ . \tag{2.49}$$

In order to compute the magnetic frequency shifts the perturbed Lorentz force needs to be used, which is defined as (Prat et al., 2019):

$$\boldsymbol{F}'_L = \frac{1}{\mu_0}\left[(\nabla \times \boldsymbol{B}) \times \boldsymbol{B}' + (\nabla \times \boldsymbol{B}') \times \boldsymbol{B}\right] \tag{2.50}$$

Proof. Perturbing the induction equation in the ideal MHD approximation:

$$\frac{\partial \boldsymbol{B}}{\partial t} = \nabla \times (\boldsymbol{v} \times \boldsymbol{B})$$

yields (keeping first-order terms):

$$\frac{\partial}{\partial t}(\boldsymbol{B} + \boldsymbol{B}') = \nabla \times (\boldsymbol{v}' \times \boldsymbol{B}) + \nabla \times (\boldsymbol{v} \times \boldsymbol{B}')\ ,$$

so that, if we assume a static equilibrium magnetic field $\frac{\partial \boldsymbol{B}}{\partial t} = 0$ and if we assume a equilibrium star without (significant) velocity fields (i.e. $\boldsymbol{v} = 0$), we obtain:

$$\begin{aligned} \frac{\partial \boldsymbol{B}'}{\partial t} &= \nabla \times (\boldsymbol{v}' \times \boldsymbol{B})\ , \\ \Leftrightarrow \frac{\partial \boldsymbol{B}'}{\partial t} &= \nabla \times \left(\frac{\partial \boldsymbol{\xi}_0}{\partial t} \times \boldsymbol{B}\right)\ , \end{aligned}$$

by integrating over time, which is equal to Equation (2.49). □

Proof. The non-perturbed Lorentz force is defined by:

$$\boldsymbol{F}_L = |q|\boldsymbol{E} + \boldsymbol{J} \times \boldsymbol{B} \ ,$$

where $\boldsymbol{J}$ is the current density. However, on the astrophysical scales considered, no large-scale electric fields (E) exist, so that the first term is negligible. Ampère's law (in its differential form) relates the (steady) magnetic field to the current distribution in any region where $\boldsymbol{B}$ and $\boldsymbol{J}$ are differentiable: (Moffatt, 1978; Charbonneau, 2013)

$$\nabla \times \boldsymbol{B} = \mu_0 \ \boldsymbol{J}$$

Utilizing the above expression yields the following expression for the Lorentz force:

$$\boldsymbol{F}_L = \mu_0^{-1} \left(\nabla \times \boldsymbol{B}\right) \times \boldsymbol{B}$$

Perturbing this equation using an Eulerian perturbation to the magnetic field then yields:

$$\begin{aligned}
\boldsymbol{F}_L + \boldsymbol{F}_L' &= \mu_0^{-1} \left[\left(\nabla \times \left(\boldsymbol{B}_0 + \boldsymbol{B}'\right)\right) \times \left(\boldsymbol{B}_0 + \boldsymbol{B}'\right)\right] \ , \\
&= \mu_0^{-1} \left[\left(\nabla \times \boldsymbol{B}_0\right) \times \boldsymbol{B}_0 + \left(\nabla \times \boldsymbol{B}_0\right) \times \boldsymbol{B}' \right. \\
&\qquad \left. + \left(\nabla \times \boldsymbol{B}'\right) \times \boldsymbol{B}_0 + \left(\nabla \times \boldsymbol{B}'\right) \times \boldsymbol{B}'\right] \ , \\
&= \mu_0^{-1} \left[\left(\nabla \times \boldsymbol{B}_0\right) \times \boldsymbol{B}_0 + \left(\nabla \times \boldsymbol{B}_0\right) \times \boldsymbol{B}' + \left(\nabla \times \boldsymbol{B}'\right) \times \boldsymbol{B}_0\right] \ ,
\end{aligned}$$

where we neglect second-order perturbations in the last equality. □

In the magnetic case, the perturbed $\boldsymbol{\mathcal{C}}(\boldsymbol{\xi})$ operator (i.e. $\boldsymbol{\mathcal{C}}_1(\boldsymbol{\xi}_0)$) in Equation (2.28) contains the extra Lorentz force term derived above.

The more general equations of motion derived by Unno et al. (1989) for a star with velocity field $\boldsymbol{v}$, rotation vector $\boldsymbol{\Omega} = \Omega_0 \boldsymbol{e}_z$ (i.e. uniform rotation), magnetic field $\boldsymbol{B}$, evaluated in the co-rotating frame are quite similar:

$$\frac{\partial \boldsymbol{v}}{\partial t} + \left(\boldsymbol{v} \cdot \nabla\right) \boldsymbol{v} + 2 \ \boldsymbol{\Omega} \times \boldsymbol{v} + \boldsymbol{\Omega} \times \boldsymbol{\Omega} \times \boldsymbol{r} = -\nabla\phi - \frac{1}{\rho}\nabla p + \frac{1}{4\pi\rho} \left(\nabla \times \boldsymbol{B}\right) \times \boldsymbol{B} \ , \tag{2.51}$$

from which one can obtain the following (Eulerian) perturbed equations (perturbing the velocity field), assuming a static equilibrium velocity and magnetic field ($\frac{\partial \boldsymbol{v}_0}{\partial t} = 0$, $\frac{\partial \boldsymbol{B}_0}{\partial t} = 0$):

$$\begin{aligned}
&\frac{\partial \boldsymbol{v}'}{\partial t} + \left(\boldsymbol{v}' \cdot \nabla\right) \boldsymbol{v}_0 + \left(\boldsymbol{v}_0 \cdot \nabla\right) \boldsymbol{v}' + 2\boldsymbol{\Omega} \times \boldsymbol{v}' = -\frac{1}{\rho_0}\nabla P' - \nabla\phi' \\
&+ \frac{\rho'}{\rho_0^2}\left[\nabla p_0 - \frac{1}{4\pi}\left(\nabla \times \boldsymbol{B}_0\right) \times \boldsymbol{B}_0\right] + \frac{1}{4\pi\rho_0}\left[\left(\nabla \times \boldsymbol{B}_0\right) \times \boldsymbol{B}' + \left(\nabla \times \boldsymbol{B}'\right) \times \boldsymbol{B}_0\right]
\end{aligned} \tag{2.52}$$

where ϕ is the gravitational potential, the subscript 0 denotes equilibrium quantities, and where we do not neglect the centrifugal term ($\boldsymbol{\Omega} \times \boldsymbol{\Omega} \times \boldsymbol{r}$) and do not neglect the perturbation of the gravitational potential. Making the Cowling approximation (i.e.

neglecting the Eulerian perturbation of the gravitational potential ϕ'), assuming the temporal dependence of the eigenfunctions to be equal to $e^{-i\omega t}$, one can show that a magnetic equivalent to the (perturbed) Equation (2.28) can be derived. As shown in the appendix, dropping the subscript 0 for the equilibrium quantities for simplicity, this yields:

$$\begin{aligned}\omega^2\boldsymbol{\xi} + 2i\omega\ \boldsymbol{\Omega}\times\boldsymbol{\xi} + \frac{\rho'}{\rho^2}\left[\nabla P - \frac{1}{4\pi}\left(\nabla\times\boldsymbol{B}\right)\times\boldsymbol{B}\right] - \frac{\nabla P'}{\rho} \\ + \frac{1}{4\pi\rho}\left[\left(\nabla\times\boldsymbol{B}\right)\times\boldsymbol{B}' + \left(\nabla\times\boldsymbol{B}'\right)\times\boldsymbol{B}\right] = 0\end{aligned} \tag{2.53}$$

so that, in the magnetic case, the operators of Equation (2.28) are defined as:

$$\boldsymbol{\mathcal{B}}(\boldsymbol{\xi}) = 2\ \boldsymbol{\Omega}\times\boldsymbol{\xi} \tag{2.54}$$

$$\begin{aligned}\boldsymbol{\mathcal{C}}(\boldsymbol{\xi}) = \frac{\rho'}{\rho^2}\left[\nabla P - \frac{1}{4\pi}\left(\nabla\times\boldsymbol{B}\right)\times\boldsymbol{B}\right] - \frac{\nabla P'}{\rho} \\ + \frac{1}{4\pi\rho}\left[\left(\nabla\times\boldsymbol{B}\right)\times\boldsymbol{B}' + \left(\nabla\times\boldsymbol{B}'\right)\times\boldsymbol{B}\right]\end{aligned} \tag{2.55}$$

However, the second term of Equation (2.55) is neglected in Prat et al. (2019), because we assume that the (equilibrium) field is not strong enough to significantly affect the background equilibrium. The first and third term (of Equation (2.55)) belong to the $\boldsymbol{\mathcal{C}}_0\left(\boldsymbol{\xi}_0\right)$ part of the operator, whereas the last two terms of Equation (2.55) belong to the $\boldsymbol{\mathcal{C}}_1\left(\boldsymbol{\xi}_0\right)$ part of the perturbed operator, if we consider the extra shift caused by magnetic fields (on top of rotational influence). Therefore, only the last two terms, which together make up the perturbed Lorentz force (see Equation (2.50)), are important for calculating magnetic frequency shifts $\delta\omega = \varepsilon\omega_1$, which are thus proportional to $\langle\boldsymbol{\xi}_0, \boldsymbol{F}_L'/\rho\rangle = \langle\boldsymbol{\xi}_0, \varepsilon\boldsymbol{\mathcal{C}}_1\left(\boldsymbol{\xi}_0\right)\rangle$. Hence, the finiteness of $\boldsymbol{F}_L'/\rho$ must be ensured in any perturbative formalism.
Essentially this shows that magnetic frequency shifts are proportional to the square of the magnetic field amplitude, as noted in Prat et al. (2019).

The first term in the denominator of Equation (2.28) is equal to (Prat et al., 2019):

$$\langle\boldsymbol{\xi}_0, \boldsymbol{\xi}_0\rangle = 2\pi\int_0^R\int_0^\pi \rho r^2\left[|\xi_r|^2 H_r^2 + |\xi_h|^2\left(H_\theta^2 + H_\varphi^2\right)\right] dr\sin\theta d\theta\ . \tag{2.56}$$

The first term in this expression is much smaller than the second one for high radial order g modes ($|\xi_r|^2 \ll |\xi_h|^2$), so that it can be neglected for such modes (as was done in Hasan et al., 2005). However, for low radial order modes, this can introduce significant errors. The second term in the denominator of Equation (2.28) is equal to (Prat et al., 2019):

$$\langle\boldsymbol{\xi}_0, i\boldsymbol{\mathcal{B}}\left(\boldsymbol{\xi}_0\right)\rangle = 8\pi\ \Omega\int_0^R \rho r^2|\boldsymbol{\xi}_h|^2 dr\int_0^\pi H_\theta H_\varphi\sin\theta\cos\theta d\theta\ . \tag{2.57}$$

Since this term scales with the spin parameter $\nu = 2\Omega/\omega$, it is negligible for low radial order modes, but not for high radial order modes. When it is negligible, Equation (2.28) implies that

$$\frac{\delta\omega}{\omega} \propto \frac{B_0^2}{\omega_0^2}\ , \tag{2.58}$$

which is equivalent to the non-rotating case, for which Hasan et al. (2005) obtained Equation (2.42), although $\mathfrak{I}$ in our case is defined as (Prat et al., 2019):

$$\mathfrak{I} = \frac{\int_0^R \left| \frac{\mathrm{d}}{\mathrm{d}r} \left(r b_r \xi_h \right) \right|^2 dr}{\int_0^R |\xi_h|^2 \left(\frac{\rho}{\rho_c} \right) x^2 dx} \ , \tag{2.59}$$

where $\frac{\mathrm{d}}{\mathrm{d}r}$ denotes a radial total derivative. Hence, we noted in Prat et al. (2019) that the magnetic field influence is stronger at lower frequencies, consistent with the fact that those frequencies are closer to the Alfvén frequency. Obtaining the explicit form for the term in the numerator $\langle \boldsymbol{\xi}_0, \boldsymbol{C}\left(\boldsymbol{\xi}_0\right) \rangle$ involves calculating a large number of terms, of which several are zero due to symmetry. The explicit expressions for the non-zero terms can be found in appendix B of Prat et al. (2019).

For high radial order modes (which have a large radial wavenumber), one can perform a Jeffreys-Wentzel-Kramers-Brillouin-like small-wavelength analysis (see e.g. Unno et al., 1989, in the context of stellar oscillations). Doing so, Prat et al. (2019) note that if the poloidal component of the magnetic field is much larger than the toroidal component, or of the same order of magnitude, the dominant term of $\langle \boldsymbol{\xi}_0, \boldsymbol{C}\left(\boldsymbol{\xi}_0\right) \rangle$ is proportional to:

$$\int_0^R \left| \frac{\mathrm{d}}{\mathrm{d}r} \left(r b_r \xi_h \right) \right|^2 dr \int_0^\pi \left(H_\theta^2 + H_\varphi^2 \right) \cos^2\theta \sin\theta d\theta \ , \tag{2.60}$$

consistent with the result obtained by Hasan et al. (2005). However, our (Prat et al., 2019) formalism can handle waves in the sub-inertial regime ($\omega < 2\Omega$) that become trapped in an equatorial belt. In contrast, for a field with a toroidal component much greater than its poloidal part, some eight other terms could have significant impact on the perturbation (Prat et al., 2019).

3 — Parameter Study

We used the Modules for Experiments in Stellar Astrophysics (MESA) code (version 10396; Paxton et al., 2011, 2013, 2015, 2016, 2018, 2019), a one-dimensional stellar evolution code, to obtain non-rotating, non-magnetic (stellar) models for a range of different fundamental parameters. In addition, we used GYRE (version 5.2; Townsend and Teitler, 2013; Townsend et al., 2018), a stellar oscillation code, to compute theoretical frequencies of gravito-inertial/gravity modes for these MESA stellar models, including the effects of rotation in the TAR for g modes. Both the stellar evolution and pulsation codes make efficient use of computational resources, were found to be robust and accurate, and are open source. Finally, a python script (supplied by Dr. Vincent Prat, CEA, and revised by myself) is used to probe the influence of internal magnetic fields on the frequencies of the gravito-inertial/gravity modes.

3.1 Constructing a grid of MESA stellar evolution models: parameter ranges

An overview of the grid parameters is given in Table (3.1). A typical inlist used to calculate the evolutionary models with MESA can be found in the appendix. The selection of the individual parameters will be explained in the following subsections.

Composition: initial metallicity Z and core hydrogen mass fraction X_c

All of our MESA models assume the Asplund et al. (2009) metal mixture, with an initial hydrogen mass fraction $X_{ini} = 0.71$, taken from the galactic B-star standard of Nieva and Przybilla (2012). Initial metallicity is varied: $Z \in [0.010, 0.018]$, with the step mentioned in Table (3.1). The initial helium mass fraction Y is then fixed by: $Y = 1 - X_{\rm ini} - Z$. The core hydrogen content X_c is a proxy for the evolutionary stage or the age of the model during the main-sequence (e.g. Mombarg et al., 2019). In our parameter grid we choose to output MESA models when X_c is approximately equal to 0.675, 0.340 and 0.005, which are taken to represent a star at the ZAMS, mid-MS and TAMS life phase, respectively. This allows us to obtain a general idea on how stellar evolution affects the magnetic field structure and thus the effect on the period spacing patterns. We terminate the evolution once $X_c < 0.001$.

The envelope mixing coefficient: $D_{\rm mix}$

Including mixing processes due to rotational and magnetic instabilities frequently induces numerical discontinuities in stellar models (Truyaert, 2016). Such disconti-

nuities lead to g mode behaviour that is not observed in *Kepler* data. Moreover, as mentioned in Section (2.2.1), these processes have not been well-calibrated using observations. Therefore, instead of using the explicit (physical) forms of equations describing the mixing induced by such processes, we approximate the envelope mixing with one global constant level $D_{\rm mix}$. This makes the approach less model-dependent, and allows us to constrain the diffusive mixing coefficients beyond the fully mixed convective cores (as noted by e.g. Moravveji et al., 2016). These parameters are not constrained from first principles, so that the values for D_{mix} were chosen based on the grids in Van Reeth et al. (2016, 2018); Mombarg et al. (2019), representative of observed γ Dor stars.

The extent of convective (core) overshooting: $f_{\rm ov}$

Several prescriptions for the convective overshooting parameter exist. We will only consider one, the exponential overshoot parameter $f_{\rm ov}$, which results in a mixing coefficient inside the core overshoot zone defined by Freytag et al. (1996); Herwig (2000):

$$D_{\rm ov} = D_0 \exp\left(\frac{-2\,(r - r_0)}{f_{\rm ov,sim} H_{\rm P,cc}}\right) \ , \tag{3.1}$$

where $r_0 = r_{cc} - f_0 H_{P,cc}$ is the radius at which core overshooting stars with f_0 a free parameter, r_{cc} the radius of the convective core, defined as the position for which $\nabla_{\rm ad} = \nabla$ (the Schwarzschild boundary), and $H_{\rm P,cc}$ the pressure scale height at r_{cc}. D_0 is the value of the (convective) mixing coefficient, evaluated from MLT at r_0. Adopting this prescription results in a smooth Brunt-Väisälä frequency transition from the overshoot region to the radiative envelope region, as was described in e.g. Moravveji et al. (2016).

In order to account for this 'step' inside the convective region in MESA, the $f_{\rm ov}$ parameter should be increased with f_0: $f_{\rm ov,sim} = f_{\rm ov} + f_0$, so that the overshooting region extends over a distance $(f_{\rm ov} + f_0)H_{\rm P,cc}$ (Paxton et al., 2011). A detailed discussion on the different ways of describing core overshooting, constrained with asteroseismology, can be found in Pedersen et al. (2018).

Typical values obtained for γ Dor stars are used for the parameter grid (represented in Table (3.1)), which we selected based on Van Reeth et al. (2016, 2018); Mombarg et al. (2019). Moreover, as was done for the modelling of a known SPB stars (Buysschaert et al., 2018), one should keep in mind that the extent of core overshooting likely is smaller in magnetic stars when compared to their non-magnetic counterparts (see Section (2.3)). Therefore we select a lower bound of $f_{ov} = 0.004$, which was picked for the modelling of a known magnetic SPB stars studied by Buysschaert et al. (2018).

The mixing length parameter: $\alpha_{\rm MLT}$

The Cox and Giuli (1968) MLT is used in this work, a variant of the Böhm-Vitense (1958) MLT. The efficiency of convection is thus parametrized by the mixing length parameter, as discussed in Section (1.1). The grids of Van Reeth et al. (2016) take a fixed solar-calibrated value: $\alpha_{\rm MLT} = 1.8$, because there is considerable uncertainty on the value needed to model other stars (Viani et al., 2018). Yet Mombarg et al. (2019) pointed out that this parameter influences the buoyancy radius Π_0, the effective

Table 3.1: Typical values for the parameters varied in the MESA grid: overshoot parameter $f_{\rm ov}$, X_c, metallicity Z, mixing parameter $D_{\rm mix}$, mass M, $\alpha_{\rm MLT}$ and atmosphere model. The unit of $D_{\rm mix}$ is cm^2 s^{-1}, the mass is given in solar masses, whereas the other quantities are unit-less. More information on the different parameters can be found in Section (3.1).

MESA Parameter	Values		
	start	end	step
Exponential overshoot factor $f_{\rm ov}$	0.004	0.024	0.010
Core hydrogen mass fraction X_c	0.005	0.675	0.335
Envelope mixing level $\log(D_{\rm mix})$	-1	1	1
MESA Parameter	Values		
Initial Mass ($M_\odot$)	1.3 ,	2.0 ,	3.0
$\alpha_{\rm MLT}$	1.5 ,	1.8 ,	2.0
Atmosphere	simple photosphere		

temperature $T_{\rm eff}$ and the surface gravity log g. Hence, this affects modelling based on individual g mode pulsation frequencies (Aerts et al., 2018). Therefore, following Mombarg et al. (2019), we vary the $\alpha_{\rm MLT}$ parameter. Mombarg et al. (2019) selected their range of $\alpha_{\rm MLT}$ based on an empirical relation derived by Viani et al. (2018). Our considered range of $\alpha_{\rm MLT}$ to consider is therefore enlarged compared to Mombarg et al. (2019), as we consider an increased fundamental stellar parameter range.

The stellar atmosphere model

A wide list of atmospheric boundary conditions is available in MESA. We will use the 'simple_photosphere' option, which estimates the surface boundary using the ATLAS 9 tables of Castelli and Kurucz (2003) with surface optical depth $\tau_s = 2/3$. We do not include any stellar winds, as they are not expected during the main-sequence phase in this mass range.

3.2 Constructing a grid of GYRE pulsation models: parameter ranges

The pulsation code GYRE solves the dimensionless pulsation equations (defined in appendix B2 of Townsend et al., 2018) numerically on a grid of points that is user-defined. Note that Townsend et al. (2018) define the full non-adiabatic system of equations to be solved, whereas we will only perform adiabatic calculations. In order to convert this non-adiabatic system of equations to its adiabatic counterpart, the variables y_5 and y_6 should be ignored (which include heat and radiation transport), so that equations B18 and B19 of Townsend et al. (2018) need not be solved. Moreover, this simplifies the boundary conditions and reduces the number of dimensionless stellar structure coefficients that need to be taken into account. A typical inlist used to calculate mode frequencies with GYRE can be

found in the appendix. Because we 'feed' GYRE with MESA evolutionary models, it clones the MESA grid. However, using purely this grid would not allow one to spatially resolve the eigenfunctions of high radial order g modes, which are rapidly varying. Therefore we oversample the grid in the regions of rapidly varying k_r (i.e. the radial wavenumber), as well as near the core. We direct the reader to e.g. https://bitbucket.org/rhdtownsend/gyre/wiki/Understanding%20Grids for a detailed discussion on how to fine-tune grid oversampling in GYRE.

3.2.1 GYRE constraints

An overview of the code input parameters that will be varied is given in Table (3.2). The selection of the individual code input parameters will be explained in the following subsections.

The rotation fraction: u

In order to quantify the effect of rotation on the period spacing patterns in the presence of a magnetic field, we vary the rotation fraction u, defined by:

$$u = \frac{\Omega_{\rm rot}}{\Omega_{\rm c,Roche}} \tag{3.2}$$

where $\Omega_{\rm rot}$ is the angular rotation frequency of the star, and $\Omega_{\rm c,Roche}$ is the Roche critical angular rotation frequency of the stellar model, estimated with Equation (2.21), and where $u \in [0.01, 0.75]$ (with the step given in Table (3.2)). This parameter range is justified because γ Dor and SPB stars are known to be moderately to fairly rapid rotators, as mentioned in Section (2.1). In addition, rapid rotation influences the effect of the magnetic field on stellar oscillations, as briefly mentioned in Prat et al. (2019). The lower bound for u is therefore chosen so as to emulate slow rotators, in order to obtain an estimate of the magnetic influence in such stars.

The boundary conditions

In order to close the (sub)set of pulsation equations solved by GYRE, normalization conditions are required. There are three boundary conditions that can be discerned: the inner boundary condition near the origin, the normalization convention used, and the outer mechanical boundary condition (e.g. Townsend, 2000; Townsend and Teitler, 2013).

The normalization convention scales the dimensionless variables y_i with l_i, i.e. the value of l_e at the inner boundary of the grid on which the pulsations equations are solved. l_e is the effective harmonic degree, which in the non-rotating limit is equal to l, but in the TAR is given by solving $l_e(l_e + 1) = \lambda$, where λ is the eigenvalue of the Laplace tidal equations (Equation (2.30)).

The inner boundary condition is regularity-enforcing: it discards roots of the characteristic equations that describe the situation at the inner boundary (see e.g. Townsend and Teitler, 2013).

The outer boundary condition is varied, as this affects the behaviour of the pulsations near the stellar surface. Two options implemented in GYRE will be used: 'VACUUM' and 'UNNO'.

The former enforces the Lagrangian perturbation of the surface pressure to be exactly equal to zero. If the latter is selected, GYRE instead uses the (possibly-leaky) outer mechanical boundary described by Unno et al. (1989). This amounts to performing a local dispersion analysis near the surface, identifying the local wave conditions (i.e. comparing frequencies of obtained waves with characteristic frequencies, to identify propagating and evanescent solutions). To obtain physical solutions, GYRE then imposes requirements on the obtained solutions of the local dispersion analysis. We will not describe these boundary conditions in full detail, instead referring the reader to Unno et al. (1989) and Townsend (2000), two excellent references.

The solver/difference scheme

As mentioned by Townsend and Teitler (2013), the differential equations and boundary conditions describing the nonradial oscillations constitute a two-point boundary value problem (BVP) in which the oscillation frequency ω serves as an eigenvalue. In general this BVP needs to be solved numerically. Different difference schemes/-solvers that do this are implemented in GYRE. Two classes of solvers are typically used to calculate adiabatic frequencies in GYRE: the Gauss-Legendre collocation scheme and the Magnus multiple shooting scheme. These are available in different orders.

The Gauss-Legendre collocation method approximates the BVP solutions (i.e. the solutions of the pulsation equations, with the appropriate boundary conditions) as a superposition of basis functions (e.g. Chebyshev polynomials, see also Section (3.2.2)), which satisfy the differential equations exactly at a set of nodes, the collocation points. The location of these points is obtained from Gauss-Legendre quadrature.

Schooting schemes on the other hand treat BVPs as a set of initial value problems (IVPs), where matching conditions are applied where pairs of the IVPs meet (i.e. at the respective 'matching' boundaries). Hence, the interval of $x = r/R$ is divided up into a grid (i.e. the oversampled grid from the stellar model), so that in each interval an IVP is solved, requiring continuity at the subinterval edges. For a grid of N points, there are therefore $N - 1$ matching conditions, which together with the two boundary conditions (i.e. at x_i and x_o) and the system of IVPs form the system of algebraic equations to be solved. The stellar eigenfrequencies can then be obtained by looking for the roots of the discriminant function, which is the determinant of the system matrix (i.e. the matrix describing the system of algebraic equations). Moreover, this system matrix will also be used for reconstruction of the mode eigenfunctions. For detailed information on the Magnus multiple shooting scheme (used in GYRE) we refer the reader to Townsend and Teitler (2013).

As mentioned in Townsend and Teitler (2013), the absolute error in dimensionless eigenfrequency scales with the order of the solver used. Moreover, it can vary from scheme to scheme, although this was not explored in Townsend and Teitler (2013), as this focused only on the Magnus multiple shooting scheme. Therefore, it is interesting to verify whether or not one of the conclusions of Townsend and Teitler (2013), namely, that the obtained dimensionless frequencies' absolute error difference between different order schemes is near-negligible for typical grid sizes (see their figure 1 for an example of a polytropic stellar model), still holds in our magnetic formalism. Thus we want to verify that, for the purpose of adiabatic calculations

Table 3.2: Values of the parameters varied for the GYRE pulsation grid: the fraction of (Roche) critical rotation (rotation fraction), the outer boundary condition (outer B.C.) and the difference schemes. More information on the different parameters can be found in Section (3.2).

GYRE Parameter	Values		
	start	end	step
Rotation fraction u	0.01[a]	0.75	0.25
GYRE Parameter	Choice		
Outer B.C.	Vacuum		Unno
Solver/difference scheme	Magnus GL2		Colloc GL2
	Magnus GL4		Colloc GL4
	Magnus GL6		Colloc GL6

[a] Initial value was chosen to be nonzero, but subsequent cycle values are calculated using zero as initial value.

(i.e. for the purpose of calculating mode frequencies), it does not matter which type and order of solver are used.

3.2.2 Computing the Hough functions

In order to solve the Laplace tidal eigenvalue problem, defined by Equation (2.30), the Hough functions need to be calculated. A method that allows us to solve this problem in a remarkably simplified way (as noted by Boyd, 2001; Prat et al., 2019) is Chebyshev collocation, or the pseudospectral method, described by Wang et al. (2016). The first use of this method in the context of solving the Laplace tidal equations was described by Boyd (1976). The latitudinal basis function used by Boyd (1976) replaces associated Legendre functions by cosine functions of colatitude θ, multiplied by a 'parity factor' equal to $\sin(\theta)$ for odd m, and 1 for even m. In addition, using the modified latitudinal variable $\mu \equiv \cos(\theta) \in [-1, 1]$ we can replace trigonometric functions by powers of μ in spherical geometry, allowing for major simplifications (Wang et al., 2016). Furthermore, denoting the Chebyshev polynomials by $T_n(\mu)$, Chebyshev's identity shows:

$$T_n(\mu) = T_n(\cos(\theta)) = \cos(n\theta), \quad n = 0, 1, \dots \ , \tag{3.3}$$

so that a Fourier cosine series in colatitude is also a Chebyshev polynomial series in μ, with the same coefficients. Hence, the radial Hough function H_r can be expanded in terms of the Chebyshev polynomials $T_n(\mu)$:

$$H_r(\mu) = (\sin\theta)^{mod(m,2)} \sum_{n=0}^{\mathcal{N}} b_n T_n(\mu) \ , \tag{3.4}$$

where b_n denote the coefficients, $\mathcal{N}$ is the total number of collocation points (in our case taken to be 200), and where the parity factor is included for odd m (as indicated in front of the summation). The presence of this parity factor is justified in the appendix. The Chebyshev collocation points are taken to be the interior points,

which are defined as (e.g. Boyd, 2001, p. 571):

$$\mu_i = \cos\left(\frac{(2i-1)\pi}{2\,\mathcal{N}}\right), \quad i = 1, \ldots, \mathcal{N}\ . \tag{3.5}$$

Hence, Laplace's tidal equations will be approximated over the interval $\mu \in [-1, 1]$ by a weighted sum of $\mathcal{N}+1$ Chebyshev polynomials (i.e. a polynomial of degree $\mathcal{N}$), where the weights are chosen so that the residual is zero at each of the $\mathcal{N}+1$ collocation (or interpolation) points (Boyd, 2001). In order to construct $H_r(\mu)$ one needs to calculate the (total) derivatives of $T_n(\mu)$, with respect to μ, including the parity factor for uneven m (as they are needed to solve Laplace's tidal equations: see Equations (2.30) and (2.31)). The other Hough functions can then be calculated in a straightforward way from the reconstructed $H_r(\mu)$ and its (total) derivative with respect to μ. The derivatives of $T_n(\mu)$ for even m are (see also Boyd, 2001):

$$T_n(\mu) = \cos(n\theta)\ , \tag{3.6}$$

$$\frac{\mathrm{d}T_n(\mu)}{\mathrm{d}\mu} = \frac{n\sin(n\theta)}{\sin(\theta)}\ , \tag{3.7}$$

$$\frac{\mathrm{d}^2T_n(\mu)}{\mathrm{d}\mu^2} = \frac{1}{\sin^3\theta}\left(-n^2\cos(n\theta)\sin\theta + n\sin(n\theta)\cos\theta\right)\ , \tag{3.8}$$

whereas the derivatives for uneven m are found to be:

$$\sin\theta\ T_n(\mu) = \cos(n\theta)\sin\theta\ , \tag{3.9}$$

$$\frac{\mathrm{d}}{\mathrm{d}\mu}\left(\sin\theta\ T_n(\mu)\right) = n\sin(n\theta) - \frac{\cos\theta}{\sin\theta}\cos(n\theta)\ , \tag{3.10}$$

$$\frac{\mathrm{d}^2}{\mathrm{d}\mu^2}\left(\sin\theta\ T_n(\mu)\right) = \frac{1}{\sin^3\theta}\left[-n^2\cos(n\theta)\sin^2\theta - n\sin(n\theta)\cos\theta\sin\theta - \cos(n\theta)\right]\ . \tag{3.11}$$

It is also useful to redefine $H_\theta(\mu)$ (equation 2.32) and $H_\varphi(\mu)$ (equation 2.33) in function of the (total) derivatives of $H_r(\mu)$ with respect to μ:

$$H_\theta(\mu) = \frac{-(\sqrt{1-\mu^2})\frac{\mathrm{d}H_r(\mu)}{\mathrm{d}\mu} - m\nu\frac{\mu}{\sqrt{1-\mu^2}}H_r(\mu)}{1-\nu^2\mu^2}\ , \tag{3.12}$$

$$H_\varphi(\mu) = \frac{\frac{mH_r(\mu)}{\sqrt{1-\mu^2}} + \nu\mu(\sqrt{1-\mu^2})\frac{\mathrm{d}H_r(\mu)}{\mathrm{d}\mu}}{1-\nu^2\mu^2}\ , \tag{3.13}$$

which is obtained using the definition of μ and $\frac{\mathrm{d}}{\mathrm{d}\mu}$, as shown in the appendix. Hence, all of the above expressions allow us to solve the Laplace tidal eigenvalue problem in a remarkably simplified way (as noted by Boyd, 2001; Prat et al., 2019), by solving in Chebyshev space for the coefficients b_n, utilizing the modified latitudinal variable μ.

Proof. The expressions for the derivatives of the Chebyshev polynomials obtained above can be obtained in the way described below. Let us first note that $\frac{\mathrm{d}}{\mathrm{d}\mu} = -\frac{1}{\sin\theta}\frac{\mathrm{d}}{\mathrm{d}\theta}$. Applying this to the above expressions yields:

$$\begin{aligned}
\frac{\mathrm{d}T_n(\mu)}{\mathrm{d}\mu} &= -\frac{1}{\sin(\theta)}\frac{\mathrm{d}}{\mathrm{d}\theta}\left(\cos(n\theta)\right) = \frac{n\sin(n\theta)}{\sin(\theta)} \ , \\
\frac{\mathrm{d}^2T_n(\mu)}{\mathrm{d}\mu^2} &= -\frac{1}{\sin\theta}\frac{\mathrm{d}}{\mathrm{d}\theta}\left[\frac{n\sin(n\theta)}{\sin(\theta)}\right] = -\frac{1}{\sin\theta}\left[\frac{n^2\cos(n\theta)}{\sin\theta} - \frac{n\sin(n\theta)\cos\theta}{\sin^2\theta}\right] \\
&= \frac{1}{\sin^3\theta}\left(-n^2\cos(n\theta)\sin\theta + n\sin(n\theta)\cos\theta\right) \ , \\
\frac{\mathrm{d}}{\mathrm{d}\mu}\left(\sin\theta\ T_n(\mu)\right) &= -\frac{1}{\sin\theta}\frac{\mathrm{d}}{\mathrm{d}\theta}\left(\sin\theta\cos(n\theta)\right) = n\sin(n\theta) - \frac{\cos\theta}{\sin\theta}\cos(n\theta) \ , \\
\frac{\mathrm{d}^2}{\mathrm{d}\mu^2}\left(\sin\theta\ T_n(\mu)\right) &= -\frac{1}{\sin\theta}\frac{\mathrm{d}}{\mathrm{d}\theta}\left[n\sin(n\theta) - \frac{\cos\theta}{\sin\theta}\cos(n\theta)\right] \\
&= -n^2\frac{\cos(n\theta)}{\sin\theta} - \frac{1}{\sin\theta}\cos(n\theta) - \frac{\cos^2\theta}{\sin^3\theta}\cos(n\theta) - n\frac{\cos\theta}{\sin^2\theta}\sin(n\theta) \\
&= \frac{1}{\sin^3\theta}\left[-n^2\cos(n\theta)\sin^2\theta - n\sin(n\theta)\cos\theta\sin\theta - \cos(n\theta)\right] \ .
\end{aligned}$$

□

3.2.3 Magnetic constraints

Although large-scale magnetic fields are detected at the surface of approximately 10% of stars with spectral types B and A (Shultz et al., 2012, 2018), internal magnetic fields are not well-characterized.

Most of the detected large-scale surface fields have simple geometries, often magnetic dipoles inclined with respect to the rotation axis (i.e. 'oblique'), with field strengths ranging from 300 G to a few tens of kG (Aurière et al., 2007; Buysschaert et al., 2018; Prat et al., 2019). Charbonneau (2013) computed field decay times for a variety of field geometries, taking into account magnetic diffusivity (Ohmic dissipation), and showed that complex geometries have markedly lower diffusive decay times. Hence, if stellar magnetic fields are left to decay long enough, any complex magnetic field geometry will end up looking dipolar.

Since these (dipole) fields were found to be stable over a time span of several decades, and because their properties do not scale with stellar parameters, they are thought to have been created during star formation (and retained when evolving to the MS), i.e. they have a fossil origin (see e.g. Ferrario et al., 2015; Neiner et al., 2015, and references therein). As discussed in Section (2.3.2), stable fields have both poloidal and toroidal components and extend deep into the radiative envelope.

Even though internal magnetic fields are not well-characterized, it might be expected that their structure is somewhat similar to that of the observed fossil fields, given their (necessary) deep extension into the radiative envelope. Therefore, we use an axisymmetric dipole magnetic field model, in order to assess the effects of such a magnetic field on the g mode frequencies. As described in Section (2.3.2), we use our general formalism (Prat et al., 2019) to derive the shifted mode frequencies

(due to the magnetic field). This requires a numerical model of the magnetic field, which is described below.

Magnetic Field Prescription

For numerical calculations, the magnetic field is defined as:

$$\boldsymbol{B} = \frac{1}{r\sin\theta}\left(\nabla\Psi \times \boldsymbol{e}_\varphi + \lambda\frac{\Psi}{R}\boldsymbol{e}_\varphi\right) , \tag{3.14}$$

where ψ is the stream function, defined as:

$$\Psi = -\mu_0\ \alpha\ \lambda\ \frac{r}{R}\left[j_1\left(\lambda\frac{r}{R}\right)\int_r^R y_1\left(\lambda\frac{x}{R}\right)\rho x^3 dx + y_1\left(\lambda\frac{r}{R}\right)\int_r^R j_1\left(\lambda\frac{x}{R}\right)\rho x^3 dx\right]\sin^2\theta\ , \tag{3.15}$$

where $\boldsymbol{e}_\varphi$ is the azimuthal unit vector, R is the stellar radius, λ is determined by solving for the smallest root of $\int_r^R j_1(\lambda x/R)(\rho x^3/\lambda^2)dx$, enforcing a vanishing $\boldsymbol{B}$ at the stellar surface (see Prat et al., 2019), μ_0 is the vacuum permeability, α is an amplitude scaling factor for the normalized field, and where j_1 and y_1 are the first-order spherical Bessel functions of the first and second kind, respectively. The stream function used in this work is the particular solution for the general stream function derived in Duez and Mathis (2010). The main assumption made during the derivation was that the Lorentz volumetric force is a perturbation compared with gravity, so that a non force-free equilibrium is obtained. Duez and Mathis (2010) further constrained their focus to so-called (hydrodynamic) barotropic equilibrium states, where $\nabla\rho \times \nabla P = \mathbf{0}$ (i.e. their density and pressure gradients are aligned) in the stellar radiative zone, for which the possible field configurations and stellar structure are inherently coupled. In fact, Duez and Mathis (2010) derived an expression for a field geometry for which the star is in magnetohydrostatic equilibrium, i.e., those states for which the following holds:

$$-\frac{\nabla\rho\times\nabla P}{\rho^2} = \nabla\times\left(\frac{\boldsymbol{F}_L}{\rho}\right) = \mathbf{0} \tag{3.16}$$

Assuming such a state allowed them to reduce the (axisymmetric) problem to a Grad-Shafranov-like equation, whose solution can be written in terms of the stream function shown above, assuming compressibility and conserving several invariants: the radiation zone mass, the mass in each flux tube, the flux of the toroidal field and a given helicity (for more details, the reader is referred to Duez and Mathis, 2010). The prescription for this field thus only holds in stellar radiative zones.

The stream function Ψ can also be written as $\Psi = A(r)\sin^2\theta$, so that the different (radial) magnetic field components of Equation (2.45) can be calculated as:

$$b_r = 2\frac{A}{r^2}\ , \qquad b_\theta = -\frac{\frac{\mathrm{d}A}{\mathrm{d}r}}{r}\ , \qquad b_\varphi = \lambda\frac{A}{rR}\ , \tag{3.17}$$

where $\frac{\mathrm{d}}{\mathrm{d}r}$ denotes a total radial derivative.

Proof. The different radial components can be derived in the following way:

$$\begin{aligned}
&\boldsymbol{\nabla}\Psi = \sin^2\theta\ \frac{\mathrm{d}A}{\mathrm{d}r}\ \boldsymbol{e}_r + \frac{2A}{r}\ \sin\theta\cos\theta\ \boldsymbol{e}_\theta\ , \\
\Leftrightarrow\ &\boldsymbol{B} = \frac{1}{r\sin\theta}\left(\left[\sin^2\theta\ \frac{\mathrm{d}A}{\mathrm{d}r}\ \boldsymbol{e}_r + \frac{2A}{r}\ \sin\theta\cos\theta\ \boldsymbol{e}_\theta\right] \times \boldsymbol{e}_\varphi + \lambda\frac{A\sin^2\theta}{R}\boldsymbol{e}_\varphi\right)\ , \\
\Leftrightarrow\ &\boldsymbol{B} = -\frac{\sin\theta}{r}\frac{\mathrm{d}A}{\mathrm{d}r}\boldsymbol{e}_\theta + \frac{2A}{r^2}\cos\theta\boldsymbol{e}_r + \lambda\frac{A}{rR}\sin\theta\boldsymbol{e}_\varphi\ ,
\end{aligned}$$

which yields the correct expressions, when comparing to Equation (2.45). □

Table 3.3: Magnetic parameter to be varied in the magnetic grid: the (log of the) magnetic field amplitude scaling factor α (in Gauss).

Magnetic Parameter	Values		
	start	end	step
$\log\alpha$	4	6	1

Selection of the magnetic field amplitude scaling factor α

In order to select a range of (reasonable) near-core field strengths over which to vary, we base ourselves on the estimates of order of magnitude of red giant field strengths discussed in Section (1.2). As was shown by Stello et al. (2016), a field of approximately $10^4 - 3{*}10^6$ G would be expected during the red giant phase. Cantiello et al. (2016) then estimated field strengths for main-sequence dynamos using the red giant phase field strengths, and concluded that main sequence dynamos should have field strengths in the range of $10^4 - 10^5$ G. Augustson et al. (2016) modelled near-core dynamos in (massive) main-sequence stars, showing that fields of $\sim 10^6$ G could also be generated.

Even though these estimates were made for dynamo field strengths, they provide us with a first estimate of a typical field strength to be expected in the considered main sequence stars. Moreover, Buysschaert et al. (2018) estimated the (fossil) near-core field strength of the ($5.8M_\odot$) SPB star, for which the surface field was characterized, to be in the range of 26.1 and 82.4 kG, motivated by simulations of Braithwaite (2008). Prat et al. (2019), which constitutes the basis for and is deeply integrated in this work, on their turn considered a maximal internal field strength of $1.5 * 10^5$ G when modelling the same star. Hence, this indicates that fossil field strengths likely fall in the same field strength range as considered for dynamo fields.

We varied the magnetic field amplitude scaling factor α (i.e. the parameter that defines the field strength in our formalism) in the range $10^4 - 10^6$ G, as indicated in Table (3.3). Furthermore, we make the limiting assumption that the axisymmetric magnetic field described in the previous section is non-oblique, i.e., the magnetic field vector is not inclined with respect to the rotation axis. Earlier work has shown that the obliquity β however is not equal to zero, typically attaining values below 20° for

slowly rotating Ap stars (e.g. Landstreet and Mathys, 2000), or larger values (see e.g. Landstreet, 1970). In future work, the obliquity should be included. Nevertheless, these non-oblique fields can serve as a useful first test case, in which the effects of magnetic fields on g mode frequencies are characterized.

Estimating plasma β

A rough estimate of plasma β (see Equations (2.40) and (2.41)) in the near-core region can be obtained by using estimates of central quantities. Assuming the ideal gas law to hold in the near-core region:

$$\rho = \frac{\mu}{\Re}\frac{P}{T} \tag{3.18}$$

and utilizing hydrostatic equilibrium, we derived simple estimates of the central pressure and temperature (similar to the estimates of Kippenhahn et al., 2012):

$$\frac{\partial P}{\partial m} = -\frac{Gm}{4\pi r^4} \Rightarrow \frac{P_0 - P_c}{M} \approx -\frac{GM/2}{4\pi(R/2)^4} \Leftrightarrow P_c \approx \frac{2GM^2}{\pi R^4} \tag{3.19}$$

$$T = \frac{\mu}{\Re}\frac{P}{\rho} \Rightarrow T_c \approx \frac{P_c}{2\Re\rho_c} = \frac{GM^2}{\pi\Re R^4\rho_c} \tag{3.20}$$

where $\Re$ is the (ideal) gas constant, $\frac{\partial P}{\partial m}$ is estimated as $\frac{P_0-P_c}{M}$, m is the Lagrangian mass coordinate (which we estimate as the rough mean value $M/2$), r is the local radius of the Lagrangian mass element (which we estimate as the rough mean $R/2$), where the pressure at the surface is deemed to be negligible compared to the central pressure ($P_0 \ll P_c$), and where we use the rough value for the mean molecular weight of $\mu = 0.5$ (i.e. the value for fully ionized H). Further assuming that the species are thermalized, β can be estimated as:

$$\beta = \frac{2\mu_0 k T_c (n_e + n_H)}{B^2} \approx \frac{4\mu_0\ k\ T_c\ \rho_c}{B^2\ m_H} \approx \frac{4\mu_0\ k\ GM^2}{B^2\ m_H\ \pi\ \Re\ R^4} \tag{3.21}$$

Assessing the validity of the collisionality assumption

The validity of the collisionality assumption (see Section (2.3.2)) can be probed using the plasma parameter $\Lambda = 6\pi\epsilon_0 kT/q^2 n^{1/3}$ (see e.g. Goedbloed and Poedts, 2004; Fitzpatrick, 2015), where ϵ_0 is the vacuum permittivity, T is the temperature of the plasma, q is the species charge, n is the number density of plasma species and k is Boltzmann's constant. This can be thought of as the ratio of the average distance between the particles $< r > \equiv n^{-1/3}$ and the distance of closest approach between particles in the plasma: $r_{cl} \equiv e^2/4\pi\epsilon_0 T$. When $< r > /r_{cl}$ is small, charged particles are dominated by the electrostatic influence (of another particle) and their kinetic energies are small compared to the interaction potential energies. The corresponding plasma is called *strongly coupled*. On the other hand, when the ratio is large, strong electrostatic interactions between individual particles are rare, and the typical particle can be considered to be influenced by all of the other particles 'x' for which $r < \lambda_{\mathrm{D,x}} = \sqrt{\epsilon_0 kT_x/|q|^2 n_x}$. Yet, only rarely the interactions cause sudden changes in the particle's motion.

These are *weakly coupled* plasma's. Hence, in order to validate the collisionality assumption, the plasma parameter should be large (and hence the plasma should be

weakly coupled). Using the central estimates developed in the previous section the plasma parameter can be estimated as:

$$\Lambda \approx \frac{6\pi\ \epsilon_0\ k\ T_c}{e^2\ (\rho_c/M)^{1/3}} = \frac{6\ \epsilon_0\ k\ G\ M^{7/3}}{e^2\ \mathfrak{R}\ R^4\ \rho_c^{4/3}} \tag{3.22}$$

where we again assumed thermalized, ionized H to be the only contributing species. Hence, for near-core conditions, we expect Λ to be large.

In addition, one can estimate the value of the so-called plasma coupling parameter Γ, defined by:

$$\Gamma = \frac{E_c}{kT}, \tag{3.23}$$

where E_c is the coulomb energy and kT is the thermal energy. Therefore, for a *strongly coupled* plasma, we expect that Γ is large, and vice versa for *weakly coupled* plasmas.

Assessing the validity of the perturbative approach

Strong internal magnetic fields will affect mode propagation of internal gravity waves, partially or completely reflecting them if their angular frequency is of the same magnitude as the magnetogravity frequency $\omega_{MG} = [2B_r^2 N^2/\pi\rho r^2]^{1/4}$, derived by Fuller et al. (2015); Cantiello et al. (2016) for red giants without rotation (where B_r signifies the radial component of the magnetic field, as in Section (1.2)). However, since we assume the magnetic field to only have a perturbative effect on the gravito-inertial frequencies, we do not consider that the Lorentz force acts as a restoring force. Therefore, the angular pulsation frequencies (in the corotating frame) ω have to be compared with the Alfvén frequency ω_A, defined by:

$$\omega_A = \frac{\boldsymbol{B}\cdot\boldsymbol{k}}{\sqrt{\mu_0\rho}} = \boldsymbol{v}_{\rm A}\cdot\boldsymbol{k}\ , \tag{3.24}$$

where $\boldsymbol{B}$ is the magnetic field vector, $\boldsymbol{k}$ is the wave vector, μ_0 is the vacuum permeability, ρ is the density, and $\boldsymbol{v}_{\rm A} = \boldsymbol{B}/\sqrt{\mu_0\rho}$ is the so-called Alfvén speed. When $\omega_A \ll \omega$ a perturbative treatment is justified. In fact, if $\omega \approx \omega_A$, one would expect reflection of the gravity waves due to magnetic field interaction (similar to the reflection and refraction of internal gravity waves described in Section (1.2). Hence, the validity domain of our approximation is defined by:

$$\frac{\omega_A}{\omega} \ll 1\ . \tag{3.25}$$

For high-radial-order modes $\boldsymbol{B}\cdot\boldsymbol{k} \approx B_r k_r = b_r(r) k_r \cos\theta$. Hence, the magnitude of the Alfvén frequency is maximal along the rotation axis ($\theta = 0°$), however, high-radial-order modes are sub-inertial (i.e. $\omega < 2\Omega$) and trapped in an equatorial waveguide defined by $|\cos\theta| \leq \omega/2\Omega = 1/|\nu|$ (see e.g. Townsend, 2003; Prat et al., 2016, 2017). The maximal Alfvén frequency that needs to be compared with ω is then:

$$\omega_A = \frac{b_r(r) k_r \cos\theta}{\sqrt{\mu_0\rho(r)}} \Rightarrow \omega_{A_{\rm max}} = \frac{b_r(r) k_r \omega}{2\Omega\sqrt{\mu_0\rho(r)}} = \frac{b_r(r) k_r}{|\nu|\sqrt{\mu_0\rho(r)}}\ , \tag{3.26}$$

so that the validity criterion becomes:

$$\frac{b_r k_r}{2\Omega\sqrt{\mu_0\rho}} \ll 1 \ . \tag{3.27}$$

In Prat et al. (2019), we then use a rough estimate for the radial wave vector $k_r \sim \frac{|n|}{R}$ (R is the stellar radius, n is the mode radial order) in order to provide an estimate of the field strength range for which the formalism is valid. Furthermore, even though $b_r/\sqrt{\rho}$ is maximal at the centre of the star, gravity modes are most sensitive to the near-core region. We can then estimate $b_r/\sqrt{\rho}$ as 0.34 $\alpha/\sqrt{\rho_c}$, so that the final validity criterion is:

$$0.17\frac{\alpha|n|}{R\Omega\sqrt{\mu_0\rho_c}} \ll 1 \ , \tag{3.28}$$

yielding the following field strength criterion:

$$\alpha \ll \frac{\Omega R\sqrt{\mu_0\rho_c}}{0.17|n|} \ , \tag{3.29}$$

where α is the magnetic field scaling factor and ρ_c is the central density. Similarly, the Alfvén frequency is then given by:

$$\omega_A = 0.34\frac{\alpha|n|}{|\nu|R\sqrt{\mu_0\rho_c}} \ . \tag{3.30}$$

Traditionally the pulsation frequency ω is compared to a wide range of characteristic frequencies (i.e. the Brunt-Väisälä frequency, Lamb frequency, Coriolis frequency), in order to define the pulsation cavities of the different modes (see e.g. Aerts et al., 2010). The characteristic Alfvén frequency estimate belongs on such a plot when considering the influence of magnetic fields. It essentially defines a new pulsation cavity, where for $\omega < \omega_{\rm A}$ the Lorentz force becomes a restoring force. Keep in mind however that the above criterion is a global estimate. As the strength of the magnetic field and density changes locally, I also compute local estimates of the Alfvén frequency, and compare this Alfvén profile to the unperturbed pulsation frequencies. Only first-order perturbations of the magnetic field on gravito-inertial pulsations are considered. These pulsation modes are transversal, so that the radial component of the wave vector (still) dominates. Therefore it follows that $\boldsymbol{B}\cdot\boldsymbol{k} \approx B_r(r,\theta)k_r(r)$, justifying the first approximation made by Prat et al. (2019).

Two different, more complete approaches were derived to estimate the Alfvén frequency, where we take into account the spatial variability of the radial component of the magnetic field vector as well as the radial density profile. The first approach uses an estimate of the (radial) wave vector which is similar to the one used in Prat et al. (2019), resulting in the following definition for the Alfvén frequency profile:

$$\omega_A(r,\theta) \sim \frac{B(r,\theta)|n|}{R\sqrt{\mu_0\rho(r)}} \ , \tag{3.31}$$

where $B(r,\theta)$ is the magnetic field strength profile evaluated at a specific colatitude θ, and where $\rho(r)$ is the density profile (which does not depend on the colatitude, as 1D stellar models are used).

The second approach uses the dispersion relation for gravito-inertial waves derived by Mathis (2009) in order to estimate the radial wave vector:

$$k_r^2(r) = \frac{N(r)^2}{\omega^2}\frac{\lambda_{l,m}(\nu)}{r^2} \ , \tag{3.32}$$

to obtain the following estimate for the Alfvén frequency profile:

$$\omega_A(r,\theta) \sim \frac{B(r,\theta)N(r)\sqrt{\lambda_{l,m}(\nu)}}{\omega r\sqrt{\mu_0\rho(r)}} \ , \tag{3.33}$$

where $N(r)$ is the local buoyancy frequency or Brunt-Väisälä frequency. Note that our estimate scales with $N(r)$. This approximation can be justified by noting that for low-frequency super-inertial waves in a stellar medium permeated by a purely toroidal field, Mathis and de Brye (2011) estimated the radial wave vector as:

$$k_r(r) \approx \left(\frac{N}{\omega_M}\right)\frac{\sqrt{\lambda_{l,m}(\nu_M)}}{r} \ , \tag{3.34}$$

where ω_M and ν_M are angular pulsation frequencies in the corotating frame and spin parameters modified by this toroidal field, respectively. They are given by (Mathis and de Brye, 2011):

$$\omega_M^2 = \omega^2 - m^2\omega_A^2 \ , \tag{3.35}$$

$$\nu_M = \nu F_M = \frac{2\Omega_{rot}}{\omega}\left[\frac{1-m\Lambda_E}{1-m^2\nu\Lambda_E/2}\right] \ , \tag{3.36}$$

where Λ_E is the wave's Elsasser number defined by:

$$\Lambda_E = \frac{\omega_A^2}{\omega\ \Omega_{rot}} \ , \tag{3.37}$$

a measure of the relative importance of the Lorentz force with respect to the Coriolis acceleration. Thus, when only considering the effect of a purely toroidal field on zonal modes ($m = 0$), the expression for the radial wavevector of Mathis and de Brye (2011) reduces to Equation (3.33), justifying our approximation for this purely toroidal field. In such a case, waves are only propagating if $\omega_M^2 > 0$.

If $\omega_M^2 < 0$, the waves are trapped in the vertical direction, as the toroidal magnetic field acts as a filter in this direction (Schatzman, 1993; Barnes et al., 1998). The Duez and Mathis (2010) field, however, also has a non-negligible poloidal term, which should be taken into account. Doing so would however require one to re-derive the equations of Mathis and de Brye (2011) for the more general case of a poloidal-toroidal field, which, within the time-frame of this thesis, was not feasible. Therefore we rather stick to the approximation we made above, to estimate the validity of our approach.

As mentioned in Section (2.2.2), for rapid rotators the pulsation become trapped in a band around the stellar equator, which gets narrower if the Coriolis force contributes more to the restoring force (i.e. for faster rotation). To best estimate the influence of the magnetic field $\boldsymbol{B}(r,\theta)$ on the pulsation frequency, we evaluate $\boldsymbol{B}(r,\theta)$ at the colatitude θ where the eigenfunction of the considered pulsation is maximal, i.e., the part of the magnetic field to which this pulsation is most sensitive. The maximum of the radial Hough function gives a good estimate of this colatitude, because the radial part of the wave vector is much larger than the horizontal part.

4 — Results and discussion

4.1 Coarse grid results

In order to grasp how magnetic fields influence period spacing patterns, the main diagnostic of gravity-mode asteroseismology, we restrict ourselves to the 'simplest' modes: dipole zonal modes ($l = 1,\ m = 0$). Typically a so-called mode cavity diagram (in which the nodes of the eigenfunctions, as well as the mode frequencies are shown and compared to characteristic frequencies) is made to analyze the propagation of pulsations inside stars (e.g. Aerts et al., 2010). However, since the eigenfunctions of the magnetically perturbed modes are not calculated in Prat et al. (2019), because the perturbation of a single eigenfunction in the TAR requires calculating a sum of infinite terms (e.g. Lee and Saio, 1997), we cannot exactly pinpoint the nodes of the magnetically altered modes. This is, in principle, needed to fully characterize the mode in terms of its radial order, and to determine which restoring forces are relevant for the mode. Therefore, in order to assess this behaviour, in first instance, we propose to look at our mode propagation or mode cavity diagrams, in which the characteristic frequencies (N, S_l, 2 Ω_{rot},ω_A) are indicated, as well as the rotationally modified and magnetically modified eigenfrequency (of specific modes). This will allow us to evaluate the condition required for describing the magnetic field influence as a perturbative effect (hereafter referred to as the perturbative criterion): $\omega \gg \omega_A$.

Estimating characteristic parameters of the stellar plasma: β, Λ and Γ

For the specific reference models mentioned in Table (4.1), we estimate the plasma parameter Λ (using Equation (3.22)) as well as the plasma coupling parameter Γ to validate the collisionality assumption, and the plasma β of the near-core plasma (using Equation (3.21)) at the specific evolution phases probed in this coarse grid. This leads us to assume that in a typical stellar model of the model grid, the assumptions for ideal MHD are valid, because the characteristic parameters adhere to the following proportionalities: $\Lambda > 0$, $\beta \gg 0$ and $\Gamma \approx 0$. An overview of the evolution of the plasma diagnostic parameters throughout main-sequence evolution, for the chosen reference model, is given in Figure (4.1). From this, we can extract that throughout the MS, at least for this reference model, the assumptions for ideal MHD seem to hold. Bi-particle collisions only begin to become important at the very end of the MS, as indicated by the plasma interaction and plasma parameter values. Given the very high values of plasma β, one does not expect the near-core plasma to be magnetized throughout MS evolution. Although not shown explicitly here, electron degeneracy effects can be shown to be negligible throughout MS evolution.

Table 4.1: Estimated characteristic parameters of the near-core plasma of the reference model in the grid. The MESA atmospheric boundary condition is 'simple_photosphere' and the maximal magnetic field strength α is 10^6 G.

	Reference model parameters					Characteristic parameters		
Life phase	Mass ($M_\odot$)	$f_{\rm ov}$ ($H_{\rm p}$)	Z	$D_{\rm mix}$ (cm^2 s^{-1})	$\alpha_{\rm MLT}$	β / 10^6	Λ	Γ
ZAMS	3.00	0.014	0.014	1.0	1.8	4.10	60.2	0.036
mid-MS	3.00	0.014	0.014	1.0	1.8	4.31	64.1	0.042
TAMS	3.00	0.014	0.014	1.0	1.8	11.8	65.5	0.074

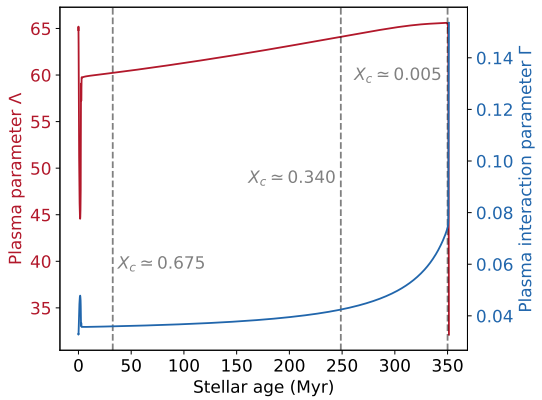

(a) Γ and Λ as a function of age.

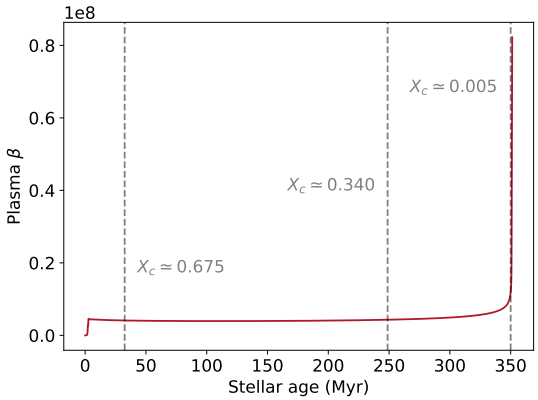

(b) Plasma β as a function of age.

Figure 4.1: Near-core plasma diagnostics for the 3 $M_\odot$ reference stellar model throughout MS evolution. $f_{\rm ov} = 0.014$, $Z = 0.014$, $D_{\rm mix} = 1$ cm^{2}s^{-1}, $\alpha_{\rm MLT} = 1.8$, $u = 0.25$. Reference life phases are indicated with grey dashed vertical lines: ZAMS ($X_c \simeq 0.675$), mid-MS ($X_c \simeq 0.340$), TAMS ($X_c \simeq 0.005$).

4.1.1 The effect of magnetic fields on a reference star throughout the main sequence

In order to assess the magnetic influence on period spacing patterns throughout main-sequence evolution, we pick a reference model and vary X_c. The reference model is a 3 $M_\odot$ star with solar metallicity ($Z = 0.014$), moderate core overshooting ($f_{\rm ov} = 0.014$), moderate envelope mixing ($D_{mix} = 1.0$ cm^2 s^{-1}), typical $\alpha_{\rm MLT}$ ($= 1.8$), rotating at $u = 0.25$, and displaying a maximal magnetic field strength $\alpha = 10^6$ G. The results for the ZAMS star are displayed in Figure (4.2), whereas the results for the mid-MS and TAMS star are displayed in Figure (4.3) and (4.4), respectively. First, there is a clear difference in normalized magnetic field models at different X_c (displayed in panel (a) of Figures (4.2), (4.3) and (4.4)). Barotropic ZAMS fields are more extended than their TAMS counterparts, influencing large parts of the near-core region. Hence, it might be expected that for these ZAMS stars, ω/ω_A typically is smaller than for their mid-MS and TAMS counterparts in the 'outer' near-core regions.

The Brunt-Väisälä profile of such stars is sharply peaked, because there is only a small near-core region with significant chemical gradients. Due to this sharp peak, the perturbative criterion is less easily fulfilled. This is confirmed by the mode cavity diagrams shown in Figure (4.2). Moreover, both the $n = -15$ and $n = -35$ modes are sub-inertial (i.e. their frequency is lower than the Coriolis frequency), indicating

that Hough functions are necessary to describe most of the zonal mode pulsations in these stars.

Figure (4.2) shows that the perturbative criterion seems to hold for every mode, if ω_A is calculated using Equations (3.30) and (3.31). However, as explained in Section (3.2.3), these estimates of the Alfvén frequency are rather crude, and are therefore deemed less reliable (especially Equation (3.30), assuming scaled core conditions). Our improved estimate of the Alfvén frequency, calculated using Equation (3.33), still is a rather crude estimate of the real local Alfvén frequency, albeit a more physically motivated one than the previous two.

Lastly, we note the significant difference in period spacing pattern between the rotating non-magnetic case and the rotating magnetic case. As was shown in Prat et al. (2019), the magnetic frequency shifts become significantly larger at higher radial orders. The trapped modes are affected most, as the magnetic field is strongest in their near-core trapping region.

The mid-MS model, displayed in Figure (4.3), displays similar trends: magnetic shifts become large and our perturbative approaches has its limitations. The distinct signature of the receding convective core can be observed in the mode cavity diagrams, as a widened peak in the Brunt-Väisälä profile. The $n = -15$ mode is super-inertial, and its magnetic shift can be well described by our perturbative approach. The $n = -15$ mode period spacing is shifted by approximately 100 seconds, a shift that could be detected observationally (although typical uncertainties on pulsation period spacing patterns are of the order of 250 seconds). The perturbative criteria (3.30) and (3.31) again assess that more modes could be described with the perturbative formalism, compared to our improved criterion (3.33).

The TAMS model, displayed in Figure (4.4), yields optimal results with respect to perturbative validity of our approach. It assesses that magnetic shifts of all modes can be described using our perturbative formalism. Moreover, all frequencies are super-inertial (at least up until $n = -35$), so that they could in principle be described without significant rotational mode trapping (e.g. Section (2.2.2)). Large deviations from 'normality' can be observed in the (simulated) magnetorotationally influenced period spacing pattern. Therefore, TAMS stars are excellent probes of internal magnetic fields. However, one should note that the region inside the stellar model with significant field strength (of the barotropic magnetic field) is very close to the stellar center. In fact, if the Brunt-Väisälä frequency is used as a probe of convective core size (N becomes small at the core boundary), a core radius of approximately 0.025 r/R can be estimated. The strongest part of the magnetic field therefore seems to be situated inside this core, a region for which the Duez and Mathis (2010) field is not valid. Obviously this fully convective region is not of relevance with respect to g mode propagation, however, since the Duez and Mathis (2010) magnetic field model is only defined within the radiative zone of a stellar model/star, questions could be raised on the validity of the field strength in the near-core regions. However, the only necessary input for calculating the Duez and Mathis (2010) magnetic field is the density profile, from which the corresponding local field strength is estimated. Hence, we deem it unlikely that the magnetic field in the regions for which the Duez and Mathis (2010) magnetic field model does not hold, affects the field in the near-core regions (gravely). This should be investigated in the near future, by calculating the numerical magnetic field model (described by Equation (3.14)) in the radiative zone only.

The apparent loops and negative spacings provide an indication that our perturbative theory is lacking a physical process that takes place between pulsations inside stars: mode interaction. Hence, one can describe the period spacing patterns of modes up to the radial order for which the characteristic 'sawtooth' pattern starts to appear. Non-perturbative approaches are needed to describe higher radial orders then. It is expected that if frequencies of two modes approach each other, they undergo an interaction reminiscent of so-called 'avoided crossings' that occur between modes of two coupled (mechanical) oscillators. This can have major implications for pulsation mode labelling, as modes undergoing avoided crossings, assimilate the (physical) geometry of the mode with which they interact. This phenomenon has major implications for the mode classification problem, for which usually the scheme proposed by Scuflaire (Scuflaire, 1974) and Osaki (Osaki, 1975) is used, so that the nomenclature (p,f,g-modes) does not always reflect the physical nature of the oscillations (Shibahashi and Osaki, 1976).

4.1.2 Varying field strength and rotation rate for a reference star throughout the main sequence

A more detailed overview of the magnetic influence on period spacing patterns for the reference model discussed in the previous section is given in Figures (4.6), (4.7), and (4.9). As can be noted in Figure (4.6), the magnetic fields with maximal field strengths of 10^4 and 10^5 G do not induce strong magnetic shifts. Only for slowly rotating models do the period spacing patterns shifted by the $\alpha = 10^5$ G field differ from their purely rotational counterpart, whereas for $\alpha = 10^4$ G fields, no marked differences are observed. A maximal shift ΔP of approximately 150 seconds is obtained for the $\alpha = 10^5$ G patterns. Increasing rotation rates significantly decrease the amplitude of expected magnetic signatures, as we noted in Prat et al. (2019). This can be explained by the fact that the Brunt-Väisälä frequency usually is much larger than the Coriolis frequency, so that the lower frequency bound for gravito-inertial waves is approximated by: $\omega_- \approx 2\Omega\cos\theta$ (e.g. Prat et al., 2016). The estimated Alfvén frequencies for the 10^4 G and 10^5 G fields are (much) lower than ω_- and increasing rotation rate (i.e. increasing Ω) shifts the lower frequency bound further upwards. Hence, the modes become less sensitive to the magnetic influence with increasing rotation rate, as is observed here (for the 10^5 G models). Therefore, we concluded in Prat et al. (2019) that one should search for the signatures of a magnetic field in period spacing patterns of slow rotators. With respect to Figure (4.6), this conclusion obviously holds. We note in this work that, with increasing rotation rate, the perturbative approach is also valid for higher radial orders, as is observed from the form of Equation (3.30), derived by Prat et al. (2019). Taking a look at Figures (4.7) and (4.9), one could thus infer strong magnetic fields in more rapid rotators as well. This is justified by the fact that the gravito-inertial modes inside a strongly magnetic, strongly rotating star display significant magnetic shifts over a large range of orders, which, according to the criterion derived in this work (Equation (3.33)), are valid in our perturbative approach. If such strong fossil fields would exist within real MS stars, they should thus readily be detectable from *Kepler* photometric light curves, because their induced shifts are (much) larger than the typical uncertainty on g mode period spacings ΔP (250 seconds).

4.1.3 Varying D_{mix} for a reference model

Keeping other parameters constant, the effect of D_{mix} will be probed for the reference model: a 3 $M_{\odot}$ star with solar metallicity ($Z = 0.014$), moderate core overshooting ($f_{ov} = 0.014$), typical α_{MLT} ($= 1.8$), rotating at $u = 0.25$, and displaying a maximal magnetic field strength $\alpha = 10^6$ G. Mixing can change the stellar model evolution on a long-term scale, by changing local composition and influencing long-term energy transport. This might change the local density and thus affect the magnetic field, pulsation modes, etc. As the mixing parameter D_{mix} is kept constant throughout the MS evolution, one would expect the greatest influence for more evolved models. The influence of the mixing parameter D_{mix}, kept constant throughout the MS evolution, can be observed in Figure (4.11). As expected, magneto-rotational shifts are larger for more evolved models. Interestingly, the high radial order modes of the TAMS model with a large amount of mixing ($D_{mix} = 10.0$ cm^2 s^{-1}) are greatly affected. Although this might be linked to a different density profile, which subsequently changes the magnetic field model (see Section (3.2.3)), no significant changes can be observed in Figure (4.13), when compared to the field models shown in the reference case, depicted in Figure (4.5). No marked changes can be observed in the Alfvén velocity structure, when comparing the models displayed in Figure (4.14) and Figure (4.5). The origin of the marked change in slope of the period spacing pattern should be investigated thoroughly in the near future, as this could affect the derivation of the near-core rotation rate, although, typically, prograde mode period spacing patterns are used (see e.g. Van Reeth et al., 2016, 2018). Such a deviation would be identified easily in observational period spacing patterns. The more equatorially confined, high radial-order modes are affected more strongly than low radial-order modes, as was mentioned before. Although there are easily visible features in the period spacing pattern, no significant/marked features of the magnetic influence are obtained from the simulated mode frequency spectra (see Figure (4.12)). The TAMS model with a (very) small degree of mixing ($D_{mix} = 0.1$ cm^2 s^{-1}) does not seem to be markedly different from the reference model shown in Figure (4.7), even though the high radial-order modes show slightly larger shifts in the low-mixing case.

We note the large jump at $P \sim 0.5$ d for this TAMS model. This is due to numerical inaccuracy in obtaining the frequency of the $n = -13$ mode using GYRE. GYRE identified two mixed modes: $n_{\rm pg} = -11, n_{\rm p} = 1$ and $n_{\rm pg} = -9, n_{\rm p} = 2$. We deem these to be a misidentification with the Osaki-Scuflaire mode labelling system implemented in GYRE (Osaki, 1975; Scuflaire, 1974). In order to remedy this, we re-calculated the MESA stellar model with additional resolution, and increased the resolution of the GYRE frequency search grid. Yet, this did not affect the GYRE mode labelling. The result of this investigation does not change because of this numerical inaccuracy.

4.1.4 Varying $\alpha_{\rm MLT}$ for a reference model

Keeping other parameters constant, the effect of $\alpha_{\rm MLT}$ will be probed for a reference model: a 3 $M_\odot$ star with solar metallicity ($Z = 0.014$), moderate core overshooting ($f_{ov} = 0.014$), moderate mixing strength ($D_{mix} = 1.0$ cm^{2}s^{-1}), rotating at $u = 0.25$, and displaying a maximal magnetic field strength $\alpha = 10^6$ G. The $\alpha_{\rm MLT}$ parameter constrains the mixing length in the mixing length theory. If it is larger, convective cells will be able to reach a larger distance before dissolving (see Equation (1.9)), exchanging chemical information over a larger area inside the star. This effectively changes the size of the convective zone and thus affects the g mode propagation in the stellar interior, since they cannot propagate in convective zones. Since we assume that convective regions are completely mixed, this affects the density profile. By looking at Figure (4.15), we deduce a small slope change for the small $\alpha_{\rm MLT}$ ($= 1.5$) TAMS model, like was observed for a high $D_{\rm mix}$ TAMS model in Figure (4.11). Unlike when varying $D_{\rm mix}$, the magnetic field model structure (depicted in Figure (4.17)) is slightly different in the near-core region of the small $\alpha_{\rm MLT}$ TAMS model (more specifically, the toroidal field structure), as would be expected when the density profile is adjusted, according to the magnetic field prescription. This also results in a slightly different (toroidal) Alfvén velocity structure (depicted in Figure (4.18) for this model, although the poloidal structure in the near-core region seems to be virtually unaffected. For ZAMS reference models, we cannot distinguish between rotationally modified g mode pulsations and magneto-rotationally modified ones. For mid-MS reference models, only deviations in low radial order modes can be observed, larger for the small $\alpha_{\rm MLT}$ model (max. ΔP deviation ≈ 500 s for the $n = -17$ mode). Even though such deviations could possibly be detected, it can only provide weak constraints on the magnetic field inside the star, as well as the stellar fundamental parameters.

4.1.5 Varying f_{ov} for a reference model

Keeping other parameters constant, the effect of $f_{\rm ov}$ will be probed for a reference model: a 3 $M_\odot$ star with solar metallicity ($Z = 0.014$), moderate mixing strength ($D_{mix} = 1.0$ cm^{2}s^{-1}), typical $\alpha_{\rm MLT}$ ($= 1.8$), rotating at $u = 0.25$, and displaying a maximal magnetic field strength $\alpha = 10^6$ G. Overshooting induces extra mixing in the convective boundary regions, and therefore locally changes the density profile (see Equation (3.1)). Moreover, as more/less hydrogen is transported to the convective core for higher/lower overshoot parameters $f_{\rm ov}$, the main sequence lifetime of the stellar model is lengthened/shortened. Therefore, the age of the star for a given X_c will increase/lower, affecting the radius, $T_{\rm eff}$ profile and the density profile. Therefore, since the trapped modes, located in such near-core regions, are most affected, we expect overshooting to modify the period spacing patterns in a strong way. As is clear by now, more confined, higher radial-order modes are sensitive to a different magnetic field, compared to the less confined, low radial-order modes, and thus experience different magnetic shifts, as illustrated rather well in Figure (4.19). Figure (4.19) also reveals a downward trend of the magnetic period spacing pattern due to extra near-core mixing being induced by $f_{\rm ov}$. The physical reasoning is a different (local) density profile, affecting the magnetic field structure, and thus affecting the magnetic frequency shifts of the pulsation modes. The Alfvén velocity $\boldsymbol{v}_{\rm A}$ is increased throughout the entire stellar model with increasing $f_{\rm ov}$, as

depicted in Figure (4.23), and is different from the more confined velocity structure for low overshoot and reference overshoot models. Figure (4.22) reveals that both the poloidal and toroidal field structure locally is different in the large $f_{\rm ov}$ model, when compared to the low $f_{\rm ov}$ model, as well as the reference $f_{\rm ov}$ model (depicted in Figure (4.5)). Indeed, as can be observed in Figure (4.21), for the TAMS models, the (radial) magnetic field profile is changed, due to a changed density profile. It is interesting to note the difference in radial field strength evaluated at an arbitrarily chosen colatitude $\theta = 5^\circ$ in the overshoot region for models with different $f_{\rm ov}$ (see Figure (4.21)), the region in which modes are trapped (due to a large ∇_μ). Hence, differences in the magnetic field structure as depicted in Figures (4.22), 4.21 and (4.5) can quite strongly affect period spacing patterns of g modes that probe this very region. It seems promising that one could in effect probe core overshooting in the presence of a strong field, a parameter that is typically conflicted with degeneracies (see e.g. Pedersen et al., 2018; Aerts et al., 2018), although further work is needed to provide additional clarification. This probing power might improve with more sophisticated magnetic field models.

4.1.6 Varying Z for a reference model

Keeping other parameters constant, the effect of Z will be probed for a reference model: a 3 $M_\odot$ star with moderate core overshooting ($f_{ov} = 0.014$), moderate mixing strength ($D_{mix} = 1.0$ cm^2 s^{-1}), typical α_{MLT} ($= 1.8$), rotating at $u = 0.25$, and displaying a maximal magnetic field strength $\alpha = 10^6$ G. Changing the initial metallicity Z affects the stellar opacity. This results in a lower radiative outward force, causing low-Z stars to be more compact and hotter compared to their higher Z counterparts (Hirschi et al., 2008). Because these stars have different radii for a specific stellar mass compared to their different Z counterparts, the critical rotation velocities (defined in Equation (2.21)) will be different. The rotation rates of low-Z stars are thus larger, compared to their higher-Z counterparts, if u is kept constant. Moreover, since nuclear burning processes in the stellar core such as the CNO-cycle are very sensitive to the metal content, as well as the core temperature, the lifetime of the stars is changed depending on metallicity, with high-Z stars living longer (Hirschi et al., 2008).

Figure (4.24) suggest no clear slope deviation. The magnetic field models slightly differ in their toroidal components, but, unlike the case for $f_{\rm ov}$, this doesn't induce the shifts/tilt noticed for those models. Moreover, a tilt due to increasing rotation rate in low-Z stars is not present. Most changes can be observed in the high radial order regime, where we stress that the closely packed frequencies might lead to mode interactions. Therefore, effectively, the change in magnetic shifts induced by varying metallicity does not seem to greatly affect the shape of the period spacing pattern for low radial order modes. The TAMS model individual frequency shifts indicate a stronger magnetic field influence for low-Z stellar models, somewhat contrary to what one would expect for the faster rotator, based on our conclusions in Prat et al. (2019). The origin of this phenomenon should be explored in further work.

4.1.7 Checking the influence of computational parameters on mode frequencies

One of the questions raised in the previous chapter was how the numerical difference scheme affects the mode frequencies of the reference model discussed earlier. It turns out, by looking at the Figures (4.28), (4.29), (4.30), (4.31), (4.32), that negligible differences in the period spacing patterns occur for all patterns generated with different numerical choices. The choice of difference scheme does not play a significant role on the period spacing level.

Another question raised was that of outer boundary conditions: does using the simplistic VACUUM boundary condition change the frequencies of the pulsation modes significantly, when compared to frequencies obtained with the UNNO boundary condition? It turns out that this is also not the case, as observed in Figure (4.33), where both the period spacings and simulated frequency spectra are shown on the left and the right, respectively. No marked changes in the period spacing pattern structure are found. Switching boundary conditions can still shift the individual mode frequencies, but individual frequency fitting will always be accompanied with matching the ΔP pattern in g-mode asteroseismology, so this is not an issue.

4.2 Mode interaction and mode bumping

4.2.1 'Classical' mode bumping

The phenomenon of 'mode bumping' can be observed when looking at the frequencies of nonradial oscillations of gradually changing stellar configurations, i.e. when following the change in mode frequencies throughout the stellar evolution. When the frequency of a certain mode approaches the frequency of another, the second mode subsequently is 'bumped' to a different frequency, whereas the original 'bumping' mode settles at approximately the frequency of the 'bumped mode', no longer following the asymptotic expression (e.g. Aizenman et al., 1977; Roth and Weigert, 1979; Christensen-Dalsgaard, 1981; Gautschy, 1992; Smeyers and Van Hoolst, 2010). This is reminiscent of 'avoided crossings' between modes of two coupled oscillators, so that Aizenman et al. (1977) developed a formalism in which they decouple the coupled oscillators. Mode bumping has mostly been studied for massive stars on the main sequence (e.g. Aizenman et al., 1977; Roth and Weigert, 1979), or for more evolved stars such as subgiants and red giants (e.g. Benomar et al., 2012; Mosser et al., 2012b; Bedding et al., 2011; Benomar et al., 2013), as it typically involves bumping between a g and a p mode. After mode interaction, both interacting modes gain an extra node, as has been shown in Smeyers and Van Hoolst (2010) and references therein. It has not received much attention for main sequence intermediate-mass stars. However, this phenomenon has major implications for the mode classification (due to the appearance of these extra nodes), for which usually the scheme proposed by Scuflaire (Scuflaire, 1974) and Osaki (Osaki, 1975) is used, so that the nomenclature (p,f,g-modes) does not always reflect the physical nature of the oscillations (Shibahashi and Osaki, 1976).

The 'classical' mode bumping diagram, as first used by Aizenman et al. (1977), for the reference model in our grid (resampled with a fine X_c step) is shown in Figure (4.34). Under the influence of rotation, bumping may occur. It clearly shows the flaws of the Scuflaire-Osaki mode labelling system, as 'specific' modes throughout the main-sequence shift frequency multiple times. Interestingly enough this shifting already takes place very close to the ZAMS for higher radial order modes (see modes enclosed in black dashed box), further rendering identification hard.

4.2.2 Magnetic mode bumping

Given the results in Section (4.1), we will consider how mode bumping is affected by an internal magnetic field, since this might introduce additional complications in mode identification that were previously not considered. As can be seen in Figure (4.34), a (moderately) strong internal magnetic field (i.e. 10^6 G) greatly influences the mode frequencies and the mode bumping as well, as indicated on Figure (4.34) with dashed line boxes. The influence is larger for more confined higher radial order modes, as is expected from the results of Section (4.1), and becomes important at earlier evolutionary stages. In fact, it is already important for our ZAMS models for the modes considered in the black dashed box in Figure (4.34). This may cause additional complications for mode identification. It should be taken into account, as the effect most certainly does not seem to be negligible. In the near future, we shall explore in detail how bumping affects the predictions made with the Prat et al. (2019) formalism.

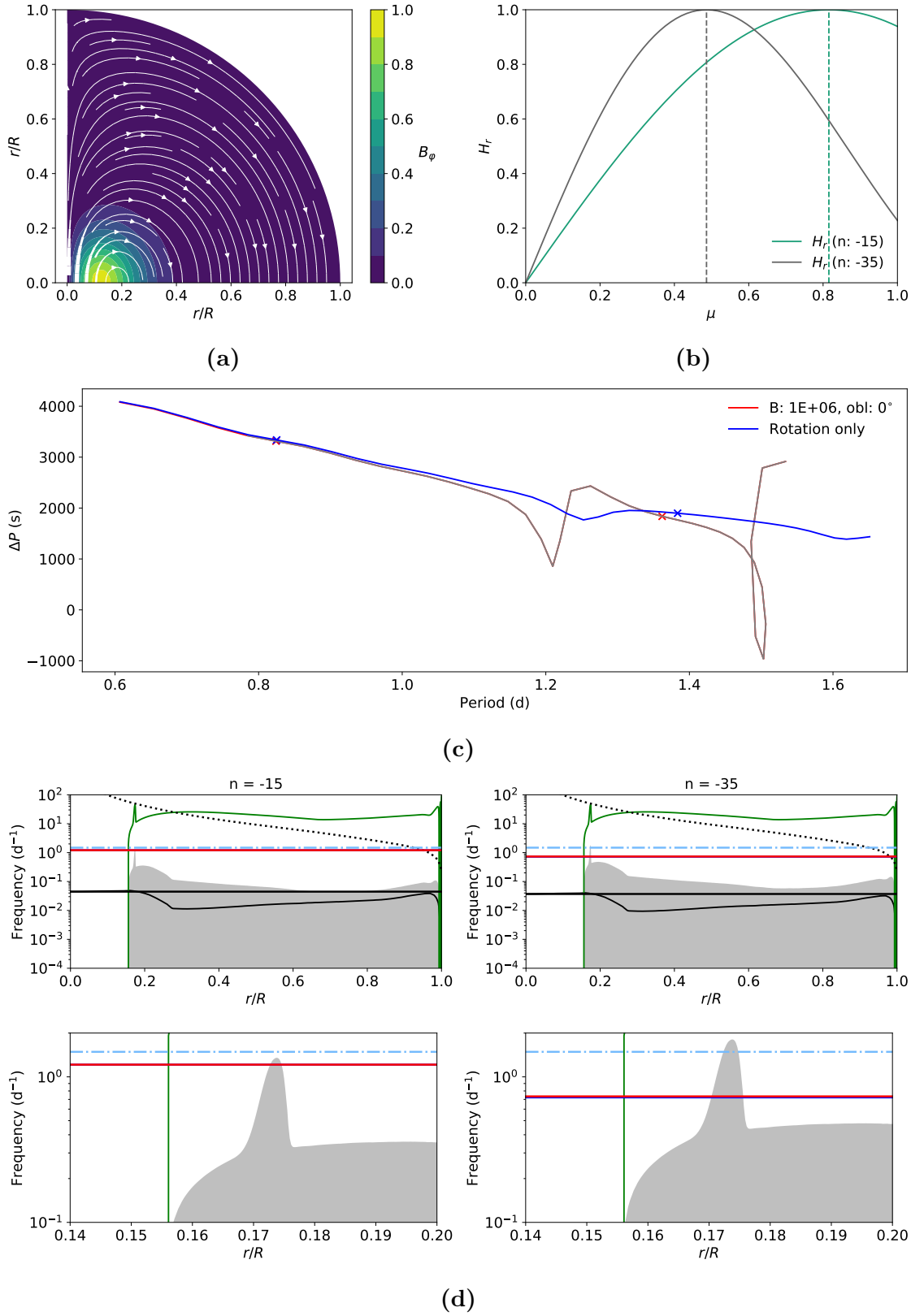

Figure 4.2: Pulsation characteristics of a 3 $M_\odot$ ZAMS ($X_c \approx 0.6740$) stellar model, $f_{ov} = 0.014$, $Z = 0.014$, $D_{mix} = 1$ cm^{2}s^{-1}, $\alpha_{MLT} = 1.8$, $f_{rot} = \Omega/2\pi = 0.7430$ d^{-1}, $\lambda \approx 26.5$. **(a):** Normalized $\boldsymbol{B}$ representation. **(b):** H_r evaluated for $\mu_{1/2}$ of specific modes: $(n = -15 : \theta \approx 35°, \nu = 1.226)$, $(n = -35 : \theta \approx 61°, \nu = 2.056)$. **(c):** Period spacing pattern ($n \in [-10, -50]$) for $u = 0.25$, including/excluding 10^6 G magnetic field (red/blue). Black parts of the period spacing pattern indicate regions where $\omega < \omega_A$ (ω_A is estimated using Equation (3.33)). Crosses indicate the specific modes ($n = -15$, $n = -35$) selected for mode cavity analysis. **(d):** Mode cavity diagrams (for the specific modes selected) with zoom-in. The dotted line is S_l, N is plotted in green, the light blue dash-dotted line is the Coriolis frequency ($2f_{rot}$), the red line is the magneto-rotationally shifted frequency, the blue line is the rotationally modified frequency, the thin black line is the local ω_A calculated with Equation (3.31), the thick black line is the ω_A estimate obtained from Equation (3.30), whereas the shaded grey area is the ω_A estimate calculated with Equation (3.33).

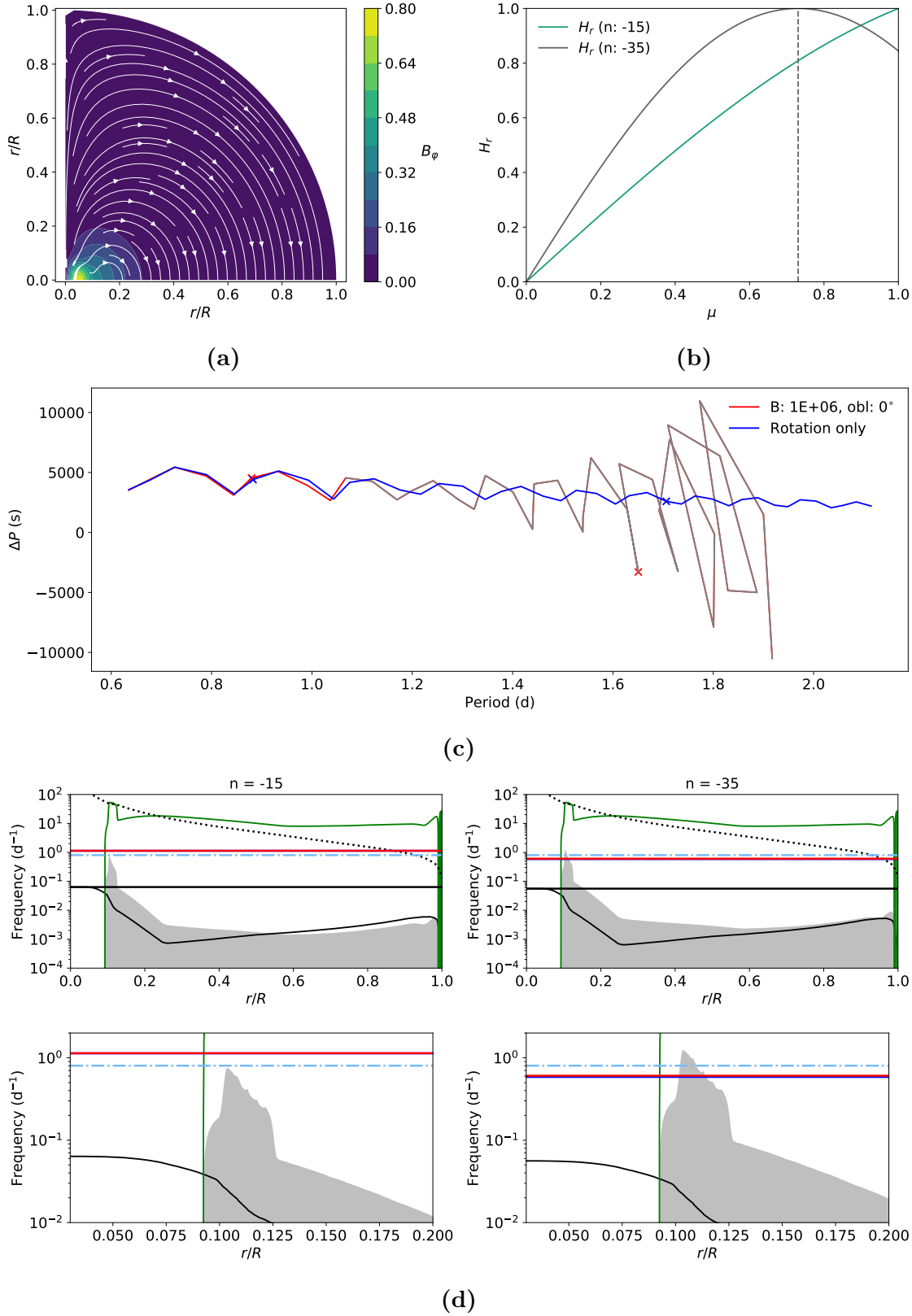

Figure 4.3: Same as Figure (4.2), but for a 3 $M_\odot$ mid-MS ($X_c \approx 0.3398$) stellar model. In this case the specific modes are characterized by $(n = -15 : \theta = 0°, \nu = 0.708)$ and $(n = -35 : \theta \approx 43°, \nu = 1.369)$. The rotation frequency is $f_{\rm rot} = 0.4011$ d^{-1}, with $\lambda \approx 55.3$.

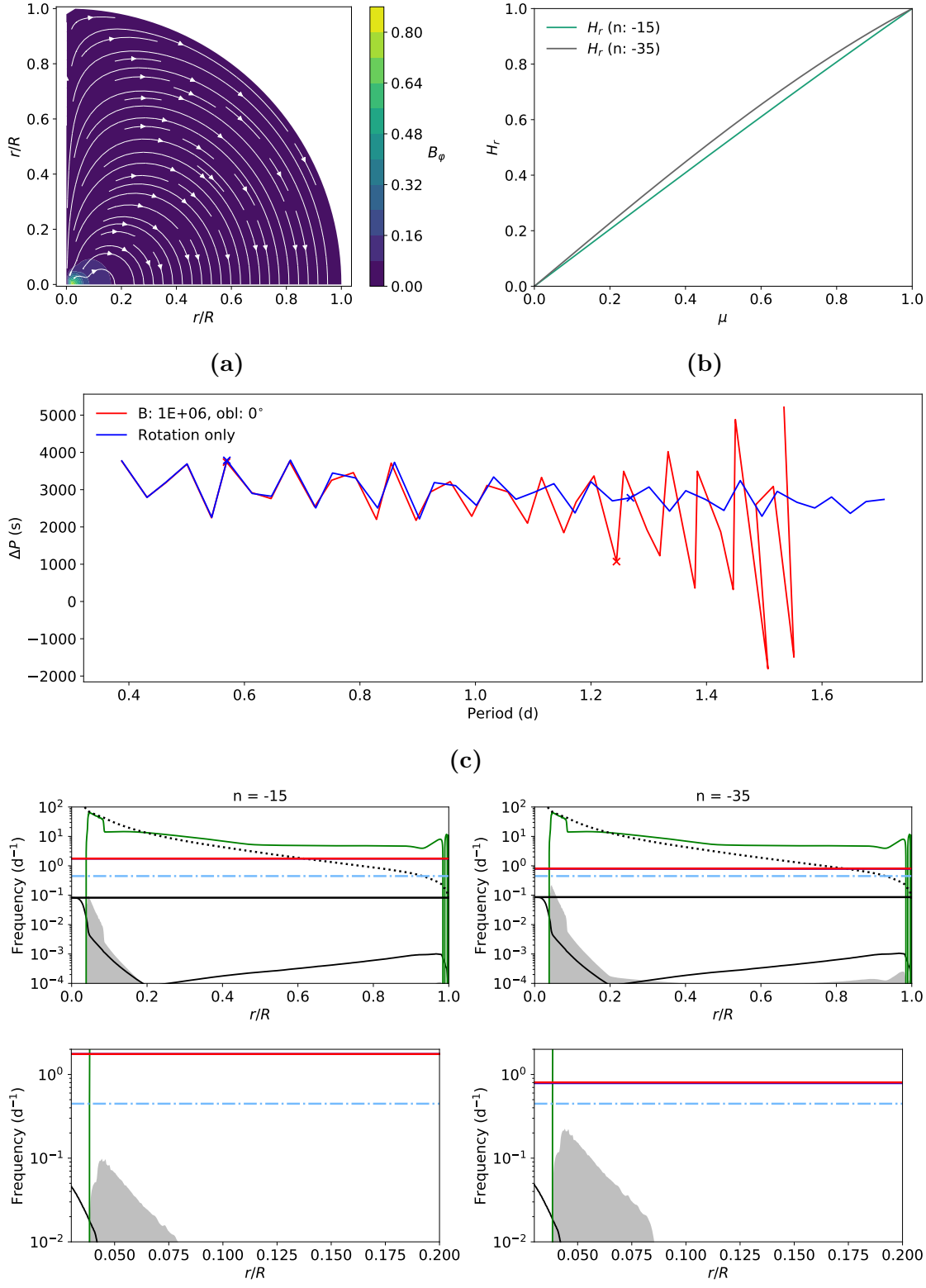

Figure 4.4: Same as Figure (4.2), but for a 3 $M_\odot$ TAMS ($X_c \approx 0.005$) stellar model. In this case the specific modes are characterized by $(n = -15 : \theta = 0°, \nu = 0.255)$ and $(n = -35 : \theta = 0°, \nu = 0.567)$. The rotation frequency is $f_{rot} = 0.2237$ d^{-1}, with $\lambda \approx 113.2$.

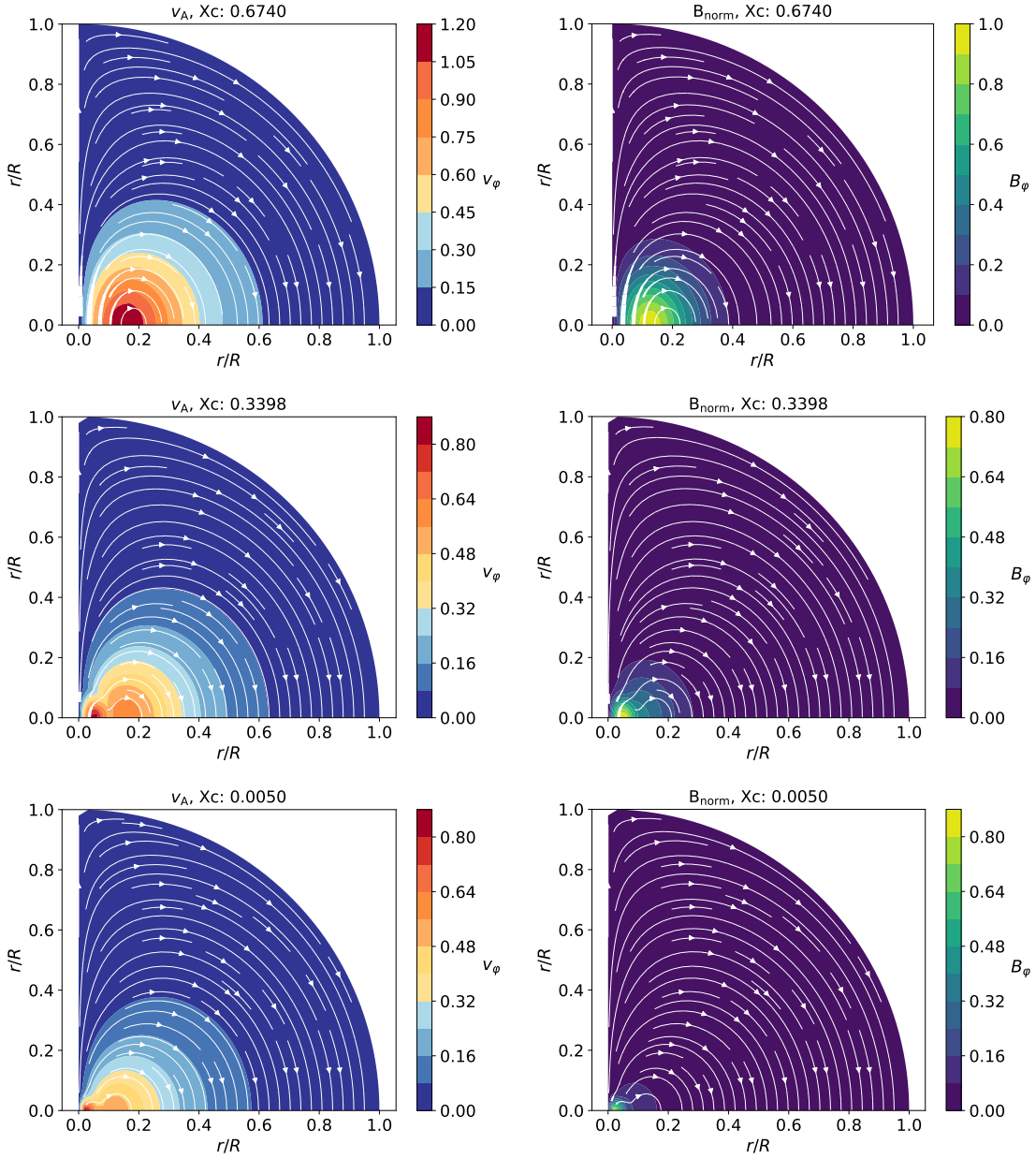

Figure 4.5: *From left to right:* Normalized Alfvén velocity structure (left), and normalized magnetic field model structure, as prescribed in Section (3.2.3) (right) for a $3M_\odot$ stellar model, $f_{ov} = 0.014$, $Z = 0.014$, $D_{mix} = 1$ cm^{2}s^{-1}, $\alpha_{MLT} = 1.8$. *From top to down:* ZAMS model ($X_c \approx 0.675$), mid-MS model ($X_c \approx 0.340$), TAMS model ($X_c \approx 0.005$).
The normalized Alfvén velocity $\boldsymbol{v}_\mathrm{A}$ is estimated as $\boldsymbol{v}_\mathrm{A} = \boldsymbol{B}_\mathrm{norm}/\sqrt{\rho}$ (the normalized version of $\boldsymbol{v}_\mathrm{A}$ defined in Equation (3.24), converted to cgs units), where $\boldsymbol{B}_\mathrm{norm}$ is the normalized magnetic field (as depicted on the right hand side).

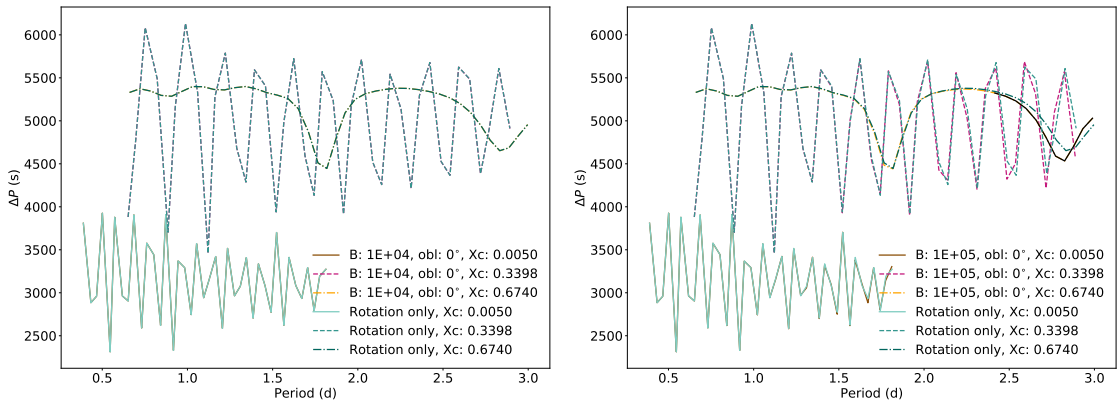

(a) *From left to right:* Period spacing patterns for $u = 0.01$ and $\alpha = 10^4$ G, 10^5 G.

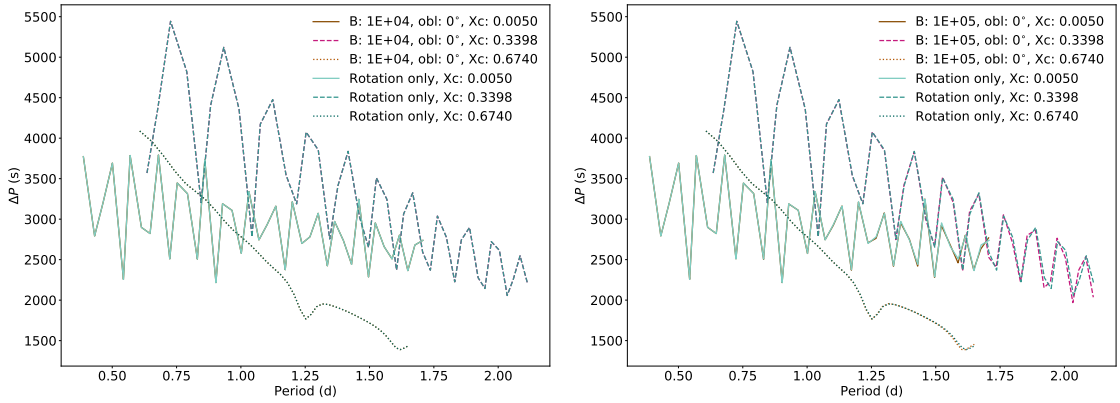

(b) *From left to right:* Period spacing patterns for $u = 0.25$ and $\alpha = 10^4$ G, 10^5 G.

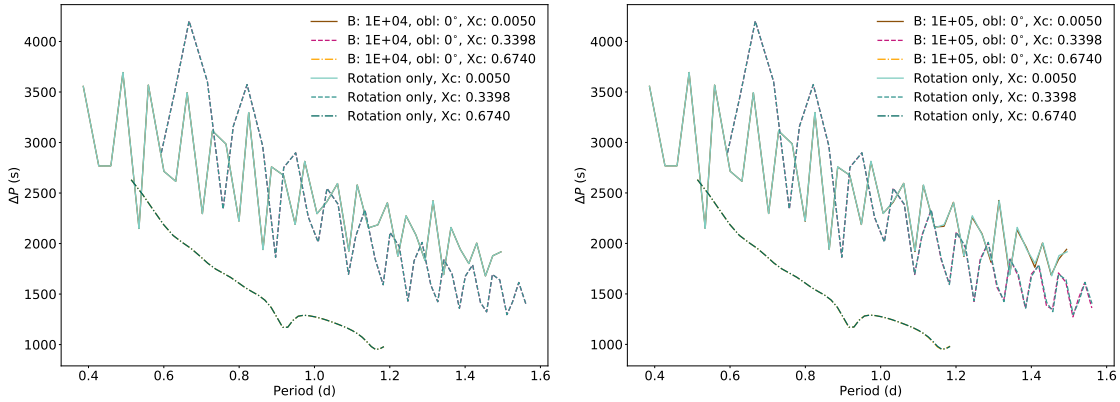

(c) *From left to right:* Period spacing patterns for $u = 0.50$ and $\alpha = 10^4$ G, 10^5 G.

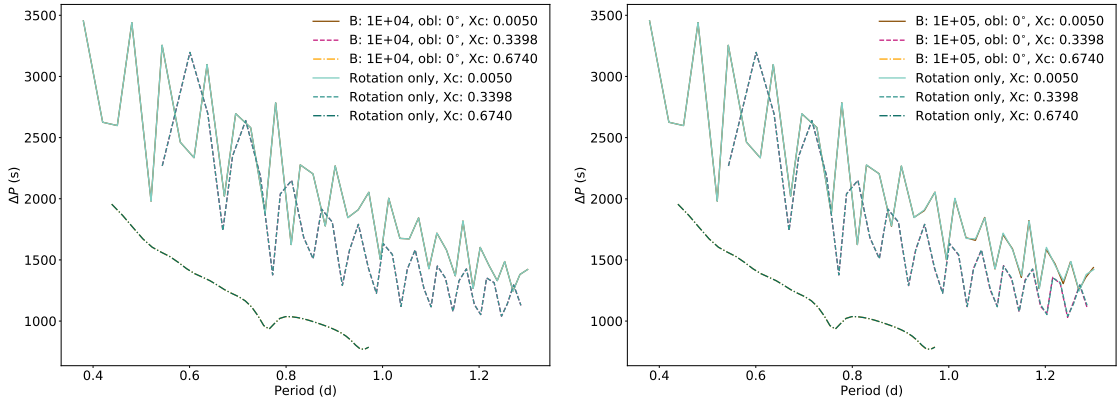

(d) *From left to right:* Period spacing patterns for $u = 0.75$ and $\alpha = 10^4$ G, 10^5 G.

Figure 4.6: Period spacing patterns for a $3M_\odot$ stellar model, $f_{ov} = 0.014$, $Z = 0.014$, $D_{mix} = 1$ cm^{2}s^{-1}, $\alpha_{MLT} = 1.8$, for the three considered evolutionary stages. All $\alpha = 10^4$ G and most $\alpha = 10^5$ G period spacing patterns have next to negligible (magnetic) shifts compared to their fully rotational counterparts. Black parts of the period spacing patterns indicate regions where $\omega < \omega_A$ (ω_A is estimated using Equation (3.33)).

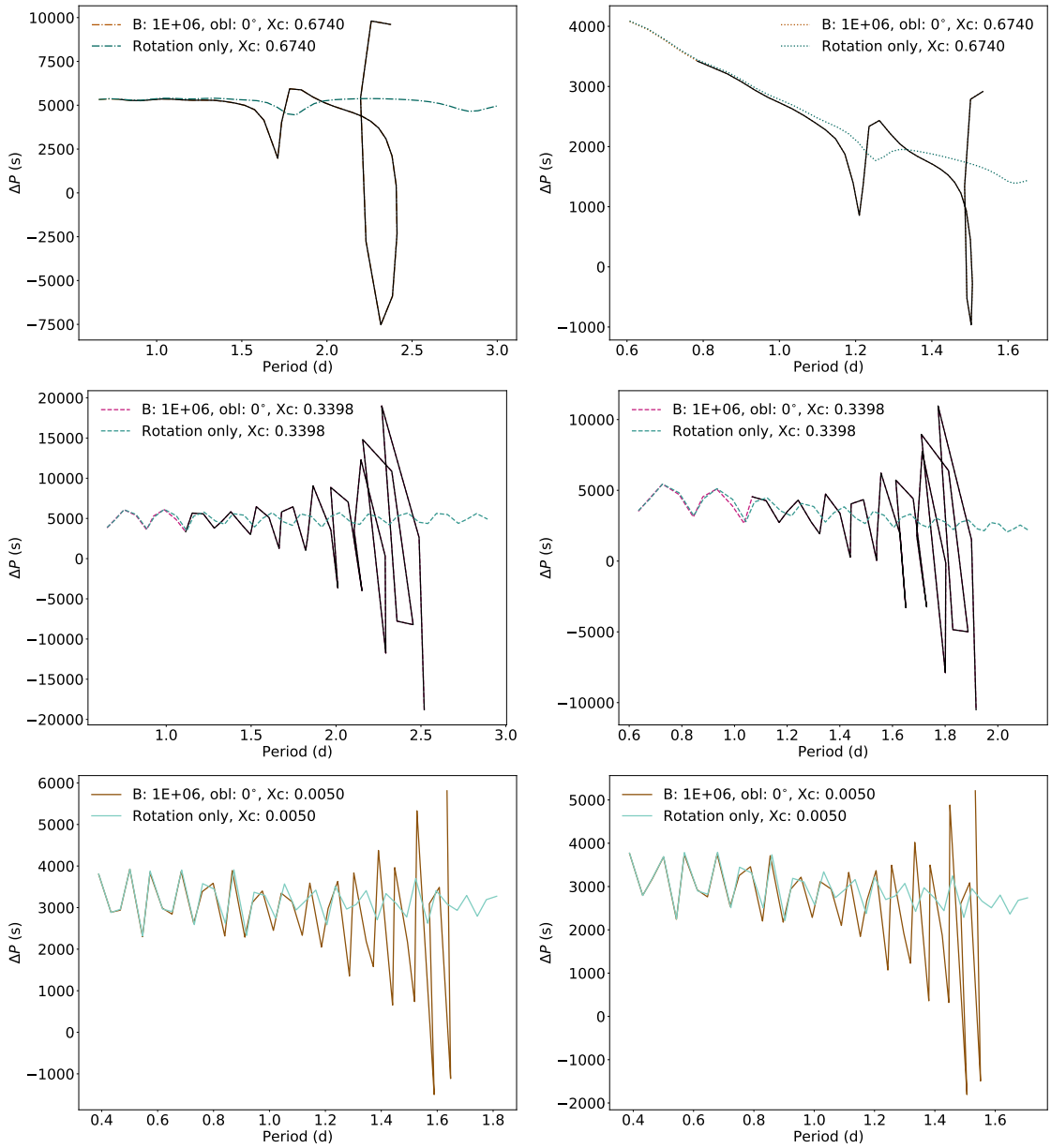

Figure 4.7: *From left to right:* period spacing patterns for a $3M_{\odot}$ stellar model at $u = 0.01$ (left) and $u = 0.25$ (right). $f_{ov} = 0.014$, $Z = 0.014$, $D_{mix} = 1$ cm^{2}s^{-1}, $\alpha_{MLT} = 1.8$ and $\alpha = 10^6$ G. *From top to down:* ZAMS model ($X_c \approx 0.675$), mid-MS model ($X_c \approx 0.340$), TAMS model ($X_c \approx 0.005$). Black parts of the period spacing patterns indicate regions where $\omega < \omega_A$ (ω_A is estimated using Equation (3.33)).

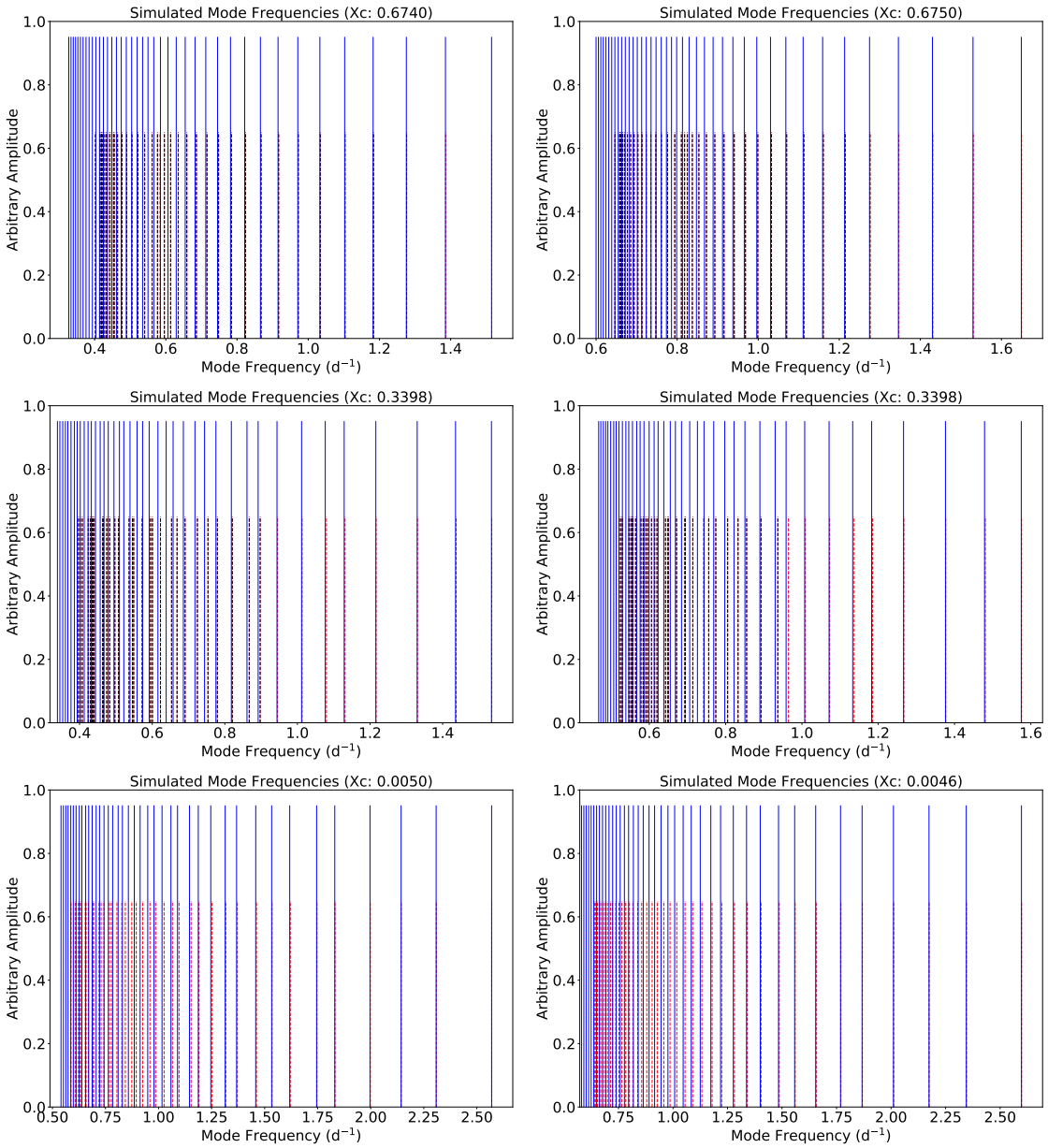

Figure 4.8: *From left to right:* simulated frequency spectra for a $3M_{\odot}$ stellar model at $u = 0.01$ (left) and $u = 0.25$ (right). $f_{ov} = 0.014$, $Z = 0.014$, $D_{mix} = 1$ cm^{2}s^{-1}, $\alpha_{MLT} = 1.8$, and $\alpha = 10^6$ G. *From top to down:* ZAMS model ($X_c \approx 0.675$), mid-MS model ($X_c \approx 0.340$), TAMS model ($X_c \approx 0.005$). Rotationally modified mode frequencies are indicated with solid blue vertical lines (of arbitrary amplitude), whereas red dashed vertical lines (of arbitrary amplitude) indicate magnetically shifted modes for strong internal fields. Black dashed vertical lines indicate mode frequency regions where $\omega < \omega_A$ (ω_A is estimated using Equation (3.33)).

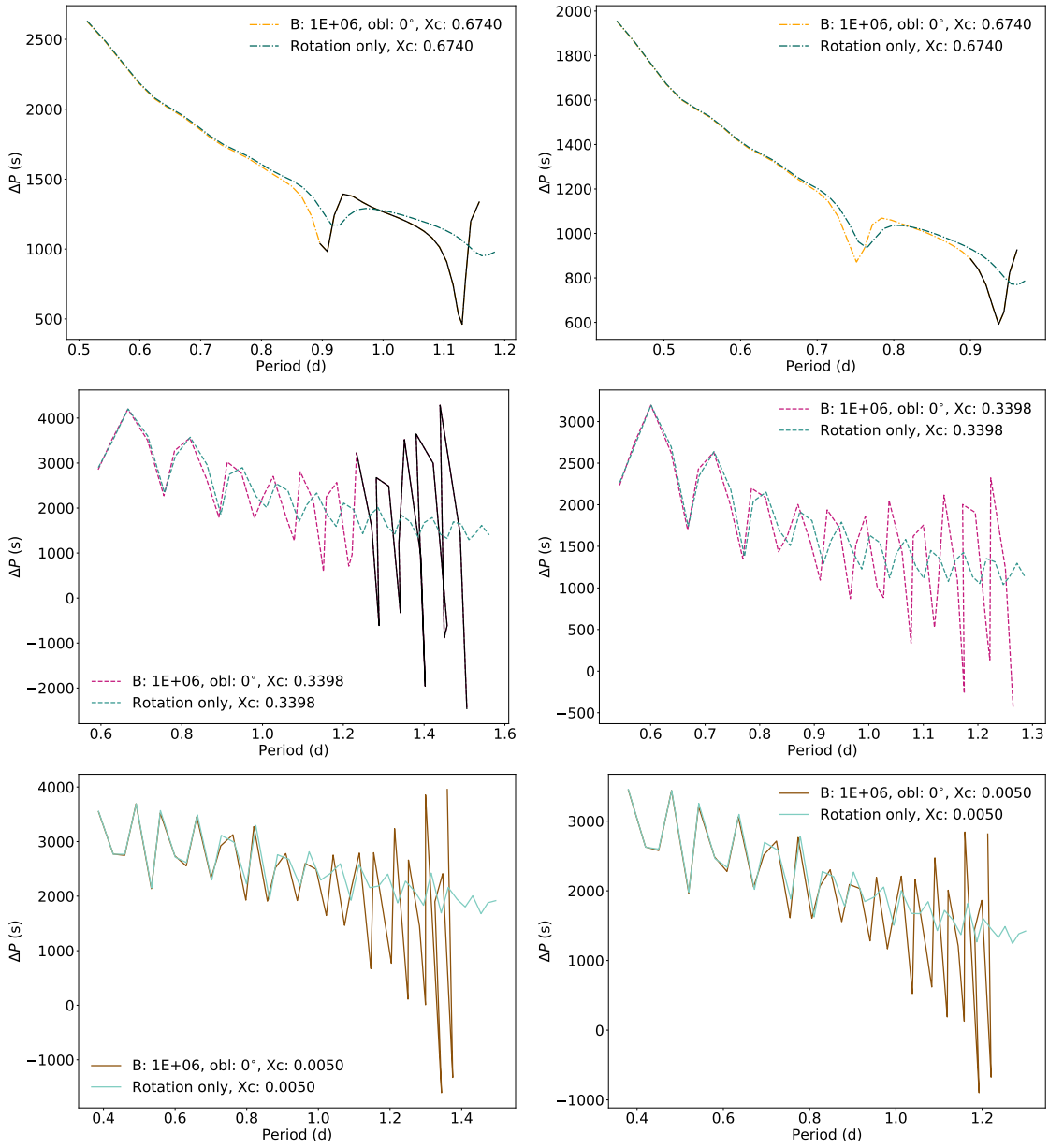

Figure 4.9: *From left to right:* Period spacing patterns for a $3M_{\odot}$ stellar model, at $u = 0.50$ (left) and $u = 0.75$ (right). $f_{ov} = 0.014$, $Z = 0.014$, $D_{mix} = 1$ cm^{2}s^{-1}, $\alpha_{MLT} = 1.8$, $\alpha = 10^6$ G. *From top to down:* ZAMS model ($X_c \approx 0.675$), mid-MS model ($X_c \approx 0.340$), TAMS model ($X_c \approx 0.005$). Black parts in the period spacing patterns indicate the same as in Figure (4.7).

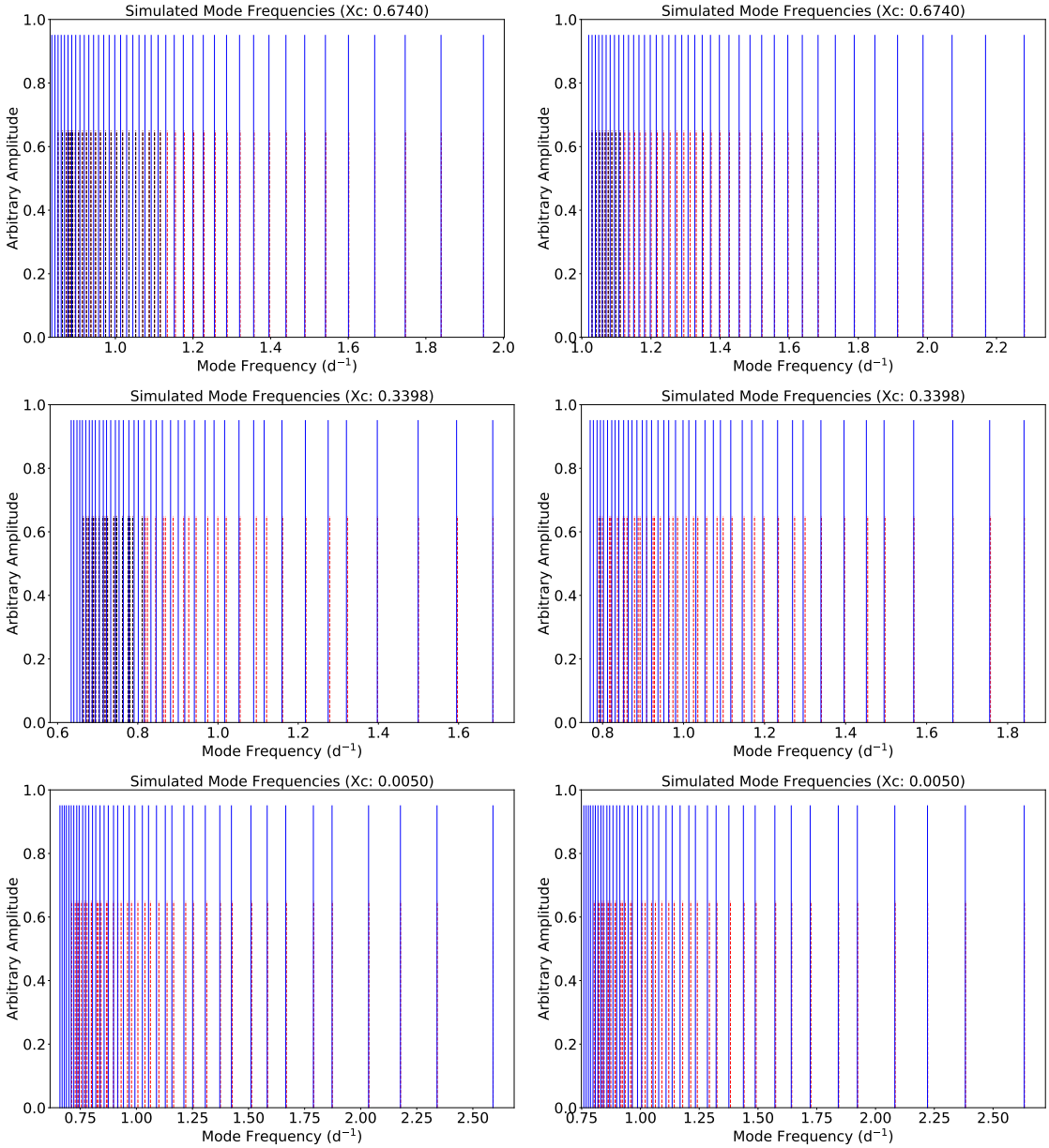

Figure 4.10: *From left to right:* simulated frequency spectra for a $3M_{\odot}$ stellar model, at $u = 0.50$ and $u = 0.75$. $f_{ov} = 0.014$, $Z = 0.014$, $D_{mix} = 1$ cm^{2}s^{-1}, $\alpha_{MLT} = 1.8$ and $\alpha = 10^6$ G. *From top to down:* ZAMS model ($X_c \approx 0.005$), mid-MS model ($X_c \approx 0.340$), TAMS model ($X_c \approx 0.675$). Colour code is the same as in Figure (4.8).

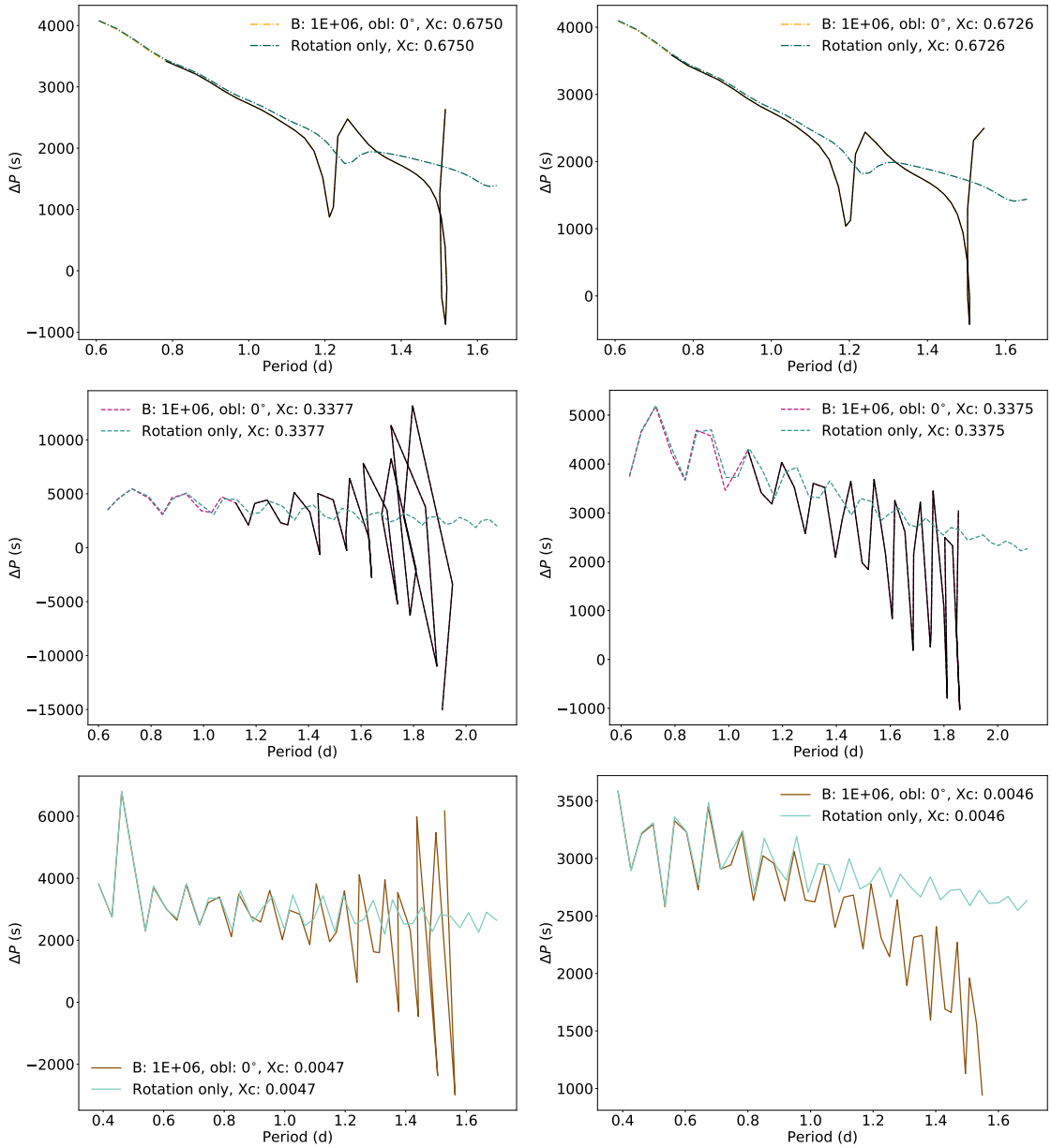

Figure 4.11: *From left to right:* Period spacing patterns for a $3M_{\odot}$ stellar model, at $u = 0.25$, where $D_{\rm mix} = 0.1$ cm^2 s^{-1} (left) and $D_{\rm mix} = 10.0$ cm^2 s^{-1} (right). $f_{ov} = 0.014$, $Z = 0.014$, $\alpha_{MLT} = 1.8$, and $\alpha = 10^6$ G. *From top to down:* ZAMS model ($X_c \approx 0.675$), mid-MS model ($X_c \approx 0.340$), TAMS model ($X_c \approx 0.005$). Black parts in the period spacing patterns indicate the same as in Figure (4.7).

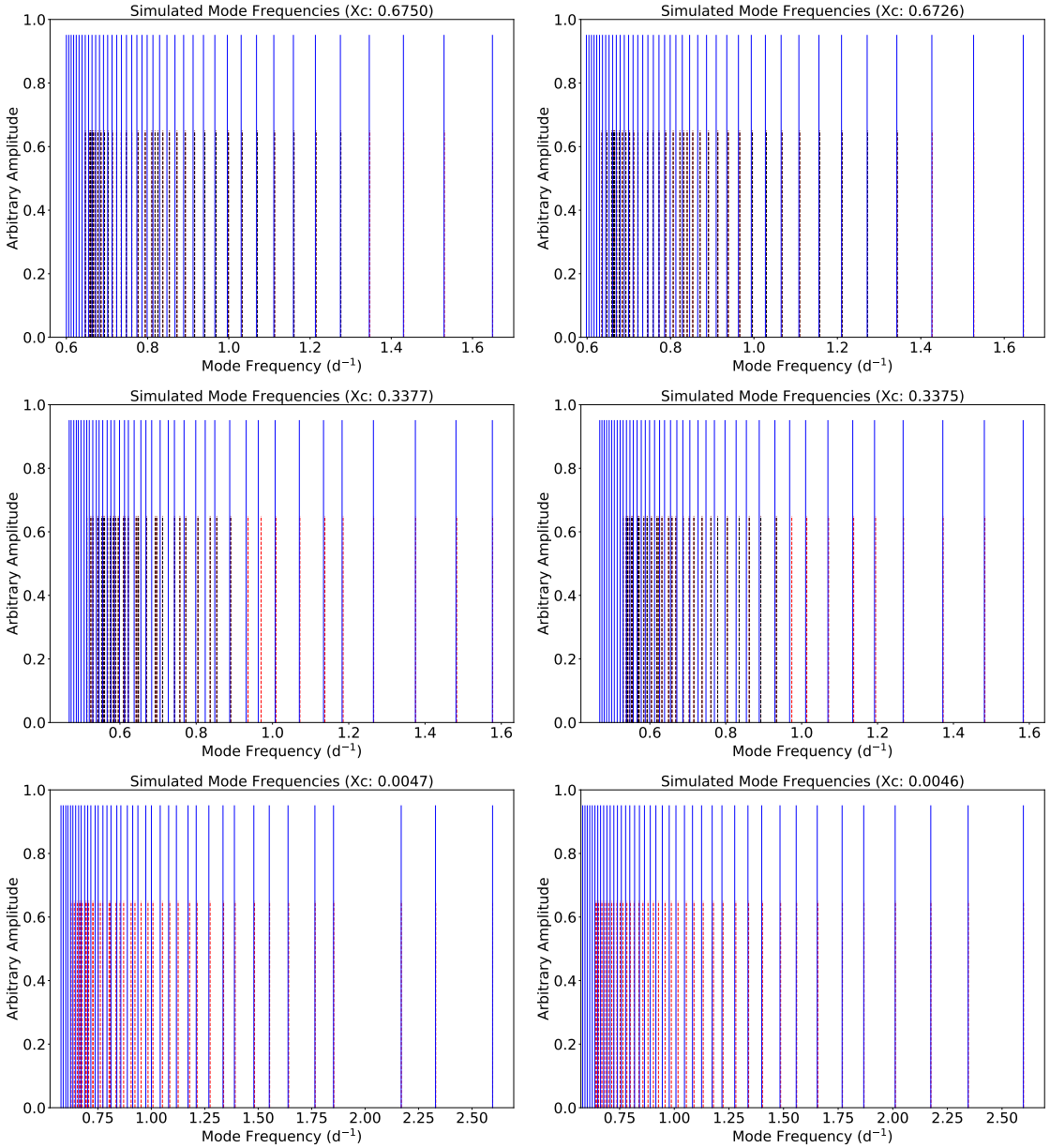

Figure 4.12: *From left to right:* Simulated frequency spectra for a $3M_{\odot}$ stellar model, at $u = 0.25$, with $D_{mix} = 0.1$ cm^2 s^{-1} (left) and $D_{mix} = 10.0$ cm^2 s^{-1} (right). $f_{\rm ov} = 0.014$, $Z = 0.014$, $\alpha_{\rm MLT} = 1.8$, and $\alpha = 10^6$ G. *From top to down:* ZAMS model ($X_c \approx 0.675$), mid-MS model ($X_c \approx 0.340$), TAMS model($X_c \approx 0.005$). Colour code is the same as in Figure (4.8).

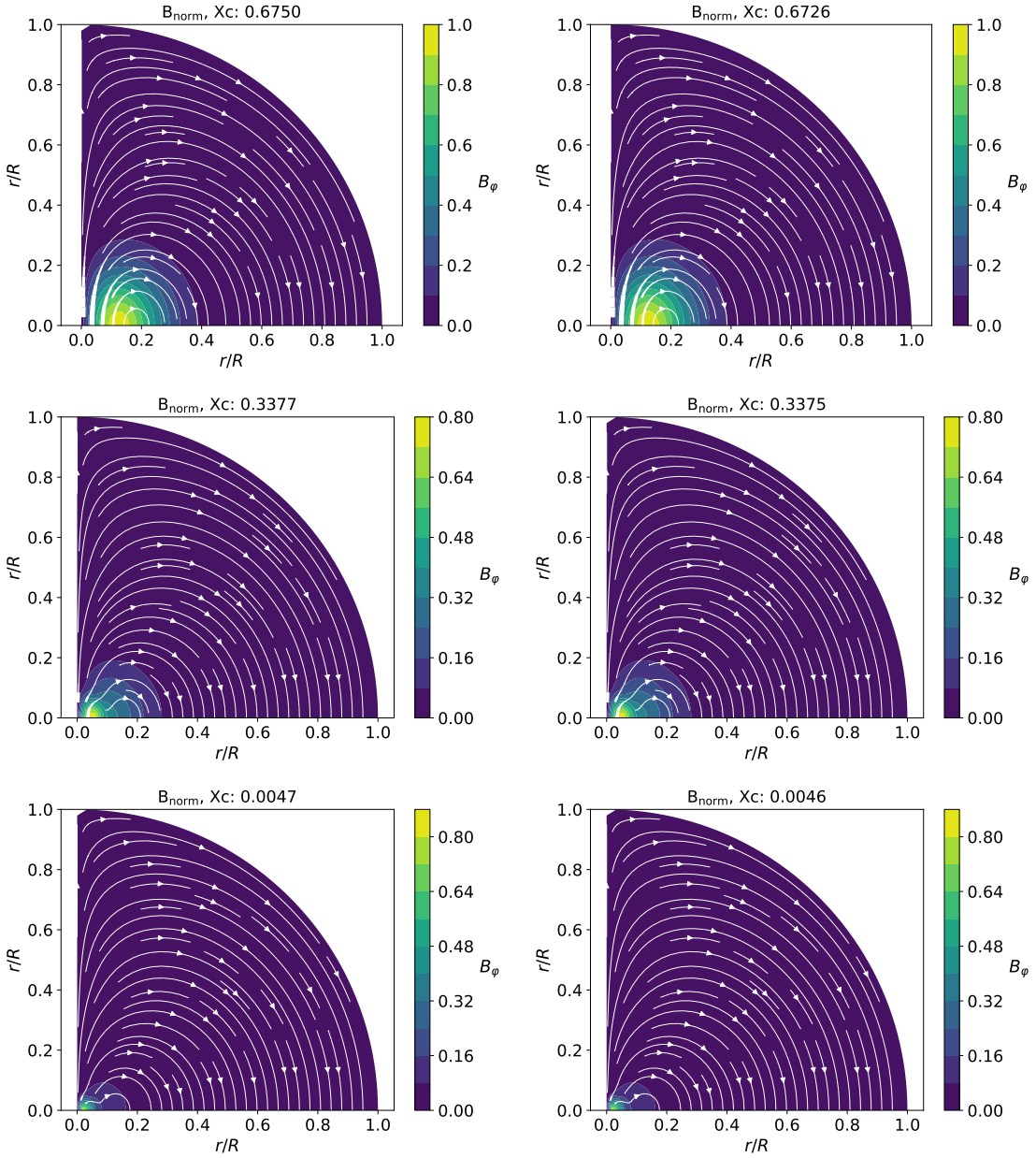

Figure 4.13: *From left to right:* Representation of the normalized magnetic field structure for a $3M_{\odot}$ stellar model, with $D_{mix} = 0.1$ cm^2 s^{-1} (left) and $D_{mix} = 10.0$ cm^2 s^{-1} (right). $f_{\rm ov} = 0.014$, $Z = 0.014$, $\alpha_{\rm MLT} = 1.8$. *From top to down:* ZAMS model ($X_c \approx 0.675$), mid-MS model ($X_c \approx 0.340$), TAMS model ($X_c \approx 0.005$).

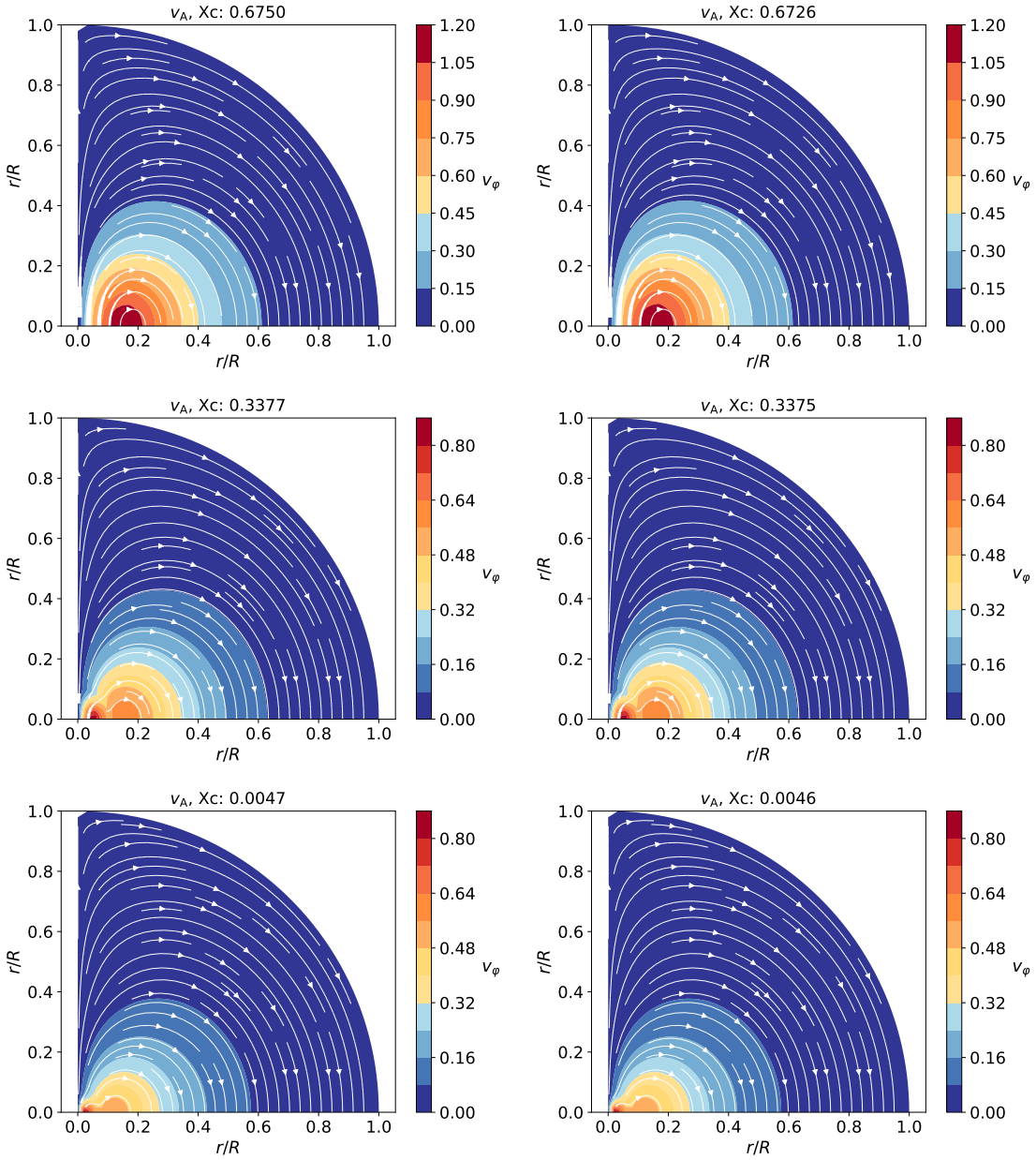

Figure 4.14: *From left to right:* Representation of the normalized Alfvén velocity structure for a $3M_\odot$ stellar model, with $D_{mix} = 0.1$ cm^{2}s^{-1} (left) and $D_{mix} = 10.0$ cm^{2}s^{-1} (right). $f_{\rm ov} = 0.014$, $Z = 0.014$, $\alpha_{\rm MLT} = 1.8$. *From top to down:* ZAMS model ($X_c \approx 0.675$), mid-MS model ($X_c \approx 0.340$), TAMS model ($X_c \approx 0.005$).

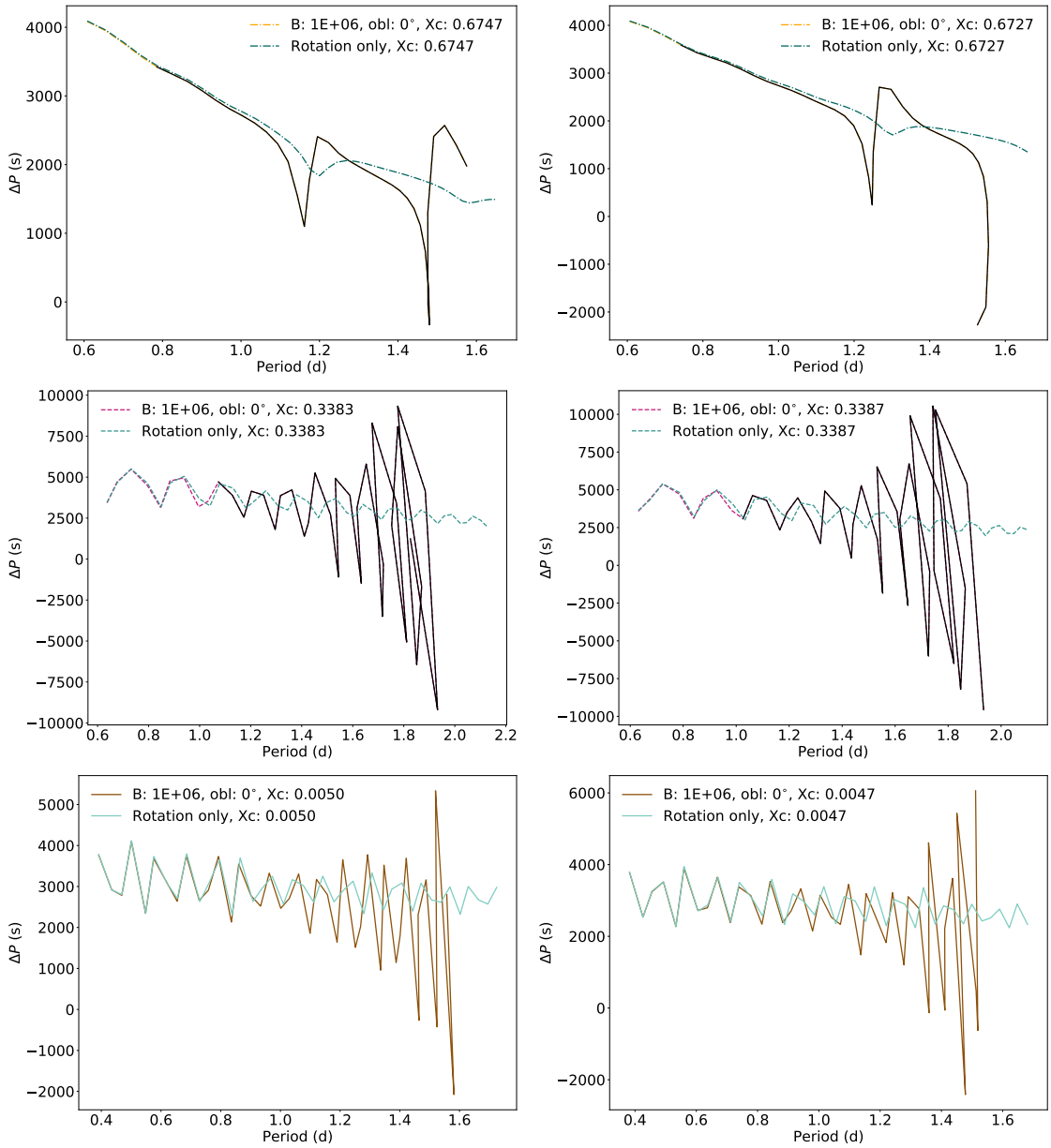

Figure 4.15: *From left to right:* Period spacing patterns for a $3M_{\odot}$ stellar model, at $u = 0.25$, with $\alpha_{\rm MLT} = 1.5$ (left) and $\alpha_{\rm MLT} = 2.0$ (right). $f_{ov} = 0.014$, $Z = 0.014$, $D_{mix} = 1$ cm^{2}s^{-1}, and $\alpha = 10^6$ G. *From top to down:* ZAMS model ($X_c \approx 0.675$), mid-MS model ($X_c \approx 0.340$), TAMS model ($X_c \approx 0.005$). Black parts in the period spacing patterns indicate the same as in Figure (4.7).

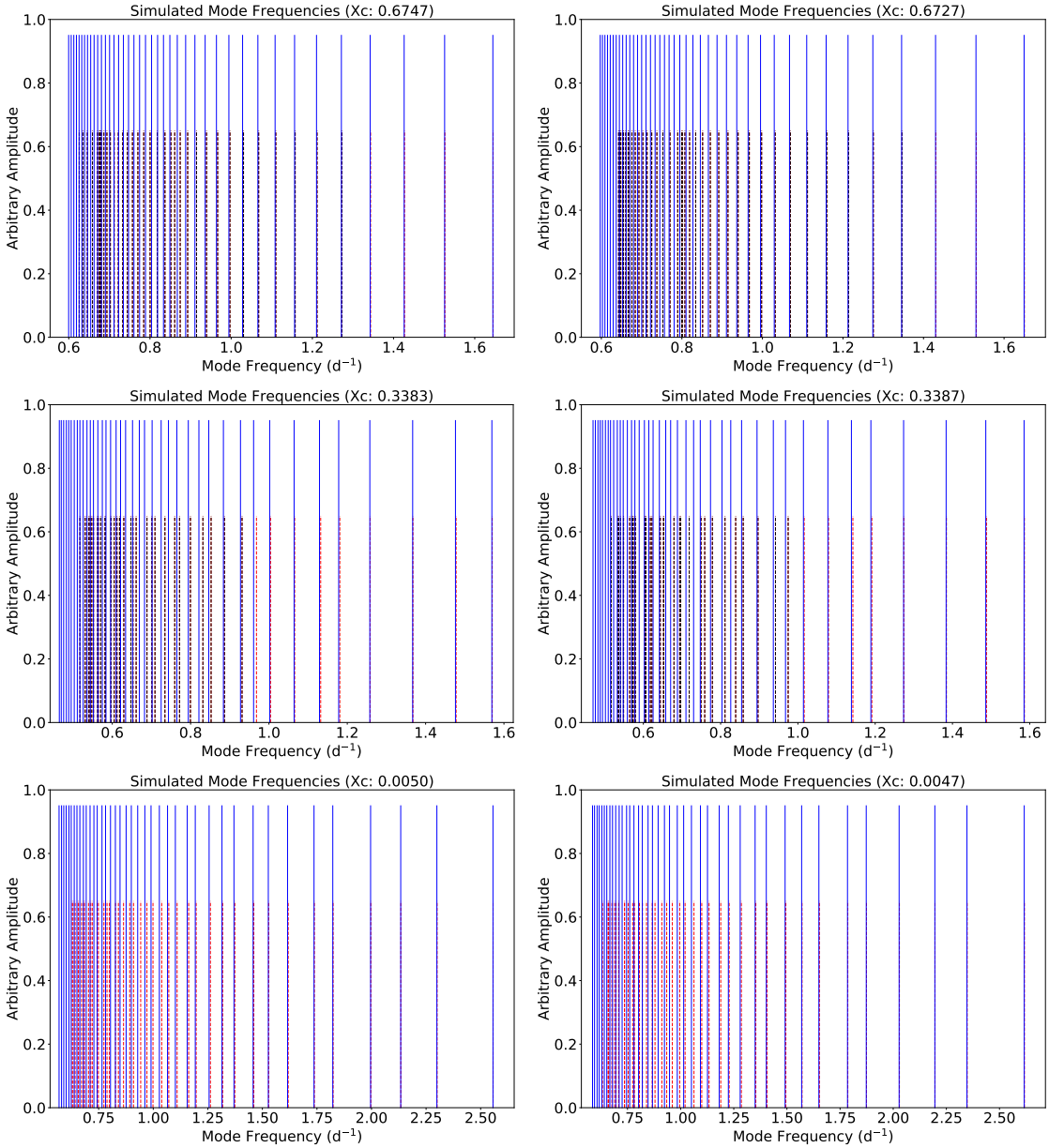

Figure 4.16: *From left to right:* Simulated frequency spectra for a $3M_{\odot}$ star, at $u = 0.25$, with $\alpha_{\rm MLT} = 1.5$ (left) and $\alpha_{\rm MLT} = 2.0$ (right). $f_{\rm ov} = 0.014$, $Z = 0.014$, $D_{mix} = 1$ cm^{2}s^{-1}, and $\alpha = 10^6$ G. *From top to down:* ZAMS model ($X_c \approx 0.675$), mid-MS model ($X_c \approx 0.340$), TAMS model ($X_c \approx 0.005$). Colour code is the same as in Figure (4.8).

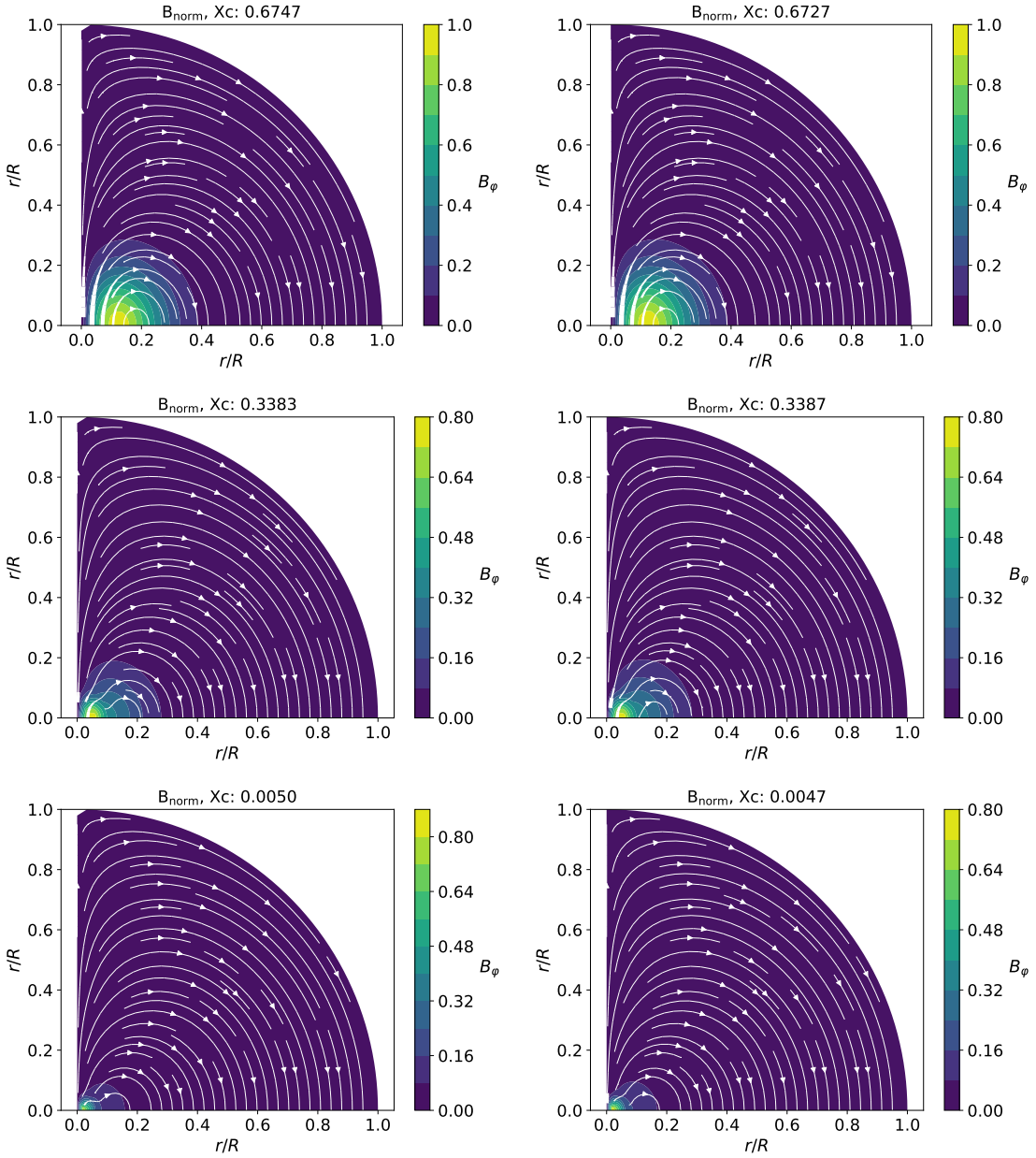

Figure 4.17: *From left to right:* Representation of the normalized magnetic field structure of a $3M_{\odot}$ stellar model, with $\alpha_{\rm MLT} = 1.5$ (left) and $\alpha_{\rm MLT} = 2.0$ (right). $f_{\rm ov} = 0.014$, $Z = 0.014$, $D_{mix} = 1$ cm^{2}s^{-1}. *From top to down:* ZAMS model ($X_c \approx 0.675$), mid-MS model ($X_c \approx 0.340$), TAMS model ($X_c \approx 0.005$).

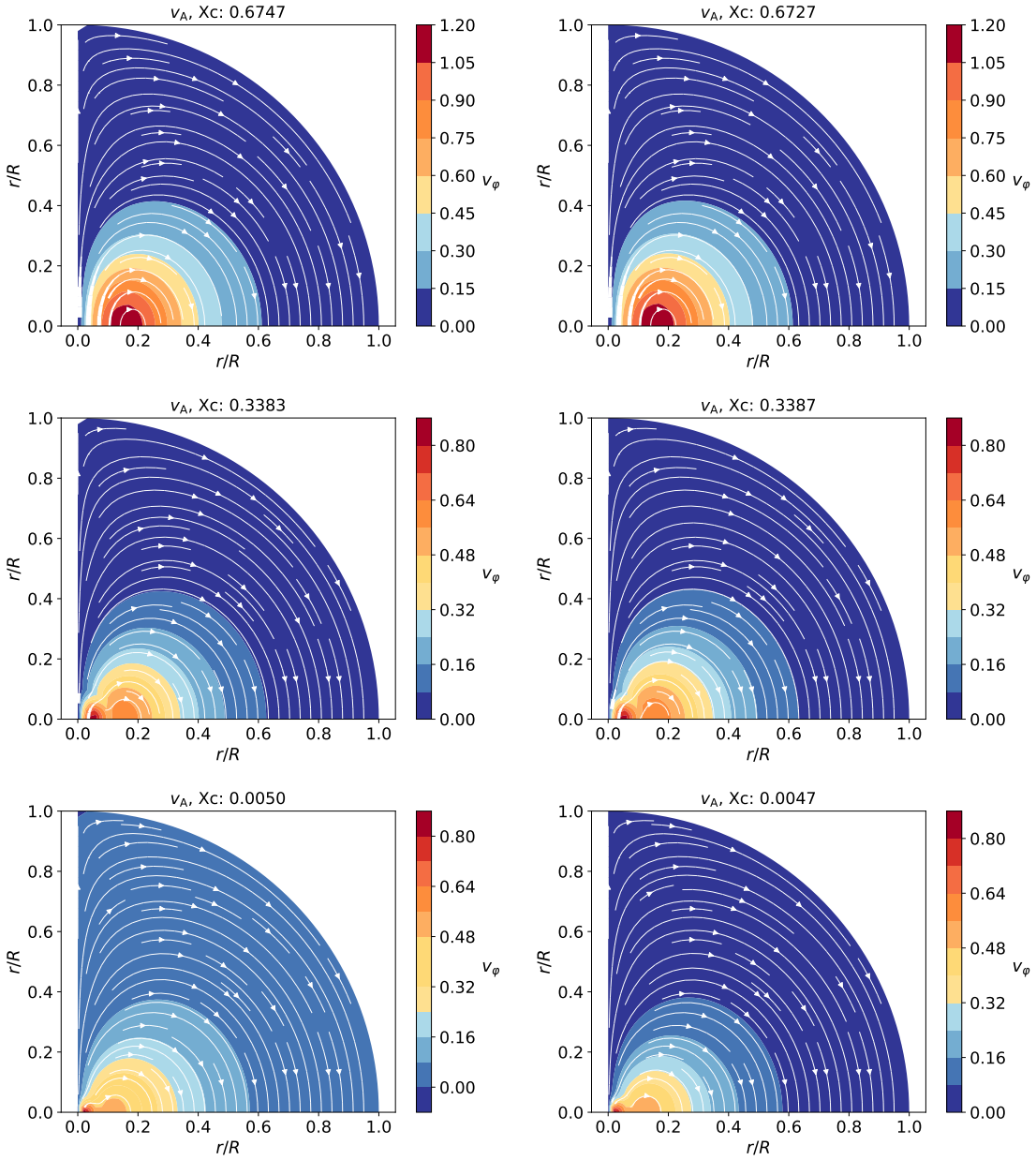

Figure 4.18: *From left to right:* Representation of the normalized Alfvén velocity structure of a $3M_\odot$ stellar model, with $\alpha_{\rm MLT} = 1.5$ (left) and $\alpha_{\rm MLT} = 2.0$ (right). $f_{\rm ov} = 0.014$, $Z = 0.014$, $D_{mix} = 1$ cm^{2}s^{-1}. *From top to down:* ZAMS model ($X_c \approx 0.675$), mid-MS model ($X_c \approx 0.340$), TAMS model ($X_c \approx 0.005$).

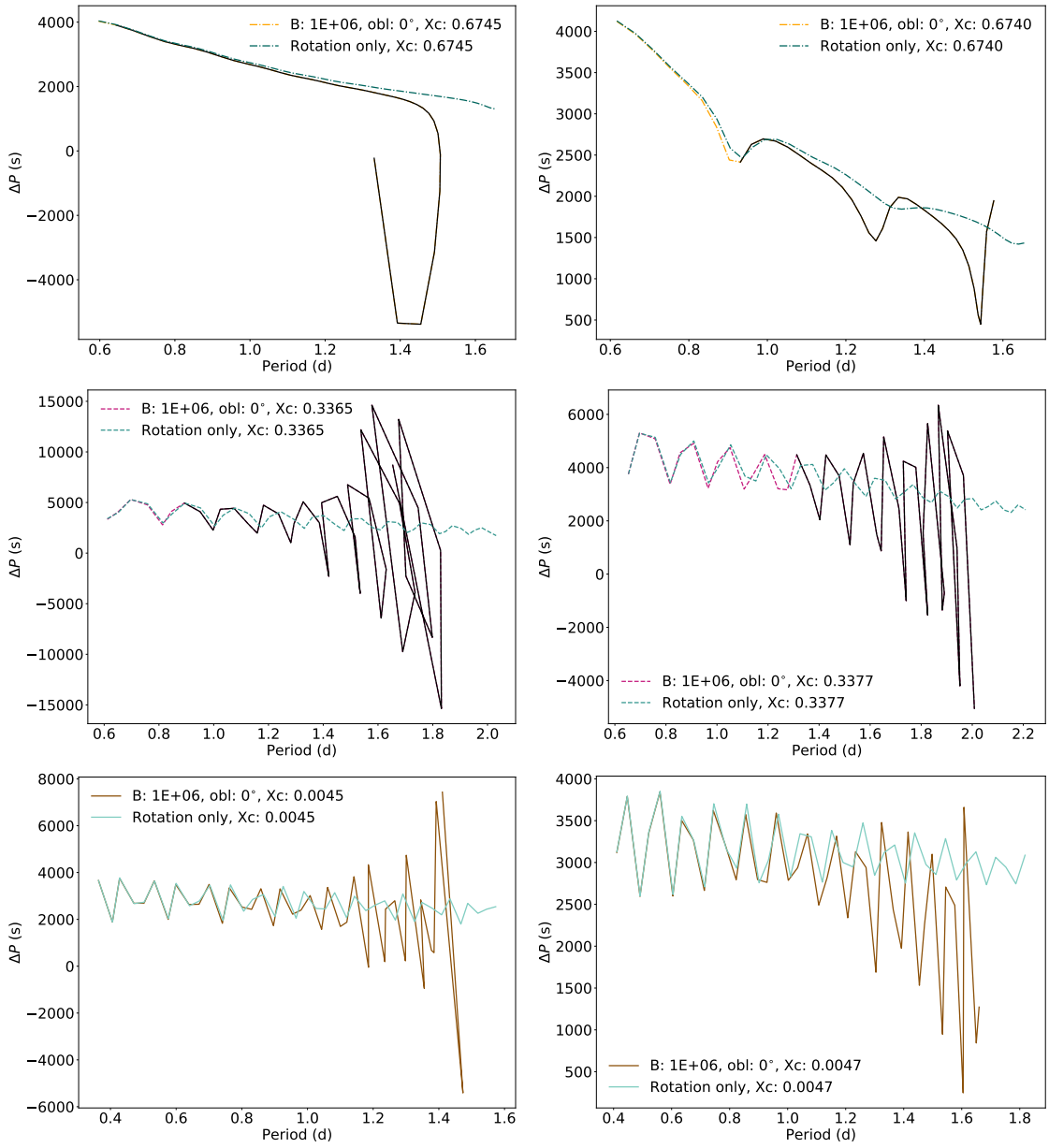

Figure 4.19: *From left to right:* period spacing patterns for a $3M_{\odot}$ stellar model, at $u = 0.25$, with $f_{\rm ov} = 0.004$ (left) and $f_{\rm ov} = 0.024$ (right). $Z = 0.014$, $D_{mix} = 1$ cm^2 s^{-1}, $\alpha_{MLT} = 1.8$. *From top to down:* ZAMS model ($X_c \approx 0.675$), mid-MS model ($X_c \approx 0.340$), TAMS model ($X_c \approx 0.005$). $\alpha = 10^6$ G. Black parts in the period spacing patterns indicate the same as in Figure (4.7).

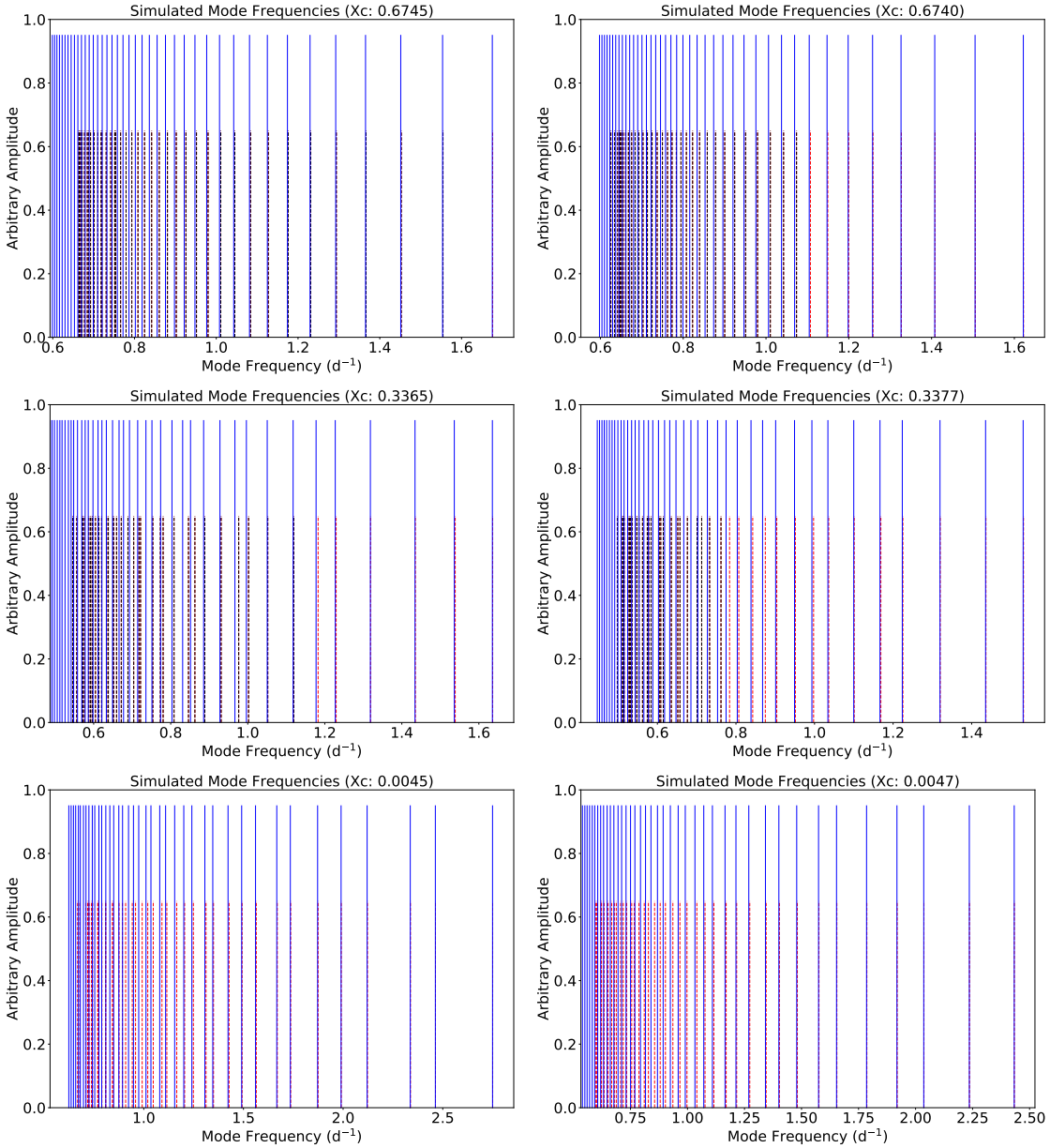

Figure 4.20: *From left to right:* Simulated frequency spectra for a $3M_{\odot}$ stellar model, at $u = 0.25$, with $f_{\rm ov} = 0.004$ (left) and $f_{\rm ov} = 0.024$ (right). $Z = 0.014$, $D_{mix} = 1$ cm^2 s^{-1}, $\alpha_{MLT} = 1.8$, and $\alpha = 10^6$ G. *From top to down:* ZAMS model ($X_c \approx 0.675$), mid-MS model ($X_c \approx 0.340$), TAMS model ($X_c \approx 0.005$). Colour code is the same as in Figure (4.8).

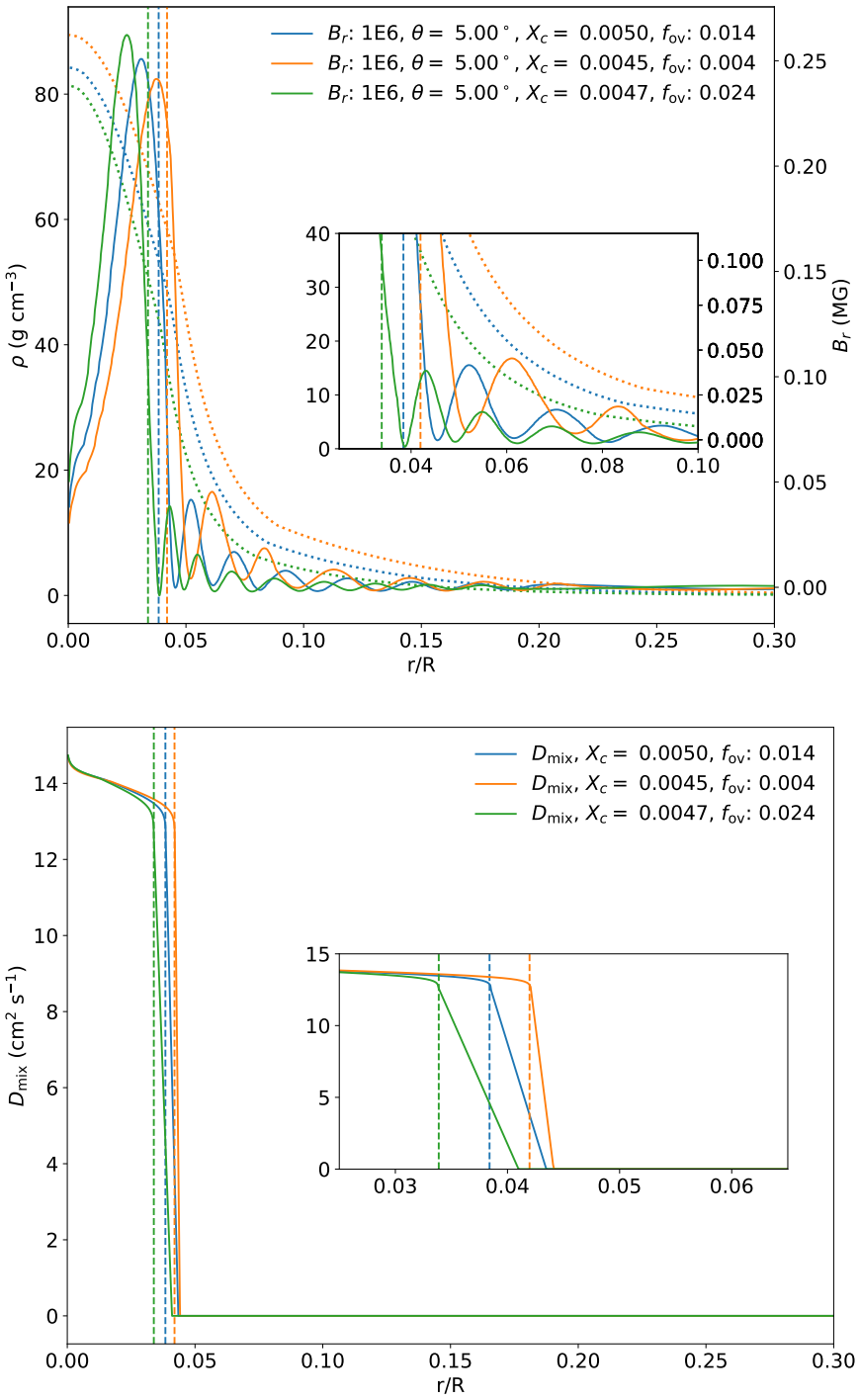

Figure 4.21: *Top:* Density (dotted lines) and radial magnetic field component at $\theta = 5°$ (full line) profile in function of normalized stellar radius for different overshoot parameters f_{ov}, for $\alpha = 10^6$ G at $u = 0.25$, in a 3.00 $M_\odot$ TAMS stellar model with the following fundamental parameters: $D_{mix} = 1.0$ cm^2 s^{-1}, $Z = 0.014$, $\alpha_{MLT} = 1.8$. The dashed vertical lines indicate the locations of the convective core boundary, obtained from the condition $\nabla = \nabla_{ad}$, i.e. the so-called Schwarzschild core boundary (Kippenhahn et al., 2012). *Bottom:* Mixing coefficient profiles (full lines) in function of normalized radius at different values of the overshoot parameter f_{ov} for the same stellar model considered above. Dashed lines indicate the same as in the figure above.

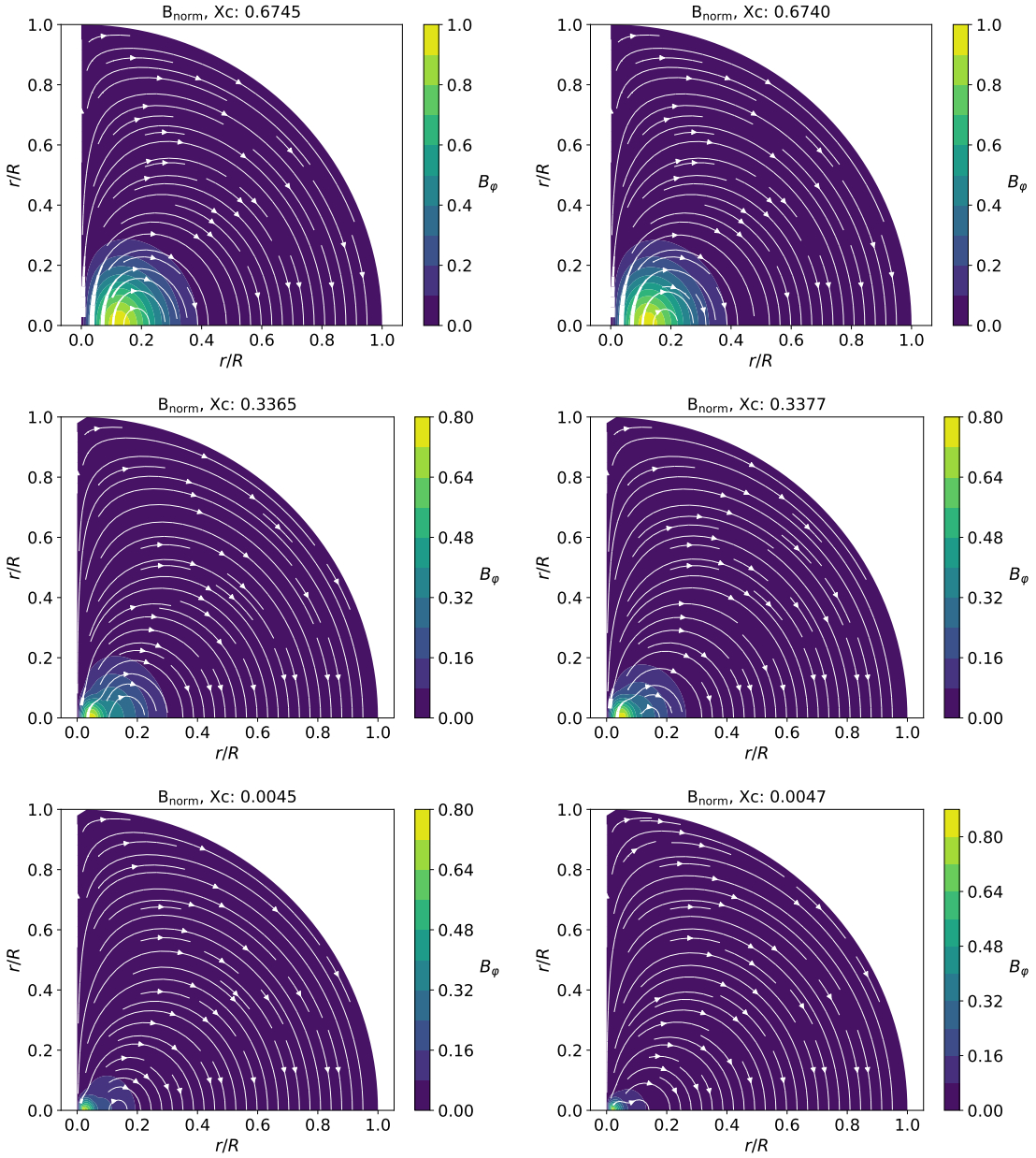

Figure 4.22: *From left to right:* Representation of the normalized magnetic field structure of $3M_{\odot}$ stellar model, with $f_{\rm ov} = 0.004$ (left) and $f_{\rm ov} = 0.024$ (right). $Z = 0.014$, $D_{mix} = 1$ cm^2 s^{-1}, $\alpha_{MLT} = 1.8$. *From top to down:* ZAMS model ($X_c \approx 0.675$), mid-MS model ($X_c \approx 0.340$), TAMS model ($X_c \approx 0.005$).

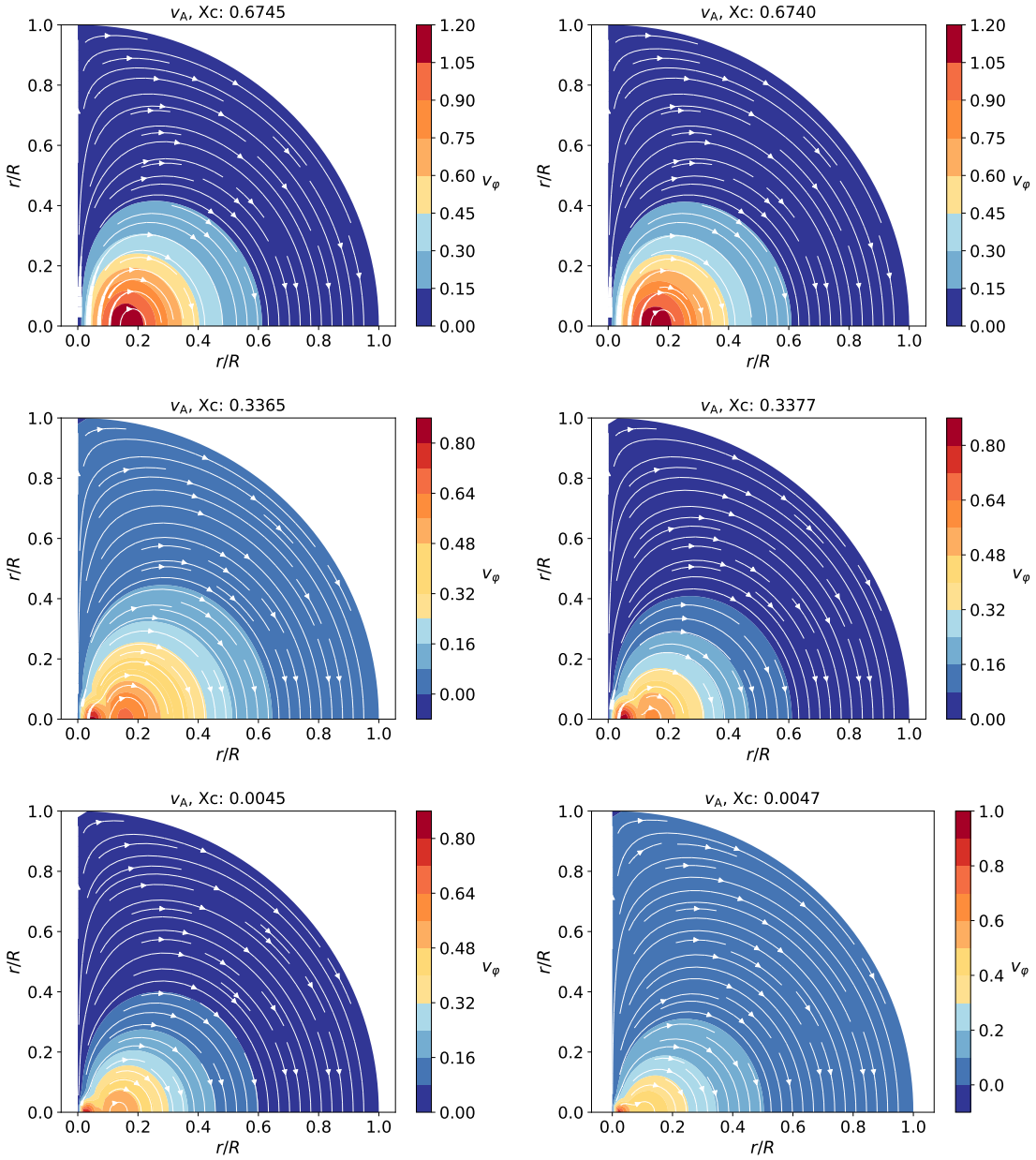

Figure 4.23: *From left to right:* Representation of the normalized Alfvén velocity structure of a $3M_\odot$ stellar model, with $f_{\rm ov} = 0.004$ (left) and $f_{\rm ov} = 0.024$ (right). $Z = 0.014$, $D_{\rm mix} = 1$ cm^{2}s^{-1}, $\alpha_{\rm MLT} = 1.8$. *From top to down:* ZAMS model ($X_c \approx 0.675$), mid-MS model ($X_c \approx 0.340$), TAMS model ($X_c \approx 0.005$).

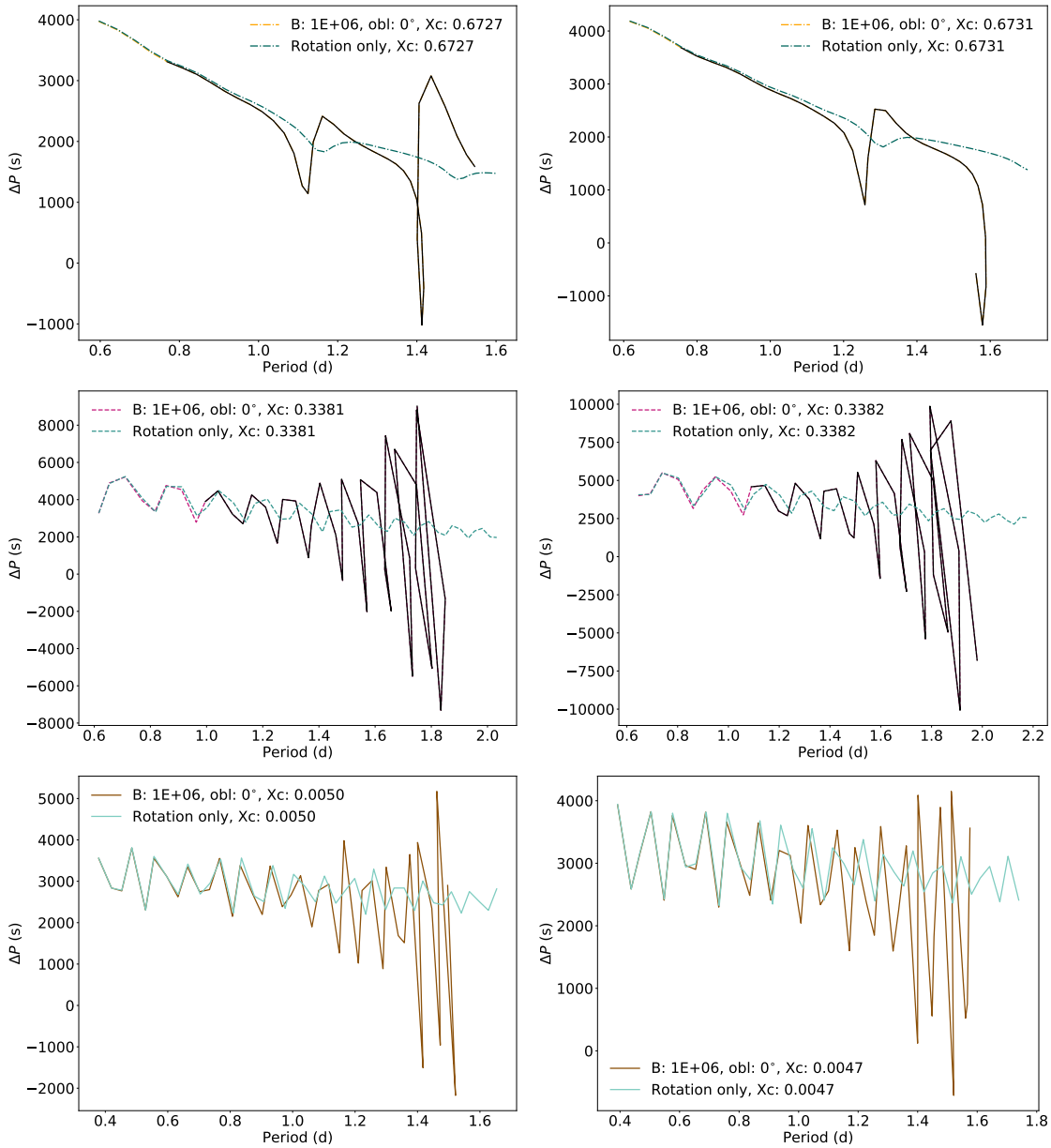

Figure 4.24: *From left to right:* period spacing patterns of a $3M_{\odot}$ stellar model, at $u = 0.25$, with $Z = 0.010$ (left) and $Z = 0.018$ (right). $f_{ov} = 0.014$, $D_{mix} = 1$ cm^{2}s^{-1}, $\alpha_{MLT} = 1.8$, $\alpha = 10^6$ G. *From top to down:* ZAMS model ($X_c \approx 0.675$), mid-MS model ($X_c \approx 0.340$), TAMS model ($X_c \approx 0.005$). Black parts in the period spacing patterns indicate the same as in Figure (4.7).

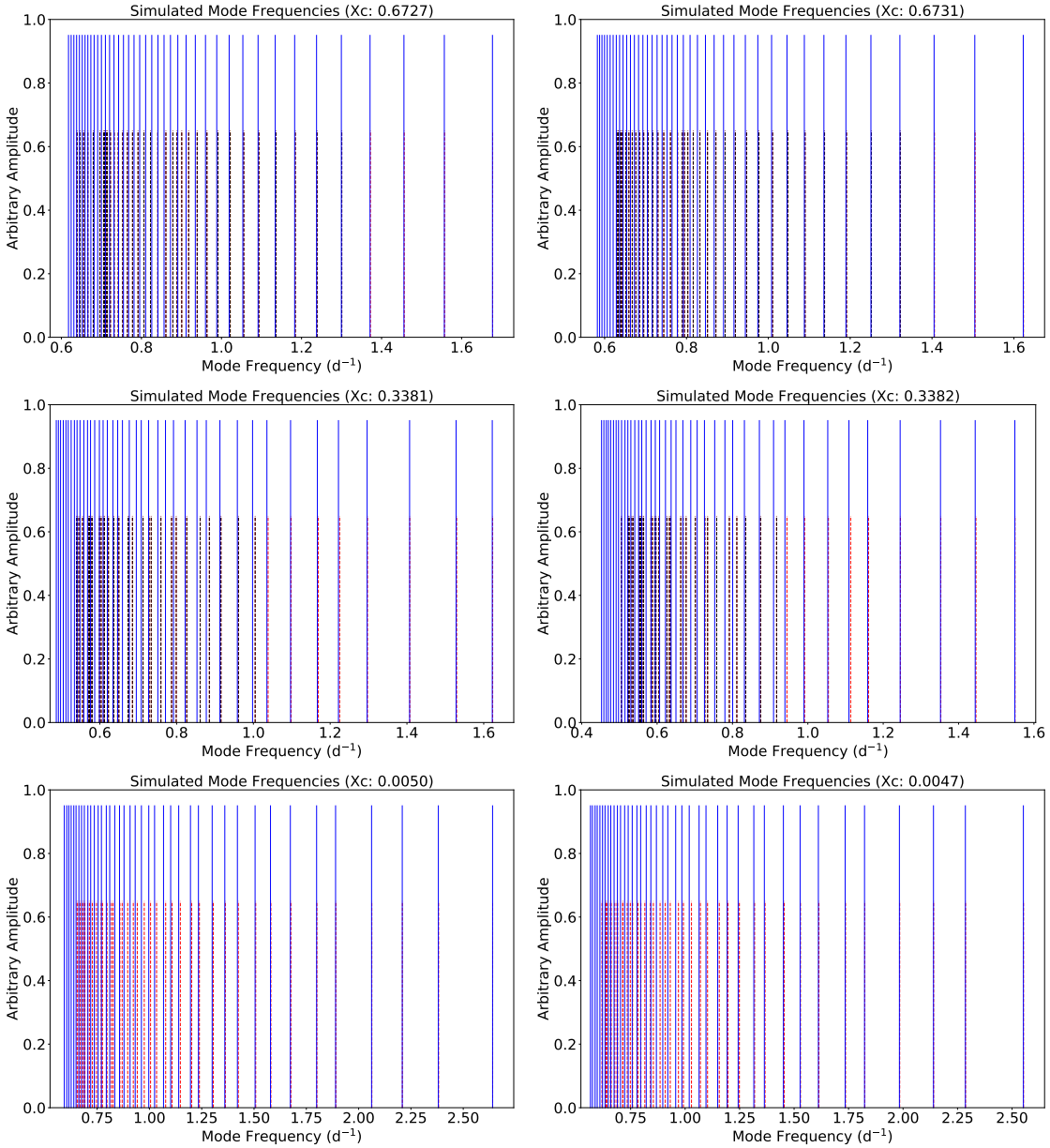

Figure 4.25: *From left to right:* Simulated frequency spectra of a $3M_{\odot}$ stellar model, at $u = 0.25$, with $Z = 0.010$ (left) and $Z = 0.018$ (right). $f_{\rm ov} = 0.014$, $D_{mix} = 1$ cm^{2}s^{-1}, $\alpha_{MLT} = 1.8$, and $\alpha = 10^6$ G. *From top to down:* ZAMS model ($X_c \approx 0.675$), mid-MS model ($X_c \approx 0.340$), TAMS model ($X_c \approx 0.005$). Colour code is the same as in Figure (4.8).

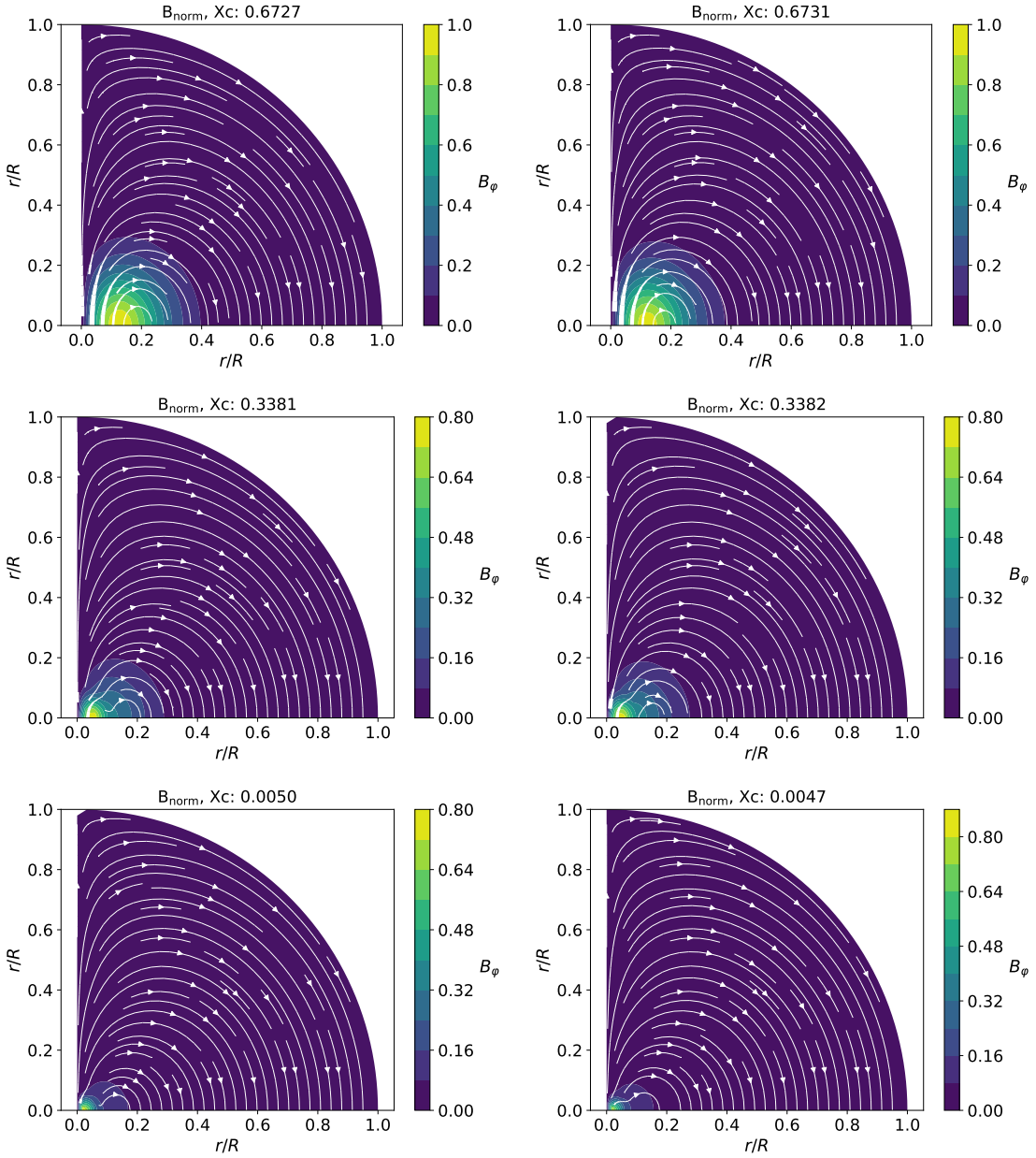

Figure 4.26: *From left to right:* Representation of the normalized magnetic field structure of a $3M_{\odot}$ stellar model, with $Z = 0.010$ (left) and $Z = 0.018$ (right). $f_{\rm ov} = 0.014$, $D_{mix} = 1$ cm^2 s^{-1}, $\alpha_{MLT} = 1.8$. *From top to down:* ZAMS model ($X_c \approx 0.675$), mid-MS model ($X_c \approx 0.340$), TAMS model ($X_c \approx 0.005$).

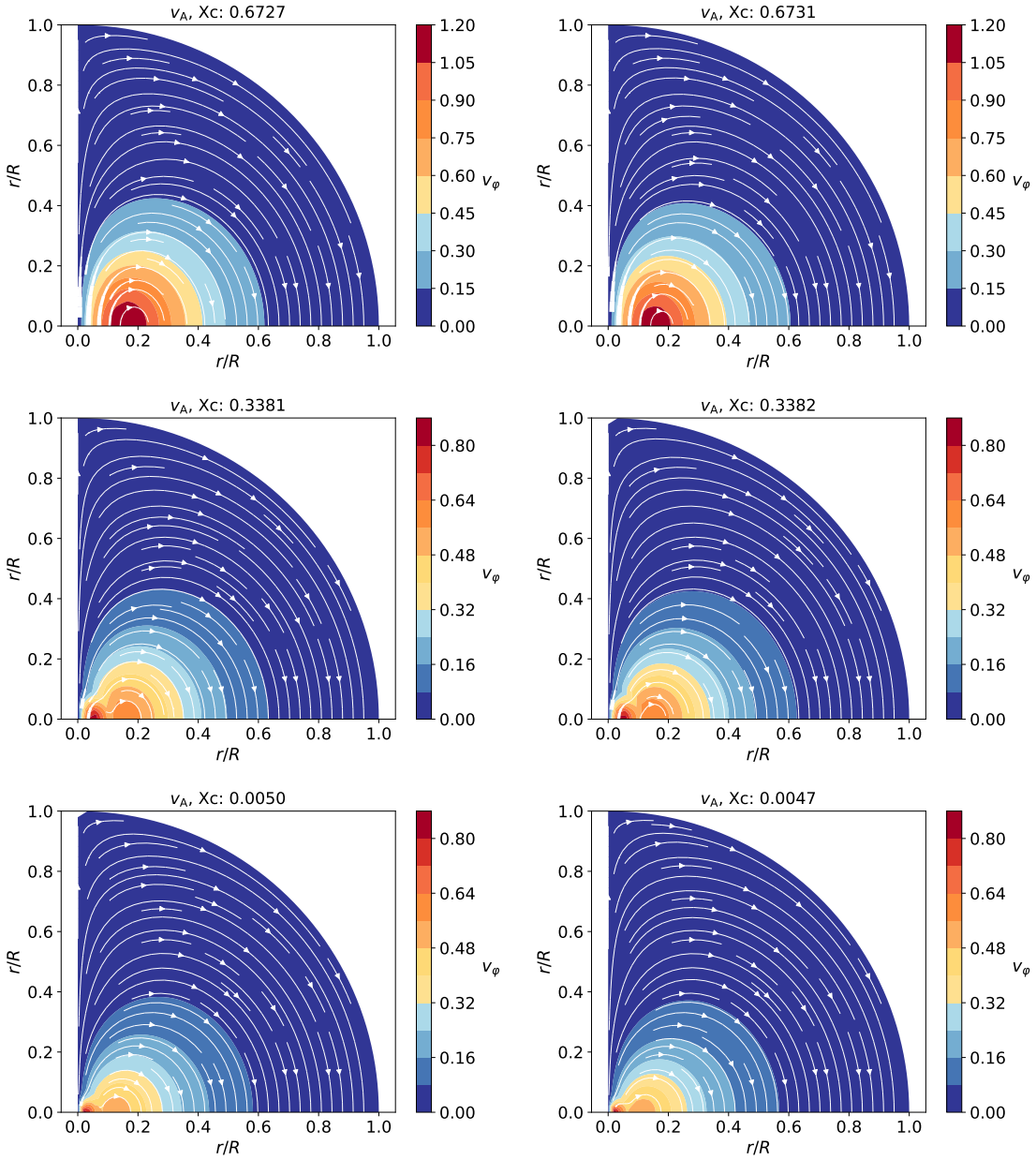

Figure 4.27: *From left to right:* Representation of the normalized Alfvén velocity structure of a $3M_\odot$ stellar model, with $Z = 0.010$ (left) and $Z = 0.018$ (right). $f_{\rm ov} = 0.014$, $D_{mix} = 1$ cm^2 s^{-1}, $\alpha_{MLT} = 1.8$. *From top to down:* ZAMS model ($X_c \approx 0.675$), mid-MS model ($X_c \approx 0.340$), TAMS model ($X_c \approx 0.005$).

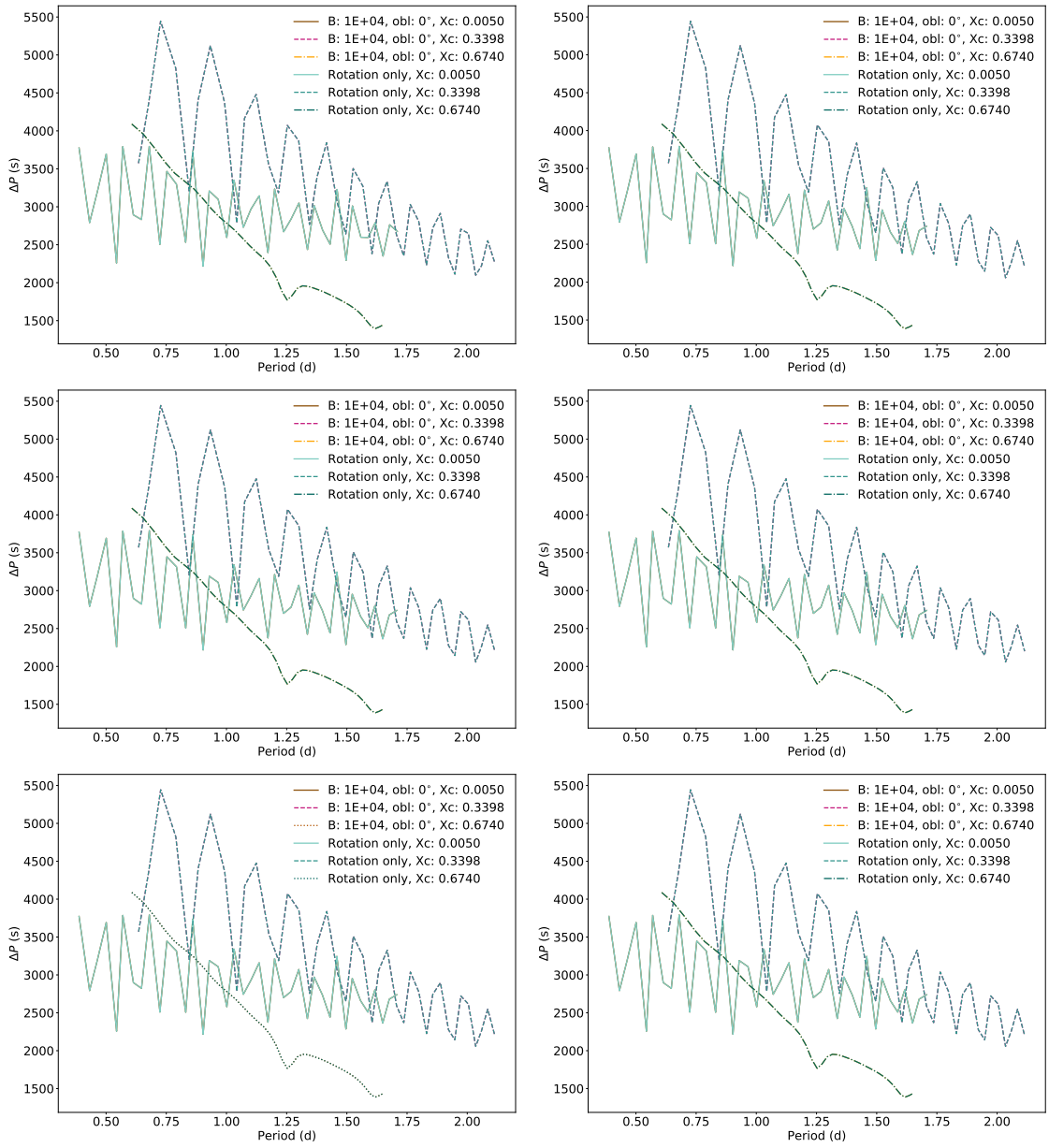

Figure 4.28: Period spacing patterns of a $3M_{\odot}$ stellar model, at $u = 0.25$, with $Z = 0.014$, $f_{ov} = 0.014$, $D_{mix} = 1$ cm^{2}s^{-1}, $\alpha_{MLT} = 1.8$, $\alpha = 10^4$ G. ZAMS model ($X_c \approx 0.675$), mid-MS model ($X_c \approx 0.340$), TAMS model ($X_c \approx 0.005$) are all included. Black parts in the period spacing patterns indicate the same as in Figure (4.7). *From top to down and left to right:* COLLOC_GL2, COLLOC_GL4, COLLOC_GL6, COLLOC_GL2, COLLOC_GL4 (standard setting for this work), and COLLOC_GL6.

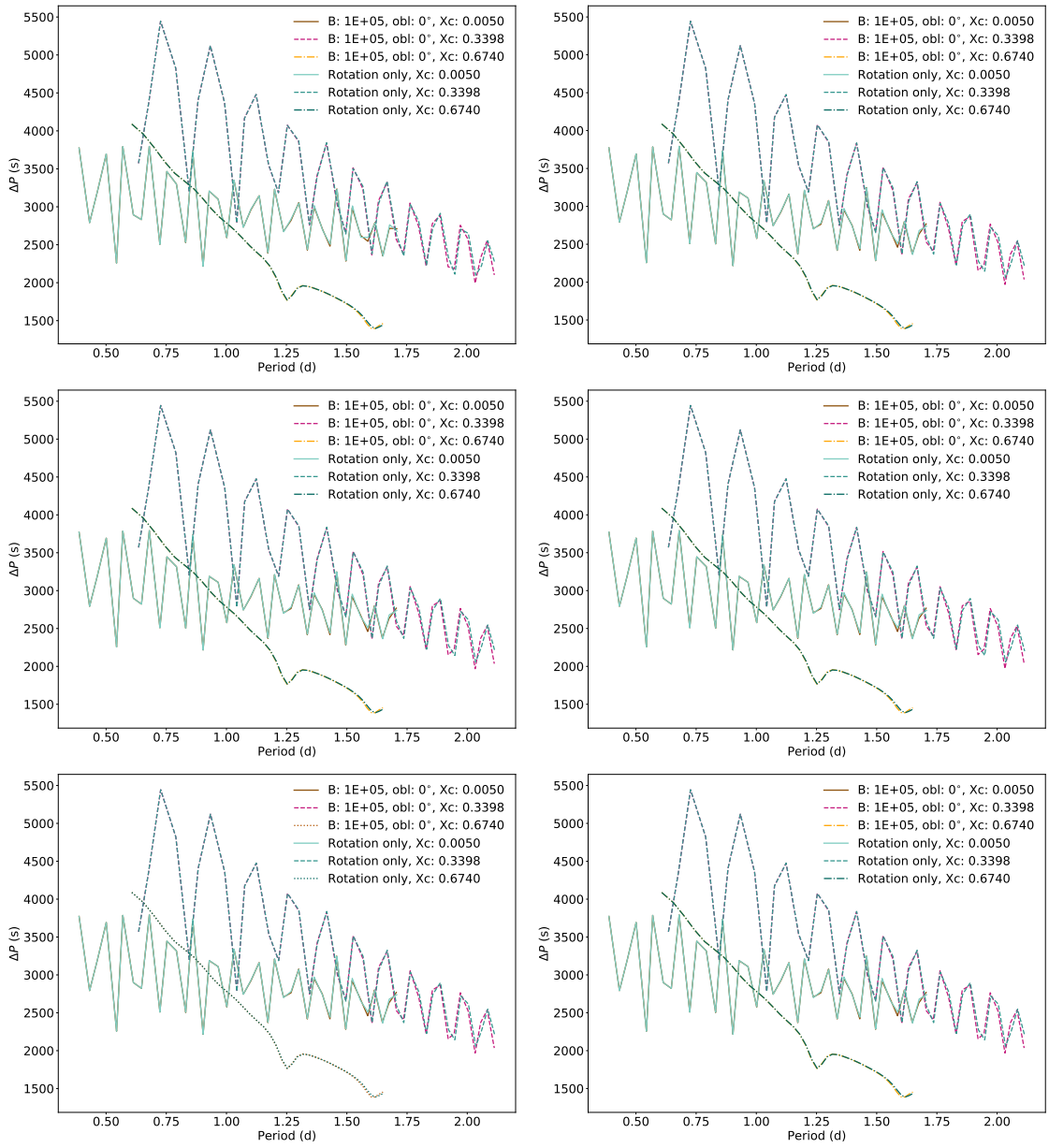

Figure 4.29: Period spacing patterns of a $3M_{\odot}$ stellar model, at $u = 0.25$, with $Z = 0.014$, $f_{ov} = 0.014$, $D_{mix} = 1$ cm^{2}s^{-1}, $\alpha_{MLT} = 1.8$, $\alpha = 10^5$ G. ZAMS model ($X_c \approx 0.675$), mid-MS model ($X_c \approx 0.340$), TAMS model ($X_c \approx 0.005$) are all included. Black parts in the period spacing patterns indicate the same as in Figure (4.7). *From top to down and left to right:* COLLOC_GL2, COLLOC_GL4, COLLOC_GL6, COLLOC_GL2, COLLOC_GL4 (standard setting for this work), and COLLOC_GL6.

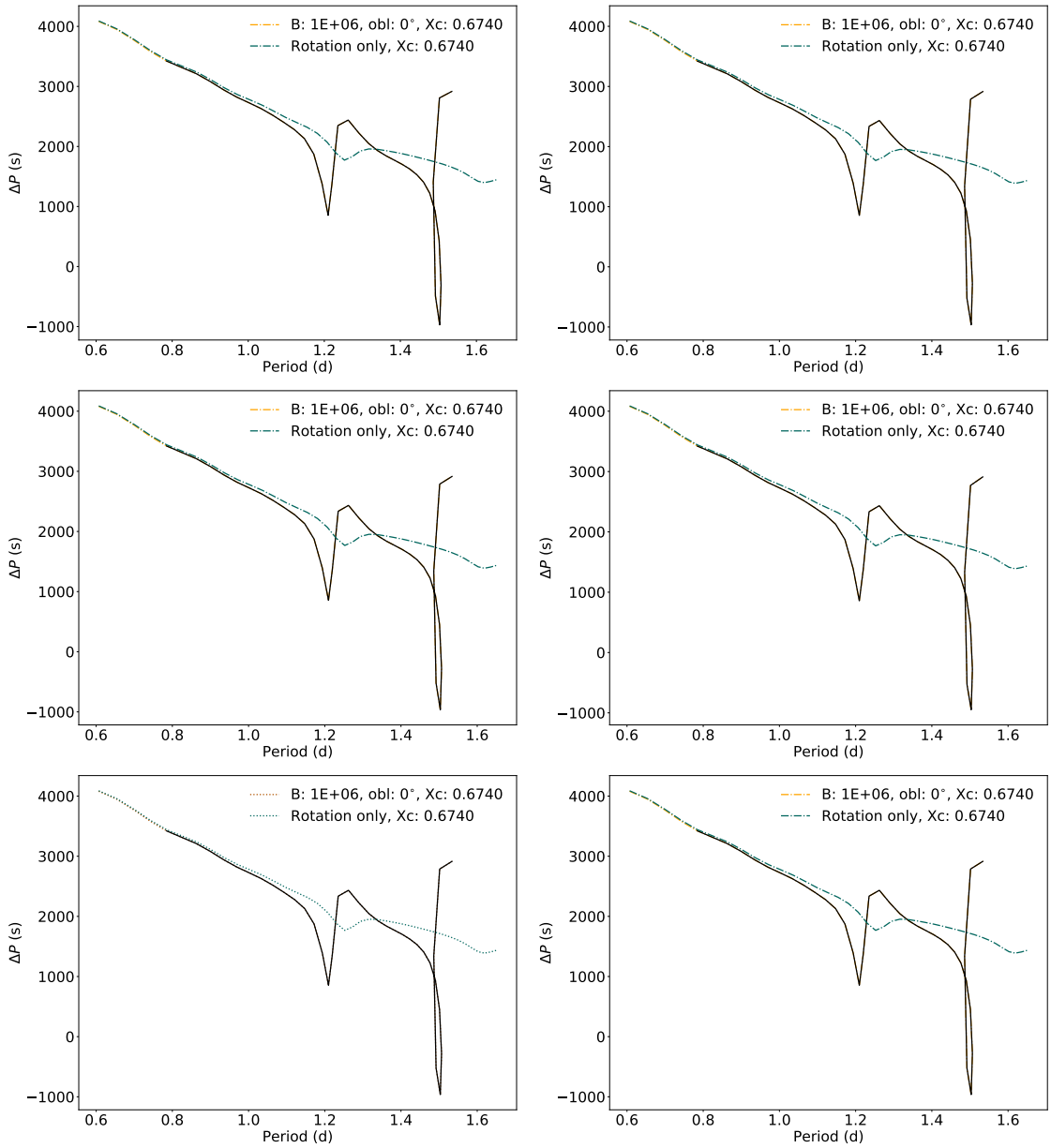

Figure 4.30: Period spacing patterns of a $3M_{\odot}$ stellar model, at $u = 0.25$, with $Z = 0.014$, $f_{ov} = 0.014$, $D_{mix} = 1$ cm^{2}s^{-1}, $\alpha_{MLT} = 1.8$, $\alpha = 10^6$ G. ZAMS model ($X_c \approx 0.675$). Black parts in the period spacing patterns indicate the same as in Figure (4.7). *From top to down and left to right:* COLLOC_GL2, COLLOC_GL4, COLLOC_GL6, COLLOC_GL2, COLLOC_GL4 (standard setting for this work), and COLLOC_GL6.

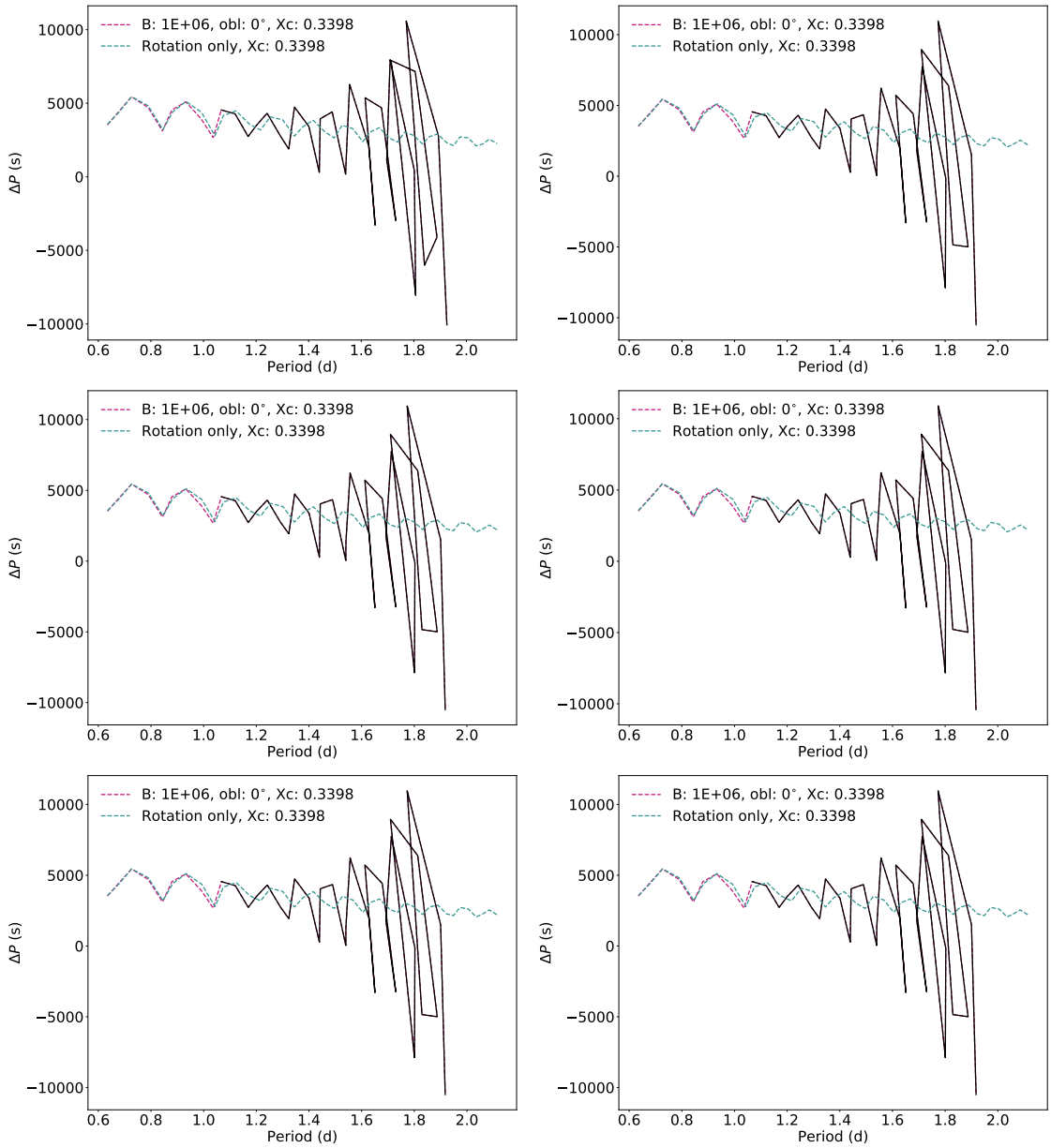

Figure 4.31: Period spacing patterns of a $3M_{\odot}$ stellar model, at $u = 0.25$, with $Z = 0.014$, $f_{ov} = 0.014$, $D_{mix} = 1$ cm^{2}s^{-1}, $\alpha_{MLT} = 1.8$, $\alpha = 10^6$ G. mid-MS model ($X_c \approx 0.3$). Black parts in the period spacing patterns indicate the same as in Figure (4.7). *From top to down and left to right:* COLLOC_GL2, COLLOC_GL4, COLLOC_GL6, COLLOC_GL2, COLLOC_GL4 (standard setting for this work), and COLLOC_GL6.

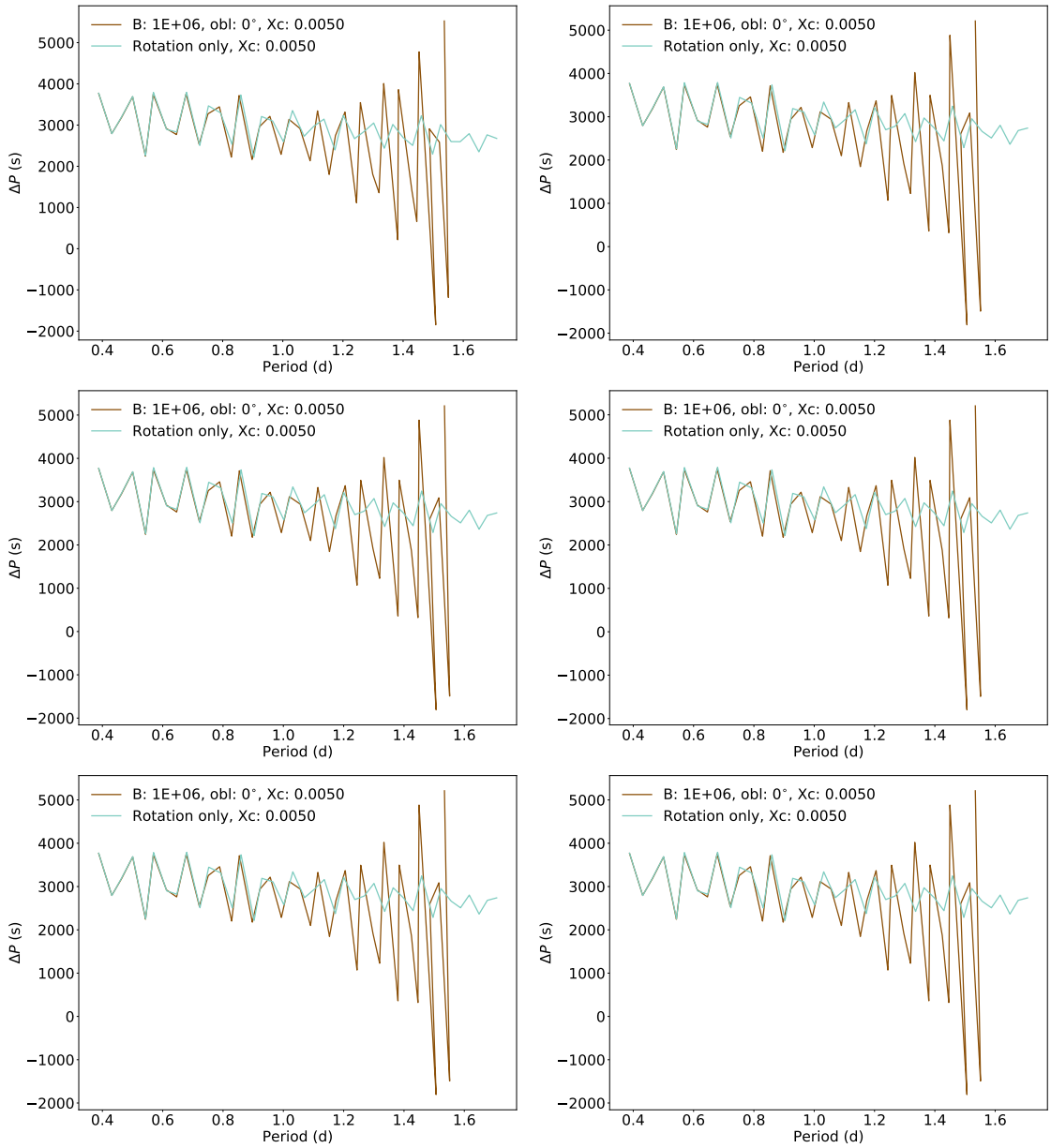

Figure 4.32: Period spacing patterns of a $3M_{\odot}$ stellar model, at $u = 0.25$, with $Z = 0.014$, $f_{ov} = 0.014$, $D_{mix} = 1$ cm^{2}s^{-1}, $\alpha_{MLT} = 1.8$, $\alpha = 10^6$ G. TAMS model ($X_c \approx 0.005$). Black parts in the period spacing patterns indicate the same as in Figure (4.7). *From top to down and left to right:* COLLOC_GL2, COLLOC_GL4, COLLOC_GL6, COLLOC_GL2, COLLOC_GL4 (standard setting for this work), and COLLOC_GL6.

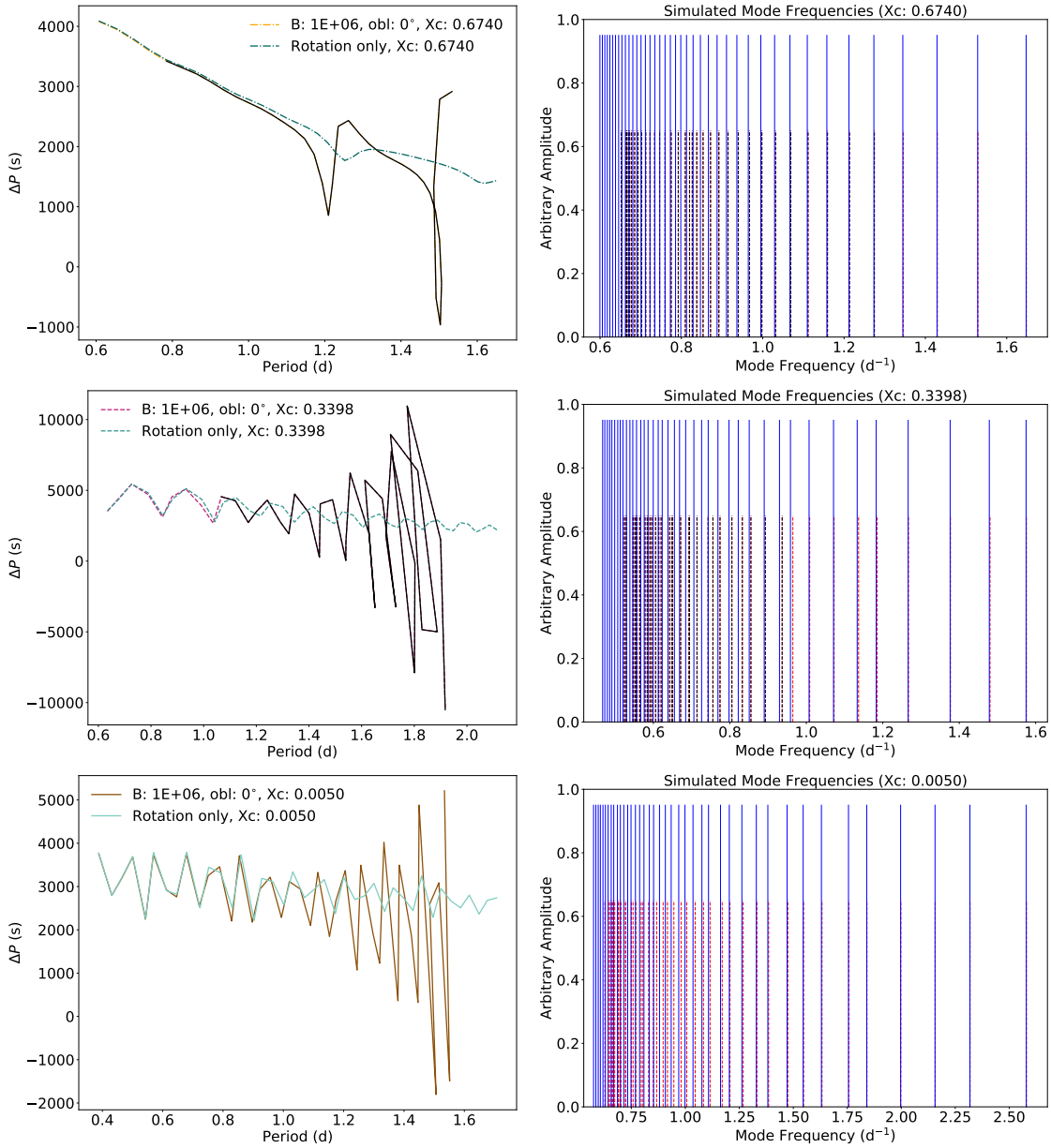

Figure 4.33: Period spacing patterns obtained with the VACUUM outer boundary condition for a $3M_{\odot}$ stellar model, at $u = 0.25$, with $Z = 0.014$, $f_{ov} = 0.014$, $D_{mix} = 1$ cm^{2}s^{-1}, $\alpha_{MLT} = 1.8$, $\alpha = 10^6$ G. Black parts in the period spacing patterns indicate the same as in Figure (4.7). *From left to right:* Period spacing pattern (left), frequency spacing pattern (right). *From top to down:* ZAMS model ($X_c \approx 0.675$), mid-MS model ($X_c \approx 0.340$), TAMS model ($X_c \approx 0.005$)

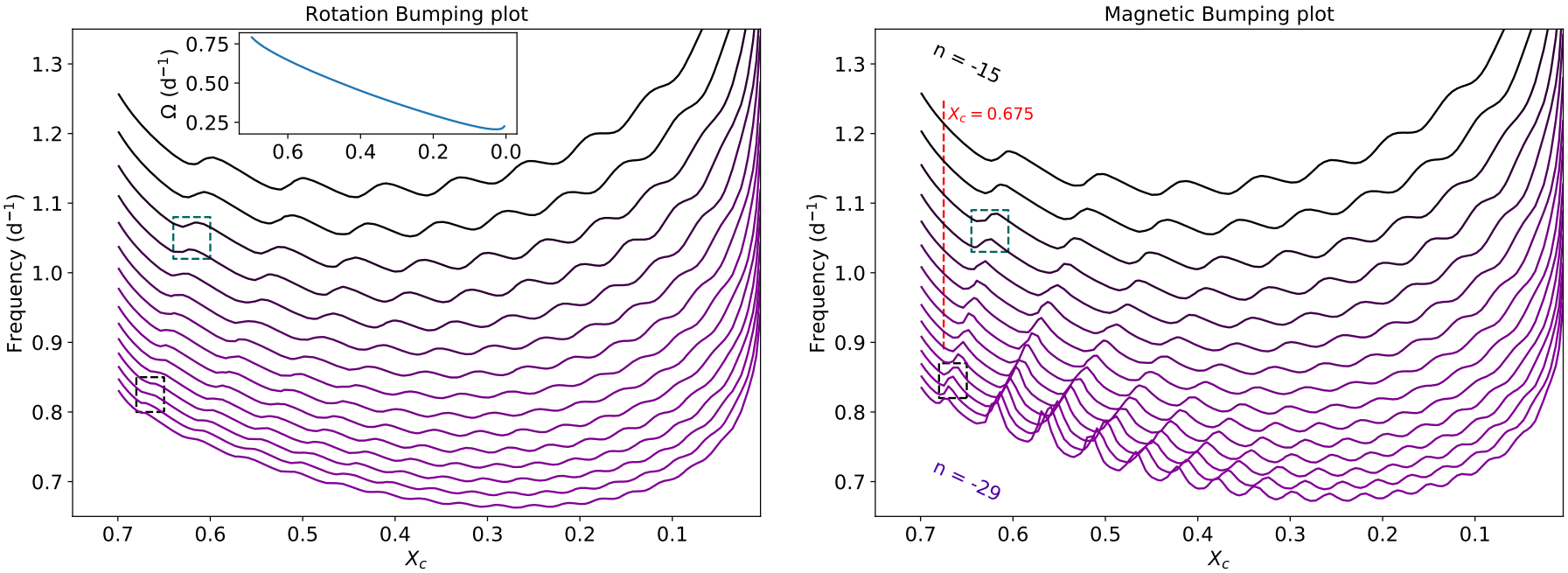

Figure 4.34: 'Classical' mode bumping plot (left) and 'magnetic' mode bumping plot (right) for the $n = -15$ to $n = -29$ g-modes in a 3 $M_\odot$ stellar model, with solar metallicity ($Z = 0.014$), where $f_{\rm ov} = 0.014$, $D_{\rm mix} = 1.0$ cm^2 s^{-1}, $\alpha_{\rm MLT} = 1.8$, $\alpha = 10^6$ G and $u = 0.25$. Black lines denote the evolution of the lower radial order modes, whereas purple lines indicate the evolution of the higher radial order modes considered (as indicated on the 'magnetic' bumping plot). For ease of reference, the red dashed vertical line on the 'magnetic' bumping plot indicates $X_c = 0.675$, the models taken to be indicative of ZAMS stars in the previous section. Since we held u constant, and because the radius of the star evolves throughout the main sequence, the near-core rotation rate Ω considered in GYRE changes. How Ω varies with X_c is shown in the insert on the 'classical' mode bumping plot. The dashed-line boxes indicate specific regions in which the changes in mode interaction due to the magnetic field are clearly visible.

5 — Conclusions and outlook

5.1 Characterizing internal magnetic fields

Internal magnetic fields of stars are poorly characterized, as there is no direct way to observe them. Moreover, the extreme conditions in the near-core region further contribute to the difficulties in characterizing such fields. As shown in Figure (4.1), the assumptions for our formalism hold throughout the entire main-sequence evolution.

We have investigated how the Duez and Mathis (2010) magnetic field model, a poloidal-toroidal, axisymmetric, internal large-scale magnetic fossil field model, affects g mode pulsation frequencies for a rotating (magnetic) star in our formalism (see e.g. Prat et al., 2019) that relies on the Traditional Approximation of Rotation (TAR). From our parameter study, the following conclusions can be drawn:

1. Period spacing patterns of g modes provide an excellent probe of near-core magnetic fields, yielding telltale signs of its presence: a 'sawtooth'-like pattern at higher radial orders, as was already discovered and announced by us in Prat et al. (2019). This contrasts the typical dips that occur due to mode trapping caused by a μ-gradient left behind in the near-core region by the shrinking convective core throughout the main-sequence evolution (Miglio et al., 2008). Some observed stars do exhibit gravity modes with appropriate radial orders down to -50 (see Van Reeth et al. (2015) for examples of F-type stars, which can exhibit detected patterns up to radial orders -100, and see Pápics et al. (2017) for examples of B-type stars). In the future, we plan to investigate how more sophisticated magnetic field models will fare in explaining pulsation mode frequencies.

2. No magnetic influence on period spacing patterns is observed for field models with maximum field strengths $\alpha = 10^4$ G. Only slight shifts are obtained for $\alpha = 10^5$ G, whereas large shifts can be observed for models for which $\alpha = 10^6$ G.

3. Increasing the near-core rotation rate decreases magnetic signatures, as was already found by Prat et al. (2019). Therefore it is crucial to take into account rotation when calculating magnetic shifts. If the shifts are small, rotation can be problematic for detection. However, for the large strength magnetic field, it can aid our cause, as it will allow more modes to be well described by our perturbative formalism.

4. Both 'classical' and 'magnetic' mode bumping can affect mode identification of g modes throughout the main sequence, as depicted in Figure (4.34).

5. The size of the strongly magnetic patch in the magnetic field structure, where the normalized field strength $\boldsymbol{B}_{\rm norm} \simeq 1$, changes in terms of evolutionary stage for the reference model: $r_{\rm B,ZAMS} > r_{\rm B,TAMS}$, where $r_{\rm B,i}$ denotes the radius of the strongly magnetic patch in a specific evolution stage i.

6. In order to conceptualize the effect of the magnetic field on the pulsations, the effect of the different stellar parameters on the density profile was analyzed. This density profile is the only necessary input for the Duez and Mathis (2010) field. Most striking are the deviations from the rotational period spacing pattern slope in case of high mixing levels.

7. Many of the ZAMS pulsation frequencies do not adhere to our newly derived validity criterion (Equation (3.33)), although more valid modes become 'available' when considering higher rotation rates. Small frequency shifts may be visible in *Kepler* data of g-mode pulsators. All of the frequencies of the TAMS star pulsation modes are valid according to our criterion.

8. Trapped modes (in the near-core region) are predominantly affected by the magnetic field, causing the signature μ-gradient dips to drastically change. In ZAMS stars, such dips should (almost) not be present. However, Mombarg et al. (2019) found such dips in their patterns. Our model grid seems to be in agreement with Mombarg et al. (2019), since we also observe (a few) μ-gradient dips for our ZAMS models.

9. In line with Townsend and Teitler (2013) the different solvers do not change the period spacing pattern. They might result in slightly different frequencies, but the effect is minimal. Changing the outer boundary condition to VACUUM in GYRE does not yield appreciable changes when compared to our standard boundary condition: UNNO.

5.2 Revisiting the Fuller et al. (2015) model

Fuller et al. (2015) conjectured that so-called 'missing' mixed modes observed in approximately one quarter of *Kepler* red giants could be attributed to the presence of a strong internal magnetic field (see Section (1.2) and Mosser et al. (2012a)).

This work provides the basis of future work that will assess the viability of the Fuller et al. (2015) origin. It provides us with a first outlook on the detectability of the magnetic fields deep inside the red giant progenitors: intermediate-mass main-sequence stars that should harbour strong internal magnetic fields. As depicted by Stello et al. (2016), the range of magnetic field strengths inside red giants is $10^4 - 3 * 10^6$ G. Cantiello et al. (2016) translated such field strengths to dynamo field strengths on the main sequence, ranging from $10^4 - 10^5$ G for F-type stars. It is clear from our results that it will be (very) difficult to characterize internal fields of such field strength from period spacing patterns of g modes in γ Dor stars. Note, however, that Augustson et al. (2016) managed to reach field strengths up to 10^6 G within their 3D simulations of core convection in massive B-type stars. This issues hope, as mega-Gauss fields can potentially be used to constrain the internal field of a B-type star from its period spacing patterns, if its fundamental parameters and rotation rate are known from asteroseismology. To achieve this, we will have

to await more general modelling of the magnetic field in terms of magnetic field geometry and perturbation.

5.3 Outlook

Several near-future projects are planned to further strengthen (or disprove) the results obtained in this work. A more sophisticated axisymmetric, oblique (i.e. inclined with respect to the rotation axis) magnetic field model will become available soon (Prat et al., in preparation). Fields that are not confined to the stellar interior should follow later, taking into account that density becomes small at the surface, invalidating the perturbative formalism locally (Bigot et al., 2000). This could be remedied by a non-perturbative treatment of the magnetic field, which would allow us to better describe very strong internal fields as well (Morsink and Rezania, 2002). Ultimately, this should be extended to a fully non-axisymmetric, 3D magnetic field model, which can then be used to provide accurate constraints on fundamental stellar parameters and model fields generated by dynamos (e.g. Augustson et al., 2016). As we found in Chapter (4), such a model might help us constrain the degree of core boundary mixing, which can lengthen the lifetime of stellar models efficiently (Pedersen et al., 2018).

The extension of this formalism to more commonly observed prograde g modes, seems promising, as it will possibly allow us to use multiple detected (prograde) patterns to characterize the magnetic field. We (Prat et al., 2019) already showed that the magnetic shift for prograde modes is smaller than the shift for zonal modes. However, if these shifts are detectable for multiple patterns, they will provide a strong diagnostic. Moreover, as noted by Saio et al. (2018), some intermediate-mass main-sequence stars rotate rapidly enough to generate Rossby modes. The influence of an internal magnetic field on such modes has not yet been thoroughly studied.

We only consider a fixed u when investigating mode bumping in Figure (4.34), leading to a near-core rotation rate of the stellar (pulsation) model that varies throughout the MS evolution in a specific way. It should be investigated (in the near future) how a different near-core rotation rate profile affects mode bumping, e.g. the profile obtained if one assumes constant stellar angular momentum, defined by $M\ \Omega\ R^2$ (Aerts et al., 2019), throughout main-sequence evolution.

Verifying the validity of the TAR in the considered regime and the inherent assumption of a weak field can further be tested by two-dimensional computations of modes in oscillation codes such as TOP (Reese et al., 2006) or ACOR (Ouazzani et al., 2012). However, such codes do not currently take into account the magnetic field. Another application of such codes would be to apply our perturbative theory to g modes computed in centrifugally deformed stars.

Another way to further generalize this work is to include the effects of differential rotation. A full treatment of differential rotation would likely render the present formalism unusable, as noted by Prat et al. (2019). However, because non-axisymmetric magnetic fields are known to inhibit differential rotation (e.g. Moss, 1992; Spruit, 1999), a perturbative treatment of differential rotation could be sufficient.

Bibliography

M. Abramowitz and I. A. Stegun. *Handbook of Mathematical Functions*. 1972.

C. Aerts, J. Christensen-Dalsgaard, and D. W. Kurtz. *Asteroseismology, Astronomy and Astrophysics Library*. Springer-Verlag, Heidelberg, 2010.

C. Aerts, G. Molenberghs, M. G. Kenward, and C. Neiner. The Surface Nitrogen Abundance of a Massive Star in Relation to its Oscillations, Rotation, and Magnetic Field. *The Astrophysical Journal*, 781:88, Feb 2014. doi: 10.1088/0004-637X/781/2/88.

C. Aerts, G. Molenberghs, M. Michielsen, M. G. Pedersen, R. Björklund, C. Johnston, J. S. G. Mombarg, D. M. Bowman, B. Buysschaert, P. I. Pápics, S. Sekaran, J. O. Sundqvist, A. Tkachenko, K. Truyaert, T. Van Reeth, and E. Vermeyen. Forward Asteroseismic Modeling of Stars with a Convective Core from Gravity-mode Oscillations: Parameter Estimation and Stellar Model Selection. *The Astrophysical Journal Supplement Series*, 237:15, Jul 2018. doi: 10.3847/1538-4365/aaccfb.

C. Aerts, S. Mathis, and T. M. Rogers. Angular momentum transport in stellar interiors. *Annual Review of Astronomy and Astrophysics*, 57(1):35–78, 2019. doi: 10.1146/annurev-astro-091918-104359. URL https://doi.org/10.1146/annurev-astro-091918-104359.

M. Aizenman, P. Smeyers, and A. Weigert. Avoided Crossing of Modes of Non-radial Stellar Oscillations. *Astronomy and Astrophysics*, 58:41, June 1977.

P. J. Armitage. *Astrophysics of Planet Formation*. Cambridge University Press, 2010.

M. Asplund, N. Grevesse, A. J. Sauval, and P. Scott. The Chemical Composition of the Sun. *Annual Review of Astronomy & Astrophysics*, 47(1):481–522, Sep 2009. doi: 10.1146/annurev.astro.46.060407.145222.

K. C. Augustson, A. S. Brun, and J. Toomre. The Magnetic Furnace: Intense Core Dynamos in B Stars. *The Astrophysical Journal*, 829(2):92, Oct 2016. doi: 10.3847/0004-637X/829/2/92.

M. Aurière, G. A. Wade, J. Silvester, F. Lignières, S. Bagnulo, K. Bale, B. Dintrans, J. F. Donati, C. P. Folsom, M. Gruberbauer, A. Hui Bon Hoa, S. Jeffers, N. Johnson, J. D. Landstreet, A. Lèbre, T. Lueftinger, S. Marsden, D. Mouillet, S. Naseri, F. Paletou, P. Petit, J. Power, F. Rincon, S. Strasser, and N. Toqué. Weak magnetic fields in Ap/Bp stars. Evidence for a dipole field lower limit and a

tentative interpretation of the magnetic dichotomy. *Astronomy and Astrophysics*, 475(3):1053–1065, Dec 2007. doi: 10.1051/0004-6361:20078189.

J. Ballot, F. Lignières, D. R. Reese, and M. Rieutord. Gravity modes in rapidly rotating stars. Limits of perturbative methods. *Astronomy and Astrophysics*, 518: A30, Jul 2010. doi: 10.1051/0004-6361/201014426.

G. Barnes, K. B. MacGregor, and P. Charbonneau. Gravity Waves in a Magnetized Shear Layer. *The Astrophysical Journal*, 498:L169–L172, May 1998. doi: 10.1086/311328.

T. R. Bedding, B. Mosser, D. Huber, J. Montalbán, P. Beck, J. Christensen-Dalsgaard, Y. P. Elsworth, R. A. García, A. Miglio, D. Stello, T. R. White, J. De Ridder, S. Hekker, C. Aerts, C. Barban, K. Belkacem, A.-M. Broomhall, T. M. Brown, D. L. Buzasi, F. Carrier, W. J. Chaplin, M. P. di Mauro, M.-A. Dupret, S. Frandsen, R. L. Gilliland, M.-J. Goupil, J. M. Jenkins, T. Kallinger, S. Kawaler, H. Kjeldsen, S. Mathur, A. Noels, V. Silva Aguirre, and P. Ventura. Gravity modes as a way to distinguish between hydrogen- and helium-burning red giant stars. *Nature*, 471:608–611, Mar. 2011. doi: 10.1038/nature09935.

O. Benomar, T. R. Bedding, D. Stello, S. Deheuvels, T. R. White, and J. Christensen-Dalsgaard. Masses of Subgiant Stars from Asteroseismology Using the Coupling Strengths of Mixed Modes. *The Astrophysical Journal Letters*, 745 (2):L33, Feb 2012. doi: 10.1088/2041-8205/745/2/L33.

O. Benomar, T. R. Bedding, B. Mosser, D. Stello, K. Belkacem, R. A. Garcia, T. R. White, C. A. Kuehn, S. Deheuvels, and J. Christensen-Dalsgaard. Properties of Oscillation Modes in Subgiant Stars Observed by Kepler. *The Astrophysical Journal*, 767(2):158, Apr 2013. doi: 10.1088/0004-637X/767/2/158.

G. Berthomieu, G. Gonczi, P. Graff, J. Provost, and A. Rocca. Low-frequency Gravity Modes of a Rotating Star. *Astronomy and Astrophysics*, 70:597, Nov. 1978.

L. Bigot, J. Provost, G. Berthomieu, W. A. Dziembowski, and P. R. Goode. Non-axisymmetric oscillations of roAp stars. *Astronomy and Astrophysics*, 356:218–233, Apr 2000.

L. Bildsten, G. Ushomirsky, and C. Cutler. Ocean g-Modes on Rotating Neutron Stars. *The Astrophysical Journal*, 460:827, Apr. 1996. doi: 10.1086/177012.

E. Böhm-Vitense. Über die Wasserstoffkonvektionszone in Sternen verschiedener Effektivtemperaturen und Leuchtkräfte. Mit 5 Textabbildungen. *Zeitschrift für Astrophysik*, 46:108, 1958.

M.-P. Bouabid, M.-A. Dupret, S. Salmon, J. Montalbán, A. Miglio, and A. Noels. Effects of the Coriolis force on high-order g modes in γ Doradus stars. *MNRAS*, 429:2500–2514, Mar. 2013. doi: 10.1093/mnras/sts517.

J. P. Boyd. *Planetary Waves and the Semiannual Wind Oscillation in the Tropical Upper Stratosphere.* PhD thesis, HARVARD UNIVERSITY., 1976.

J. P. Boyd. *Chebyshev and Fourier Spectral Methods*. 2001.

J. Braithwaite. The stability of poloidal magnetic fields in rotating stars. *Astronomy and Astrophysics*, 469(1):275–284, Jul 2007. doi: 10.1051/0004-6361:20065903.

J. Braithwaite. On non-axisymmetric magnetic equilibria in stars. *MNRAS*, 386(4): 1947–1958, Jun 2008. doi: 10.1111/j.1365-2966.2008.13218.x.

J. Braithwaite. Axisymmetric magnetic fields in stars: relative strengths of poloidal and toroidal components. *MNRAS*, 397:763–774, Aug. 2009. doi: 10.1111/j.1365-2966.2008.14034.x.

J. Braithwaite and Å. Nordlund. Stable magnetic fields in stellar interiors. *Astronomy and Astrophysics*, 450(3):1077–1095, May 2006. doi: 10.1051/0004-6361:20041980.

J. Braithwaite and H. C. Spruit. A fossil origin for the magnetic field in A stars and white dwarfs. *Nature*, 431(7010):819–821, Oct 2004. doi: 10.1038/nature02934.

A. Brandenburg and K. Subramanian. Astrophysical magnetic fields and nonlinear dynamo theory. *Physics Reports*, 417(1-4):1–209, Oct 2005. doi: 10.1016/j.physrep.2005.06.005.

M. K. Browning, A. S. Brun, and J. Toomre. Simulations of Core Convection in Rotating A-Type Stars: Differential Rotation and Overshooting. *The Astrophysical Journal*, 601(1):512–529, Jan 2004. doi: 10.1086/380198.

B. Buysschaert, C. Aerts, D. M. Bowman, C. Johnston, T. Van Reeth, M. G. Pedersen, S. Mathis, and C. Neiner. Forward seismic modeling of the pulsating magnetic B-type star HD 43317. *Astronomy & Astrophysics*, 616:A148, Sep 2018. doi: 10.1051/0004-6361/201832642.

M. Cantiello, J. Fuller, and L. Bildsten. Asteroseismic Signatures of Evolving Internal Stellar Magnetic Fields. *The Astrophysical Journal*, 824(1):14, Jun 2016. doi: 10.3847/0004-637X/824/1/14.

F. Castelli and R. L. Kurucz. New Grids of ATLAS9 Model Atmospheres. In N. Piskunov, W. W. Weiss, and D. F. Gray, editors, *Modelling of Stellar Atmospheres*, volume 210 of *IAU Symposium*, page A20, 2003.

P. Charbonneau. Solar and Stellar Dynamos. *Solar and Stellar Dynamos: Saas-Fee Advanced Course 39 Swiss Society for Astrophysics and Astronomy, Saas-Fee Advanced Courses, Volume 39. ISBN 978-3-642-32092-7. Springer-Verlag Berlin Heidelberg, 2013*, 39, 2013. doi: 10.1007/978-3-642-32093-4.

J. Christensen-Dalsgaard. The effect of non-adiabaticity on avoided crossings of non-radial stellar oscillations. *MNRAS*, 194:229–250, Jan. 1981. doi: 10.1093/mnras/194.2.229.

J. Christensen-Dalsgaard. Some aspects of the theory of solar oscillations. *Geophysical and Astrophysical Fluid Dynamics*, 62:123–152, 1991. doi: 10.1080/03091929108229129.

S. Christophe, J. Ballot, R. M. Ouazzani, V. Antoci, and S. J. A. J. Salmon. Deciphering the oscillation spectrum of γ Doradus and SPB stars. *Astronomy & Astrophysics*, 618:A47, Oct 2018. doi: 10.1051/0004-6361/201832782.

T. G. Cowling. The non-radial oscillations of polytropic stars. *MNRAS*, 101:367, 1941. doi: 10.1093/mnras/101.8.367.

J. P. Cox and R. T. Giuli. *Principles of stellar structure* . 1968.

I. de Pater and J. J. Lissauer. *Planetary Sciences*. Cambridge University Press, Jan. 2015.

B. Dintrans and M. Rieutord. Oscillations of a rotating star: a non-perturbative theory. *Astronomy and Astrophysics*, 354:86–98, Feb 2000.

V. Duez and S. Mathis. Relaxed equilibrium configurations to model fossil fields . I. A first family. *Astronomy and Astrophysics*, 517:A58, Jul 2010. doi: 10.1051/0004-6361/200913496.

M.-A. Dupret, A. Grigahcène, R. Garrido, J. De Ridder, R. Scuflaire, and M. Gabriel. Time-dependent convection seismic study of five γ Doradus stars. *MNRAS*, 360:1143–1152, July 2005a. doi: 10.1111/j.1365-2966.2005.09114.x.

M.-A. Dupret, A. Grigahcène, R. Garrido, M. Gabriel, and R. Scuflaire. Convection-pulsation coupling. II. Excitation and stabilization mechanisms in δ Sct and γ Dor stars. *Astronomy and Astrophysics*, 435:927–939, June 2005b. doi: 10.1051/0004-6361:20041817.

W. A. Dziembowski, P. Moskalik, and A. A. Pamyatnykh. The Opacity Mechanism in B-Type Stars - Part Two - Excitation of High-Order G-Modes in Main Sequence Stars. *MNRAS*, 265:588, Dec. 1993. doi: 10.1093/mnras/265.3.588.

C. Eckart and J. Gillis. Hydrodynamics of Oceans and Atmospheres. *Physics Today*, 14(8):52, Jan 1961. doi: 10.1063/1.3057700.

A. S. Eddington. *The Internal Constitution of the Stars*. 1926.

P. V. F. Edelmann, R. P. Ratnasingam, M. G. Pedersen, D. M. Bowman, V. Prat, and T. M. Rogers. Three-dimensional Simulations of Massive Stars. I. Wave Generation and Propagation. *The Astrophysical Journal*, 876(1):4, May 2019. doi: 10.3847/1538-4357/ab12df.

P. Eggenberger, N. Lagarde, A. Miglio, J. Montalbán, S. Ekström, C. Georgy, G. Meynet, S. Salmon, T. Ceillier, and R. A. García. Constraining the efficiency of angular momentum transport with asteroseismology of red giants: the effect of stellar mass. *Astronomy & Astrophysics*, 599:A18, Mar 2017. doi: 10.1051/0004-6361/201629459.

N. A. Featherstone, M. K. Browning, A. S. Brun, and J. Toomre. Effects of Fossil Magnetic Fields on Convective Core Dynamos in A-type Stars. *The Astrophysical Journal*, 705(1):1000–1018, Nov 2009. doi: 10.1088/0004-637X/705/1/1000.

L. Ferrario, A. Melatos, and J. Zrake. Magnetic field generation in stars. *Space Science Reviews*, 191(1):77–109, Oct 2015. ISSN 1572-9672. doi: 10.1007/s11214-015-0138-y. URL https://doi.org/10.1007/s11214-015-0138-y.

V. C. A. Ferraro. The non-uniform rotation of the Sun and its magnetic field. *MNRAS*, 97:458, Apr 1937. doi: 10.1093/mnras/97.6.458.

R. Fitzpatrick. *Plasma Physics: An Introduction*. CRC Press, 2015.

B. Freytag, H. G. Ludwig, and M. Steffen. Hydrodynamical models of stellar convection. The role of overshoot in DA white dwarfs, A-type stars, and the Sun. *Astronomy and Astrophysics*, 313:497–516, Sep 1996.

J. Fuller, M. Cantiello, D. Stello, R. A. Garcia, and L. Bildsten. Asteroseismology can reveal strong internal magnetic fields in red giant stars. *Science*, 350(6259): 423–426, Oct 2015. doi: 10.1126/science.aac6933.

J. Fuller, A. L. Piro, and A. S. Jermyn. Slowing the Spins of Stellar Cores. *MNRAS*, page 505, Feb 2019. doi: 10.1093/mnras/stz514.

F. Gallet, C. Charbonnel, and L. Amard. Host Star Evolution for Planet Habitability. *Origins of Life and Evolution of the Biosphere*, 46:395–401, Nov 2016. doi: 10.1007/s11084-016-9491-4.

A. Gautschy. Nonradial, nonadiabatic pulsations of evolving massive stars. *Astronomy and Astrophysics*, 260:175–182, July 1992.

A. Gautschy and H. Saio. On non-radial oscillations of B-type stars. *MNRAS*, 262: 213–219, May 1993. doi: 10.1093/mnras/262.1.213.

J. P. H. Goedbloed and S. Poedts. *Principles of Magnetohydrodynamics*. Aug. 2004.

D. J. Griffiths. *Introduction to Quantum Mechanics*. Cambridge University Press, 2017.

A. Grigahcène, M.-A. Dupret, M. Gabriel, R. Garrido, and R. Scuflaire. Convection-pulsation coupling. I. A mixing-length perturbative theory. *Astronomy and Astrophysics*, 434:1055–1062, May 2005. doi: 10.1051/0004-6361:20041816.

S. S. Hasan and J. Christensen-Dalsgaard. The Influence of a Vertical Magnetic Field on Oscillations in an Isothermal Stratified Atmosphere. *Astrophysical Journal*, 396:311, Sep 1992. doi: 10.1086/171718.

S. S. Hasan, J. P. Zahn, and J. Christensen-Dalsgaard. Probing the internal magnetic field of slowly pulsating B-stars through g modes. *Astronomy and Astrophysics*, 444(2):L29–L32, Dec 2005. doi: 10.1051/0004-6361:200500203.

L. Hendriks and C. Aerts. Deep Learning Applied to the Asteroseismic Modeling of Stars with Coherent Oscillation Modes. *arXiv e-prints*, art. arXiv:1811.03639, Nov 2018.

F. Herwig. The evolution of AGB stars with convective overshoot. *Astronomy and Astrophysics*, 360:952–968, Aug. 2000.

R. Hirschi, C. Chiappini, G. Meynet, A. Maeder, and S. Ekström. Stellar Evolution at Low Metallicity. In F. Bresolin, P. A. Crowther, and J. Puls, editors, *Massive Stars as Cosmic Engines*, volume 250 of *IAU Symposium*, pages 217–230, Jun 2008. doi: 10.1017/S1743921308020528.

P. F. Hopkins, D. Kereš, J. Oñorbe, C.-A. Faucher-Giguère, E. Quataert, N. Murray, and J. S. Bullock. Galaxies on FIRE (Feedback In Realistic Environments): stellar feedback explains cosmologically inefficient star formation. *MNRAS*, 445:581–603, Nov. 2014. doi: 10.1093/mnras/stu1738.

S. S. Hough. On the Application of Harmonic Analysis to the Dynamical Theory of the Tides. Part II: On the General Integration of Laplace's Dynamical Equations. *Philosophical Transactions of the Royal Society of London Series A*, 191:139–185, 1898. doi: 10.1098/rsta.1898.0005.

W. Huang, D. R. Gies, and M. V. McSwain. A Stellar Rotation Census of B Stars: From ZAMS to TAMS. *The Astrophysical Journal*, 722(1):605–619, Oct 2010. doi: 10.1088/0004-637X/722/1/605.

R. Kippenhahn, A. Weigert, and A. Weiss. *Stellar Structure and Evolution*. Springer, 2012. doi: 10.1007/978-3-642-30304-3.

D. G. Koch, W. J. Borucki, G. Basri, N. M. Batalha, T. M. Brown, D. Caldwell, J. Christensen-Dalsgaard, W. D. Cochran, E. DeVore, E. W. Dunham, T. N. Gautier, III, J. C. Geary, R. L. Gilliland, A. Gould, J. Jenkins, Y. Kondo, D. W. Latham, J. J. Lissauer, G. Marcy, D. Monet, D. Sasselov, A. Boss, D. Brownlee, J. Caldwell, A. K. Dupree, S. B. Howell, H. Kjeldsen, S. Meibom, D. Morrison, T. Owen, H. Reitsema, J. Tarter, S. T. Bryson, J. L. Dotson, P. Gazis, M. R. Haas, J. Kolodziejczak, J. F. Rowe, J. E. Van Cleve, C. Allen, H. Chandrasekaran, B. D. Clarke, J. Li, E. V. Quintana, P. Tenenbaum, J. D. Twicken, and H. Wu. Kepler Mission Design, Realized Photometric Performance, and Early Science. *The Astrophysical Journal Letters*, 713:L79–L86, Apr. 2010. doi: 10.1088/2041-8205/713/2/L79.

S. Kwok. The synthesis of organic and inorganic compounds in evolved stars. *Nature*, 430:985–991, Aug. 2004. doi: 10.1038/nature02862.

S. Kwok. Synthesis of organic compounds in the circumstellar environment. In S. Kwok and S. Sanford, editors, *Organic Matter in Space*, volume 251 of *IAU Symposium*, pages 175–184, Oct. 2008. doi: 10.1017/S1743921308021510.

J. D. Landstreet. The Orientation of Magnetic Axes in the Magnetic Variables. *Astrophysical Journal*, 159:1001, Mar 1970. doi: 10.1086/150377.

J. D. Landstreet and G. Mathys. Magnetic models of slowly rotating magnetic Ap stars: aligned magnetic and rotation axes. *Astronomy and Astrophysics*, 359: 213–226, Jul 2000.

D. Lecoanet, G. M. Vasil, J. Fuller, M. Cantiello, and K. J. Burns. Conversion of internal gravity waves into magnetic waves. *MNRAS*, 466(2):2181–2193, Apr 2017. doi: 10.1093/mnras/stw3273.

P. Ledoux and R. Simon. Sur les oscillations d'une étoile gazeuse possédant un champ magnétique faible. *Annales d'Astrophysique*, 20:185, Jan 1957.

U. Lee and H. Saio. Low-frequency nonradial oscillations in rotating stars. i. angular dependence. *The Astrophysical Journal*, 491(2):839–845, dec 1997. doi: 10.1086/304980. URL https://doi.org/10.1086%2F304980.

G. Li, T. R. Bedding, S. J. Murphy, T. Van Reeth, V. Antoci, and R.-M. Ouazzani. Period spacings of γ Doradus pulsators in the Kepler field: detection methods and application to 22 slow rotators. *MNRAS*, 482(2):1757–1785, Jan 2019a. doi: 10.1093/mnras/sty2743.

G. Li, T. Van Reeth, T. R. Bedding, S. J. Murphy, and V. Antoci. Period spacings of γ Doradus pulsators in the Kepler field: Rossby and gravity modes in 82 stars. *MNRAS*, page 1126, Apr 2019b. doi: 10.1093/mnras/stz1171.

R. D. Lindzen. Planetary Waves on Beta-Planes. *Monthly Weather Review*, 95:441, 1967. doi: 10.1175/1520-0493(1967)095⟨0441:PWOBP⟩2.3.CO;2.

M. S. Longuet-Higgins. The Eigenfunctions of Laplace's Tidal Equations over a Sphere. *Philosophical Transactions of the Royal Society of London Series A*, 262 (1132):511–607, Feb 1968. doi: 10.1098/rsta.1968.0003.

K. B. MacGregor and T. M. Rogers. Reflection and Ducting of Gravity Waves Inside the Sun. *Solar Physics*, 270(2):417–436, Jun 2011. doi: 10.1007/s11207-011-9771-0.

A. Maeder. *Physics, Formation and Evolution of Rotating Stars*. Springer, 2009. doi: 10.1007/978-3-540-76949-1.

A. Maeder, C. Georgy, and G. Meynet. Convective envelopes in rotating OB stars. *Astronomy and Astrophysics*, 479(2):L37–L40, Feb 2008. doi: 10.1051/0004-6361:20079007.

P. Markey and R. J. Tayler. The adiabatic stability of stars containing magnetic fields. II. Poloidal fields. *MNRAS*, 163:77–91, Mar 1973. doi: 10.1093/mnras/163.1.77.

S. Mathis. Transport by gravito-inertial waves in differentially rotating stellar radiation zones. I - Theoretical formulation. *Astronomy and Astrophysics*, 506(2):811–828, Nov 2009. doi: 10.1051/0004-6361/200810544.

S. Mathis and N. de Brye. Low-frequency internal waves in magnetized rotating stellar radiation zones. I. Wave structure modification by a toroidal field. *Astronomy and Astrophysics*, 526:A65, Feb 2011. doi: 10.1051/0004-6361/201015571.

S. Mathis and J. P. Zahn. Transport and mixing in the radiation zones of rotating stars. II. Axisymmetric magnetic field. *Astronomy and Astrophysics*, 440(2):653–666, Sep 2005. doi: 10.1051/0004-6361:20052640.

T. Matsuno. Quasi-geostrophic motions in the equatorial area. *Journal of the Meteorological Society of Japan. Ser. II*, 44(1):25–43, 1966. doi: 10.2151/jmsj1965.44.1_25.

A. Miglio, J. Montalbán, A. Noels, and P. Eggenberger. Probing the properties of convective cores through g modes: high-order g modes in SPB and γ Doradus stars. *MNRAS*, 386:1487–1502, May 2008. doi: 10.1111/j.1365-2966.2008.13112.x.

H. K. Moffatt. *Magnetic field generation in electrically conducting fluids*. Cambridge University Press, 1978.

J. S. G. Mombarg, T. Van Reeth, M. G. Pedersen, G. Molenberghs, D. M. Bowman, C. Johnston, A. Tkachenko, and C. Aerts. Asteroseismic masses, ages, and core properties of γ Doradus stars using gravito-inertial dipole modes and spectroscopy. *MNRAS*, page 495, Feb 2019. doi: 10.1093/mnras/stz501.

E. Moravveji, R. H. D. Townsend, C. Aerts, and S. Mathis. Sub-inertial Gravity Modes in the B8V Star KIC 7760680 Reveal Moderate Core Overshooting and Low Vertical Diffusive Mixing. *The Astrophysical Journal*, 823(2):130, Jun 2016. doi: 10.3847/0004-637X/823/2/130.

S. M. Morsink and V. Rezania. Normal Modes of Rotating Magnetic Stars. *The Astrophysical Journal*, 574:908–919, Aug. 2002. doi: 10.1086/341190.

D. Moss. Magnetic fields and differential rotation in stars. *MNRAS*, 257(4):593–601, Aug 1992. doi: 10.1093/mnras/257.4.593.

B. Mosser, Y. Elsworth, S. Hekker, D. Huber, T. Kallinger, S. Mathur, K. Belkacem, M. J. Goupil, R. Samadi, C. Barban, T. R. Bedding, W. J. Chaplin, R. A. García, D. Stello, J. De Ridder, C. K. Middour, R. L. Morris, and E. V. Quintana. Characterization of the power excess of solar-like oscillations in red giants with Kepler. *Astronomy & Astrophysics*, 537:A30, Jan 2012a. doi: 10.1051/0004-6361/201117352.

B. Mosser, M. J. Goupil, K. Belkacem, E. Michel, D. Stello, J. P. Marques, Y. Elsworth, C. Barban, P. G. Beck, T. R. Bedding, J. De Ridder, R. A. García, S. Hekker, T. Kallinger, R. Samadi, M. C. Stumpe, T. Barclay, and C. J. Burke. Probing the core structure and evolution of red giants using gravity-dominated mixed modes observed with Kepler. *Astronomy & Astrophysics*, 540:A143, Apr. 2012b. doi: 10.1051/0004-6361/201118519.

B. Mosser, K. Belkacem, C. Pinçon, M. Takata, M. Vrard, C. Barban, M. J. Goupil, T. Kallinger, and R. Samadi. Dipole modes with depressed amplitudes in red giants are mixed modes. *Astronomy & Astrophysics*, 598:A62, Feb 2017. doi: 10.1051/0004-6361/201629494.

C. Neiner, M. Floquet, R. Samadi, F. Espinosa Lara, Y. Frémat, S. Mathis, B. Leroy, B. de Batz, M. Rainer, E. Poretti, P. Mathias, J. Guarro Fló, C. Buil, J. Ribeiro, E. Alecian, L. Andrade, M. Briquet, P. D. Diago, M. Emilio, J. Fabregat, J. Gutiérrez-Soto, A. M. Hubert, E. Janot-Pacheco, C. Martayan, T. Semaan, J. Suso, and J. Zorec. Stochastic gravito-inertial modes discovered by CoRoT in the hot Be star HD 51452. *Astronomy & Astrophysics*, 546:A47, Oct 2012. doi: 10.1051/0004-6361/201219820.

C. Neiner, S. Mathis, E. Alecian, C. Emeriau, J. Grunhut, BinaMIcS, and MiMeS Collaborations. The origin of magnetic fields in hot stars. In K. N. Nagendra, S. Bagnulo, R. Centeno, and M. Jesús Martínez González, editors, *Polarimetry*, volume 305 of *IAU Symposium*, pages 61–66, Oct 2015. doi: 10.1017/S1743921315004524.

M. F. Nieva and N. Przybilla. Present-day cosmic abundances. A comprehensive study of nearby early B-type stars and implications for stellar and Galactic evolution and interstellar dust models. *Astronomy & Astrophysics*, 539:A143, Mar 2012. doi: 10.1051/0004-6361/201118158.

J. Osaki. Nonradial oscillations of a 10 solar mass star in the main-sequence stage. *Publications of the Astronomical Society of Japan*, 27:237–258, 1975.

R.-M. Ouazzani, M.-A. Dupret, and D. R. Reese. Pulsations of rapidly rotating stars. I. The ACOR numerical code. *Astronomy & Astrophysics*, 547:A75, Nov. 2012. doi: 10.1051/0004-6361/201219548.

R.-M. Ouazzani, S. J. A. J. Salmon, V. Antoci, T. R. Bedding, S. J. Murphy, and I. W. Roxburgh. A new asteroseismic diagnostic for internal rotation in γ Doradus stars. *MNRAS*, 465:2294–2309, Feb. 2017. doi: 10.1093/mnras/stw2717.

R.-M. Ouazzani, J. P. Marques, M.-J. Goupil, S. Christophe, V. Antoci, and S. J. A. J. Salmon. γ Doradus stars as test of angular momentum transport models. *arXiv e-prints*, art. arXiv:1801.09228, Jan 2018.

A. A. Pamyatnykh. Pulsational Instability Domains in the Upper Main Sequence. *Acta Astronomica*, 49:119–148, June 1999.

P. I. Pápics, A. Tkachenko, T. Van Reeth, C. Aerts, E. Moravveji, M. Van de Sande, K. De Smedt, S. Bloemen, J. Southworth, J. Debosscher, E. Niemczura, and J. F. Gameiro. Signatures of internal rotation discovered in the Kepler data of five slowly pulsating B stars. *Astronomy & Astrophysics*, 598:A74, Feb 2017. doi: 10.1051/0004-6361/201629814.

B. Paxton, L. Bildsten, A. Dotter, F. Herwig, P. Lesaffre, and F. Timmes. Modules for Experiments in Stellar Astrophysics (MESA). *The Astrophysical Journal Supplement*, 192:3, Jan. 2011. doi: 10.1088/0067-0049/192/1/3.

B. Paxton, M. Cantiello, P. Arras, L. Bildsten, E. F. Brown, A. Dotter, C. Mankovich, M. H. Montgomery, D. Stello, F. X. Timmes, and R. Townsend. Modules for Experiments in Stellar Astrophysics (MESA): Planets, Oscillations, Rotation, and Massive Stars. *The Astrophysical Journal Supplement*, 208:4, Sept. 2013. doi: 10.1088/0067-0049/208/1/4.

B. Paxton, P. Marchant, J. Schwab, E. B. Bauer, L. Bildsten, M. Cantiello, L. Dessart, R. Farmer, H. Hu, N. Langer, R. H. D. Townsend, D. M. Townsley, and F. X. Timmes. Modules for Experiments in Stellar Astrophysics (MESA): Binaries, Pulsations, and Explosions. *The Astrophysical Journal Supplement Series*, 220:15, Sept. 2015. doi: 10.1088/0067-0049/220/1/15.

B. Paxton, P. Marchant, J. Schwab, E. B. Bauer, L. Bildsten, M. Cantiello, L. Dessart, R. Farmer, H. Hu, N. Langer, R. H. D. Townsend, D. M. Townsley, and F. X. Timmes. Erratum: Modules for Experiments in Stellar Astrophysics (MESA): Binaries, Pulsations, and Explosions. *The Astrophysical Journal Supplement Series*, 223:18, Mar. 2016. doi: 10.3847/0067-0049/223/1/18.

B. Paxton, J. Schwab, E. B. Bauer, L. Bildsten, S. Blinnikov, P. Duffell, R. Farmer, J. A. Goldberg, P. Marchant, E. Sorokina, A. Thoul, R. H. D. Townsend, and F. X. Timmes. Modules for Experiments in Stellar Astrophysics (MESA): Convective Boundaries, Element Diffusion, and Massive Star Explosions. *The Astrophysical Journal Supplement Series*, 234:34, Feb. 2018. doi: 10.3847/1538-4365/aaa5a8.

B. Paxton, R. Smolec, A. Gautschy, L. Bildsten, M. Cantiello, A. Dotter, R. Farmer, J. A. Goldberg, A. S. Jermyn, S. M. Kanbur, P. Marchant, J. Schwab, A. Thoul, R. H. D. Townsend, W. M. Wolf, M. Zhang, and F. X. Timmes. Modules for Experiments in Stellar Astrophysics (MESA): Pulsating Variable Stars, Rotation, Convective Boundaries, and Energy Conservation. *arXiv e-prints*, Mar. 2019.

M. G. Pedersen, C. Aerts, P. I. Pápics, and T. M. Rogers. The shape of convective core overshooting from gravity-mode period spacings. *Astronomy & Astrophysics*, 614:A128, Jul 2018. doi: 10.1051/0004-6361/201732317.

M. Pinsonneault. Mixing in Stars. *Annual Review of Astronomy and Astrophysics*, 35:557–605, 1997. doi: 10.1146/annurev.astro.35.1.557.

V. Prat, F. Lignières, and J. Ballot. Asymptotic theory of gravity modes in rotating stars. I. Ray dynamics. *Astronomy & Astrophysics*, 587:A110, Mar 2016. doi: 10.1051/0004-6361/201527737.

V. Prat, S. Mathis, F. Lignières, J. Ballot, and P. M. Culpin. Period spacing of gravity modes strongly affected by rotation. Going beyond the traditional approximation. *Astronomy & Astrophysics*, 598:A105, Feb 2017. doi: 10.1051/0004-6361/201629637.

V. Prat, S. Mathis, B. Buysschaert, **Van Beeck, J.**, D. M. Bowman, C. Aerts, and C. Neiner. Period spacings of gravity modes in rapidly rotating magnetic stars. I. Axisymmetric fossil field with poloidal and toroidal components. *Astronomy & Astrophysics*, 627:A64, Jul 2019. doi: 10.1051/0004-6361/201935462.

W. H. Press. Radiative and other effects from internal waves in solar and stellar interiors. *Astrophysical Journal*, 245:286–303, Apr 1981. doi: 10.1086/158809.

D. Reese, F. Lignières, and M. Rieutord. Acoustic oscillations of rapidly rotating polytropic stars. II. Effects of the Coriolis and centrifugal accelerations. *Astronomy and Astrophysics*, 455(2):621–637, Aug 2006. doi: 10.1051/0004-6361:20065269.

G. R. Ricker, J. N. Winn, R. Vanderspek, D. W. Latham, G. Á. Bakos, J. L. Bean, Z. K. Berta-Thompson, T. M. Brown, L. Buchhave, N. R. Butler, R. P. Butler, W. J. Chaplin, D. Charbonneau, J. Christensen-Dalsgaard, M. Clampin, D. Deming, J. Doty, N. De Lee, C. Dressing, E. W. Dunham, M. Endl, F. Fressin, J. Ge, T. Henning, M. J. Holman, A. W. Howard, S. Ida, J. M. Jenkins, G. Jernigan,

J. A. Johnson, L. Kaltenegger, N. Kawai, H. Kjeldsen, G. Laughlin, A. M. Levine, D. Lin, J. J. Lissauer, P. MacQueen, G. Marcy, P. R. McCullough, T. D. Morton, N. Narita, M. Paegert, E. Palle, F. Pepe, J. Pepper, A. Quirrenbach, S. A. Rinehart, D. Sasselov, B. Sato, S. Seager, A. Sozzetti, K. G. Stassun, P. Sullivan, A. Szentgyorgyi, G. Torres, S. Udry, and J. Villasenor. Transiting Exoplanet Survey Satellite (TESS). *Journal of Astronomical Telescopes, Instruments, and Systems*, 1(1):014003, Jan. 2015. doi: 10.1117/1.JATIS.1.1.014003.

H. Robe. Les oscillations non radiales des polytropes. *Annales d'Astrophysique*, 31: 475, Feb. 1968.

T. M. Rogers and K. B. MacGregor. On the interaction of internal gravity waves with a magnetic field - I. Artificial wave forcing. *MNRAS*, 401:191–196, Jan. 2010. doi: 10.1111/j.1365-2966.2009.15618.x.

M. L. Roth and A. Weigert. More on avoided level crossing of non-radial stellar oscillations. *Astronomy and Astrophysics*, 80:48–52, Nov. 1979.

H. Saio, D. W. Kurtz, S. J. Murphy, V. L. Antoci, and U. Lee. Theory and evidence of global Rossby waves in upper main-sequence stars: r-mode oscillations in many Kepler stars. *MNRAS*, 474(2):2774–2786, Feb 2018. doi: 10.1093/mnras/stx2962.

E. Schatzman. Filtering of gravity waves. *Astronomy and Astrophysics*, 271:L29, Apr. 1993.

M. Schönberg and S. Chandrasekhar. On the Evolution of the Main-Sequence Stars. *Astrophysical Journal*, 96:161, Sept. 1942. doi: 10.1086/144444.

R. Scuflaire. The Non Radial Oscillations of Condensed Polytropes. *Astronomy and Astrophysics*, 36:107, Nov. 1974.

H. Shibahashi. Modal Analysis of Stellar Nonradial Oscillations by an Asymptotic Method. *Publications of the Astronomical Society of Japan*, 31:87–104, 1979.

H. Shibahashi and Y. Osaki. Overstability of Gravity Modes in Massive Stars with the Semiconvective Zone. *Publications of the Astronomical Society of Japan*, 28: 199–214, 1976.

H. Shibahashi and M. Takata. Theory for the Distorted Dipole Modes of the Rapidly Oscillating AP Stars: A Refinement of the Oblique Pulsator Model. *Publications of the Astronomical Society of Japan*, 45:617–641, Aug 1993.

M. Shultz, G. A. Wade, J. Grunhut, S. Bagnulo, J. D. Landstreet, C. Neiner, E. Alecian, D. Hanes, and MiMeS Collaboration. Critical Evaluation of Magnetic Field Detections Reported for Pulsating B-type Stars in Light of ESPaDOnS, Narval, and Reanalyzed FORS1/2 Observations. *The Astrophysical Journal*, 750(1):2, May 2012. doi: 10.1088/0004-637X/750/1/2.

M. E. Shultz, G. A. Wade, T. Rivinius, C. Neiner, E. Alecian, D. Bohlender, D. Monin, J. Sikora, MiMeS Collaboration, and BinaMIcS Collaboration. The magnetic early B-type stars I: magnetometry and rotation. *MNRAS*, 475(4): 5144–5178, Apr 2018. doi: 10.1093/mnras/sty103.

P. Smeyers and T. Van Hoolst. *Linear Isentropic Oscillations of Stars: Theoretical Foundations*. Springer, 2010.

H. C. Spruit. Differential rotation and magnetic fields in stellar interiors. *Astronomy & Astrophysics*, 349:189–202, Sep 1999.

D. Stello, M. Cantiello, J. Fuller, D. Huber, R. A. García, T. R. Bedding, L. Bildsten, and V. Silva Aguirre. A prevalence of dynamo-generated magnetic fields in the cores of intermediate-mass stars. *Nature*, 529:364–367, Jan. 2016. doi: 10.1038/nature16171.

M. Takata. Asymptotic analysis of dipolar mixed modes of oscillations in red giant stars. *Publications of the Astronomical Society of Japan*, 68(6):109, Dec 2016a. doi: 10.1093/pasj/psw104.

M. Takata. Physical formulation of mixed modes of stellar oscillations. *Publications of the Astronomical Society of Japan*, 68(6):91, Dec 2016b. doi: 10.1093/pasj/psw093.

M. Tassoul. Asymptotic approximations for stellar nonradial pulsations. *Astrophysical Journal, Suppl. Ser.*, 43:469–490, Aug 1980. doi: 10.1086/190678.

J. Tayar and M. H. Pinsonneault. Testing Angular Momentum Transport and Wind Loss in Intermediate-mass Core-helium Burning Stars. *The Astrophysical Journal*, 868(2):150, Dec 2018. doi: 10.3847/1538-4357/aae979.

R. J. Tayler. The adiabatic stability of stars containing magnetic fields-I.Toroidal fields. *MNRAS*, 161:365, 1973. doi: 10.1093/mnras/161.4.365.

R. H. D. Townsend. Surface trapping and leakage of low-frequency g modes in rotating early-type stars - II. Global analysis. *MNRAS*, 319:289–304, Nov. 2000. doi: 10.1046/j.1365-8711.2000.03853.x.

R. H. D. Townsend. Asymptotic expressions for the angular dependence of low-frequency pulsation modes in rotating stars. *MNRAS*, 340:1020–1030, Apr. 2003. doi: 10.1046/j.1365-8711.2003.06379.x.

R. H. D. Townsend and S. A. Teitler. GYRE: an open-source stellar oscillation code based on a new Magnus Multiple Shooting scheme. *MNRAS*, 435:3406–3418, Nov. 2013. doi: 10.1093/mnras/stt1533.

R. H. D. Townsend, J. Goldstein, and E. G. Zweibel. Angular momentum transport by heat-driven g-modes in slowly pulsating B stars. *MNRAS*, 475(1):879–893, Mar 2018. doi: 10.1093/mnras/stx3142.

K. Truyaert. The influence of rotational mixing on stellar models and gravity-mode oscillations of intermediate-mass stars, 2016.

W. Unno, Y. Osaki, H. Ando, H. Saio, and H. Shibahashi. *Nonradial oscillations of stars*. 1989.

T. Van Reeth. *Asteroseismology of γ Doradus stars with the Kepler space mission*. PhD thesis, KU Leuven., 2017.

T. Van Reeth, A. Tkachenko, C. Aerts, P. I. Pápics, S. A. Triana, K. Zwintz, P. Degroote, J. Debosscher, S. Bloemen, V. S. Schmid, K. De Smedt, Y. Fremat, A. S. Fuentes, W. Homan, M. Hrudkova, R. Karjalainen, R. Lombaert, P. Nemeth, R. Østensen, G. Van De Steene, J. Vos, G. Raskin, and H. Van Winckel. Gravity-mode Period Spacings as a Seismic Diagnostic for a Sample of γ Doradus Stars from Kepler Space Photometry and High-resolution Ground-based Spectroscopy. *The Astrophysical Journal Supplement Series*, 218(2):27, Jun 2015. doi: 10.1088/0067-0049/218/2/27.

T. Van Reeth, A. Tkachenko, and C. Aerts. Interior rotation of a sample of γ Doradus stars from ensemble modelling of their gravity-mode period spacings. *Astronomy & Astrophysics*, 593:A120, Oct 2016. doi: 10.1051/0004-6361/201628616.

T. Van Reeth, J. S. G. Mombarg, S. Mathis, A. Tkachenko, J. Fuller, D. M. Bowman, B. Buysschaert, C. Johnston, A. García Hernández, J. Goldstein, R. H. D. Townsend, and C. Aerts. Sensitivity of gravito-inertial modes to differential rotation in intermediate-mass main-sequence stars. *Astronomy & Astrophysics*, 618: A24, Oct 2018. doi: 10.1051/0004-6361/201832718.

L. S. Viani, S. Basu, M. Joel Ong J., A. Bonaca, and W. J. Chaplin. Investigating the Metallicity-Mixing-length Relation. *The Astrophysical Journal*, 858(1):28, May 2018. doi: 10.3847/1538-4357/aab7eb.

H. von Zeipel. The radiative equilibrium of a rotating system of gaseous masses. *MNRAS*, 84:665–683, June 1924. doi: 10.1093/mnras/84.9.665.

C. Waelkens. Slowly pulsating B stars. *Astronomy and Astrophysics*, 246:453–468, June 1991.

H. Wang, J. P. Boyd, and R. A. Akmaev. On computation of hough functions. *Geoscientific Model Development*, 9(4):1477–1488, 2016. doi: 10.5194/gmd-9-1477-2016.

D. Ward-Thompson and A. P. Whitworth. *An Introduction to Star Formation*. Cambridge University Press, May 2015.

M. Yanai and T. Maruyama. Stratospheric wave disturbances propagating over the equatorial pacific. *Journal of the Meteorological Society of Japan. Ser. II*, 44(5): 291–294, 1966. doi: 10.2151/jmsj1965.44.5_291.

J. P. Zahn. Les marées dans une étoile double serrée. *Annales d'Astrophysique*, 29: 313, Feb 1966.

J.-P. Zahn. Circulation and turbulence in rotating stars. *Astronomy & Astrophysics*, 265:115–132, Nov. 1992.

J.-P. Zahn. Rapid rotation and mixing in active OB stars - Physical processes. In C. Neiner, G. Wade, G. Meynet, and G. Peters, editors, *Active OB Stars: Structure, Evolution, Mass Loss, and Critical Limits*, volume 272 of *IAU Symposium*, pages 14–25, Jul 2011. doi: 10.1017/S1743921311009926.

Appendices

Connecting our equations of motion with literature

Purely rotating case

The general equations of motion for a rotating star with velocity field $\boldsymbol{v}$, rotation vector $\boldsymbol{\Omega} = \Omega \boldsymbol{e}_z$ (i.e. uniformly rotating), evaluated in the co-rotating frame are given by (Unno et al., 1989):

$$\frac{\mathrm{d}\boldsymbol{v}}{\mathrm{d}t} + (\boldsymbol{v} \cdot \nabla)\, \boldsymbol{v} + 2\, \boldsymbol{\Omega} \times \boldsymbol{v} + \boldsymbol{\Omega} \times \boldsymbol{\Omega} \times \boldsymbol{r} = -\nabla\phi - \frac{1}{\rho}\nabla P \ ,$$

from which one can obtain the following (Eulerian) perturbed equations (perturbing the velocity field), assuming a static equilibrium velocity and magnetic field ($\frac{\partial \boldsymbol{v}_0}{\partial t} = 0$, $\frac{\partial \boldsymbol{B}_0}{\partial t} = 0$):

$$\frac{\partial \boldsymbol{v}'}{\partial t} + (\boldsymbol{v}' \cdot \nabla)\, \boldsymbol{v}_0 + (\boldsymbol{v}_0 \cdot \nabla)\, \boldsymbol{v}' + 2\boldsymbol{\Omega} \times \boldsymbol{v}' = -\frac{1}{\rho_0}\nabla P' + \frac{\rho'}{\rho_0^2}\nabla P - \nabla\phi'$$

where ϕ is the gravitational potential, the subscript 0 denotes equilibrium quantities, and where we do not neglect the centrifugal term ($\boldsymbol{\Omega} \times \boldsymbol{\Omega} \times \boldsymbol{r}$) and do not neglect the perturbation of the gravitational potential. Making the Cowling approximation (i.e. neglecting the Eulerian perturbation of the gravitational potential ϕ'; Cowling, 1941), assuming the temporal dependence of the eigenfunctions to be equal to $e^{-i\omega t}$ and an equilibrium star at rest: $||\boldsymbol{v}_0|| = v_0 = 0$, one can obtain the linearized equations of motion used in the main text (Equation (2.22)). In order to do so, we need to exploit the relation between the Eulerian perturbation of the velocity field $\boldsymbol{v}'$, the Lagrangian displacement vector $\boldsymbol{\xi}$ and the Lagrangian perturbation of the velocity field $\delta\boldsymbol{v}$ (e.g. Smeyers and Van Hoolst, 2010):

$$\boldsymbol{v}' = \delta\boldsymbol{v} - (\boldsymbol{\xi} \cdot \nabla)\, \boldsymbol{v}_0 \ .$$

The Lagrangian perturbation of $\boldsymbol{v}$ is also given by:

$$\begin{aligned} \delta\boldsymbol{v} = \boldsymbol{v}\,(\boldsymbol{r}_0 + \boldsymbol{\xi}) - \boldsymbol{v}_0\,(\boldsymbol{r}_0) &= \frac{\mathrm{d}\boldsymbol{\xi}}{\mathrm{d}t} \ , \\ \Leftrightarrow \delta\boldsymbol{v} &= \frac{\partial \boldsymbol{\xi}}{\partial t} + (\boldsymbol{v} \cdot \nabla)\, \boldsymbol{\xi} \ , \\ \Leftrightarrow \delta\boldsymbol{v} &\simeq \frac{\partial \boldsymbol{\xi}}{\partial t} + (\boldsymbol{v}_0 \cdot \nabla)\, \boldsymbol{\xi} \ , \end{aligned}$$

resulting in the following expression for the Eulerian perturbation of the velocity:

$$\boldsymbol{v}' = \frac{\partial \boldsymbol{\xi}}{\partial t} + (\boldsymbol{v}_0 \cdot \nabla)\, \boldsymbol{\xi} - (\boldsymbol{\xi} \cdot \nabla)\, \boldsymbol{v}_0 \ .$$

Since we assume the temporal dependence of $\boldsymbol{\xi}$ to be $e^{-i\omega t}$, we can derive the following expressions (taking into account the assumptions above) for the different terms in the Unno et al. (1989) equation:

$$\begin{aligned}
\frac{\partial \boldsymbol{v}'}{\partial t} &= -\omega^2\boldsymbol{\xi} + i\omega\left(\boldsymbol{\xi}\cdot\nabla\right)\boldsymbol{v}_0 - i\omega\left(\boldsymbol{v}_0\cdot\nabla\right)\boldsymbol{\xi} = -\omega^2\boldsymbol{\xi}\ , \\
2\boldsymbol{\Omega}\times\boldsymbol{v}' &= 2\Omega\times\left(-i\omega\boldsymbol{\xi} + \left(\boldsymbol{v}_0\cdot\nabla\right)\boldsymbol{\xi} - \left(\boldsymbol{\xi}\cdot\nabla\right)\boldsymbol{v}_0\right) = -2i\omega\left(\boldsymbol{\Omega}\times\boldsymbol{\xi}\right)\ , \\
\left(\boldsymbol{v}'\cdot\nabla\right)\boldsymbol{v} &\simeq \left(\boldsymbol{v}'\cdot\nabla\right)\boldsymbol{v}_0 = 0\ , \\
\left(\boldsymbol{v}_0\cdot\nabla\right)\boldsymbol{v}' &= 0\ , \\
\nabla\phi' &= 0\ .
\end{aligned}$$

In the purely rotating case, the equations of motion then simplify to:

$$\begin{aligned}
-\omega^2\boldsymbol{\xi} - 2i\omega\left(\boldsymbol{\Omega}\times\boldsymbol{\xi}\right) &= \frac{\rho'}{\rho^2}\nabla P - \frac{\nabla P'}{\rho}\ , \\
\Leftrightarrow \omega^2\boldsymbol{\xi} + 2i\omega\left(\boldsymbol{\Omega}\times\boldsymbol{\xi}\right) &+ \frac{\rho'}{\rho^2}\nabla P - \frac{\nabla P'}{\rho} = 0\ ,
\end{aligned}$$

from which, using the operators are the ones defined in Section (2.2.2):

$$\boldsymbol{\mathcal{B}}(\boldsymbol{\xi}) = 2\ \boldsymbol{\Omega}\times\boldsymbol{\xi}\ ,$$

$$\boldsymbol{\mathcal{C}}(\boldsymbol{\xi}) = \frac{\rho'}{\rho^2}\nabla P - \frac{\nabla P'}{\rho}\ ,$$

one obtains Equation (2.22).

Magnetorotational case

Starting from the general perturbed equations of motion derived by Unno et al. (1989) (Equation (2.52)), one can derive Equation (2.53). Making the same assumptions as in the purely rotating case, taking into account the same temporal dependence of $\boldsymbol{\xi}$, but instead starting from Equation (2.52), one arrives at

$$\begin{aligned}
-\omega^2\boldsymbol{\xi} - 2i\omega\left(\boldsymbol{\Omega}\times\boldsymbol{\xi}\right) &= \frac{\rho'}{\rho^2}\left[\nabla P - \frac{1}{4\pi}\left(\nabla\times\boldsymbol{B}\right)\times\boldsymbol{B}\right] - \frac{\nabla P'}{\rho} \\
&\quad + \frac{1}{4\pi\rho}\left[\left(\nabla\times\boldsymbol{B}\right)\times\boldsymbol{B}' + \left(\nabla\times\boldsymbol{B}'\right)\times\boldsymbol{B}\right]\ , \\
\Leftrightarrow \omega^2\boldsymbol{\xi} + 2i\omega\left(\boldsymbol{\Omega}\times\boldsymbol{\xi}\right) &+ \frac{\rho'}{\rho^2}\left[\nabla P - \frac{1}{4\pi}\left(\nabla\times\boldsymbol{B}\right)\times\boldsymbol{B}\right] - \frac{\nabla P'}{\rho} \\
&\quad + \frac{1}{4\pi\rho}\left[\left(\nabla\times\boldsymbol{B}\right)\times\boldsymbol{B}' + \left(\nabla\times\boldsymbol{B}'\right)\times\boldsymbol{B}\right] = 0\ ,
\end{aligned}$$

where the magnetic terms in Equation (2.52) stay the same.

We can clearly distinguish the operators defined in Equation (2.22), where:

$$\boldsymbol{\mathcal{B}}(\boldsymbol{\xi}) = 2\ \boldsymbol{\Omega}\times\boldsymbol{\xi}\ ,$$

$$\begin{aligned}
\boldsymbol{\mathcal{C}}(\boldsymbol{\xi}) &= \frac{\rho'}{\rho^2}\left[\nabla P - \frac{1}{4\pi}\left(\nabla\times\boldsymbol{B}\right)\times\boldsymbol{B}\right] - \frac{\nabla P'}{\rho} \\
&\quad + \frac{1}{4\pi\rho}\left[\left(\nabla\times\boldsymbol{B}\right)\times\boldsymbol{B}' + \left(\nabla\times\boldsymbol{B}'\right)\times\boldsymbol{B}\right]\ .
\end{aligned}$$

The last operator can be subdivided into two constituents:

$$\boldsymbol{\mathcal{C}_0}(\boldsymbol{\xi}_0) = \frac{\rho'}{\rho^2}\nabla P - \frac{\nabla P'}{\rho} \ ,$$

$$\begin{aligned}\boldsymbol{\mathcal{C}_1}(\boldsymbol{\xi}_0) = &\frac{\rho'}{4\pi\rho^2}\left(\nabla \times \boldsymbol{B}\right) \times \boldsymbol{B} \\ &+ \frac{1}{4\pi\rho}\left[(\nabla \times \boldsymbol{B}) \times \boldsymbol{B}' + (\nabla \times \boldsymbol{B}') \times \boldsymbol{B}\right] \ ,\end{aligned}$$

since $\boldsymbol{B}' \propto \boldsymbol{\xi}_0$ and $\boldsymbol{B}' \propto \boldsymbol{B}$ (see Equation (2.49)).

Deriving the Hough functions

In order to derive the expression for the Hough functions we need to derive the components of the linearized equation of motion (Equation (2.22)):

$$\omega^2\boldsymbol{\xi} + 2i\omega\left(\boldsymbol{\Omega} \times \boldsymbol{\xi}\right) \ + \ \frac{\rho'}{\rho^2}\nabla P - \frac{\nabla P'}{\rho} = 0 \ .$$

This amounts to calculating the different components of $\boldsymbol{\Omega} \times \boldsymbol{\xi}$, where the Ω and $\boldsymbol{\xi}$ are decomposed in the following components (in spherical coordinates):

$$\begin{aligned}\boldsymbol{\Omega} &= \Omega\cos\theta\boldsymbol{e}_r - \Omega\sin\theta\boldsymbol{e}_\theta \ , \\ \boldsymbol{\xi} &= \xi_r\boldsymbol{e}_r + \xi_\theta\boldsymbol{e}_\theta + \xi_\varphi\boldsymbol{e}_\varphi \ ,\end{aligned}$$

as already defined in the main text. The components of the vector product are then:

$$\begin{aligned}\left(\boldsymbol{\Omega} \times \boldsymbol{\xi}\right)_r &= -\Omega\sin\theta\xi_\varphi \ , \\ \left(\boldsymbol{\Omega} \times \boldsymbol{\xi}\right)_\theta &= -\Omega\cos\theta\xi_\varphi \ , \\ \left(\boldsymbol{\Omega} \times \boldsymbol{\xi}\right)_\varphi &= \Omega\sin\theta\xi_r + \Omega\cos\theta\xi_\theta \ .\end{aligned}$$

In the TAR however, the components with $\Omega\ \sin\theta$ are neglected. Doing so, results in the following component equations:

$$\begin{aligned}\omega^2\xi_r - 2i\omega\Omega\sin\theta\xi_\varphi + \frac{\rho'}{\rho^2}\frac{\mathrm{d}P}{\mathrm{d}r} - \frac{\frac{\partial P'}{\partial r}}{\rho} &= 0 \ , \\ \Leftrightarrow \rho\omega^2\xi_r - \rho' g - \frac{\partial P'}{\partial r} &= 0 \ , \\ \omega^2\xi_\theta - 2i\omega\Omega\cos\theta\xi_\varphi - \frac{\frac{\partial P'}{\partial \theta}}{r\ \rho} &= 0 \ , \\ \Leftrightarrow \rho\omega^2\xi_\theta - 2i\rho\omega\Omega\cos\theta\xi_\varphi - \frac{1}{r}\frac{\partial P'}{\partial \theta} &= 0 \ , \\ \omega^2\xi_\varphi + 2i\omega\left(\Omega\sin\theta\xi_r + \Omega\cos\theta\xi_\theta\right) - \frac{\frac{\partial P'}{\partial \varphi}}{r\ \sin\theta\ \rho} &= 0 \ , \\ \Leftrightarrow \rho\omega^2\xi_\varphi + 2i\rho\omega\Omega\cos\theta\xi_\theta - \frac{1}{r\ \sin\theta}\frac{\partial P'}{\partial \varphi} &= 0 \ .\end{aligned}$$

From the last two equations we obtain an expression for ξ_θ and ξ_φ, after some manipulations. In order to derive the expression for ξ_φ we start by rewriting the second equation:

$$\rho\omega^2\xi_\theta - 2i\rho\omega\Omega\cos\theta\xi_\varphi - \frac{1}{r}\frac{\partial P'}{\partial\theta} = 0 \Leftrightarrow \xi_\theta = \frac{1}{\rho\omega^2 r}\frac{\partial P'}{\partial\theta} + \frac{2i\Omega\cos\theta}{\omega}\xi_\varphi \ .$$

Subsequently filling this in in the third equation, we obtain the expression for ξ_φ:

$$\rho\omega^2\xi_\varphi + \frac{2i\Omega\cos\theta}{r\ \omega}\frac{\partial P'}{\partial\theta} - 4\rho\Omega^2\cos^2\theta\xi_\varphi - \frac{1}{r\ \sin\theta}\frac{\partial P'}{\partial\varphi} = 0 \ ,$$

$$\Leftrightarrow\ \xi_\varphi = \frac{1}{\rho\ \omega^2\ r}\frac{\sqrt{1-\mu^2}}{1-\nu^2\mu^2}\left[i\nu\mu\frac{\partial P'}{\partial\mu} + \frac{1}{1-\mu^2}\frac{\partial P'}{\partial\varphi}\right] \ ,$$

where we used the definitions of the modified latitudinal variable $\mu = \cos\theta$ and the spin parameter $\nu = 2\Omega/\omega$.

Similarly, we rewrite the third equation as:

$$\rho\omega^2\xi_\varphi + 2i\rho\omega\Omega\cos\theta\xi_\theta - \frac{1}{r\ \sin\theta}\frac{\partial P'}{\partial\varphi} = 0 \Leftrightarrow \xi_\varphi = \frac{1}{\rho\omega^2 r\sin\theta}\frac{\partial P'}{\partial\varphi} - \frac{2i\Omega\cos\theta}{\omega}\xi_\theta \ .$$

Subsequently filling this in in the second equation, we obtain the expression for ξ_θ:

$$\rho\omega^2\xi_\theta - 2i\rho\omega\Omega\cos\theta\left[\frac{1}{\rho\omega^2 r\sin\theta}\frac{\partial P'}{\partial\varphi} - \frac{2i\Omega\cos\theta}{\omega}\xi_\theta\right] - \frac{1}{r}\frac{\partial P'}{\partial\theta} = 0$$

$$\Leftrightarrow\ \xi_\theta = \frac{1}{\rho\ \omega^2\ r}\frac{1}{1-\nu^2\mu^2}\left[\frac{i\nu\mu}{\sqrt{1-\mu^2}}\frac{\partial P'}{\partial\varphi} - \sqrt{1-\mu^2}\frac{\partial P'}{\partial\mu}\right]$$

The linearized continuity equation is given by (Aerts et al., 2010):

$$\rho' + \nabla\cdot(\rho\boldsymbol{\xi}) = 0 \ ,$$

which, in spherical coordinates, is given by:

$$\rho' + \frac{1}{r^2}\frac{\partial}{\partial r}\left(r^2\rho\xi_r\right) + \frac{1}{r\sin\theta}\frac{\partial}{\partial\theta}\left(\sin\theta\rho\xi_\theta\right) + \frac{1}{r\sin\theta}\frac{\partial}{\partial\varphi}\left(\rho\xi_\varphi\right) = 0 \ .$$

Writing P', ρ' and ξ_r as (as was done in Lee and Saio, 1997):

$$\rho' = \rho'(r)H_r(\mu;\nu)e^{i(m\varphi-\omega t)} \ ,$$
$$P' = p'(r)H_r(\mu;\nu)e^{i(m\varphi-\omega t)} \ ,$$
$$\xi_r = \xi_r(r)H_r(\mu;\nu)e^{i(m\varphi-\omega t)} \ ,$$

the first two components of the linearized continuity equation become:

$$\rho' + \frac{1}{r^2}\frac{\partial}{\partial r}\left(r^2\rho\xi_r\right) = \rho'(r)H_r(\mu;\nu)e^{i(m\varphi-\omega t)} + \frac{1}{r^2}\frac{\partial}{\partial r}\left(r^2\rho\xi_r(r)\right)H_r(\mu;\nu)e^{i(m\varphi-\omega t)}$$

The latter two components can be rewritten using the expressions for ξ_θ and ξ_φ:

$$\frac{1}{r\sin\theta}\frac{\partial}{\partial\theta}\left(\sin\theta\rho\xi_\theta\right) = \frac{p'(r)}{r\sin\theta}\frac{\partial}{\partial\theta}\left[\frac{\sin\theta}{\omega^2 r}\left(\frac{e^{i(m\varphi-\omega t)}}{1-\nu^2\cos^2\theta}\right)\right.$$
$$\left.\left\{\frac{i\nu\cos\theta}{\sin\theta}H_r(im) + \frac{1}{r}\frac{\partial H_r}{\partial\theta}\right\}\right] \ ,$$

$$\Leftrightarrow\ \frac{1}{r\sin\theta}\frac{\partial}{\partial\theta}\left(\sin\theta\rho\xi_\theta\right) = \frac{p'(r)e^{i(m\varphi-\omega t)}}{\omega^2 r^2\sin\theta}\frac{\partial}{\partial\theta}\left[\left(\frac{1}{1-\nu^2\cos^2\theta}\right)\left(-m\nu\cos\theta H_r + \frac{\sin\theta}{r}\frac{\partial H_r}{\partial\theta}\right)\right] \ ,$$

$$\frac{1}{r\sin\theta}\frac{\partial}{\partial\varphi}\left(\rho\xi_\varphi\right) = \frac{p'(r)}{r\sin\theta}\frac{\partial}{\partial\varphi}\left[\frac{1}{\omega^2 r}\left(\frac{e^{i(m\varphi-\omega t)}}{1-\nu^2\cos^2\theta}\right)\left(-i\nu\cos\theta\frac{\partial H_r}{\partial\theta}+\frac{im}{\sin\theta}H_r\right)\right] ,$$

$$\Leftrightarrow \frac{1}{r\sin\theta}\frac{\partial}{\partial\varphi}\left(\rho\xi_\varphi\right) = \frac{p'(r)e^{i(m\varphi-\omega t)}}{r^2\omega^2\sin\theta}\left(\frac{1}{1-\nu^2\cos^2\theta}\right)\left(m\nu\cos\theta\frac{\partial H_r}{\partial\theta}-\frac{m^2}{\sin\theta}H_r\right) .$$

where we dropped the latitudinal dependence of the Hough function, in order to ease the notation (i.e. $H_r(\mu;\nu) = H_r$). Combining the obtained expressions yields (after some manipulations):

$$\frac{1}{r\sin\theta}\frac{\partial}{\partial\varphi}\left(\rho\xi_\varphi\right)+\frac{1}{r\sin\theta}\frac{\partial}{\partial\theta}\left(\sin\theta\rho\xi_\theta\right) = \frac{p'(r)e^{i(m\varphi-\omega t)}}{r^2\omega^2}$$
$$\left[-\frac{m^2}{\sin^2\theta}\left(\frac{1}{1-\nu^2\cos^2\theta}H_r\right)+\frac{H_r}{\sin\theta}\frac{\partial}{\partial\theta}\left(-\frac{\nu\cos\theta m}{1-\nu^2\cos^2\theta}\right)+\frac{1}{\sin\theta}\frac{\partial}{\partial\theta}\left(\frac{\sin\theta}{1-\nu^2\cos^2\theta}\frac{\partial H_r}{\partial\theta}\right)\right] ,$$

$$\Leftrightarrow \frac{1}{r\sin\theta}\frac{\partial}{\partial\varphi}\left(\rho\xi_\varphi\right)+\frac{1}{r\sin\theta}\frac{\partial}{\partial\theta}\left(\sin\theta\rho\xi_\theta\right) = \frac{p'(r)e^{i(m\varphi-\omega t)}}{r^2\omega^2}$$
$$\left[\left(\frac{1}{1-\nu^2\mu^2}\right)\left(\frac{-m^2}{1-\mu^2}+\frac{\nu m\left(1+\nu^2\mu^2\right)}{1-\nu^2\mu^2}\right)H_r+\frac{\partial}{\partial\mu}\left(\frac{1-\mu^2}{1-\nu^2\mu^2}\frac{\partial H_r}{\partial\mu}\right)\right] ,$$

which is the Laplace tidal operator defined in Equation (2.31). Writing ξ_θ and ξ_φ in a similar way allows one to reconstruct the expressions for the latitudinal and azimuthal Hough functions (basing ourselves on Lee and Saio, 1997):

$$\xi_\theta = \frac{1}{r\omega^2\rho}p'(r)H_\theta e^{i(m\varphi-\omega t)} ,$$
$$\xi_\varphi = \frac{i}{r\omega^2\rho}p'(r)H_\varphi e^{i(m\varphi-\omega t)} ,$$

so that we obtain:

$$\xi_\theta = \frac{p'(r)}{\rho\ \omega^2\ r}\frac{e^{i(m\varphi-\omega t)}}{1-\nu^2\mu^2}\left[-\frac{m\nu\mu}{\sqrt{1-\mu^2}}H_r-\sqrt{1-\mu^2}\frac{\partial H_r}{\partial\mu}\right] ,$$
$$\Leftrightarrow \xi_\theta = \frac{p'(r)}{\rho\ \omega^2\ r}\frac{e^{i(m\varphi-\omega t)}}{1-\nu^2\cos^2\theta}\frac{1}{\sin\theta}\left[-m\nu\cos\theta H_r+\sin\theta\frac{\partial H_r}{\partial\theta}\right] ,$$

$$\xi_\varphi = \frac{p'(r)e^{i(m\varphi-\omega t)}}{\rho\ \omega^2\ r}\frac{\sqrt{1-\mu^2}}{1-\nu^2\mu^2}\left[i\nu\mu\frac{\partial H_r}{\partial\mu}+\frac{im}{1-\mu^2}H_r\right] ,$$
$$\Leftrightarrow \xi_\varphi = \frac{1}{\rho\ \omega^2\ r}\frac{\sin\theta}{1-\nu^2\cos^2\theta}\left[-\frac{i\nu\cos\theta}{\sin\theta}\frac{\partial H_r}{\partial\theta}+\frac{im}{\sin^2\theta}H_r\right] .$$

Therefore, the latitudinal and azimuthal Hough functions are given by:

$$H_\theta\sin\theta = \frac{1}{1-\nu^2\cos^2\theta}\left[-m\nu\cos\theta H_r+\sin\theta\frac{\partial H_r}{\partial\theta}\right] ,$$
$$H_\varphi\sin\theta = \frac{1}{1-\nu^2\cos^2\theta}\left[-\nu\cos\theta\sin\theta\frac{\partial H_r}{\partial\theta}+mH_r\right] ,$$

the expressions given in the main text (and in Prat et al. (2019)).

The Townsend (2003) approximation

In a uniformly rotating star, assuming the Cowling approximation (Cowling, 1941), assuming a temporal dependence $\boldsymbol{\xi} \propto e^{i\omega t}$ for adiabatic oscillations in the corotating frame, the pulsation equations are given by (Lee and Saio, 1997):

$$
\begin{aligned}
&-\rho\omega^2\xi_r - 2i\rho\omega\Omega\sin\theta\xi_\theta = -\frac{\partial p'}{\partial r} - g\rho' \ , \\
&-\rho\omega^2\xi_\theta - 2i\rho\omega\Omega\cos\theta\xi_\phi = -\frac{1}{r}\frac{\partial p'}{\partial \theta} \ , \\
&-\rho\omega^2\xi_\phi + 2i\rho\omega\Omega\sin\theta\xi_r + 2i\rho\omega\Omega\cos\theta\xi_\theta = -\frac{1}{r\ \sin\theta}\frac{\partial p'}{\partial \phi} \ , \\
&\rho' + \frac{1}{r^2}\frac{\partial}{\partial r}\left(\rho r^2\xi_r\right) + \frac{\rho}{r\ \sin\theta}\frac{\partial}{\partial\theta}\left(\sin\theta\ \xi_\theta\right) + \frac{\rho}{r\ \sin\theta}\frac{\partial \xi_\phi}{\partial\phi} = 0 \ , \\
&\frac{\rho'}{\rho} = \frac{1}{\Gamma_1}\frac{p'}{p} + \xi_r\frac{N^2}{g} \ .
\end{aligned}
$$

In the TAR it reduces to (Townsend, 2003):

$$
\begin{aligned}
&-\rho\omega^2\xi_r = -\frac{\partial p'}{\partial r} - g\rho' \ , \\
&-\rho\omega^2\xi_\theta - 2i\rho\omega\Omega\cos\theta\xi_\phi = -\frac{1}{r}\frac{\partial p'}{\partial \theta} \ , \\
&-\rho\omega^2\xi_\phi + 2i\rho\omega\Omega\cos\theta\xi_\theta = -\frac{1}{r\ \sin\theta}\frac{\partial p'}{\partial \phi} \ , \\
&\rho' + \frac{1}{r^2}\frac{\partial}{\partial r}\left(\rho r^2\xi_r\right) + \frac{\rho}{r\ \sin\theta}\frac{\partial}{\partial\theta}\left(\sin\theta\ \xi_\theta\right) + \frac{\rho}{r\ \sin\theta}\frac{\partial \xi_\phi}{\partial\phi} = 0 \ , \\
&\frac{\rho'}{\rho} = \frac{1}{\Gamma_1}\frac{p'}{p} + \xi_r\frac{N^2}{g} \ .
\end{aligned}
$$

ξ_r, p', and ρ' share the same polar dependence, whereas ξ_θ and ξ_ϕ share the same radial dependence. All equations are homogeneous and first order in ϕ, yielding a $e^{im\phi}$ azimuthal dependence, where the azimuthal order m is constrained to integral values in order to preserve the single-valuedness of the solutions under a transformation $\phi \to \phi + 2\pi$. Hence, the following general solutions are found:

$$
\begin{aligned}
\xi_r &= Y_r(r)\ \Theta(\theta)\ e^{im\phi+i\omega t} \ , \\
p' &= Y_p(r)\ \Theta(\theta)\ e^{im\phi+i\omega t} \ , \\
\rho' &= Y_\rho(r)\ \Theta(\theta)\ e^{im\phi+i\omega t} \ , \\
\sin\theta\xi_\theta &= Y_\perp(r)\ \hat{\Theta}(\theta)\ e^{im\phi+i\omega t} \ , \\
i\sin\theta\xi_\phi &= Y_\perp(r)\ \tilde{\Theta}(\theta)\ e^{im\phi+i\omega t} \ ,
\end{aligned}
$$

where $\sin\theta$ is introduced for convenience in the last two expressions. **$\Theta(\theta)$, $\hat{\Theta}(\theta)$ and $\tilde{\Theta}(\theta)$ are equivalent to H_r, H_θ and H_φ, respectively (the Hough functions defined in the main text).** These general solutions can then be substituted into the pulsation equations, making use of the following (defined) differential operator: (wrongly defined in Townsend (2003))

$$
\mathcal{D} \equiv -\sin\theta\frac{\mathrm{d}}{\mathrm{d}\theta} \equiv (1-\mu^2)\frac{\mathrm{d}}{\mathrm{d}\mu} \ ,
$$

where μ is the modified latitudinal variable defined before, yielding the following radial pulsation equations:

$$
\begin{aligned}
&-\rho\omega^2 Y_r = -\frac{\mathrm{d}Y_p}{\mathrm{d}r} - gY_\rho \ , \\
&Y_\perp = \frac{1}{\rho\omega^2 r} Y_p \ , \\
&Y_\rho + \frac{1}{r^2}\frac{\mathrm{d}}{\mathrm{d}r}\left(\rho r^2 Y_r\right) - \frac{\rho\lambda Y_\perp}{r} = 0 \ , \\
&\frac{Y_\rho}{\rho} = \frac{1}{\Gamma_1}\frac{Y_p}{p} + Y_r\frac{N^2}{g} \ ,
\end{aligned}
$$

and the following polar pulsation equations:

$$
\begin{aligned}
&-\hat{\Theta}(\theta) - \nu\mu\tilde{\Theta}(\theta) = \mathcal{D}\Theta(\theta) \ , \\
&-\tilde{\Theta}(\theta) - \nu\mu\hat{\Theta}(\theta) = m\Theta(\theta) \ , \\
&\lambda\left(1-\mu^2\right)\Theta(\theta) - \mathcal{D}\hat{\Theta}(\theta) + m\tilde{\Theta}(\theta) = 0 \ ,
\end{aligned}
$$

where the eigenvalue λ has been introduced as a separation constant.

Proof. Three of these pulsations equations are obtained in the following way:

$$
\begin{aligned}
&-\rho\omega^2\xi_r = -\frac{\partial p'}{\partial r} - g\rho' \ , \\
\Leftrightarrow\ &-\rho\omega^2\ Y_r(r)\ \Theta(\theta)\ e^{im\phi+i\omega t} = -\frac{\partial\left(Y_p(r)\ \Theta(\theta)\ e^{im\phi+i\omega t}\right)}{\partial r} - gY_\rho(r)\ \Theta(\theta)\ e^{im\phi+i\omega t} \ , \\
\Leftrightarrow\ &\left(-\rho\omega^2\right) Y_r(r)\ \left(\Theta(\theta)\right) = \left(-\frac{\mathrm{d}Y_p}{\mathrm{d}r} - gY_\rho\right)\left(\Theta(\theta)\right) \ , \\
\Leftrightarrow\ &-\rho\omega^2\ Y_r(r) = -\frac{\mathrm{d}Y_p}{\mathrm{d}r} - gY_\rho \ ,
\end{aligned}
$$

$$
\begin{aligned}
&-\rho\omega^2\xi_\theta - 2i\rho\omega\Omega\cos\theta\xi_\phi = -\frac{1}{r}\frac{\partial p'}{\partial\theta} \ , \\
\Leftrightarrow\ &-\rho\omega^2 Y_\perp(r)\left(\frac{\hat{\Theta}(\theta)}{\sin\theta}\right) - 2\rho\omega\Omega Y_\perp(r)\left(\frac{\cos\theta}{\sin\theta}\tilde{\Theta}(\theta)\right) = -\frac{1}{r}Y_p(r)\left(\frac{\partial\Theta(\theta)}{\partial\theta}\right) \ , \\
\Leftrightarrow\ &\left(\rho\omega^2\right)\left(Y_\perp(r)\right)\left[\frac{\hat{\Theta}(\theta)}{\sin\theta} - \mu\nu\ \frac{\tilde{\Theta}(\theta)}{\sin\theta}\right] = \frac{1}{r}Y_p(r)\left(\frac{\partial\Theta(\theta)}{\partial\theta}\right) \ , \\
\Leftrightarrow\ &Y_\perp(r) = \frac{1}{r\ \rho\omega^2}Y_p(r) \ , \\
\Leftrightarrow\ &\hat{\Theta}(\theta) + \mu\nu\ \tilde{\Theta}(\theta) = \sin\theta\ \frac{\partial\Theta(\theta)}{\partial\theta} \ , \\
\Leftrightarrow\ &-\hat{\Theta}(\theta) - \mu\nu\ \tilde{\Theta}(\theta) = \mathcal{D}\Theta(\theta) \ .
\end{aligned}
$$

□

Proof. The other pulsation equations are obtained in the following way:

$$
\begin{aligned}
&-\rho\omega^2\xi_\phi + 2i\rho\omega\Omega\cos\theta\xi_\theta = -\frac{1}{r\ \sin\theta}\frac{\partial p'}{\partial\phi}\ ,\\
\Leftrightarrow\ & i\rho\omega^2\left(Y_\perp(r)\right)\left(\frac{\tilde\Theta(\theta)}{\sin\theta}\right) + i\rho\omega^2(Y_\perp(r))\left(\nu\ \frac{\cos\theta}{\sin\theta}\hat\Theta(\theta)\right) = -im\left(\frac{1}{r}\ Y_p(r)\right)\left(\frac{\Theta(\theta)}{\sin\theta}\right)\ ,\\
\Leftrightarrow\ & Y_\perp(r) = \frac{1}{r\ \rho\omega^2}Y_p(r)\ ,\\
\Leftrightarrow\ & \tilde\Theta(\theta) + \mu\nu\ \hat\Theta(\theta) = -m\ \Theta(\theta)\ ,
\end{aligned}
$$

$$
\begin{aligned}
&\rho' + \frac{1}{r^2}\frac{\partial}{\partial r}\left(\rho r^2\xi_r\right) + \frac{\rho}{r\ \sin\theta}\frac{\partial}{\partial\theta}\left(\sin\theta\ \xi_\theta\right) + \frac{\rho}{r\ \sin\theta}\frac{\partial\xi_\phi}{\partial\phi} = 0\ ,\\
\Leftrightarrow\ & Y_\rho(r)\ \Theta(\theta)\ + \frac{1}{r^2}\frac{\partial}{\partial r}\left(\rho r^2 Y_r(r)\ \Theta(\theta)\ \right) + \frac{\rho}{r\ \sin\theta}\frac{\partial}{\partial\theta}\left(Y_\perp(r)\ \hat\Theta(\theta)\ \right)\\
&+ \frac{\rho}{r\ \sin\theta}\frac{\partial}{\partial\phi}\left(-i\frac{\tilde\Theta(\theta)}{\sin\theta}Y_\perp(r)\ \right) = 0\ ,\\
\Leftrightarrow\ & \Theta(\theta)\ \left[Y_\rho(r)\ + \frac{1}{r^2}\frac{\partial}{\partial r}\left(\rho r^2 Y_r(r)\right)\right] + \frac{Y_\perp(r)\rho}{r}\left[\frac{1}{\sin\theta}\frac{\mathrm{d}\hat\Theta(\theta)}{\mathrm{d}\theta}\right.\\
&\left.+\frac{m\ \tilde\Theta(\theta)}{\sin^2\theta}\right] - \Theta(\theta)\left(\frac{\rho\lambda Y_\perp(r)}{r}\right) + \Theta(\theta)\left(\frac{\rho\lambda Y_\perp(r)}{r}\right) = 0\ ,\\
\Leftrightarrow\ & Y_\rho(r)\ + \frac{1}{r^2}\frac{\partial}{\partial r}\left(\rho r^2 Y_r(r)\right) - \frac{\rho\lambda Y_\perp(r)}{r} = 0\ ,\\
\Leftrightarrow\ & \frac{1}{\sin\theta}\frac{\mathrm{d}\hat\Theta(\theta)}{\mathrm{d}\theta} + \frac{m\ \tilde\Theta(\theta)}{\sin^2\theta} + \lambda\Theta(\theta) = 0\ ,\\
\Leftrightarrow\ & \lambda\left(1-\mu^2\right)\Theta(\theta) - \mathcal{D}\hat\Theta(\theta) + m\tilde\Theta(\theta) = 0\ ,
\end{aligned}
$$

$$
\begin{aligned}
&\frac{\rho'}{\rho} = \frac{1}{\Gamma_1}\frac{p'}{p} + \xi_r\frac{N^2}{g}\ ,\\
\Leftrightarrow\ & \frac{Y_\rho(r)\ \Theta(\theta)}{\rho} = \frac{1}{\Gamma_1}\frac{Y_p(r)\ \Theta(\theta)}{p} + \frac{N^2}{g}Y_r(r)\ \Theta(\theta)\ \ ,\\
\Leftrightarrow\ & \frac{Y_\rho}{\rho} = \frac{1}{\Gamma_1}\frac{Y_p}{p} + Y_r\frac{N^2}{g}\ .
\end{aligned}
$$

□

Laplace's tidal equations in a first order form are obtained when the second polar equation is used to eliminate $\tilde\Theta(\theta)$ in equations the first and third polar equations:

$$
\begin{aligned}
&\left(\mathcal{D} - m\nu\mu\right)\Theta(\theta) = \left(\nu^2\mu^2 - 1\right)\hat\Theta(\theta)\ ,\\
&\left(\mathcal{D} + m\nu\mu\right)\hat\Theta(\theta) = \left[\lambda\left(1-\mu^2\right) - m^2\right]\Theta(\theta)\ ,\\
&-\tilde\Theta(\theta) - \nu\mu\hat\Theta(\theta) = m\Theta(\theta)\ .
\end{aligned}
$$

Proof. This can be proven in the following way:

$$
\begin{aligned}
& -\tilde{\Theta}(\theta) - \nu\mu\hat{\Theta}(\theta) = m\Theta(\theta) \ , \\
\Leftrightarrow\ & \tilde{\Theta}(\theta) = -\nu\mu\hat{\Theta}(\theta) - m\Theta(\theta) - \hat{\Theta}(\theta) - \nu\mu\tilde{\Theta}(\theta) = \mathcal{D}\Theta(\theta) \ , \\
\Leftrightarrow\ & -\hat{\Theta}(\theta) + \nu\mu\left(\nu\mu\hat{\Theta}(\theta) + m\Theta(\theta)\right) = \mathcal{D}\Theta(\theta) \ , \\
\Leftrightarrow\ & \left(\mathcal{D} - m\nu\mu\right)\Theta(\theta) = \left(\nu^2\mu^2 - 1\right)\hat{\Theta}(\theta) \\
& \lambda\left(1-\mu^2\right)\Theta(\theta) - \mathcal{D}\hat{\Theta}(\theta) + m\tilde{\Theta}(\theta) = 0 \ , \\
\Leftrightarrow\ & \lambda\left(1-\mu^2\right)\Theta(\theta) - \mathcal{D}\hat{\Theta}(\theta) - m\left(\nu\mu\hat{\Theta}(\theta) + m\Theta(\theta)\right) = 0 \ , \\
\Leftrightarrow\ & \left(\mathcal{D} + m\nu\mu\right)\hat{\Theta}(\theta) = \left[\lambda\left(1-\mu^2\right) - m^2\right]\Theta(\theta) \ .
\end{aligned}
$$

□

Solving these analytically needs appropriate boundary conditions: for non-axisymmetric modes the solutions should decay to zero when points where $\mu = \pm 1$ are approached (ensuring single-valuedness at the stellar poles), whereas for axisymmetric modes the polar gradient should decay to zero (ensuring the smoothness of solutions at the poles). Note that ν always appears in product with μ (a latitudinal coordinate), so that (by intuition) for large values of ν, the Hough functions can only differ appreciably from zero in a narrow equatorial region of small $|\mu|$, forming a so-called Coriolis-force originated 'equatorial waveguide', preventing low-frequency waves from propagating to high latitudes (Townsend, 2003). For such equatorially trapped waves μ is small, so that terms of the order of μ^2 in the tidal equations can be neglected ('the equatorial beta-plane approximation', as dubbed in geophysical literature), and the differential operator $\mathcal{D}$ can be approximated by (Matsuno, 1966; Lindzen, 1967):

$$\mathcal{D} \approx \frac{\mathrm{d}}{\mathrm{d}\mu} \ .$$

Two cases should in general be considered, those where $\lambda \approx m^2$ and those where it does not. However, in order to describe g modes we only need to consider the case when $\lambda \neq m^2$ (Townsend, 2003), so that the tidal equations become (neglecting terms in μ^2):

$$
\begin{aligned}
\left(\frac{\mathrm{d}}{\mathrm{d}\mu} - m\nu\mu\right)\Theta(\theta) &= \left(\nu^2\mu^2 - 1\right)\hat{\Theta}(\theta) \ , \\
\left(\frac{\mathrm{d}}{\mathrm{d}\mu} + m\nu\mu\right)\hat{\Theta}(\theta) &= \left[\lambda - m^2\right]\Theta(\theta) \ .
\end{aligned}
$$

$\Theta(\theta)$ can be eliminated from the system of equations defined above, yielding the following second-order differential equation for $\hat{\Theta}(\theta)$:

$$\frac{\mathrm{d}^2\hat{\Theta}(\theta)}{\mathrm{d}\mu^2} + \left(m\nu - m^2 + \lambda - \lambda\nu^2\mu^2\right)\hat{\Theta}(\theta) = 0 \ .$$

Proof. The second-order approximate version of Laplace's tidal equations is obtained in the following way:

$$
\begin{aligned}
&\left(\frac{\mathrm{d}}{\mathrm{d}\mu} + m\nu\mu\right)\hat{\Theta}(\theta) = \left[\lambda - m^2\right]\Theta(\theta) \ , \\
\Leftrightarrow\ &\Theta(\theta) = \frac{\left(\frac{\mathrm{d}}{\mathrm{d}\mu} + m\nu\mu\right)\hat{\Theta}(\theta)}{\lambda - m^2} \\
&\left(\frac{\mathrm{d}}{\mathrm{d}\mu} - m\nu\mu\right)\Theta(\theta) = \left(\nu^2\mu^2 - 1\right)\hat{\Theta}(\theta) \ , \\
\Leftrightarrow\ &\left(\frac{\mathrm{d}}{\mathrm{d}\mu} - m\nu\mu\right)\left[\left(\frac{\mathrm{d}}{\mathrm{d}\mu} + m\nu\mu\right)\hat{\Theta}(\theta)\right] \\
&= \left(\nu^2\mu^2 - 1\right)\left(\lambda - m^2\right)\hat{\Theta}(\theta) \\
&\left(\frac{\mathrm{d}}{\mathrm{d}\mu} - m\nu\mu\right)\Theta(\theta) = \left(\nu^2\mu^2 - 1\right)\hat{\Theta}(\theta) \ , \\
\Leftrightarrow\ &\left(\mathrm{d}\,\mu + m\nu + m\nu\mu\frac{\mathrm{d}}{\mathrm{d}\mu} - m\nu\mu\frac{\mathrm{d}}{\mathrm{d}\mu} - m^2\nu^2\mu^2\right)\hat{\Theta}(\theta) = \\
&\left(\nu^2\mu^2\lambda - m^2\nu^2\mu^2 - \lambda + m^2\right)\hat{\Theta}(\theta) \ , \\
\Leftrightarrow\ &\frac{\mathrm{d}^2\hat{\Theta}(\theta)}{\mathrm{d}\mu^2} + \left(m\nu - m^2 + \lambda - \lambda\nu^2\mu^2\right)\hat{\Theta}(\theta) = 0 \ .
\end{aligned}
$$

□

Changing parameters:

$$
\begin{aligned}
&\sigma \equiv (L\nu)^{1/2}\mu \ , \\
&L^2 \equiv \lambda \ , \\
&S \equiv \frac{m\nu - m^2 + L^2}{L\nu} \ ,
\end{aligned}
$$

allows one to simplify the equation:

$$
\frac{\mathrm{d}^2\hat{\Theta}(\theta)}{\mathrm{d}\sigma^2} + \left(S - \sigma^2\right)\hat{\Theta}(\theta) = 0 \ .
$$

Proof. This simplification is obtained in the following way:

$$\begin{aligned}
&\frac{\mathrm{d}^2\hat{\Theta}(\theta)}{\mathrm{d}\mu^2} + \left(m\nu - m^2 + \lambda - \lambda\nu^2\mu^2\right)\hat{\Theta}(\theta) = 0 \ , \\
\Leftrightarrow &(L\nu)\,\frac{\mathrm{d}^2\hat{\Theta}(\theta)}{\mathrm{d}\sigma^2} + \left(m\nu - m^2 + \lambda - L\nu\sigma^2\right)\hat{\Theta}(\theta) = 0 \ , \\
\Leftrightarrow &(L\nu)\,\frac{\mathrm{d}^2\hat{\Theta}(\theta)}{\mathrm{d}\sigma^2} + (L\nu)\left(\frac{m\nu - m^2 + L^2}{L\nu} - \sigma^2\right)\hat{\Theta}(\theta) = 0 \ , \\
\Leftrightarrow &\frac{\mathrm{d}^2\hat{\Theta}(\theta)}{\mathrm{d}\sigma^2} + \left(S - \sigma^2\right)\hat{\Theta}(\theta) = 0 \ .
\end{aligned}$$

□

This resembles the time-independent Schrödinger equation for a quantum harmonic oscillator, which can only solved when $S = 2s + 1$ for an integer 'meridional order' $s \geq 0$, yielding the following solutions (Griffiths, 2017):

$$\hat{\Theta}(\sigma) = H_s(\sigma)\ e^{-\sigma^2/2} \ ,$$

where H_s is the Hermite polynomial of order s, defined in the following way:

$$H_s(\sigma) = (-1)^s\, e^{\sigma^2}\frac{d^s e^{-\sigma^2}}{d\sigma^s} \ .$$

Proof. The time-independent Schrödinger-like equation can be solved using the Frobenius method (Griffiths, 2017). Rewriting the equation in the following way:

$$\begin{aligned}
&\frac{\mathrm{d}^2\hat{\Theta}(\theta)}{\mathrm{d}\sigma^2} + \left(S - \sigma^2\right)\hat{\Theta}(\theta) = 0 \ , \\
\Leftrightarrow &\frac{\mathrm{d}^2\hat{\Theta}(\theta)}{\mathrm{d}\sigma^2} = \left(\sigma^2 - S\right)\hat{\Theta}(\theta) \ ,
\end{aligned}$$

one obtains for large σ:

$$\frac{\mathrm{d}^2\hat{\Theta}(\theta)}{\mathrm{d}\sigma^2} - \left(\sigma^2\right)\hat{\Theta}(\theta) \approx 0 \ ,$$

which can trivially be solved by:

$$\hat{\Theta}(\theta) \approx A\ e^{-\sigma^2/2} + B\ e^{\sigma^2/2} \ .$$

However, keeping in mind that the solution needs to be normalizable (for all σ), one should discard the B term, so that the following asymptotic form is obtained for large σ:

$$\hat{\Theta}(\theta) \to A\ e^{-\sigma^2/2} \Leftrightarrow\ \sigma = \text{large} \ .$$

Therefore, one can separate the following asymptotic term from the general solution:

$$\hat{\Theta}(\theta) = h(\sigma)\ e^{-\sigma^2/2}.$$

Differentiating this equation with respect to σ, one obtains:

$$\begin{aligned}
\frac{\mathrm{d}\hat{\Theta}(\theta)}{\mathrm{d}\sigma} &= \left(\frac{\mathrm{d}h(\sigma)}{\mathrm{d}\sigma} - \sigma h(\sigma)\right) e^{-\sigma^2/2}\ , \\
\frac{\mathrm{d}^2\hat{\Theta}(\theta)}{\mathrm{d}\sigma^2} &= \left(\frac{\mathrm{d}^2h(\sigma)}{\mathrm{d}\sigma^2} - 2\sigma\frac{\mathrm{d}h(\sigma)}{\mathrm{d}\sigma} + (\sigma^2-1)h(\sigma)\right) e^{-\sigma^2/2}\ ,
\end{aligned}$$

which, when filled in in the time-independent Schrödinger-like equation, yields:

$$\begin{aligned}
&\left(\frac{\mathrm{d}^2h(\sigma)}{\mathrm{d}\sigma^2} - 2\sigma\frac{\mathrm{d}h(\sigma)}{\mathrm{d}\sigma} + (\sigma^2-1)h(\sigma)\right) e^{-\sigma^2/2} \\
&= \left(\sigma^2 - S\right) h(\sigma)\ e^{-\sigma^2/2}\ , \\
\Leftrightarrow\ &\frac{\mathrm{d}^2h(\sigma)}{\mathrm{d}\sigma^2} - 2\sigma\frac{\mathrm{d}h(\sigma)}{\mathrm{d}\sigma} + (S-1)\ h(\sigma) = 0\ .
\end{aligned}$$

By now looking for a solution in the form of a power series (Frobenius method) in σ, one obtains:

$$h(\sigma)\ = a_0 + a_1\sigma + a_2\sigma^2 + a_3\sigma^3 + \ldots = \sum_{j=0}^{\infty} a_j\ \sigma^j\ ,$$

which, when differentiated term by term, yields:

$$\begin{aligned}
\frac{\mathrm{d}h(\sigma)}{\mathrm{d}\sigma} &= a_1 + 2a_2\sigma + 3a_3\sigma^2 + \ldots = \sum_{j=0}^{\infty} j\ a_j\ \sigma^{j-1}\ , \\
\frac{\mathrm{d}^2h(\sigma)}{\mathrm{d}\sigma^2} &= 2a_2 + (2*3)\ a_3\sigma + \ldots \\
&= \sum_{j=0}^{\infty}(j+1)(j+2)\ a_{j+2}\ \sigma^j\ ,
\end{aligned}$$

which can now be put in the previously obtained equation:

$$\sum_{j=0}^{\infty}\left[(j+1)(j+2)\ a_{j+2} - 2\ j\ a_j\ + (S-1)\,a_j\right]\sigma^j = 0\ .$$

Therefore, since the coefficient of each power of σ must vanish, the following equation must vanish:

$$\begin{aligned}
&(j+1)(j+2)\ a_{j+2} - 2\ j\ a_j\ + (S-1)\,a_j = 0\ , \\
\Leftrightarrow\ &a_{j+2} = \left(\frac{2\ j+1-S}{(j+1)(j+2)}\right) a_j\ ,
\end{aligned}$$

which is the recursion formula equivalent to the time-independent Schrödinger-like equation. If one starts with a_0, it will generate all even-numbered coefficients:

$$a_2 = \frac{(1-S)}{2}a_0, \qquad a_4 = \frac{(5-S)}{12}a_2, \dots \ ,$$

whereas if one starts with a_1, it will generate all odd-numbered coefficients:

$$a_3 = \frac{(3-S)}{6}a_1, \qquad a_5 = \frac{(7-S)}{20}a_3, \dots \ .$$

The complete solution can thus be written as being comprised of these even- and odd-numbered coefficient parts:

$$\begin{aligned} h(\sigma) &= h_{\text{even}}(\sigma) + h_{\text{odd}}(\sigma) \ , \\ h_{\text{even}}(\sigma) &\equiv a_0 + a_2\sigma^2 + a_4\sigma^4 + \dots \ , \\ h_{\text{odd}}(\sigma) &\equiv a_1\sigma + a_3\sigma^3 + a_5\sigma^5 + \dots \ . \end{aligned}$$

Hence, the equation is determined by two arbitrary constants a_0 and a_1. However, not all the solutions obtained in such a way are normalizable: at very large j the recursion formula can be approximated by:

$$a_{j+2} \approx \frac{2}{j}a_j \ ,$$

with the approximate solution:

$$a_j \approx \frac{C}{(j/2)!} \ ,$$

for some constant C, which yields (at large σ, so that only the highest powers contribute significantly):

$$h(\sigma) \approx C\sum_{j=0}^{\infty}\frac{1}{(j/2)!}\sigma^j \approx C\sum_{j=0}^{\infty}\frac{1}{j!}\sigma^{2j} \approx Ce^{\sigma^2} \ ,$$

which yields the following asymptotic behaviour for $\hat{\Theta}(\theta)$:

$$\hat{\Theta}(\theta) = h(\sigma)\ e^{-\sigma^2/2} \approx Ce^{\sigma^2/2} \ ,$$

which is the non-normalizable asymptotic behaviour. Therefore, the power series needs to terminate, in order for solutions to be normalizable: there must be some 'highest' j (which we will call s) for which the recursion formula becomes $a_{j+2} = 0$. This truncates either the series h_{even} or h_{odd}, as the other one needs to be zero from the start: $a_1 = 0$ if s is even, $a_0 = 0$ if s is odd. For

physically acceptable solutions the recursion formula thus requires solutions for which $S = 2s + 1$, so that it becomes:

$$a_{j+2} = \left(\frac{-2(s-j)}{(j+1)(j+2)} \right) a_j \ .$$

If $s = 0$ there is only 1 term in the series:

$$h_0(\sigma) = a_0 \ ,$$
$$\hat{\Theta}_0(\theta) = a_0 e^{-\sigma^2/2} \ ,$$

For $s = 1$ one obtains:

$$h_1(\sigma) = a_1 \sigma \ ,$$
$$\hat{\Theta}_1(\theta) = a_1 \sigma e^{-\sigma^2/2} \ .$$

For $s = 2$, the following holds:

$$h_2(\sigma) = a_0 \left(1 - 2\sigma^2\right) \ ,$$
$$\hat{\Theta}_2(\theta) = a_0 \left(1 - 2\sigma^2\right) e^{-\sigma^2/2} \ ,$$

and so on ...
In general $h_s(\sigma)$ is a polynomial of degree s in σ, involving odd powers only if s is odd, and even powers only if s is even. Apart from the factors a_0 and a_1, these polynomials can be shown to be equivalent to the Hermite polynomials, so that one obtains the following equation for $\hat{\Theta}_s(\theta)$:

$$\hat{\Theta}_s(\theta) = H_s(\sigma) e^{-\sigma^2/2} \ ,$$

which is the time-indepedent Schrödinger-like equation. □

Using the recurrence relation of these Hermite polynomials ($\sigma H_s(\sigma) = s H_{s-1}(\sigma) + \frac{1}{2} H_{s+1}(\sigma)$) and previously defined equations, one obtains the approximative expressions for the other Hough functions:

$$\Theta(\sigma) = \frac{(L\nu)^{1/2}}{L^2 - m^2} \left[s \left(\frac{m}{L} + 1 \right) H_{s-1}(\sigma) + \frac{1}{2} \left(\frac{m}{L} - 1 \right) H_{s+1}(\sigma) \right] e^{-\sigma^2/2} \ ,$$
$$\tilde{\Theta}(\sigma) = m \, \frac{(L\nu)^{1/2}}{m^2 - L^2} \left[s \left(\frac{L}{m} + 1 \right) H_{s-1}(\sigma) + \frac{1}{2} \left(\frac{L}{m} - 1 \right) H_{s+1}(\sigma) \right] e^{-\sigma^2/2} \ .$$

Proof. The expressions for $\Theta(\sigma)$ and $\tilde{\Theta}(\sigma)$ are obtained in the following way:

$$\left(\frac{\mathrm{d}}{\mathrm{d}\mu}+m\nu\mu\right)\hat{\Theta}(\sigma)=\left[\lambda-m^2\right]\Theta(\sigma)\ ,$$

$$\Leftrightarrow\frac{(L\nu)^{1/2}}{L^2-m^2}\left[\frac{\mathrm{d}}{\mathrm{d}\sigma}+\frac{m\sigma}{L}\right]H_s(\sigma)\ e^{-\sigma^2/2}=\Theta(\sigma)\ ,$$

$$H_{s+1}(\sigma)=-\left(-1\right)^s e^{\sigma^2}\frac{d^s}{d\sigma^s}\left(\frac{d\left(e^{-\sigma^2}\right)}{d\sigma}\right)\ ,$$

$$\frac{\mathrm{d}}{\mathrm{d}\sigma}\ \left[(-1)^s\, e^{\frac{\sigma^2}{2}}\frac{d^s e^{-\sigma^2}}{d\sigma^s}\right]=(-1)^s\, e^{\frac{\sigma^2}{2}}\frac{d^s e^{-\sigma^2}}{d\sigma^s}\left[\sigma+\frac{\mathrm{d}e^{-\sigma^2}}{\mathrm{d}\sigma}\right]\ ,$$

$$\Leftrightarrow\frac{\mathrm{d}}{\mathrm{d}\sigma}\left[(-1)^s\, e^{\frac{\sigma^2}{2}}\frac{d^s e^{-\sigma^2}}{d\sigma^s}\right]=\left[\sigma H_s(\sigma)-H_{s+1}(\sigma)\right]e^{-\frac{\sigma^2}{2}}\ ,$$

$$\Leftrightarrow\frac{\mathrm{d}}{\mathrm{d}\sigma}\hat{\Theta}(\sigma)=\left[sH_{s-1}(\sigma)-\frac{1}{2}H_{s+1}(\sigma)\right]e^{-\frac{\sigma^2}{2}}\ ,$$

$$\Leftrightarrow\frac{(L\nu)^{1/2}}{L^2-m^2}\left[\frac{\mathrm{d}}{\mathrm{d}\sigma}+\frac{m\sigma}{L}\right]H_s(\sigma)\ e^{-\sigma^2/2}=$$

$$\frac{(L\nu)^{1/2}}{L^2-m^2}\left[s\left(\frac{m}{L}+1\right)H_{s-1}(\sigma)+\frac{1}{2}\left(\frac{m}{L}-1\right)H_{s+1}(\sigma)\right]e^{-\sigma^2/2}=\Theta(\theta)\ ,$$

$$m\Theta(\sigma)=m\frac{(L\nu)^{1/2}}{m^2-L^2}\left[s\left(\frac{m}{L}+1\right)H_{s-1}(\sigma)+\frac{1}{2}\left(\frac{m}{L}-1\right)H_{s+1}(\sigma)\right]e^{-\sigma^2/2}\ ,$$

$$\nu\mu\hat{\Theta}(\sigma)=\left(\frac{L}{\nu}\right)^{1/2}\sigma\left[H_s(\sigma)e^{-\sigma^2/2}\right]\ ,$$

$$\Leftrightarrow\nu\mu\hat{\Theta}(\sigma)=(L\nu)^{1/2}\ \left[\frac{\sigma}{L}H_s(\sigma)e^{-\sigma^2/2}\right]\ ,$$

$$\Leftrightarrow\nu\mu\hat{\Theta}(\sigma)=m\frac{(L\nu)^{1/2}}{m^2-L^2}\left[\left(\frac{\sigma m}{L}-\frac{\sigma L}{m}\right)H_s(\sigma)e^{-\sigma^2/2}\right]\ ,$$

$$\tilde{\Theta}(\sigma)=-\nu\mu\hat{\Theta}(\sigma)-m\Theta(\sigma)\ ,$$

$$\Leftrightarrow\tilde{\Theta}(\sigma)=-m\frac{(L\nu)^{1/2}e^{-\sigma^2/2}}{m^2-L^2}\left[s\left(\frac{m}{L}+1\right)H_{s-1}(\sigma)+\frac{1}{2}\left(\frac{m}{L}-1\right)H_{s+1}(\sigma)\right.$$

$$\left.+\left(\frac{\sigma m}{L}-\frac{\sigma L}{m}\right)H_s(\sigma)\right]\ ,$$

$$\Leftrightarrow\tilde{\Theta}(\sigma)=m\ \frac{(L\nu)^{1/2}}{m^2-L^2}\left[s\left(\frac{L}{m}+1\right)H_{s-1}(\sigma)+\frac{1}{2}\left(\frac{L}{m}-1\right)H_{s+1}(\sigma)\right]e^{-\sigma^2/2}\ .$$

□

Equating the two expressions for the parameter S, one can obtain a characteristic equation for L, which appears explicitly in the definitions of $\Theta(\sigma)$ and $\tilde{\Theta}(\sigma)$:

$$L^2 - \nu(2s+1)L + (m\nu - m^2) = 0 \ .$$

Proof. This is proven in the following way:

$$\begin{aligned} S = 2s - 1 &= \frac{m\nu - m^2 + L^2}{L\nu} \ , \\ \Leftrightarrow \nu(2s-1)L &= m\nu - m^2 + L^2 \ , \\ \Leftrightarrow L^2 - \nu(2s+1)L &+ (m\nu - m^2) = 0 \ . \end{aligned}$$

□

The roots of this equation are given by:

$$L = \frac{1}{2}\nu(2s+1) \pm \frac{1}{2}\left[\nu^2(2s+1)^2 - 4(m\nu - m^2)\right]^{1/2} \ .$$

The eigenvalue λ can therefore be found using the following equation:

$$\lambda_\pm \equiv L^2 = -(m\nu - m^2) + \frac{1}{2}\nu^2(2s+1)^2 \left\{1 \pm \left[1 - \frac{4(m\nu - m^2)}{\nu^2(2s+1)^2}\right]^{1/2}\right\} \ .$$

Proof. This can be proven in the following way:

$$\begin{aligned} & L = \frac{1}{2}\nu(2s+1) \pm \frac{1}{2}\left[\nu^2(2s+1)^2 - 4(m\nu - m^2)\right]^{1/2} \ , \\ \Leftrightarrow \ & L = \frac{1}{2}\nu(2s+1)\left[1 \pm \left[1 - \frac{4(m\nu - m^2)}{\nu^2(2s+1)^2}\right]^{1/2}\right] \ , \\ & L^2 - \nu(2s+1)L + (m\nu - m^2) = 0 \ , \\ \Leftrightarrow \ & L^2 = -(m\nu - m^2) + \frac{1}{2}\nu^2(2s+1)^2 \left\{1 \pm \left[1 - \frac{4(m\nu - m^2)}{\nu^2(2s+1)^2}\right]^{1/2}\right\} \ . \end{aligned}$$

□

This can be approximated using a (non-vanishing, lowest-order) Taylor's series expansion in ν^{-1} around $\nu^{-1} = 0$ (i.e. for infinitely large ν), yielding:

$$\begin{aligned} \lambda_+ &\approx \nu^2(2s+1)^2 + \mathcal{O}(\nu) \ , \\ \lambda_- &\approx \frac{(m\nu - m^2)^2}{\nu^2(2s+1)^2} + \mathcal{O}(\nu^{-1}) \ , \end{aligned}$$

where each of the two branches is associated with a class of equatorially trapped waves/modes. The λ_+ branch corresponds to gravito-inertial (g) modes, and hence we only consider this branch.

Proof. Since we only consider g modes in this work, I will only derive the λ_+ expression, noting that, in order to derive the λ_- expression, one ought to expand to fourth order in the parameter ν^{-1}. First, we rewrite the fraction in the square root in function of the parameter $X = \nu^{-1}$:

$$\begin{aligned}\frac{4(m\nu - m^2)}{\nu^2(2s+1)^2} &= \frac{4m}{(2s+1)^2}\left[\nu^{-1} - m\nu^{-2}\right] \ , \\ &= \frac{4m}{(2s+1)^2}\left[X - mX^2\right] \ ,\end{aligned}$$

so that the function $f(X)$ needs to be Taylor-approximated is the following:

$$f(X) = \left\{1 - \frac{4m}{(2s+1)^2}\left[X - mX^2\right]\right\}^{1/2} \ .$$

Let us also further trim down the notation by introducing a new constant $A = \frac{4m}{(2s+1)^2}$, so that the function $f(X)$ becomes:

$$f(X) = \left\{1 - A\left[X - mX^2\right]\right\}^{1/2} \ .$$

The derivative with respect to X is then the following:

$$\frac{\mathrm{d}f(X)}{\mathrm{d}X} = \frac{1}{2}\left\{1 - A\left[X - mX^2\right]\right\}^{-1/2}\left(-A + 2AmX\right) \ .$$

Evaluating these in the point $X = 0$ (Maclaurin approximation), one obtains:

$$\begin{aligned}f(0) &= 1 \ , \\ f'(0) &= -\frac{A}{2} \ .\end{aligned}$$

Hence for the λ_+ branch, one obtains approximately:

$$\begin{aligned}\lambda_+ &= -(m\nu - m^2) + \frac{1}{2}\nu^2(2s+1)^2\left\{1 + f(X)\right\} \ , \\ f(X) &\approx f(0) + f'(0)X \ , \\ \Leftrightarrow \lambda_+ &\approx -(m\nu - m^2) + \frac{1}{2}\nu^2(2s+1)^2\left\{1 + 1 - \frac{A}{2\nu}\right\} \ , \\ \Leftrightarrow \lambda_+ &\approx -m\nu + m^2 + \frac{1}{2}\nu^2(2s+1)^2\left\{1 + 1 - \frac{2m}{(2s+1)^2\nu}\right\} \ , \\ \Leftrightarrow \lambda_+ &\approx -m\nu + m^2 + \nu^2(2s+1)^2 - m\nu \ , \\ \Leftrightarrow \lambda_+ &\approx \nu^2(2s+1)^2 + \mathcal{O}\left(\nu\right) \ .\end{aligned}$$

□

The solutions hold for g modes of meridional order $s \geq 1$, and any solutions $\lambda = m^2$ should be ruled out, as they violate our initial assumption. The $s = 0$ solutions comprise a special case, as the eigenvalues of the λ_+ branches reduces to the following

exact form:

$$\lambda_+ = \begin{cases} m^2 & \text{when } 0 < m\nu < 2m^2 \\ (\nu - m)^2 & \text{otherwise} \end{cases} .$$

Furthermore $\lambda = (\nu - m)^2$ solutions should be disallowed over the interval $0 < m\nu < m^2$, as they arise as $L = (\nu - m)$ solutions from the characteristic equation of L, leading to imaginary values of σ. Therefore, at most one valid solution is possible for the $s = 0$ case, which has g mode ($\lambda = \lambda_+$, $m\nu > 2m^2$ or $m\nu \leq 0$) character, and is known as the Yanai wave/ are known as Yanai modes (Yanai and Maruyama, 1966). We did not consider such modes in this work and therefore we do not expand on this topic.

Since we neglect terms in μ^2, the error introduced by asymptotic analysis, should be of the order of $\mu_{1/2}^2$, the half-width of the equatorial waveguide, so that the $\hat{\Theta}(\theta)$ Hough function transitions from a oscillatory behaviour to an exponential behaviour at points $\pm\mu_{1/2}$, hence representing the points where the latitudinally propagating waves become evanescent. The second derivative with respect to μ in these points should vanish, so that, in order to solve the equation $\frac{\mathrm{d}^2\hat{\Theta}(\theta)}{\mathrm{d}\sigma^2} + (S - \sigma^2)\,\hat{\Theta}(\theta) = 0$, σ^2 needs to be equal to S, resulting in the following expression for the half-width:

$$\mu_{1/2} = \left(\frac{2s+1}{L\nu}\right)^{1/2} .$$

For g modes, using the Taylor approximation obtained above, taking into account that $L = \lambda_+^{1/2}$, this becomes:

$$\mu_{1/2} \approx \frac{1}{|\nu|} .$$

The g mode solutions will converge approximately quadratically (in ν) towards the exact solutions (the relative error $\propto \mu_{1/2}^2$) of the full tidal equations (Townsend, 2003). Hence, for modest values of $m\nu$ ($> m^2$), the solutions will show poor convergence towards the exact solutions. In addition, it can be seen that $\mu_{1/2}$ must be smaller than 1 in order to have a physical meaning, so that g-mode solutions are only valid for $|\nu| \geq 1$ (Townsend, 2003).

Justifying the parity factor in Hough function estimation

When expanding (scalar) functions on a sphere, the following Fourier series can be used (see chapter 18.8 of Boyd, 2001):

$$f(\lambda, \theta) = \sum_{m=0}^{\infty} f_m(\theta)\cos(m\lambda) + \sum_{m=1}^{\infty} g_m(\theta)\sin(m\lambda) .$$

When m is odd, the component $g_m(\theta)\sin(m\lambda)$ changes sign as the pole is crossed. Hence, $g_m(\theta)\sin(m\lambda)$ must have a discontinuity at the poles unless for odd m the following holds:

$$g_m(0) = g_m(\pi) = 0 .$$

The colatitude cosine coefficients can be shown to be always zero when the longitudinal wavenumber m is odd (see Boyd, 2001), so that $f(\lambda, \theta)$ is void of discontinuities if $f_m(\theta)$ and $g_m(\theta)$ are the sums of Fourier sine series in θ.

When m is even, $\sin(m\lambda) = \sin(m[\lambda + \pi])$, so that:

$$g_m(\delta)\sin(m\lambda) = g_m(\delta)\sin(m[\lambda+\pi]) \ \forall \delta, \lambda \ [m = 0, 2, 4, \ldots] \ .$$

This is thus symmetric around the pole, so that the following must hold for its derivative:

$$\frac{\mathrm{d}g_m(\theta)}{\mathrm{d}\theta} = \frac{\mathrm{d}g_m(\theta)}{\mathrm{d}\theta} = 0 \ .$$

Hence, Boyd (2001) concluded that all sine coefficients must be zero when m is even, if this argument is extended to higher derivatives.

Taking into account the previous limitations, a scalar function $f(\lambda, \theta)$ void of singularities on the sphere can thus be expanded as the following Fourier series:

$$\begin{aligned} f(\lambda,\theta) = &\sum_{m=0,2,4,\ldots;n=0}^{\infty} \{a^c_{mn}\cos(m\lambda) + a^s_{mn}\sin(m\lambda)\}\cos(n\theta) \\ &+ \sum_{m=1,3,5,\ldots;n=1}^{\infty} \{b^c_{mn}\cos(m\lambda) + b^s_{mn}\sin(m\lambda)\}\sin(n\theta) \end{aligned}$$

Finally, note the following trigonometric identity (wrong in Boyd (2001)):

$$\sin\theta\cos(n\theta) = \tfrac{1}{2}\{\sin([1-n]\theta) + \sin([n+1]\theta)\} = \tfrac{1}{2}\{-\sin([n-1]\theta) + \sin([n+1]\theta)\} \ ,$$

which can be derived from one of Simpson's identities (e.g. Abramowitz and Stegun, 1972):

$$\sin\alpha + \sin\beta = 2\sin\left([\alpha+\beta]/2\right)\cos\left([\alpha-\beta]/2\right)$$

Proof. Filling in Simpson's identity given above, where $\alpha = [1-n]\theta$ and $\beta = [1+n]\theta$, yields the wanted trigonometric identity:

$$\begin{aligned} \sin([1-n]\theta) + \sin([n+1]\theta) = 2 \ &\sin\left(\frac{1}{2}[[1-n]\theta + [n+1]\theta]\right) \\ &\cos\left(\frac{1}{2}[[1-n]\theta - [n+1]\theta]\right) \ , \\ \Leftrightarrow \sin([1-n]\theta) + \sin([n+1]\theta) = 2 \ &\sin\theta\cos\left(-n\theta\right) = 2 \ \sin\theta\cos\left(n\theta\right) \ . \end{aligned}$$

Similarly, the second equivalence is proven with $\sin(-\theta) = -\sin\theta$. □

It shows that one can replace the $\sin(n\theta)$ term for odd m in the Fourier series with a basis whose elements are $\sin\theta\cos(n\theta)$, so that the parity factor $\sin\theta$ appears in the equation.

These Fourier series can then be transformed into Chebyshev series (using Equation (3.3)) if the modified latitudinal variable μ is used, justifying the approach Wang et al. (2016) take to calculate the Hough functions.

Exemplary Code Inlists

Exemplary MESA inlist

```
&star_job

  ! Avoid printing a lot of stuff in the terminal to begin with. We don't need this.
    show_log_description_at_start = .false.

  ! We do not want to load from a saved model or use PMS model
    load_saved_model = .false. ! no stellar model saved for memory conservation
    create_pre_main_sequence_model = .true. ! start evolving from the pre-main-sequence

  ! Set metal fractions consistently with the opacity
    kappa_file_prefix = 'OP_a09_p13'
    kappa_lowT_prefix = 'lowT_fa05_a09p'
    kappa_CO_prefix = 'a09_p13_co'

  ! a09+Prz metal fractions
    initial_zfracs = 8

  ! Nuclear Network
  ! We use the extended isotope network for surface abundances
    change_net = .true.
    new_net_name = 'pp_cno_extras_o18_ne22_extraiso.net'
    change_initial_net = .true.

  ! Custom history file
    history_columns_file = './history_columns_changed_JVB.list' ! custom selection of output parameters in history files

  ! Custom profile file
    profile_columns_file = './profile_columns_changed_JVB.list' ! custom selection of output parameters in profiles

  ! for pgstar set to True --> no visual output during the simulation
    !pgstar_flag = .true.
    !save_pgstar_files_when_terminate = .false.

    pause_before_terminate = .false. ! no pause before the MESA simulation is terminated

  ! Some terminate options to help control the output generated by mesa
    save_photo_when_terminate = .false.
```

```
38      save_model_when_terminate = .false.
39      write_profile_when_terminate = .false.
40      save_pulse_data_when_terminate = .false.
41
42    ! save_model_filename = 'terminated_model.model' ! name of model
       saved at end of the evolution --> not used
43
44    ! Rotation flags
45    ! We choose to calculate non-rotating non-magnetic equilibrium models
46      new_rotation_flag = .false.
47      change_rotation_flag = .false.
48      change_initial_rotation_flag = .false.
49
50      new_omega = 0
51      set_omega = .false.
52      set_initial_omega = .false.
53
54    ! color information
55      color_num_files=2
56      color_file_names(1)='lcb98cor.dat'
57      color_num_colors(1)=11
58      color_file_names(2)='HST_filters.dat'
59      color_num_colors(2)=12
60
61
62  / !end of star_job namelist
63
64
65  &controls
66
67    !!!!!!!!!!!!!!!!!!!!!!!!!!!!!!!!!!!!!!!!!!!!
68    !! THINGS TO VARY
69    !!!!!!!!!!!!!!!!!!!!!!!!!!!!!!!!!!!!!!!!!!!!
70
71      initial_mass = 2.1 ! varied by script
72      mixing_length_alpha = 1.8 ! varied by script
73      overshoot_f_above_burn_h_core = 0.010 ! varied by script
74
75      min_D_mix = 10.0  ! envelope mixing parameter in cm^2/sec
76
77      initial_y = 0.2795    ! initial helium content: held constant
78      initial_z = 0.0002    ! initial metallicity: varied by script
79
80
81    !!!!!!!!!!!!!!!!!!!!!!!!!!!!!!!!!!!!!!!!!!!!
82    !! TIMESTEP CONTROLS
83    !!!!!!!!!!!!!!!!!!!!!!!!!!!!!!!!!!!!!!!!!!!!
84
85      varcontrol_target = 5d-5 ! parameter determining size of simulation
       timestep
86
87      ! extra timestep controls
88      delta_lg_XH_cntr_max = -1 ! Ignore changes in lg_XH_cntr if value
       is more than this.
89      delta_lg_XH_cntr_limit = 0.05 ! if max delta is greater than this,
       reduce timestep
90
91    !!!!!!!!!!!!!!!!!!!!!!!!!!!!!!!!!!!!!!!!!!!!
```

```
92  !! OUTPUT CONTROLS
93  !!!!!!!!!!!!!!!!!!!!!!!!!!!!!!!!!!!!!!!!!!!!!!!!
94
95  ! Setting up LOG directory
96    log_directory = './LOGS'
97    star_history_name = 'Zini00140_MLT180_Mini0210_fov00100_logDext100.
     history' ! name of history output file
98    history_interval = 1 ! history file records every time step
99
100 ! Specify how often to write info to the terminal
101   terminal_interval = 20 ! every 20 timesteps
102
103 ! Specify when to write out photos
104   photo_interval = 1000000 ! never write photos
105   photo_directory = './photos'
106
107 ! We choose not to save the profiles using these parameters because
     we developed a way to specify it in run_star_extras, saving at
     specific Xc
108   write_profiles_flag = .false.
109   profile_interval = 10000
110   profile_data_prefix = 'M3_test' !---> changing profile names
111   max_num_profile_models = 5 ! only keep 5 profiles in order to ease
     on data storage
112
113 ! Save output files to be used for GYRE calculations
114   write_pulse_data_with_profile = .true.
115   pulse_data_format = 'GYRE'
116   add_atmosphere_to_pulse_data = .true.
117   add_center_point_to_pulse_data = .true.
118   keep_surface_point_for_pulse_data = .true.
119   add_double_points_to_pulse_data = .true.
120   interpolate_rho_for_pulse_data = .true.
121   threshold_grad_mu_for_double_point = 5d0
122
123 !!!!!!!!!!!!!!!!!!!!!!!!!!!!!!!!!!!!!!!!!!!!!!!!
124 !! CORE BOUNDARY CONTROLS
125 !!!!!!!!!!!!!!!!!!!!!!!!!!!!!!!!!!!!!!!!!!!!!!!!
126   alpha_bdy_core_overshooting = 5 ! standard setting
127   he_core_boundary_h1_fraction = 1d-2 ! standard setting
128
129 !!!!!!!!!!!!!!!!!!!!!!!!!!!!!!!!!!!!!!!!!!!!!!!!
130 !! STOPPING CONTROLS
131 !!!!!!!!!!!!!!!!!!!!!!!!!!!!!!!!!!!!!!!!!!!!!!!!
132
133 ! stop when the center mass fraction of h1 drops below this limit
134   xa_central_lower_limit_species(1) = 'h1'
135   xa_central_lower_limit(1) = 1d-12              ! This is end core-
     H burning
136
137
138 !!!!!!!!!!!!!!!!!!!!!!!!!!!!!!!!!!!!!!!!!!!!!!!!
139 !! MIXING CONTROLS
140 !!!!!!!!!!!!!!!!!!!!!!!!!!!!!!!!!!!!!!!!!!!!!!!!
141
142   remove_small_D_limit = 1d-6 ! If MLT diffusion coeffient D (cm^2/
     sec) is less than this limit,
143   ! set D to zero and change the point to mixing_type == no_mixing.
```

```
144     use_Ledoux_criterion = .true. ! The Ledoux criterion for is used to
        determine convection zones
145
146     ! if > 0, N^2 is smoothed, introducing noise in the period spacing
       patterns: we do not want this!
147     num_cells_for_smooth_gradL_composition_term = 0
148
149     ! no semiconvection or thermohaline convection considered
150     alpha_semiconvection = 0d0
151     semiconvection_option = 'Langer_85 mixing; gradT = gradr'
152     thermohaline_coeff = 0d0
153
154     ! Set Mixing length theory options
155     alt_scale_height_flag = .true.
156     MLT_option = 'Cox' ! Giuli and Cox (1968)
157     mlt_gradT_fraction = -1
158     okay_to_reduce_gradT_excess = .false.
159
160     ! Define a minimum diffusive mixing (applicable in the radiative
       zones)
161     set_min_D_mix = .true.
162
163   !!!!!!!!!!!!!!!!!!!!!!!!!!!!!!!!!!!!!!!!!!!!!!!
164   !! OVERSHOOTING/CONVECTION CONTROLS
165   !!!!!!!!!!!!!!!!!!!!!!!!!!!!!!!!!!!!!!!!!!!!!!!
166
167     D_mix_ov_limit = 0d0 ! We do not wish to shut off overshooting at
       all!
168     max_brunt_B_for_overshoot = 0
169     limit_overshoot_Hp_using_size_of_convection_zone = .true.
170     overshoot_alpha = -1              ! --> We don't want to change this
171
172     predictive_mix(1) = .true.
173     predictive_zone_type(1) = 'burn_H'
174     predictive_zone_loc(1) = 'core'
175     predictive_bdy_loc(1) = 'any'
176
177     predictive_mix(2) = .true.
178     predictive_zone_type(2) = 'burn_He'
179     predictive_zone_loc(2) = 'core'
180     predictive_bdy_loc(2) = 'any'
181
182     predictive_mix(3) = .true.
183     predictive_zone_type(3) = 'nonburn'
184     predictive_zone_loc(3) = 'shell'
185     predictive_bdy_loc(3) = 'any'
186
187     predictive_mix(4) = .true.
188     predictive_zone_type(4) = 'burn_H'
189     predictive_zone_loc(4) = 'shell'
190     predictive_bdy_loc(4) = 'any'
191
192     conv_bdy_mix_softening_f0 = 0.002
193     conv_bdy_mix_softening_f = 0.001
194     conv_bdy_mix_softening_min_D_mix = 1d-1
195
196   ! Set overshooting parameters for the different types of overshooting
       considered
```

```
197     overshoot_f0_above_burn_h_core = 0.002
198
199     overshoot_f0_above_burn_h_shell = 0.002
200     overshoot_f_above_burn_h_shell  = 0.005
201     overshoot_f0_below_burn_h_shell = 0.002
202     overshoot_f_below_burn_h_shell  = 0.005
203
204     overshoot_f0_above_burn_he_core = 0.002
205
206     overshoot_f0_above_nonburn_shell = 0.002
207     overshoot_f_above_nonburn_shell  = 0.005
208     overshoot_f0_below_nonburn_shell = 0.002
209     overshoot_f_below_nonburn_shell  = 0.005
210
211
212     smooth_convective_bdy = .false.
213
214   !!!!!!!!!!!!!!!!!!!!!!!!!!!!!!!!!!!!!!!!!!!!!!!!
215   !! ELEMENTAL DIFFUSION CONTROLS
216   !!!!!!!!!!!!!!!!!!!!!!!!!!!!!!!!!!!!!!!!!!!!!!!!
217
218     do_element_diffusion = .false. ! no element diffusion considered
219
220   !!!!!!!!!!!!!!!!!!!!!!!!!!!!!!!!!!!!!!!!!!!!!!!!
221   !! ATMOSPHERE CONTROLS
222   !!!!!!!!!!!!!!!!!!!!!!!!!!!!!!!!!!!!!!!!!!!!!!!!
223
224     which_atm_option = 'simple_photosphere' ! simple atmosphere
      selected
225
226   !!!!!!!!!!!!!!!!!!!!!!!!!!!!!!!!!!!!!!!!!!!!!!!!
227   !! OPACITY CONTROLS
228   !!!!!!!!!!!!!!!!!!!!!!!!!!!!!!!!!!!!!!!!!!!!!!!!
229
230     cubic_interpolation_in_X = .false.
231     cubic_interpolation_in_Z = .false.
232
233   !!!!!!!!!!!!!!!!!!!!!!!!!!!!!!!!!!!!!!!!!!!!!!!!
234   !! ASTEROSEISMOLOGY CONTROLS
235   !!!!!!!!!!!!!!!!!!!!!!!!!!!!!!!!!!!!!!!!!!!!!!!!
236
237     calculate_Brunt_N2 = .true. ! calculate the Buoyancy frequency
238     num_cells_for_smooth_brunt_B = 0 ! no smoothing
239     interpolate_rho_for_pulsation_info = .true. ! density at face of
      cells is interpolated
240
241   !!!!!!!!!!!!!!!!!!!!!!!!!!!!!!!!!!!!!!!!!!!!!!!!
242   !! MESH & RESOLUTION CONTROLS
243   !!!!!!!!!!!!!!!!!!!!!!!!!!!!!!!!!!!!!!!!!!!!!!!!
244
245   ! This is important to properly resolve the gravity modes near the
      convective core boundary
246     max_allowed_nz = 60000 ! number of zones maximally allowed
247
248   ! global mesh resolution factor
249     mesh_delta_coeff = 0.4 ! lower value decreases max allowed deltas
      and increases number of grid points: lowered to 0.2 for bumping
      simulations
```

```
250     mesh_adjust_use_quadratic = .true. ! quadratic reconstruction
        polynomials for mesh adjustments
251     mesh_adjust_get_T_from_E = .true. ! use internal energy
        conservation to set new temperature
252
253   ! Additional resolution based on the pressure and temperature
        profiles
254     P_function_weight = 40
255     T_function1_weight = 110
256
257     T_function2_weight = 0
258     T_function2_param = 2d4
259
260     gradT_function_weight = 0
261
262     xtra_coef_os_above_burn_h = 0.1d0
263     xtra_dist_os_above_burn_h = 2d0
264
265     mesh_dlogX_dlogP_extra = 0.15                    ! resol coeff for
        chemical gradients
266     mesh_dlogX_dlogP_full_on = 1d-6                  ! additional resol
        on for gradient larger than this
267     mesh_dlogX_dlogP_full_off = 1d-12                ! additional resol
        off for gradient smaller than this
268
269     mesh_logX_species(1) = 'he4'                      ! taking into
        account abundance of He4
270
271
272   ! Additional resolution near the boundaries of the convective regions
273     xtra_coef_czb_full_on = 1.0d0                     ! Always on
274     xtra_coef_czb_full_off = 1.0d0                    ! Always on
275
276     xtra_coef_a_l_hb_czb = 0.5d0                      ! resol coeff
        above lower nonburn convective boundary
277     xtra_dist_a_l_hb_czb = 1d0                        ! distance above
        lower nonburn convective boundary
278     xtra_coef_b_l_hb_czb = 0.5d0                      ! resol coeff
        below lower nonburn convective boundary
279     xtra_dist_b_l_hb_czb = 1d0                        ! distance below
        lower nonburn convective boundary
280
281     xtra_coef_a_l_hb_czb = 0.5d0                      ! resol coeff
        above lower nonburn convective boundary
282     xtra_dist_a_l_hb_czb = 1d0                        ! distance above
        lower nonburn convective boundary
283     xtra_coef_b_l_hb_czb = 0.5d0                      ! resol coeff
        below lower nonburn convective boundary
284     xtra_dist_b_l_hb_czb = 1d0                        ! distance below
        lower nonburn convective boundary
285
286   ! non-burning zone
287     xtra_coef_a_l_nb_czb = 0.5d0                      ! resol coeff
        above lower nonburn convective boundary
288     xtra_dist_a_l_nb_czb = 1d0                        ! distance above
        lower nonburn convective boundary
289     xtra_coef_b_l_nb_czb = 0.5d0                      ! resol coeff
        below lower nonburn convective boundary
```

```
290     xtra_dist_b_l_nb_czb = 1d0                    ! distance below
      lower nonburn convective boundary
291
292     xtra_coef_a_l_nb_czb = 0.5d0                  ! resol coeff
      above lower nonburn convective boundary
293     xtra_dist_a_l_nb_czb = 1d0                    ! distance above
      lower nonburn convective boundary
294     xtra_coef_b_l_nb_czb = 0.5d0                  ! resol coeff
      below lower nonburn convective boundary
295     xtra_dist_b_l_nb_czb = 1d0                    ! distance below
      lower nonburn convective boundary
296
297   ! He burning zone
298     xtra_coef_a_l_heb_czb = 0.5d0                 ! resol coeff
      above lower nonburn convective boundary
299     xtra_dist_a_l_heb_czb = 1d0                   ! distance above
      lower nonburn convective boundary
300     xtra_coef_b_l_heb_czb = 0.5d0                 ! resol coeff
      below lower nonburn convective boundary
301     xtra_dist_b_l_heb_czb = 1d0                   ! distance below
      lower nonburn convective boundary
302
303     xtra_coef_a_l_heb_czb = 0.5d0                 ! resol coeff
      above lower nonburn convective boundary
304     xtra_dist_a_l_heb_czb = 1d0                   ! distance above
      lower nonburn convective boundary
305     xtra_coef_b_l_heb_czb = 0.5d0                 ! resol coeff
      below lower nonburn convective boundary
306     xtra_dist_b_l_heb_czb = 1d0                   ! distance below
      lower nonburn convective boundary
307
308
309   ! Additional Resolution in overshooting region
310     xtra_coef_os_full_on = 1.0d0
311     xtra_coef_os_full_off = 1.0d0
312
313     xtra_coef_os_above_burn_h = 0.5d0
314     xtra_dist_os_above_burn_h = 0.5d0
315     xtra_coef_os_below_burn_h = 0.5d0
316     xtra_dist_os_below_burn_h = 0.5d0
317
318     xtra_coef_os_above_nonburn = 0.5d0
319     xtra_dist_os_above_nonburn = 0.5d0
320     xtra_coef_os_below_nonburn = 0.5d0
321     xtra_dist_os_below_nonburn = 0.5d0
322
323     xtra_coef_os_above_burn_he = 0.5d0
324     xtra_dist_os_above_burn_he = 0.5d0
325     xtra_coef_os_below_burn_he = 0.5d0
326     xtra_dist_os_below_burn_he = 0.5d0
327
328
329 / ! end of controls namelist
```

Listing 1: Exemplary MESA inlist. Several parameters were varied automatically by making use of scripts that change the corresponding variables such as the initial metallicity.

Exemplary GYRE inlist

```
&constants
/

&model
  model_type = 'EVOL'
  file = ! name filled in by script
  file_format = 'MESA' ! MESA evolutionary model will be used
  repair_As = .False. ! Use the Brunt-Vaisala frequency profile
   computed by MESA
  uniform_rot = .True. ! impose uniform rotation
  Omega_rot = ! rotation filled in by script: typically 0.25
  Omega_units = 'CRITICAL' ! rotation rate in percent critical rotation
/

&mode
  l = 1
  m = 0
  tag = 'l1' ! Tag for namelist matching
  n_pg_min = -50 ! minimal radial order of g modes
  n_pg_max = -1 ! maximal radial order of g modes
  rossby = .FALSE.
/


&osc
  nonadiabatic = .False. ! Adiabatic frequency calculation!
  rotation_method = 'TAR'
  outer_bound = ! Outer B.C. filled in by script: typically UNNO
/

&num
  diff_scheme = ! Solver/difference scheme filled in by script
  n_iter_max = 50
/

&scan
  grid_type = 'INVERSE' ! grid is spaced evenly in period
  grid_frame = 'COROT_I'     ! co-rotating frame at inner boundary

  freq_min = ! freq_min filled in by script
  freq_max = ! freq_max filled in by script
  freq_max_units = 'CYC_PER_DAY' ! frequencies expressed in cycles per
   day
  freq_min_units = 'CYC_PER_DAY'
  n_freq = ! n to be filled in by script: typically n_freq = 400
  tag_list = 'l1'            ! Comma-separated list of tags to match
/


&grid
    n_inner = 5
  alpha_osc = 10      ! At least 10 points per oscillatory wavelength
  alpha_exp = 2     ! At least 2 points per exponential 'wavelength'

/
```

```
54
55 &ad_output
56   summary_file = ! adiabatic summary name filled in by script
57   freq_units = 'CYC_PER_DAY' ! frequencies outputted in cycles per day
       (in the inertial frame)
58   summary_file_format = 'HDF'
59   summary_item_list = 'M_star,R_star,L_star,l,m,j,n_p,n_g,n_pg,omega,
       freq,E_norm,Delta_g,beta' ! Items to appear in summary file
60
61   mode_template = ! adiabatic mode file name filled in by script
62   mode_file_format = 'HDF'
63   mode_item_list = 'M_star,R_star,L_star,lambda,l,m,n,j,n_p,n_g,n_pg,
       freq,freq_units,xi_h,xi_r,x,dW_dx,Gamma_1,P,rho,T,dE_dx,Omega_rot,
       Yt_1,Yt_2,prop_type,dbeta_dx'
64
65 /
66
67 &nad_output
68
69 ! NO NONADIABATIC OUTPUT
70
71 ! summary_file = 'summary_nad.h5'
72 ! freq_units = 'CYC_PER_DAY'
73 ! summary_file_format = 'HDF'
74 ! summary_item_list = 'M_star,R_star,L_star,l,m,n_p,n_g,n_pg,omega,freq
       ,E_norm,W' ! Items to appear in summary file
75
76 ! mode_template = 'nad_mode_l%L_n%N_j%J.h5'
77 ! mode_item_list = 'M_star,R_star,L_star,l,m,n,n_p,n_g,n_pg,freq,xi_h,
       xi_r,x,dW_dx,W,Gamma_1,P,rho,T,dE_dx'
78
79 /
80 /
```

Listing 2: Exemplary GYRE inlist. Several parameters were varied automatically by making use of scripts that fill the corresponding 'commented' variables such as 'Omega_rot'. The frequency bounds of the frequency search grid were automatically calculated by making use of the corresponding asymptotic expressions in the TAR.

Acronyms

γ Dor γ Doradus. 15, 16, 18, 20, 21, 32, 34, 88

BVP boundary value problem. 35

CEA Le Commissariat à l'énergie atomique et aux énergies alternatives. iv, 31

COLLOC_GL2 Second order collocation scheme to solve GYRE pulsation equations. 80–84

COLLOC_GL2 Second order Magnus shooting scheme to solve GYRE pulsation equations. 80–84

COLLOC_GL4 Fourth order collocation scheme to solve GYRE pulsation equations. 80–84

COLLOC_GL4 Fourth order Magnus shooting scheme to solve GYRE pulsation equations. 80–84

COLLOC_GL6 Sixth order collocation scheme to solve GYRE pulsation equations. 80–84

COLLOC_GL6 Sixth order Magnus shooting scheme to solve GYRE pulsation equations. 80–84

EOS equation of state. 3

IGW (non-standing) internal gravity wave. 24

IVP initial value problem. 35

MAMSIE Mixing and Angular Momentum tranSport of massIvE stars. iv

MESA Modules for Experiments in Stellar Astrophysics. x, 31–34, 46, 49, 125

MHD magneto-hydrodynamics. 8, 24, 26, 27, 45

MLT mixing length theory. 4, 32, 50

MS main-sequence. 2, 14, 21, 31, 38, 45, 46

NAC *Nederlandse Astronomenconferentie*. iii, iv

NASA the National Aeronautics and Space Administration. ii, vi, viii, 1, 9

SC Schönberg-Chandrasekhar. 5

SPB stars Slowly pulsating B-type stars. 15, 16, 32, 34

SSE stellar structure and evolution. 1

TAMS terminal age main sequence. 5, 8, 16, 31, 46, 47, 49–51, 56, 57, 59–81, 84, 85, 88

TAR Traditional Approximation of Rotation. vi, 18, 20–23, 34, 45, 87, 89, 107, 110, 133

TESS Transiting Exoplanet Survey Satellite. 1

YSO young stellar object. 1

ZAMS zero-age main sequence. 4, 31, 46, 50, 54, 57, 59–72, 74–82, 85, 88

INSTITUUT VOOR STERRENKUNDE
Celestijnenlaan 200D bus 2401
3000 LEUVEN, BELGIË
tel. + 32 16 37 46 28
www.kuleuven.be